DISS. ETH NO. 21900

Silicon-Based Anode Materials and Conducting Nano Frameworks for Rechargeable Lithium Batteries

A thesis submitted to attain the degree of

DOCTOR OF SCIENCES of ETH ZURICH

(Dr. sc. ETH Zurich)

presented by

Frédéric Martin Hilty

M. Sc. Chemistry, ETH Zurich

born on *12.01.1984*

citizen of Grabs SG

accepted on the recommendation of

Prof. Dr. Reinhard Nesper, examiner

Prof. Dr. Maksym Kovalenko, co examiner

2014

Acknowledgements

First and foremost, I would like to thank Prof. Dr. Reinhard Nesper for giving me the opportunity to work under his guidance. I am very grateful for his constant support, scientific supervision and the high degree of freedom concerning the research of this work.

I want to thank Prof. Dr. Maksym Kovalenko for accepting the task to be my co-examiner.

I would like to extend my gratitude to:

Christian Mensing, for his technical assistance and thermal characterization of my samples.

Dr. Frank Krumeich, for electron microscopy characterization.

Dr. Barbara Hellermann, for her help in administrative issues.

Dr. Serhiy Budnyk, for his advice and the introduction to solid state chemistry synthesis methods.

Dr. Florian Wächter and Dr. Jose Antonio Gonzalez Martinez, for the theoretical and practical introduction to electrochemistry.

My labmates: Dr. Semih Afyon, Dr. Adam Slabon, Michele Furlotti and Fabian von Rohr. It was a lot of fun working with you.

Abstract

Increasing energy demand due to raising world-wide consumption per capita as well as to growing population leads to depletion of fossil fuels and of wood. Alternative energy sources in form of solar-, hydro- and windpower are already widely coming up, but the incorporation of more renewable sources is necessary for a sufficient energy supply. Due to their sporadic nature, electrochemical energy storage through batteries is a promising candidate for intermediate energy storage, to power portable electronic devices and vehicles as well as to support electric power grids on the large scale. This may lead to hierarchical grids with large local power distribution, in future. In this respect, rechargeable lithium batteries are the most promising candidates due to their high energy density, long cycle life as well as variable and relatively fast charge and discharge rates. Graphite is the current anode material used in commercialized Li-ion batteries with a theoretical capacity of 372 mAh g^{-1} and a working potential of 0.5 V vs. Li/Li^{+}. A lot of research was performed in recent years in order to find new solutions which can substitute graphite as an anode material. The most promising one of them seems to be silicon because it combines a lot of advantages: It has the highest known theoretical capacity so far of 4008 mAh g^{-1} ($Li_{21}Si_5$) and a low working potential versus Li metal. Additionally, silicon is highly abundant as the second most frequent element in the Earth's crust. There is a major disadvantage though: The large volume expansion during lithiation and consequently large volume decrease during delithiation leads to fracture of the anode accompanied by loss of electronic contact and thus loss of percolation. Moreover, due to cracking, new surfaces of Si become exposed to electrolyte solvents leading to ongoing deposition of

SEI layers. The electronically insulating SEI does degrade capacity when becoming too thick. These effects lead to a very poor cycling performance for practically all kinds of silicon employment as battery anode, up to now. In this work, various novel approaches are presented trying to circumvent these problems for silicon based anode materials.

In the first chapter, $Li_{12}Si_7$, $Li_{14}Si_6$ and $Li_{13}Si_4$ are examined as starting materials instead of pure Si, reducing the overall relative volume change during cycling by starting from the more voluminous compound stages. This behavior is expected to reduce the fracture and pulverizing of bulk Si-based anodes. Additionally, these compounds are lithiated starting anode materials (as opposed to commercial anode materials which are generally non-lithiated) which may allow to incorporate a higher total amount of Li into the Li ion battery. Synthesis of $Li_{12}Si_7$, $Li_{14}Si_6$ and $Li_{13}Si_4$ as well as their electrochemical performances in the Li ion battery are presented. In addition, carbon based composite of these phases were tested and optimized in order to increase cycling stability of these materials. Furthermore, the deposition of metals through the reaction of lithiumsilicides with transition metal chlorides such as $CuCl_2$ and $NiCl_2$ and their influence on the cycling behavior was examined. The best performance was achieved with a mixture containing $Li_{12}Si_7$, graphite (with a Li to C ratio of 1:6) and 12.5 wt. % $CuCl_2$, whereas 600 mAh g^{-1} was retained after 20 cycles. The deposition of Cu metal upon reaction of $CuCl_2$ with $Li_{12}Si_7$ was shown to have a stabilizing effect in terms of cycling behavior. However, severe capacity fading was still observed for all samples, mainly caused by a growing SEI layer on the surface of particles as shown by post mortem analysis. Insufficient maximum capacity and insufficient cycle life will make further

modifications necessary for a successful implementation of these materials in a Li ion battery.

Furthermore, ternary alkali- and alkaline earth metal lithium silicide compounds were examined which all contain oligo- or polymeric silicon units and as such can be thought of as precursors for nano-silicon materials: Li_3NaSi_6, $CaAl_2Si_2$ and Ca_2LiSi_3. Their structures can be described by arrangements of layered silicon, e.g. polyanionic tubes connected into layers of silicon in Li_3NaSi_6, puckered double layers of $Al_2Si_2{}^{2-}$ in $CaAl_2Si_2$ and planar anionic chains of silicon in Ca_2LiSi_3. For long, specific Zintl phases were known to undergo topochemical reactions which lead to new forms of low dimensional silicon. Recently, a few papers claimed that rod-like nano silicon shows enhanced cycle life in such batteries. Consequently, it was tested whether the topochemically prepared nanoscopic forms of Si would exhibit better electrochemical behaviour upon cycling in Li ion batteries. As a rule of thumb, topochemical decomposition of the chosen compounds is achieved through reaction with selected oxidation agents. A low-dimensional structure is believed to better accommodate the volume changes between the electrochemically active species by the free interparticle spaces and provide for fast Li-diffusion path. A synthesis procedure is described and electrochemical behavior in a Li ion battery analyzed for all three compounds. Furthermore, composite materials upon treatment with various reagents (e.g. $CuCl_2$, graphite and graphene oxide) were synthetized and electrochemically tested.

It is well known that eutectic systems of metals and silicon can be used to fabricate nano particular two-phase products, i.e metal silicide plus nano silicon. This strategy was employed in another section for the four binary systems Ti/Si, Mn/Si, Co/Si and Cu/Si. It is believed that this transition metal silicide arrangement could act as a stable domain to accommodate volume

changes of Si upon cycling in Li ion battery as well as facilitate the diffusion of Li ions to the silicon crystals. Furthermore, transition metal silicides are electronic conductors therefore facilitating electron percolation. On the other hand, these silicides are electrochemically inactive in the Li ion battery, thus preventing lithiation and volume conversion of the matrix material. Indeed, the syntheses yield the expected products which were then tested electrochemically. In all cases anodic behavior was found which can be traced back to the elemental silicon contributions of the samples. The best capacity retentions have been found for the Mn and Cu systems at comparatively low total capacities, though. This may be taken as an indication for surface stabilization due to larger silicon-to-silicide interphase contacts (due to the low Si fraction). However, there may still be a long way to go for making such matrix formulations successful.

In chapter 5, $LiCu_2Si$ was tested as a precursor for a $Cu_{19}Si_6$ ($Cu_{3.17}Si$) based conductive matrix to incorporate the active electrode material. The irreversible in-situ matrix formation upon electrochemical or chemical delitiation of $LiCu_2Si$ is composed of connected amorphous $Cu_{19}Si_6$ particles surrounding the electrochemical active species. The as-formed coppersilicide matrix is a good electronic conductor, electrochemically inert and has a low volume occupancy. Although electrochemical extraction of Li from $LiCu_2Si$ was hindered through surface coating of the binary $Cu_{19}Si_6$, chemical reaction of $LiCu_2Si$ and $FePO_4$ leads to the formation of $LiFePO_4$ and $Cu_{19}Si_6$. Cycling of $LiFePO_4$ was successfully demonstrated in a sample using 10 Vol. % $LiCu_2Si$. Cu precipitation upon reaction of $LiCu_2Si$ and graphite was observed and the as-formed amorphous silicon was identified as the electrochemically active material. The following addition of Si did not improve the cycling behavior of this composite material. The maximum capacity was increased with higher amount of Si, but at

the same time, the rate of capacity decay was enhanced leading to an overall worse cycling behavior.

In the last chapter, methods for carbon coating of micron-sized silicon particles via pyrolysis of organic polymers are examined. The aim of the pyrolysis of a polymer is to form a carbon based matrix which is a good electronic as well as lithium ion conductor and envelops the silicon particles in a proper way. Thus, the volume expansion during lithiation of silicon was expected to be buffered and the formation of SEI controlled. Three different types of polymers were examined: polyacrylonitrile (PAN), polyvinylpyrrolidone (PVP) and polystyrene (PS). They are all elastomers which melt during the heating process and coat the silicon particles evenly. Additionally, lactose monohydrate was examined as a carbon source in analogous manner. PAN shows the best coating behavior in terms of carbon amount formed as well as electrochemical performance. PVP has lower C residue, whereas in the case of PS, carbon coating is almost non-existent. Pyrolysis of lactose shows good carbon coating, while no accompanying oxidation of Si particles was observed. In addition, by systematic film thickness investigations it was found that mechanical film stability and diffusion behavior are only granted for very thin films – by extrapolation at around 20 μm thickness, only. The best electrochemical performance was achieved by a 150 μm thin film of a Si / PAN mixture with a weight ratio of 4:1 treated at 750 °C for 6 h in argon. A stable charge capacity > 1100 mAh g^{-1} was observed over 80 cycles when discharge capacity was limited to 1200 mAh g^{-1}.

All results of this work imply that even more flexible matrices have to be developed for a successful employment of large capacity silicon anodes in Li-ion batteries. If so in future, many of the here explored ways of producing low dimensional silicon materials and their composites by electrochemical in-situ methods may render valuable due to easiness of process and of low production costs.

Kurzfassung

Der erhöhte Energieverbrauch pro Kopf sowie die stetig wachsende Weltbevölkerung führen zum Abbau von Erdgas und Brennholz. Alternative Energiequellen wie Solar-, Wind und Hydroenergie werden bereits rege genutzt. Wegen deren sporadischen Charakters sind in Zukunft speicherfähige Netzwerke von grosser Bedeutung, die - wenn möglich - lokale Speicherformen anbieten. Die elektrochemische Energiespeicherung ist eine dafür geeignete Form, welche immer stärker für tragbare elektronische Geräte eingesetzt wird. Wiederaufladbare Lithium Ionen Batterien eignen sich besonders für diesen Zweck durch ihre hohe Energiedichte, lange Lebensdauer sowie vergleichsweise schnelle und variable Ladungs- und Entladungsraten. Graphit ist das gegenwärtige Anodenmaterial in herkömmlichen Lithium Ionen Batterien mit einer theoretischen Kapazität von 372 mAh g^{-1} und einem Potential von 0.5 V gegen Li/Li$^+$. In den letzten Jahren wurden immense Nachforschungen betrieben auf der Suche nach neuen Materialien um Graphit als Anodenmaterial zu ersetzen. Am meisten Erfolg verspricht hierbei Silizium durch die Kombination mehrerer Vorteile: die höchste bekannte theoretische Kapazität von 4008 mAh g^{-1} ($Li_{21}Si_5$) sowie einer tiefer Spannung gegenüber Lithium Metall betreffend der Aufnahme und Abgabe von Lithium. Zusätzlich ist Silizium nach Sauerstoff das am Häufigsten anzutreffende Element in der Erdkruste; ein reichhaltiger Bestand ist gewährleistet. Allerdings existiert hierbei ein bedeutendes Problem: Die enorme Volumenänderung durch Aufnahme und Abgabe von Lithium führt zur Pulverisierung der Elektrode und dem Verlust des elektrischen Kontakts. Des Weiteren führt dies zu einer zusätzlichen Abscheidung der SEI Schicht auf der nunmehr freigelegten Oberfläche von Silizium Partikeln durch Kontakt mit der Elektrolytlösung. Das

Wachsen dieser isolierenden Schicht wirkt sich negativ auf die Erhaltung der Kapazität aus. Die Kombination dieser Effekte führt zu einer mangelhaften Zyklierung. In dieser Arbeit werden mehrere mögliche Lösungsvorschläge vorgestellt um die Probleme von Silizium-basierten Anodenmaterialien zu beheben.

Im ersten Kapitel wurden $Li_{12}Si_7$, $Li_{14}Si_6$ und $Li_{13}Si_4$ als Elektrodenmaterialien an Stelle von Silizium untersucht. Die Verwendung dieser ausgedehnten Phasen als Startmaterial reduziert die gesamthafte relative Volumenänderung. Dadurch wird die Fraktur und Pulverisierung von Silizium-basierten Anoden vermindert. Zusätzlich ermöglicht die Verwendung dieser lithiierten Verbindungen einen höheren Lithiumgehalt in der Lithium Ionen Batterie, da herkömmliche Anodenmaterialien nicht lithiiert sind. Die Synthese von $Li_{12}Si_7$, $Li_{14}Si_6$ und $Li_{13}Si_4$ sowie deren elektrochemische Leistung in der Lithium Ionen Batterie werden vorgestellt. Kohlenstoff-basierte Verbundstrukturen wurden getestet und optimiert um die Zyklierung dieser Materialien zu verbessern. Zusätzlich wurde die Abscheidung von Metall durch Reaktion von Lithiumsiliziden mit Übergangsmetall Chloriden wie $CuCl_2$ und $NiCl_2$ untersucht sowie deren Einfluss auf die Erhaltung der Kapazität getestet. Die beste Leistung wurde von einer Mischung erzielt, die $Li_{12}Si_7$, Graphit (mit einem Li zu C Verhältnis von 1:6) und 12.5 Massenprozent $CuCl_2$ enthält. Hierbei konnte eine Kapazität von 600 mAh g^{-1} nach 20 Zyklen bewahrt werden. Es wurde gezeigt, dass die Abscheidung von elementarem Kupfer durch Reaktion von $CuCl_2$ mit $Li_{12}Si_7$ das Zyklierungsverhalten stabilisiert. Dennoch wurde für alle Proben ein schwerwiegender Zerfall der Kapazität mit zunehmender Anzahl Zyklen beobachtet. Dies ist hauptsächlich durch das ständige Anwachsen der SEI Schicht auf der Oberfläche der aktiven Teilchen bedingt, was durch post mortem Analyse gezeigt wurde. Eine ungenügende maximale Kapazität sowie

eine nicht zufrieden stellende Zyklierung bedingen weitere Modifikationen dieser Materialien um eine erfolgreiche Verwendung innerhalb der Lithium Ionen Batterie zu ermöglichen.

Des Weiteren wurden ternäre Alkali- und Erdalkalimetall Lithiumsilizid Verbindungen untersucht, welche oligo- oder polymere Silizium Einheiten aufweisen und daher als Ausgangsstoffe für nano-Silizium in Frage kommen: Li_3NaSi_6, $CaAl_2Si_2$ und Ca_2LiSi_3. Deren Aufbau lässt sich durch Silizium Schichtstrukturen beschreiben: Polyanionische Tunnel aus Si in Li_3NaSi_6, $Al_2Si_2^{2-}$ Doppelschichten in $CaAl_2Si_2$ und planare anionische Ketten aus Silizium in Ca_2LiSi_3. Seit Langem ist bekannt dass durch topochemische Reaktionen von bestimmten Zintl Phasen neue Formen von Silizium entstehen. Kürzlich wurde eine verbesserte Zyklierung von Stabförmigen nano-Silizium in mehreren Publikationen berichtet. Es wurde daher untersucht, ob solche topochemisch gebildeten, nanoskopischen Formen von Si ein besseres Zyklierungsverhalten in der Lithium Ionen Batterie aufweisen. Topochemische Zersetzung der vorgestellten Verbindungen erfolgt hierbei durch eine Reaktion mit ausgewählten Oxidationsmitteln. Es wird vermutet dass eine Struktur niederer Dimension die Volumenänderung der elektrochemisch aktiven Spezies durch freie Räume zwischen den Partikel ausgleichen kann sowie einen schnellen Lithium Ionen Diffusionspfad bereitstellt. Für alle drei Verbindungen wurden Synthesevorschriften gezeigt sowie das elektrochemische Verhalten in der Lithium Ionen Batterie analysiert. Des Weiteren wurden Verbundstruktur Materialien durch Reaktion mit verschiedenen Reagenzien ($CuCl_2$, Graphit und Graphen Oxid) hergestellt und elektrochemisch getestet.

Es ist weitläufig bekannt, dass eutektische Systeme von Metallen und Silizium zur Herstellung spezieller nano Produkte zweier Phasen verwendet werden: Metallsilizide und nano Silizium. Dieses Verfahren wurde für die folgenden vier

binären Systeme angewandt: Ti/Si, Mn/Si, Co/Si und Cu/Si. Es wird vermutet, dass die Anordnung der Übergangsmetallsilizid-partikel um Silizium eine stabile Domäne bildet, was die Volumenänderung von Letzterem während des Zyklierens in der Lithium Ionen Batterie ausgleicht sowie die Diffusion der Lithium Ionen zu den Silizium Kristallen erleichtert. Des Weiteren wird der Elektronenfluss durch die elektrische Leitfähigkeit der Übergangsmetallsilizide unterstützt. Zudem sind diese Verbindungen elektrochemisch inaktiv in der Lithium Ionen Batterie für ausgewählte Spannungsbereiche. Daher wird Lithiation und Volumenänderung des Matrixmaterials verhindert. Die Synthesen führten zu den erwarteten Produkten, welche dann elektrochemisch getestet wurden. In allen Fällen wurde anodisches Verhalten beobachtet was auf die Anwesenheit von elementarem Silizium zurückzuführen ist. Das beste Zyklierungsverhalten wurde für Systeme mit Mangan und Kupfer erhalten, jedoch mit vergleichsweise tiefen Werten der Kapazität. Dies könnte auf eine Oberflächenstabilisierung hinweisen aufgrund ausgedehnter Kontaktstellen der Phasen Silizium und Metallsilizid bedingt durch einen kleineren Si Anteil. Dennoch wird es noch ein langer Weg sein bis zur Herstellung einer solchen viel versprechenden Matrixstruktur.

In Kapitel 5 wurde $LiCu_2Si$ als Ausgangsstoff für eine $Cu_{19}Si_6$ ($Cu_{3.17}Si$) basierte leitfähige Matrix untersucht, welche das aktive Elektrodenmaterial einschliessen soll. Die irreversible in-situ Bildung dieses Grundgerüstes erfolgt durch die elektrochemische oder chemische Entfernung von Lithium aus $LiCu_2Si$ und führt zu einer Struktur bestehend aus verbunden amorphen $Cu_{19}Si_6$ Partikeln, welche die elektrochemisch aktiven Teilchen umschliessen. Die so geformte Kupfersilizid Matrix ist ein guter elektrischer Leiter, elektrochemisch inert und kompakt. Elektrochemische Extraktion von Lithium aus $LiCu_2Si$ war nicht erfolgreich; jedoch führte die chemische Reaktion von $LiCu_2Si$ und $FePO_4$

zur Bildung von $Cu_{19}Si_6$ und $LiFePO_4$. Die Zyklierung von Letzterem in der Lithium Ionen Batterie wurde in einer Mischung bestehend aus $FePO_4$ und 10 Gewichtsprozent $LiCu_2Si$ erfolgreich nachgewiesen. Die Abscheidung von elementarem Kupfer durch Reaktion von $LiCu_2Si$ mit Graphit wurde beobachtet und dadurch entstandenes amorphes Silizium als elektrochemisch aktives Material identifiziert. Die darauf folgende Zugabe von Si führte zu keiner Verbesserung des Zyklierungsverhalten. Zwar wurde die maximale Kapazität wurde durch steigenden Gehalt an Silizium erhöht, jedoch führte dies auch zu einem schnelleren Zerfall der Kapazität und somit zu einem schlechteren Zyklierungsverhalten.

Im letzten Kapitel wurden Methoden zur Kohlenstoffbeschichtung von Mikrometer Siliziumpartikel durch Pyrolyse von organischen Polymeren untersucht. Durch diesen Prozess soll eine Kohlenstoff-basierte Matrix geformt werden, welche ein guter Leiter für Lithium Ionen sowie elektrische Ladungen darstellt und die Siliziumteilchen vollständig umschliesst. Hierbei wird die Volumenausdehnung von Silizium durch Aufnahme von Lithium ausgeglichen und die Bildung der SEI Schicht kontrolliert. Drei verschiedene Polymere wurden untersucht: Polyacrylnitril (PAN), Polyvinylpyrrolidon (PVP) und Polystyrol (PS). Diese Elastomere schmelzen während des Heizprozesses und umschliessen die Si Partikel gleichmässig. Zusätzlicher wurde Laktose Monohydrat als Kohlenstoffquelle in analoger Weise untersucht. PAN weist das beste Beschichtungsverhalten auf bezüglich geformter Kohlenstoffmenge sowie elektrochemischer Leistung. Pyrolyse von PVP führt zu einem geringeren Rückstand an Kohlenstoff, wo hingegen die Kohlenstoffbeschichtung durch Pyrolyse von PS beinahe nicht vorhanden ist. Die Pyrolyse von Laktose führt zu einer gleichmässigen Kohlenstoffbeschichtung; eine zeitgliche Oxidation der Silizium Partikel wurde nicht beobachtet. Zusätzlich wurde durch eine

systematische Studie der Dicke von Elektrodenfilmen gezeigt, dass die mechanische Stabilität und ein optimales Diffusionsverhalten nur für sehr dünne Filme garantiert ist. Die Dicke solcher Filme wurde durch Extrapolation auf 20 µm bestimmt. Ein 150 µm dünner Elektrodenfilm einer Mischung bestehend aus Si und PAN in einem Massenverhältnis von 4:1, welche bei 750 °C für 6 h unter Argon behandelt wurde, zeigte die die beste elektrochemische Leistung in der Lithium Ionen Batterie: Für eine Begrenzung der Entladekapazität auf 1200 mAh g^{-1} wurde eine stabile Ladekapazität > 1100 mAh g^{-1} für 80 Zyklen gewährleistet.

Die Resultate dieser Arbeit zeigen auf, dass für die erfolgreiche Verwendung von Silizium-basierten Anoden mit hoher Kapazität in der Lithium Ionen Batterie die Entwicklung noch flexiblerer Matrizen nötig ist. Die hier vorgestellten Wege zur Produktion von Silizium Materialien tiefer Dimension sowie deren Verbundstrukturen durch elektrochemische in-situ Methoden können für künftige Experimente in dieser Richtung von grossem Nutzen sein aufgrund der einfachen Herstellung sowie geringen Kosten.

Abbreviations

CV	Cyclic voltammetry
DMC	Dimethyl carbonate
DTA	Differential thermal analysis
EC	Ethylene carbonate
EDX	Energy dispersive X-ray
EELS	Electron energy loss spectroscopy
EV	Electric vehicles
HAADF	High angle annular dark field
HV	Hybrid vehicles
NMP	N-methyl-2-pyrrolidone
OCV	Open circuit voltage
PAN	Polyacrylonitrile
PHEV	Plug-in hybrid electric vehicles
PP	Polypropylene
PS	Polystyrene
PVDF	Polyvinylidene fluoride
PVP	Polyvinylpyrrolidone
SEI	Solid electrolyte interface
SEM	Scanning electron microscopy
TEM	Transmission electron microscopy
THF	Tetrahydrofuran
XRD	X-ray diffraction

Table of Contents

1. Introduction

1.1. Energy Storage

Hydrocarbon fossil fuels and wood are the easiest way to access stored energy. However, increasing energy demand due to new technologies as well as growing population leads to depletion of these sources which are not infinitely available on earth. Combined with environmental effects like pollution and global warming due to the emission of CO_2, the search for sustainable and clean energy sources has become more and more important in recent years. Alternative energy sources in form of solar-, hydro – and windpower belong to this class. Although already widely used, the sporadic nature of such sources (solar- and windpower) as well as eventual impairment of the ecosystem (hydropower) demand for the incorporation of other wide-spread and very efficient storage devices for a satisfactory energy supply.

Electrochemical energy storage through batteries is a promising candidate, not only for powering portable electronic devices and vehicles but also for supporting electric power grids on the large scale. Although rechargeable batteries are widely used in portable devices like laptops, watches and calculators, combustion engine vehicles are still the dominant species in the car market. They have fairly low energy efficiency and give rise to a strong CO_2 footprint. That is why more and more efforts are being taken in order to replace combustion technology by full electric (EV) or hybrid vehicles (HV). For the latter one, plug-in hybrid vehicles (PHEV) contain both an electric motor as well as an internal combustion engine. Due to the low power of nickel-metal hydride batteries used in these vehicles, only short driving ranges are possible by electrochemical power, whereas the combustion engine provides the necessary energy for longer distances.

Rechargeable lithium batteries are the most promising candidates to deliver electric energy for PHEVs as well as for full EVs due to their high energy density, long cycle life as well as variable and fast charge and discharge rates. Up to date, electrical vehicles powered by lithium ion batteries based on $LiFePO_4$ and graphite provide a driving range up to 160 km, which is not yet competitive with combustion engine cars.[1-3] However, the search of new materials for those batteries is believed to be able to substantially improve specific energies in order to increase this range drastically.

High energy lithium ion batteries are also considered for supporting electric power grids balancing sporadic and inconstant energy sources like wind turbines. For this purpose, a powerful standby energy source is necessary once again identifying lithium batteries as the most promising candidate here.

In addition to the improvement of current lithium ion batteries by incorporation of new materials, other problems and barriers, such as cost and safety issues have to be overcome in order to commercialize this technology in the as mentioned fields.

1.2. Electrochemical energy storage in batteries

Spontaneous redox reactions are the basis for generation of electric energy in electrochemical cells. In an electrolytic cell, an external current is applied in order to power such a reaction meaning that electrical energy is converted into chemical energy. On the other hand, a difference in chemical potential of two phases, compounds and materials in a full galvanic cell leads to an electron flow therefore converting chemical into electrical energy. One of the oldest and best known galvanic cells is the Daniel element, which is displayed in Figure 1.1.
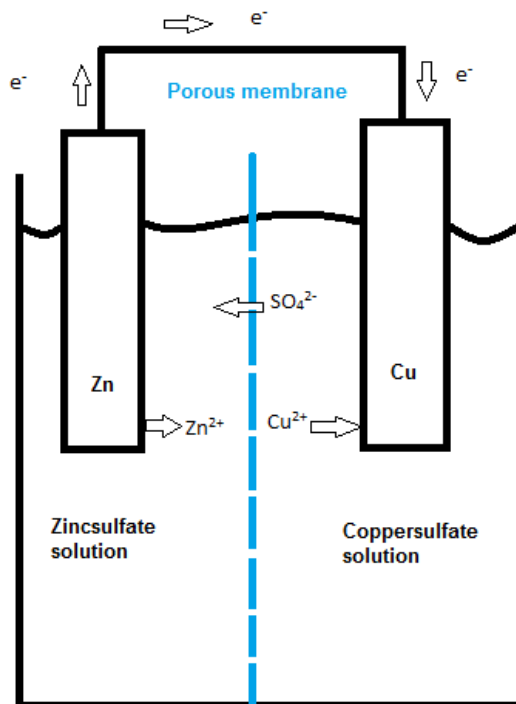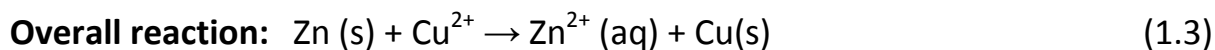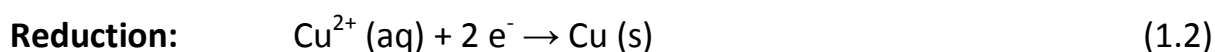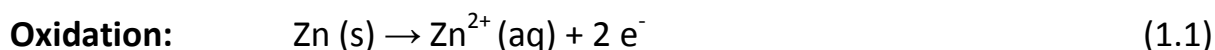
Fig. 1.1: Schematic representation of the "Daniel element".

In a galvanic cell, the oxidation and reduction process are spatially separated into two half cells by a porous membrane or a salt bridge. In order to maintain charge balance, an electrolyte solution contains ions which are able to pass this ion conducting link. Electrons are transferred through an external circuit from the anode to the cathode. This electron flow leads to the generation of a current. In a Daniel element, the two half cells are made up by Cu and Zn metal electrodes, whereas zinc is oxidized at the anode (negative pole) and Cu^{2+} is reduced at the cathode (positive pole). The half-cell reactions as well as the corresponding overall balance are shown below:

Oxidation: $Zn\ (s) \rightarrow Zn^{2+}\ (aq) + 2\ e^-$ (1.1)

Reduction: $Cu^{2+}\ (aq) + 2\ e^- \rightarrow Cu\ (s)$ (1.2)

Overall reaction: $Zn\ (s) + Cu^{2+} \rightarrow Zn^{2+}\ (aq) + Cu(s)$ (1.3)

The standard electrode potential E^0 of a half cell depends on the standard Gibbs free energy of the chemical reaction, whereas ΔG_r^0 denotes the difference between standard Gibbs free energy of products and of educts. E^0 can be calculated according to:

$$E^0 = \frac{-\Delta G_r^0}{zF} \tag{1.4}$$

The number of transferred electrons is denoted by z and F is the Faraday constant (96'485 C mol^{-1}). Variations from standard conditions in terms of pH, temperature and concentration are taken into account by the Nernst equation (1.5):

$$E = E^0 - \frac{RT}{zF} \sum_i \ln a_i^{v_i} \tag{1.5}$$

The gas constant is denoted by R, T is the absolute temperature and a_i as well as v_i are the activity and stoichiometric coefficient of the species i, respectively.

The cell voltage of an electrochemical cell ΔE^0 is calculated from the electrode potentials of the half-cell reactions, whereas the negative electrode potential (anode) is subtracted from the positive electrode potential (cathode):

$$\Delta E_{cell}^0 = E_{cathode}^0 - E_{anode}^0 \tag{1.6}$$

With standard reduction potentials of -0.76 V for Zn / Zn^{2+} and + 0.34 V for Cu / Cu^{2+} using standard hydrogen electrode as reference electrode, the standard cell voltage of the Daniel element is calculated to be 1.10 V.

Based on the reversibility of electrochemical reactions, batteries can be categorized into primary and secondary ones. Primary batteries can be used for one irreversible discharge meaning they are not rechargeable or reloadable. They are widely used in small electronics like calculators and watches. The most commonly employed batteries of this type are Alkaline (Zn/MnO_2), Zinc-air (Zn/O_2) and Lithium (Li/MnO_2) with practical working potentials of 1.5, 1.4 and 3.0 V, respectively. Secondary batteries are rechargeable due to reversibility of electrochemical reactions. Although they generate higher initial costs than primary batteries, they are cheaper during their life-time. One of the oldest and well known secondary battery is the Lead-acid battery (Pb/PbO_2), which is used to power starting system of combustion engines. Lithium ion batteries also belong to this class and are nowadays mostly used to power portable electronics like laptops and smartphones due to their high specific energy.

1.3. Relevant definitions and concepts

1.3.1. Battery characterization

In this section, important parameters and definitions for battery characterization are described.

Anode: The electrode with the lower chemical potential.

Cathode: The electrode with the higher chemical potential.

Charge and Discharge: Electrical energy is produced by spontaneous electrochemical reactions during discharge, whereas an external current is applied in order to reverse these reactions during charging.

Current density: The amount of current I flowing through the electrode area A.

$$j(t) = \frac{I(t)}{A} \tag{1.7}$$

Capacity: The amount of charge delivered by a cell.

$$Q = \int_{t_1}^{t_2} I(t)dt \quad [Ah] \tag{1.8}$$

Theoretical specific charge capacity q_{th} and theoretical specific charge density $Q_{V,th}$: The amount of charge per mass unit *m* or volume unit *V* of the electrochemically active material, respectively.

$$q_{th} = \frac{zF}{\sum_i m_i} = \frac{1}{m} Q \quad [\frac{Ah}{kg}] \tag{1.9}$$

$$Q_{V,th} = \frac{zF}{\sum_i V_i} = \frac{1}{V} Q \quad [\frac{Ah}{l}] \tag{1.10}$$

Theoretical specific energy w_{th} and theoretical specific energy density $W_{V,th}$:
The total amount of energy per mass unit m or volume unit V of the electrochemically active material, respectively, whereas energy is obtained by multiplication of cell voltage and capacity.

$$w_{th} = q_{th} * \Delta E^0 = \frac{zF\Delta E^0}{\sum_i m_i} = \frac{1}{m} \int_{t_1}^{t_2} I(t)U(t)dt \quad [\frac{Wh}{kg}] \qquad (1.11)$$

$$W_{V,th} = Q_{V,th} * \Delta E^0 = \frac{zF\Delta E^0}{\sum_i V_i} = \frac{1}{V} \int_{t_1}^{t_2} I(t)U(t)dt \quad [\frac{Wh}{l}] \qquad (1.12)$$

Specific power and power density: The amount of power per mass unit m or volume unit V, respectively, whereas power is obtained by multiplication of current I and voltage U of an electrical device.

$$P = \frac{IU}{\sum_i m_i} \quad [\frac{W}{kg}] \qquad (1.13)$$

$$P = \frac{IU}{\sum_i V_i} \quad [\frac{W}{l}] \qquad (1.14)$$

Coulombic efficiency: The ratio of charge to discharge capacity for a given cycle.

C-rate: Applied current rate to charge or discharge a battery. C denotes the theoretical specific capacity and n the number of hours to reach theoretical capacity. Therefore, rates of C/2 and C/10 correspond to a current for full charge or discharge in 2 and 10 hours, respectively.

1.3.2. Electrochemical characterization

Investigated materials in this study were tested in Swagelok-type electrochemical cells as shown in Figure 1.2.
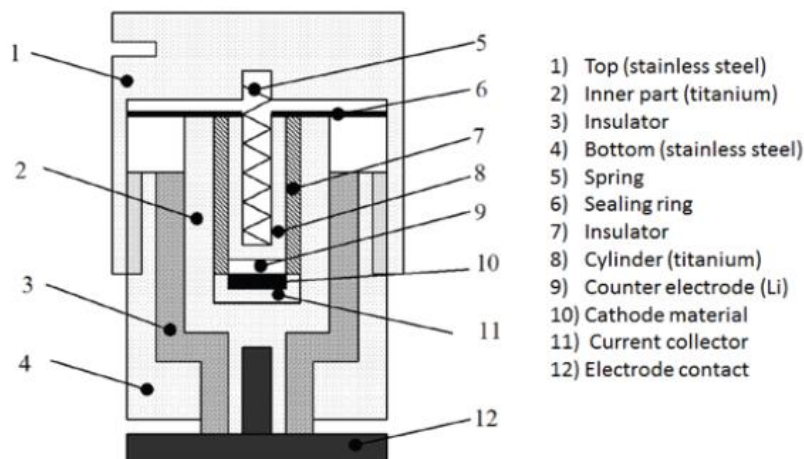

1) Top (stainless steel)
2) Inner part (titanium)
3) Insulator
4) Bottom (stainless steel)
5) Spring
6) Sealing ring
7) Insulator
8) Cylinder (titanium)
9) Counter electrode (Li)
10) Cathode material
11) Current collector
12) Electrode contact

Fig. 1.2: Swagelok-type cell for electrochemical measurement.[4]

Electrochemical cells were constructed in an argon filled glove box, whereas the outer part of the cell is made of a stainless steel and inner parts in contact with electrochemically active materials are made of titanium: *Lithium metal disks with a diameter of 13 mm prepared from 0.75 mm thick Li ribbon (Aldrich) are used as counter electrodes. The working electrode containing the investigated material is placed on a titanium current collector, where the electrode is made of a thin film containing active material, conductive carbon additives and binder. This electrode is covered by a polypropylene (PP) (Celgard®) separator followed by a second silica separator on top, which is soaked in liquid electrolyte.*

Electrochemical measurements were performed at room temperature in a two electrode configuration using a BAT-SMALL potentiostat and ASTROL software

8

package (both from Astrol Electronic AG). The electrochemical behavior of the investigated materials was analyzed through galvanostatic and cyclic voltammetry tests. For the latter one, the potential is varied with a constant rate over a chosen potential window and the measured current flow is plotted against voltage. Positive values denote oxidation (anodic) and negative values reduction (cathodic) processes. This kind of measurement is particularly useful in determining potential values for different redox processes therefore identifying binding energies of electrochemically active species. During galvanostatic cycling, a constant current is applied through a fixed potential window whereas potential is plotted against time or capacity.

1.4. Rechargeable lithium batteries

Among metals, lithium is the most electropositive (-3.04 V versus standard hydrogen electrode) as well as the lightest one with a molar mass of 6.94 g mol^{-1} identifying Li metal anodes as promising candidates for the design of storage systems with a high energy density. Already in the 1970s, primary non-rechargeable Li batteries like Li/MnO_2 were commercialized.[5] During the same period, various inorganic compounds were reported to undergo reversible insertion and extraction of lithium therefore initializing the design of rechargeable secondary Li batteries. In 1972, Exxon reported the first rechargeable lithium ion battery using a TiS_2 as cathode, Li metal as anode and lithium perchlorate in dioxolane as electrolyte.[6] TiS_2 has a layered structure which undergoes reversible intercalation of lithium. Subsequent research for positive electrode materials led to the discovery of transition metal oxides which represent intercalation materials with higher binding energies and thus with higher voltages. In the 1980s, Goodenough et al. reported the layered structures Li_xMO_2 (M = Co, Ni or Mn) which displayed working potentials up to

4 V vs. Li/Li$^+$ and excellent insertion properties.[7-12] However, the dendritic growth of lithium on extensive cycling was a serious safety issue in terms of explosion hazards, which implied the need for a safer negative electrode material. The substitution of metallic Li for a negative insertion material led to the concept of the Li-ion rocking chair technology, whereas Li is present in a "pseudo ionic" rather than metallic state therefore solving the problem of dendritic growth[13-14] through reversible intercalation of Li$^+$ ions into graphite at voltage very close to Li/Li$^+$. Therefore Li metal was replaced as anode material and graphite anode became the choice for lithium ion batteries, up to date.[15] In 1991, SONY Corp. commercialized the C/LiCoO$_2$ rocking chair cell with a potential exceeding 3.6 V and specific energy of ca. 150 W h kg^{-1}, which is shown in Figure 1.3.[16]

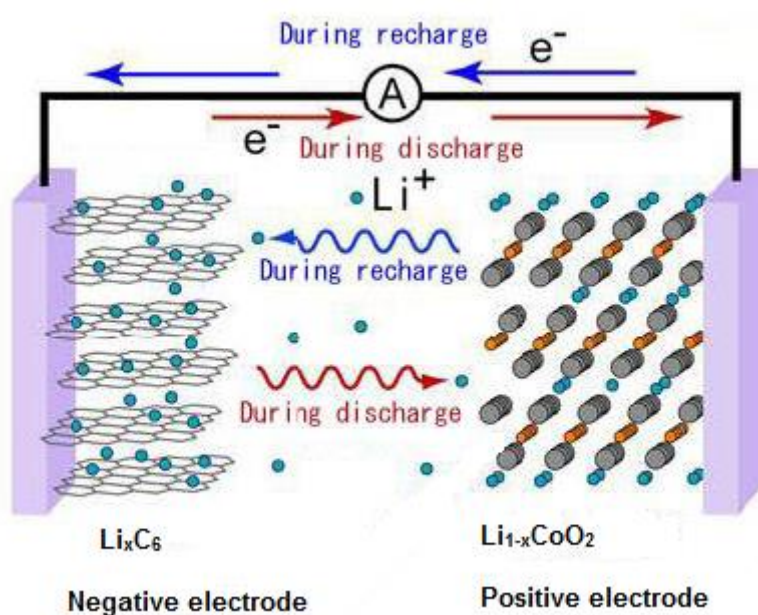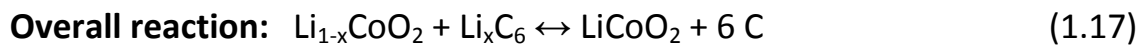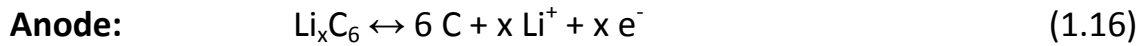During recharge e$^-$

e$^-$ During discharge

• Li$^+$

During recharge

During discharge

Li$_x$C$_6$ Li$_{1-x}$CoO$_2$

Negative electrode   Positive electrode

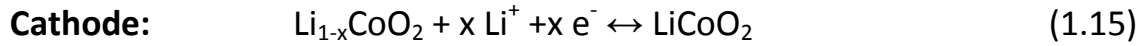*Fig. 1.3:* Schematic representation of the LiCoO$_2$ / C rocking-chair battery.[17]

During discharge, oxidation of the negative host (graphite) occurs accompanied by extraction of lithium ions and insertion of lithium ions into the positive host material (Li$_{1-x}$CoO$_2$), whereas the latter one is reduced. This process is reversed

during charge. These reversible reactions are formulated in the equations given below:

Cathode: $Li_{1-x}CoO_2 + x\ Li^+ + x\ e^- \leftrightarrow LiCoO_2$ (1.15)

Anode: $Li_xC_6 \leftrightarrow 6\ C + x\ Li^+ + x\ e^-$ (1.16)

Overall reaction: $Li_{1-x}CoO_2 + Li_xC_6 \leftrightarrow LiCoO_2 + 6\ C$ (1.17)

Usually, a lithium salt in an organic solvent is used as electrolyte, whereas $LiPF_6$ in a mixture of ethylene carbonate (EC) and dimethyl carbonate (DMC) is the most common one. Compared to other secondary batteries, Li ion batteries have the advantage of high energy density, long cycle life, low self-discharge rates as well as minimized use of electrolytes since it is not directly involved in the electrochemical reactions. In order to further increase specific energy of the lithium ion battery, the search for new cathode materials with high working potentials and specific capacities as well as anode materials with high specific capacities is of great interest. Such materials are discussed in the following section.

1.4.1. Positive electrode materials

Widely used anode materials have working potentials close to the Li $/Li^+$ reference potential and capacities two to three times as large as cathode materials. This implies that the overall cell potential of a lithium ion battery can mainly be tuned by the positive electrode materials, therefore identifying them as important and extensively studied future targets. For a successful implementation of electropositive materials in a lithium ion battery, various requirements need to be fulfilled like high specific energy due to light weight and high operating potentials, structural stability during lithiation and

11

delithiation as well as reversibility of those electrochemical reactions, good electronic and ionic conductivity as well as low cost and low toxicity precursors and products. Selected positive electrode materials are described and discussed in the following subsections.

1.4.1.1. Layered transition metal oxides

The isostructural compounds Li_xMO_2, where M = Co, Mn and Ni, belong to this class, whereas $LiCoO_2$ is the most famous one since it has been the cathode material of choice for a long time since commercialization of lithium ion batteries. $LiCoO_2$ can be described as α-$NaFeO_2$ type layered structure which is depicted in Figure 1.4 below.
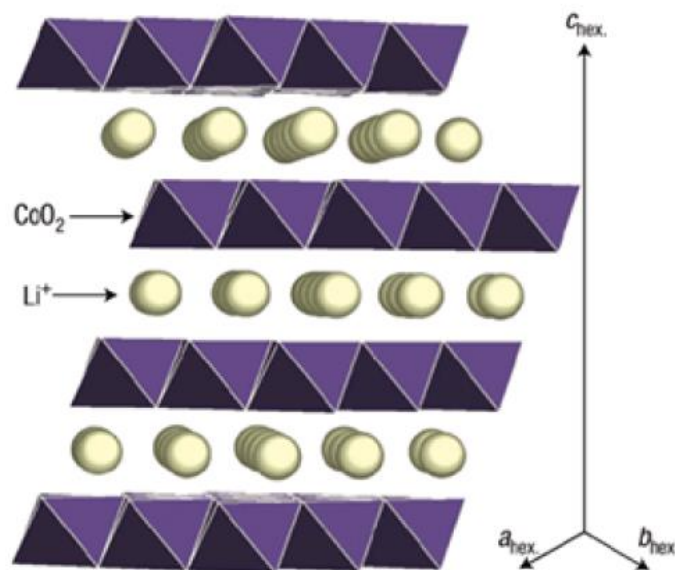

Fig. 1.4: Crystal structure of $LiCoO_2$ in a skew [110] projection.[18]

In a reversible way up to x = 0.5 lithium can be extracted and inserted into $Li_{1-x}CoO_2$ leading to a specific capacity of 140 mAh g^{-1} at 4.2 V vs. Li / Li^+.[19, 20] Extraction of lithium at x > 0.5 leads to the formation of unstable CoO_2

intermediates, which show development of molecular oxygen leading to electrolyte decomposition and eventually to ignition of the battery. [21, 22] The high world market price of cobalt as well as the abovementioned safety issues led to the development of layered transition metal oxides $LiCo_xMn_yNi_zO_2$ (with x + y + z = 1) containing multiple metal centers. These compounds were used in so-called core shell structures, where the concentration of transition metals is varied from bulk to the surface in order to optimize the electrochemical properties such that compositions on the surface were designed to have maximum stability against the electrolyte while the core consists of less stable but high capacity compositions.[23, 24] However, complicated and expensive synthesis keeps these compounds away from commercialization.

1.4.1.2. Spinel structure based compounds

$Li_xMn_2O_4$ has a cubic spinel structure, whereas Li^+ and $Mn^{3+/4+}$ ions occupy the tetrahedral and octahedral sites in a cubic-closed O^{2-} package. [23] The crystal structure of $LiMn_2O_4$ is shown in Figure 1.5 below.
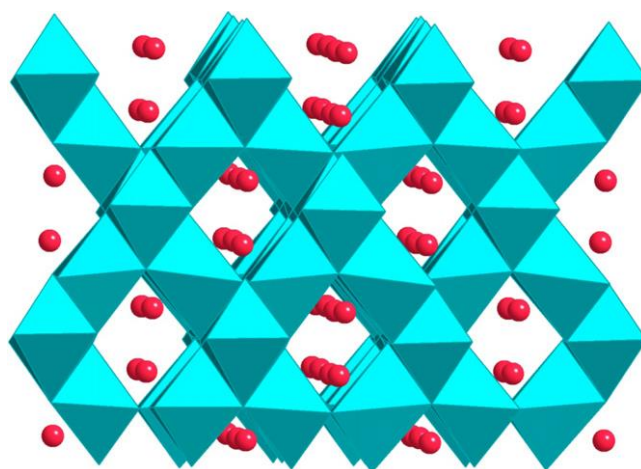
*Fig. 1.5:* Crystal structure of $LiMn_2O_4$, where Li^+ ions are depicted in red and MnO_6 octahedra in cyan, respectively. [25]

$LiMn_2O_4$ has a theoretical capacity of 148 mAh g^{-1} and a practical capacity of 120 mAh g^{-1} at 4.1 V vs. Li/Li^+ was reported. [26-29] Disproportion of Mn^{3+} to Mn^{2+} and Mn^{4+} leads to etching of this phase and was identified as the main effect responsible for insufficient cycling behavior. It is due to the solubility of Mn^{2+} species in the electrolyte. [30-31] This problem can be partially solved by applying surface coatings as well as metal site doping. [32-34]

1.4.1.3. Olivine-type phosphates

$LiFePO_4$ has an olivine type crystal structure consisting of FeO_6 and LiO_6 octahedra as well as phosphate groups. The crystal structure is shown in Figure 1.6 below.
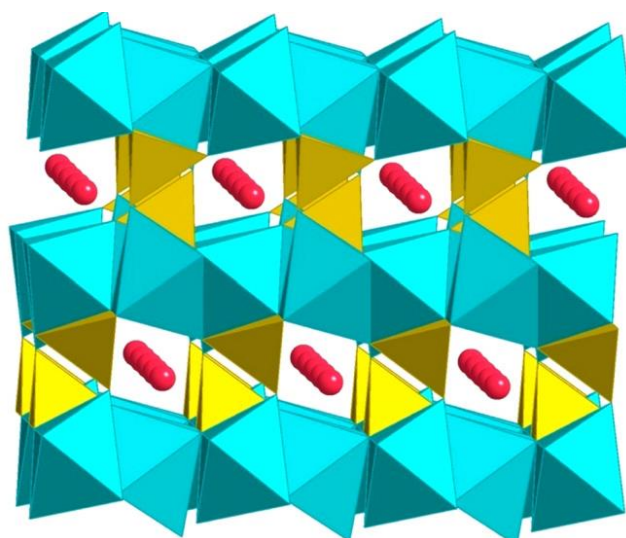
Fig. 1.6: Crystal structure of $LiFePO_4$; lithium ions are depicted in red, FeO_6 octahedra in cyan and PO_4^{3-} tetrahedra in yellow. [25]

The use of $LiFePO_4$ as cathode material in lithium ion batteries was first reported by Goodenough et al. in 1997.[35] $LiFePO_4$ has a theoretical specific capacity of 170 mAh g^{-1} at a working potential of 3.5 V against Li metal

determined by the Fe^{2+}/Fe^{3+} redox couple. The insertion and extraction of lithium is a two phase reaction resulting in a flat voltage profile; the non-lithiated phase $FePO_4$ has the same structure type as $LiFePO_4$.[36] However, due to the low electronic conductivity of $1x10^{-9}$ S cm^{-1} at room temperature, phosphates only show electrochemical activity when conductive coatings are employed on nano particular products.[37] Using these techniques, practical capacities close to the theoretical ones were obtained by various research groups at very high current rates and with excellent cycling behavior.[38-42] So far, $LiFePO_4$ is currently the best positive electrode material for lithium ion batteries due to high rate capability and excellent capacity retention as well as low cost and environmental friendliness of its elements.

1.4.2. Negative electrode materials

In the early stages of the development of the Li ion battery, various problems were identified when elemental lithium was used as negative electrode. The stochastic growth processes on a flat electrode surface during electro-deposition of lithium metal leads to the formation of dendrites during extensive cycling. This dendritic growth can lead to a possible shortcut of the battery. Additionally, organic solvent electrolytes are not stable in the presence of elemental lithium activity and react with lithium to form steadily growing crystalline or amorphous product layers on the surface of the electrode. These reactions are exothermic and cause local heating. In combination with an increase of surface area of lithium due to dendritic growth, this process can lead to a thermal runaway [43] generating serious safety risks. Consequently, the use of elemental lithium as electrode material was abandoned.   New anode materials with high specific capacities and good cycling properties had to be

developed with very low cell potentials. At potentials above 0.5 V vs. Li / Li$^+$ dendritic growth of lithium is suppressed and safety of the battery is raised. However that means that a compromise between energy density and safety needs to be taken into account.

1.4.2.1. Insertion materials

The most common insertion material of this class is graphite, which consists of graphene layers stacked onto each other in alternate ways forming either an ABAB or an ABC sequence. Graphene itself consists of interconnected hexagon net formed by sp^2 hybridized carbon atoms, as depicted in Figure 1.7 below.
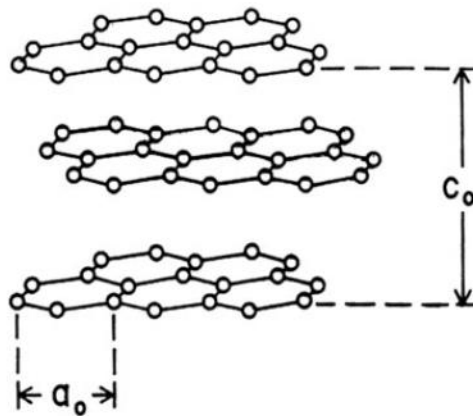

Fig. 1.7: Sketch of the crystal structure of graphite.[43]

Lithium can be inserted into graphite between the graphene layers, whereas the host structure becomes negatively charged due to the low lying π^*band of graphene. A maximum of 1 Li can be inserted per 6 carbon atoms because of cation-cation repulsion. This process can be formulated as following:

$$Li^+ + e^- + 6\ C \leftrightarrow Li^+[C_6]^-$$ (1.18)

Insertion of lithium into graphite changes the stacking order of graphene layers to an A-A-A sequence, due to better coordination of the Li centers between the layers as shown in Figure 1.8 below.
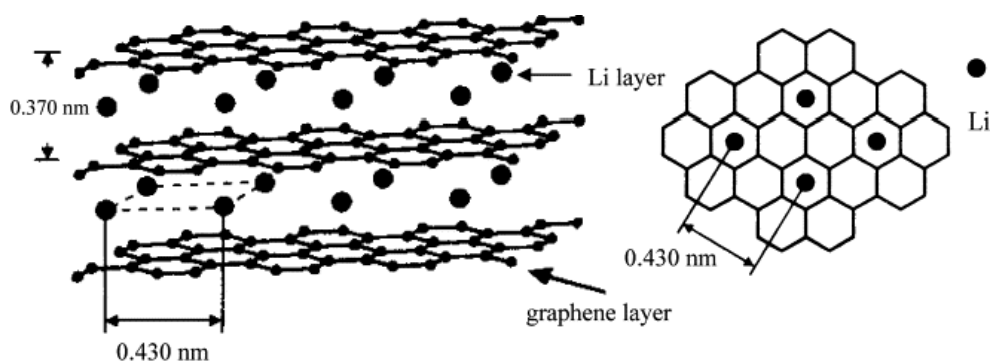

Fig. 1.8: Intercalation structure LiC_6.[44]

Lithium is inserted stagewise into graphite starting at 400 mV vs. Li/Li^+, where three composition ranges with different structural orders are formed resulting in three voltage plateaus at 250, 150 and 100 mV, respectively.[45] A maximum theoretical capacity of 372 mAh g^{-1} is found for LiC_6, but practical values are in the order of 350 mAh g^{-1}. During initial discharge, a solid electrolyte interface (SEI) is formed at 700 to 800 mV vs. Li/Li^+ composed mainly of LiF, Li_2O as well as of Li_2CO_3 and polymeric organic compounds.[46-48] Although SEI formation results in an irreversible initial capacity loss, the surface of graphite is passivated in order to prevent delamination of the negative electrode material as well as further decomposition of the electrolyte. After SEI formation insertion of lithium into graphite is a reversible process occurring at potentials close to the Li/Li^+ reference electrode with minimal volume changes and excellent cycling stability. As graphite is cheap and does not lead to damage of the environment it is the negative electrode material of choice for lithium ion batteries, up to now.

1.4.2.2. Conversion materials

Various Transition metal oxides (CoO, NiO, Co_3O_4 and Fe_3O_4) and –nitrides (Cu_3N, Fe_3N, Co_3N) are shown to undergo conversion reactions with lithium resulting in the formation of transition metal particles embedded in Li_2O and Li_3N, respectively.[49-53] In the year 2000, Tarascon et al. reported excellent cycling behavior of transition metal oxide nanoparticles with reversible capacities of 700 to 800 mAh g^{-1} over 100 cycles.[51] However, high operating potentials vs. Li/Li^+, large polarization between charge and discharge potential as well as instability under ambient conditions for certain products keeps this kind of material away from commercialization in lithium ion batteries.

1.4.2.3. Other lithium compounds

One of the earliest explored alloys was LiAl with a theoretical specific capacity of 790 mAh g^{-1} and a working potential of 0.3 V vs. Li/Li^+.[54-55] However, extreme volume changes during lithiation and delithiation lead to a poor cycling performance of this compound. In recent years, various lithium alloys containing Al, Ga, In, Si, Ge, Sn, Pb, Sb and Bi have been extensively studied.[55-60] The most promising one of them seems to be silicon because it combines a number of advantages: It has the highest known theoretical capacity so far of 4008 mAh g^{-1} for the intermetallic compound $Li_{21}Si_5$ and operates at low potential vs. Li/Li^+. Additionally, silicon is highly abundant on earth. Lithiation of silicon is a stepwise process of a series of phase formations with increasing lithium content ($Li_{12}Si_7$, $Li_{14}Si_6$, $Li_{13}Si_4$, and $Li_{21}Si_5$) which results in multiple plateaus during discharge as shown in Figure 1.9.
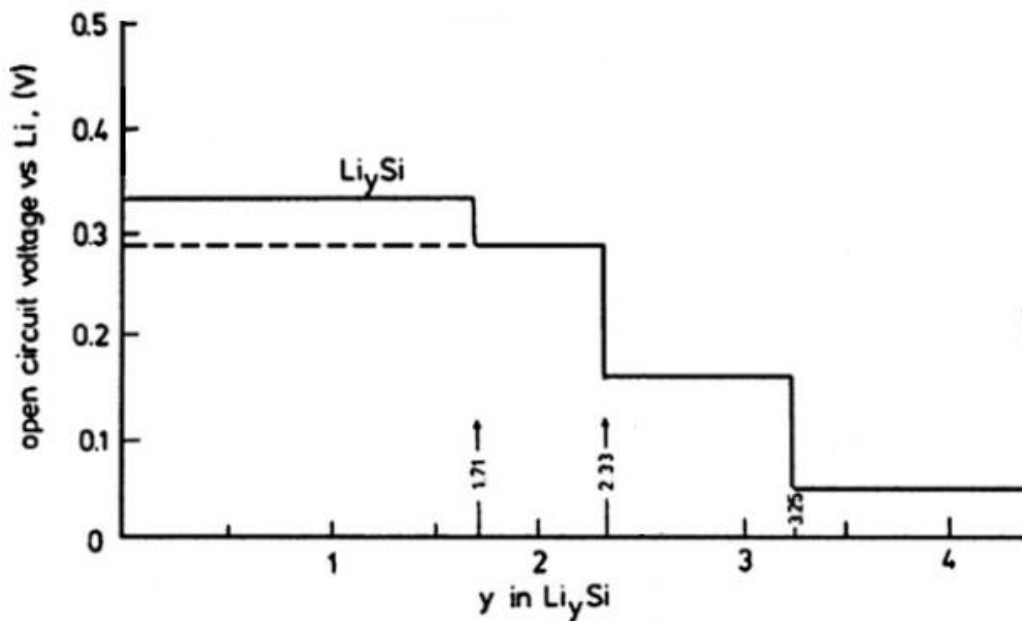
Fig. 1.9: Stepwise formation of different lithiumsilicide alloys.[61]

Crystalline micron-sized silicon has a major disadvantage though: there is a large volume expansion during lithiation and consequently a large volume decrease during delithiation. This induces mechanical stress leading to a fracture of the anode and loss of electronic percolation. Additionally, due to the cracking, pristine surfaces of Si are exposed to the electrolyte solvents, giving rise to additional deposition of SEI layers. As SEI is electronically insulating it must impair capacity retention on growing thicker. These effects lead to a very poor cycling performance which has not be overcome up to now.

To prevent the deposition of SEI on Si, it is necessary to avoid the direct contact with the electrolyte solvent by surface coating. The coating material should be electrically conducting as well as permeable for Li^+ ions. Low dimensional carbon is a perfect candidate here, since it has a large surface area, forms a thin stable SEI layer and is soft enough to accommodate volume changes of Si during cycling. Si/C composite materials are therefore of great future interest for anode applications.

19

Nano silicon composites

As bulk silicon was investigated for anode application without real success since the 1970th it does not seem to be a feasible material without a major new idea for functional composite formation in order to overcome its shortcomings, the worst of it is the volume change of up to 400%. Consequently recent investigations targeted nanoscopic forms of silicon which indeed did bring about some hope for much better cycling stabilities. One encouraging approach was the synthesis of silicon nanowires by the gold catalyst process on a conducting support.[60] The anode did show fairly stable cycling above 3000 mAh g^{-1} for some ten cycles. Obviously, nano sizing and anisotropic morphology allows strain relaxation as well as a short diffusion pathway improving kinetics. Cui et al. coated carbon nano fibers by silicon and reported 55 cycles at around 2000 mAh g^{-1} with a Coulombic efficiency of 98% to 99% at a rate of C/5. Seemingly, the carbon core of these nanowires improves electron transport and provides a mechanically stable support. This arrangement is called core-shell C/Si nanowire. Cui et al. coated carbon nanowires with Si by chemical vapor deposition (CVD) of SiH_4.[62] However, after a few cycles more, the core shell structure was lost and there was no longer a distinction between C and Si zones. Kim et al. reported the use of mesoporous Si/C nanowires using a template route.[63] This ordered mesopores buffer the volume changes between nanowires. The composite consisted of Si nanocrystals deposited on the porous C nanowire network with a pore size of 2.3 nm. An initial charge capacity of 3163 mAh g^{-1} was reported when cycled at a rate of C/5. After 80 cycles, the capacity was still high at 2740 mAh g^{-1}, but some of the porous nanowires were pulverized and others aggregated to form nanoparticles. So far, this core-shell nanowires seem unable to retain their structure during cycling.

There are a lot of other morphologies for Si/C nano composites reported. Magasaki et all reported a bottom up approach for such a composite.[64] Annealing of Carbon Black lead to graphitization and linkage of neighbour particles, followed by deposition of Si nanoparticles by CVD of SiH_4. Simultaneous granulation and carbon deposition was obtained by decompositon of propylene at 700°C. In the end, porous C spheres (pore size: 30 to 100 nm) of a diameter of 15 to 35 µm were obtained with small Si nanoparticles on their surface. At a rate of C/20, a reversible capacity of 1950 mAh g^{-1} was obtained. When cycled at a rate of 1 C, 1500 mAh g^{-1} was retained after 100 cycles. In 2010, Cho reported the synthesis of porous Si anode materials.[65] These ordered pores were supposed to act as a buffer layer for the volume changes of Si upon lithiation. Si nanowires and bulk Si particles with ordered pores were synthesized by using templates (ordered mesoporous silica or Al_2O_3), which were afterwards removed by NaOH or HF (for silica). Additionally, the Si nanotubes or bulk silicon particles were coated by a thin carbon layer to prevent aggregation of these particles and protect them against NaOH and HF, respectively. When cycled at 0.2 C, the 3D porous Si particles show a capacity retention of 99% after 100 cycles at 2820 to 2780 mAh g^{-1}. The mesoporous Si nanowires showed an initial charge capacity of 3160 mAh g^{-1} when cycled at the same rate. After 80 cycles, 87% of the initial capacity was retained (2740 mAh g^{-1}). Two years later, Luo et al. reported the synthesis of a silicon graphene composite material.[66] Si nanoparticles wrapped by crumbled graphene shells were obtained by an aqueous dispersion of graphene oxide layers (GO) and Si nanoparticles, which was nebulized to form aerosol droplets and passed trough a preheated tube furnace with N_2 as carrier gas. As the water evaporated, the GO shells migrate to the surface of the particles and form a shell. GO was then reduced later by thermal treatment to graphene. In

the end, Si nanoparticles (diameter: 50 to 100 nm) crumbled in a graphene shell (thickness: 5 to 10 nm) were obtained. When cycled in a Li ion battery at a rate of 1 A g^{-1}, 950 mAh g^{-1} were retained after 250 cycles (initial capacity: 1100 mAh g^{-1}).

Other non-carbon based composites also show enhanced performance. In 2012, Wu et al. reported the synthesis of double walled Si nanotubes coated by a SiO_x layer which prevents both large volume expansion as well as continuous SEI formation. They found a capacity retention up to 88% after 6000 cycles at quite high current rates.[67]

Another approach for Si composite materials is the addition of a conductive polymer binder to Si nanoparticles. The conductive polymer maintains electric conductivity and mechanical integrity by accomodating volume changes of Si during cycling. Therefore, binder and conductive additive are combined into one material. Liu et al. reported the use of conductive polymers based on polyfluorene type polymers functionalized with ester and carbonyl groups to improve polymer adhesion.[68] A composite material with a Si nanoparticle to polymer weight ratio of 2:1 showed a stable cycling performance with a reversible capacity of 1400 mAh g^{-1} over 650 cycles at a rate of C/10. In 2011, Yushin et al. reported the use of an alginate based binder instead of a commercial binder like PVDF with Si nanoparticles.[69] When cycled in a Li ion battery (Si to C weight ratio was 3:1, 15 wt.% binder), capacities of 1200 mAh g^{-1} for Si over 1300 cycles or 1800 mAh g^{-1} over 100 cycles were recorded. When cycled at 140 A kg^{-1}, an initial charge capacity of 3000 mAh g^{-1} was observed.

Additionally, low dimensional pure Si-based devices were tested. A popular example of this category are thin film anodes with nano Si-particles. Normal anodes contain 10-20 wt.% inactive binders and conductive materials, whereas

in thin films, no additional inactive additives are needed. There are two key parameters determining specific capacity and cycle life of thin films: film thickness and electronic conductivity. When the thickness of films is reduced, there is a shorter diffusion path for Li ions as well as a stronger adherence to the current collector. The electronic conductivity can be tuned by the type of Si employed: n-type, p-type and pure intrinsic amorphous Si. In 2004, a 50 nm thin film n-type Si anode was reported which showed a stable reversible capacity of 3600 mAh g^{-1} for 200 cycles.[70] Although thin film Si anodes show the highest specific capacities, best capacity retention and cycle life, they have two major disadvantages which prevent their commercialization: First of all, deposition of Si thin films on current collector substrate occurs by physical vapor deposition and / or vacuum evaporation, which are high cost processes. Second, since cycling performance decreases with increasing film thickness, only a limited amount of sample (e.g. limited thickness) can be inserted inside battery leading to a small volumetric capacity. Therefore, Si thin films should be regarded as proof of concept and not as industrially applicable solutions. In 2011, Yao et al. reported nanostructured interconnected hollow spheres of Si.[71] They were synthesized using a template approach: SiH_4 was deposited via CVD on 350 nm silica spheres, which were afterwards removed by diluted HF. When cycled at C/10, an initial discharge capacity of 2725 mAh g^{-1} was reached and capacity decreased 8% after 100 cycles. Interestingly, none of the spheres cracked during cycling. Since these particles are interconnected, there is a reduced need for binders and conductive additives.

Such improvements in silicon-based anode formulations by nanisation were the starting point for our investigations on nano-silicon materials prepared from silicide compounds (Zintl phases) by topochemical reaction mechanisms.

2. Test of binary lithiumsilicides as anode materials in Li ion batteries

2.1. Introduction

There are four well known crystalline phases in the Li-Si phase diagram at ambient pressure: $Li_{12}Si_7$, $Li_{14}Si_6$, $Li_{13}Si_4$, and $Li_{21}Si_5$.[72] Their volume expansion rates are 117%, 157%, 236%, and 311% in comparison with pure Si. This huge volume expansion of Si during lithiation and subsequent volume decrease during delithiation is one of the major problems for the successful implementation of silicon as anode material in a commercial Li-ion battery. Quite recently, $Li_{15}Si_4$ was found to be the highest lithiated silicide when lithiation was performed at room temperature, at ambient pressure and in an electrochemical cell.[73] However, this does not change much for the principle volume problem. In this work, a different approach was chosen to solve the volume problem: Instead of starting from elemental silicon, already lithiated phases, namely $Li_{12}Si_7$, $Li_{14}Si_6$ and $Li_{13}Si_4$, were explored for their suitability as starting materials. This approach has two advantages: First of all, the overall volume expansion during cycling will be reduced as already expanded phases are employed. As an example, selecting $Li_{12}Si_7$ as the active starting material, the volume expansion is reduced to 70% concerning further lithiation to form $Li_{15}Si_4$ (fully lithiated metastable phase of Si at room temperature[73]). For delithiation, the volume contraction is only 54% to form Si. This is illustrated in Figure 2.1.
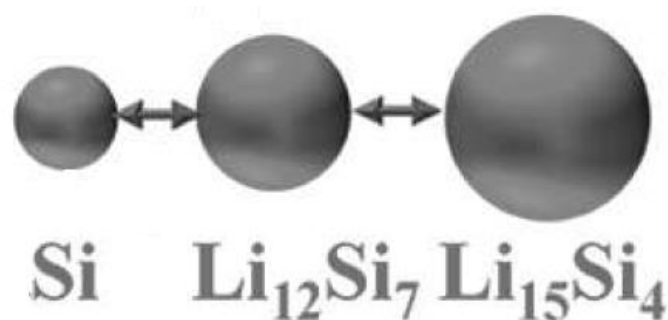
Fig. 2.1: Volume expansion of Si during lithiation.[74]

Thus, the relative volume change is significantly lower than if starting from pure Si (270%).[75] This approach was expected to reduce the fracture and pulverization of bulk Si-based anodes during cycling. Additionally, this compounds are lithiated starting anode materials (as opposed to commercial anode materials which are generally non-lithiated), which allows to incorporate a higher amount of Li inside the Li ion battery. This approach also has some disadvantages, though. First of all, the handling of lithiated material is more demanding than the handling of pure Si: Lithiumsilicides are sensitive to water and air and have therefore to be kept under an inert atmosphere (e.g. in a glove box). Additionally, the preparation of single-phase Li–Si alloys can be challenging regarding the high discrepancy between the melting points of Li and Si, which differ by 1230 °C. Nevertheless, the advantages are believed to outweight the disadvantages rendering this a promising and viable approach to improve the cycling behavior of Si based anode materials in the Li ion battery.

In this work, an easy approach for the synthesis of $Li_{12}Si_7$, $Li_{14}Si_6$ and $Li_{13}Si_4$ as well as their electrochemical performance in the Li ion battery is shown. Carbon based composite materials were tested and optimized to increase cycling stability of these materials. Furthermore, the deposition of metals through the reaction of lithiumsilicides with transition metal chlorides and their influence on the cycling behavior was examined.

2.2. Li$_{12}$Si$_7$

Li$_{12}$Si$_7$ crystallizes in the orthorhombic spacegroup *Pnma* and is a diamagnetic semiconductor with an optical band gap of 0.6 eV; electrical measurements indicate to a metallic phase which is in accordance to quantum mechanical band structure investigations. The structure can be described by two partial substructures: $_\infty^1[Li_{12}Si_4]$ and $_\infty^1[Li_6Si_5]$, which are consisting of Si$_4$-stars and Si$_5$-rings, respectively. The 26 electron fragment Li$_6$Si$_5$ is an infinite one dimensional sandwich stack of Si$_5$-rings; in the 28 electron fragment Li$_{12}$Si$_4$, all of the surrounding Li atoms stabilize the single bonds between the Si atoms in the Si$_4$-stars.[76] Upon hydrolysis, the vigorous formation of silanes is observed. It is quite likely that there is some electron equilibration between these two virtual fragments.
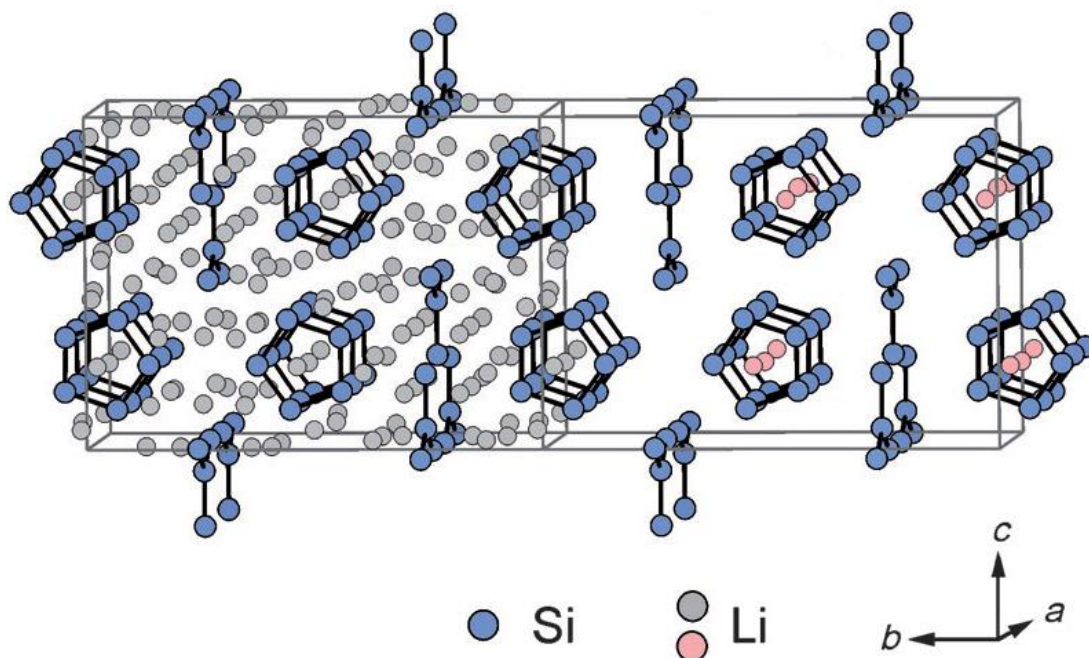
Fig. 2.2: Crystal structure of Li$_{12}$Si$_7$.[77]

Synthesis

A stoichiometric amount of the elements is transferred into a molybdenum crucible and treated at 350 °C for 30 min under argon atmosphere. The reaction product is pressed to a pellet, sealed in a niobium ampoule under dry argon and then heated at 950 °C for 2 h. $Li_{12}Si_7$ is obtained as a dark grey powder with a metallic lustre.
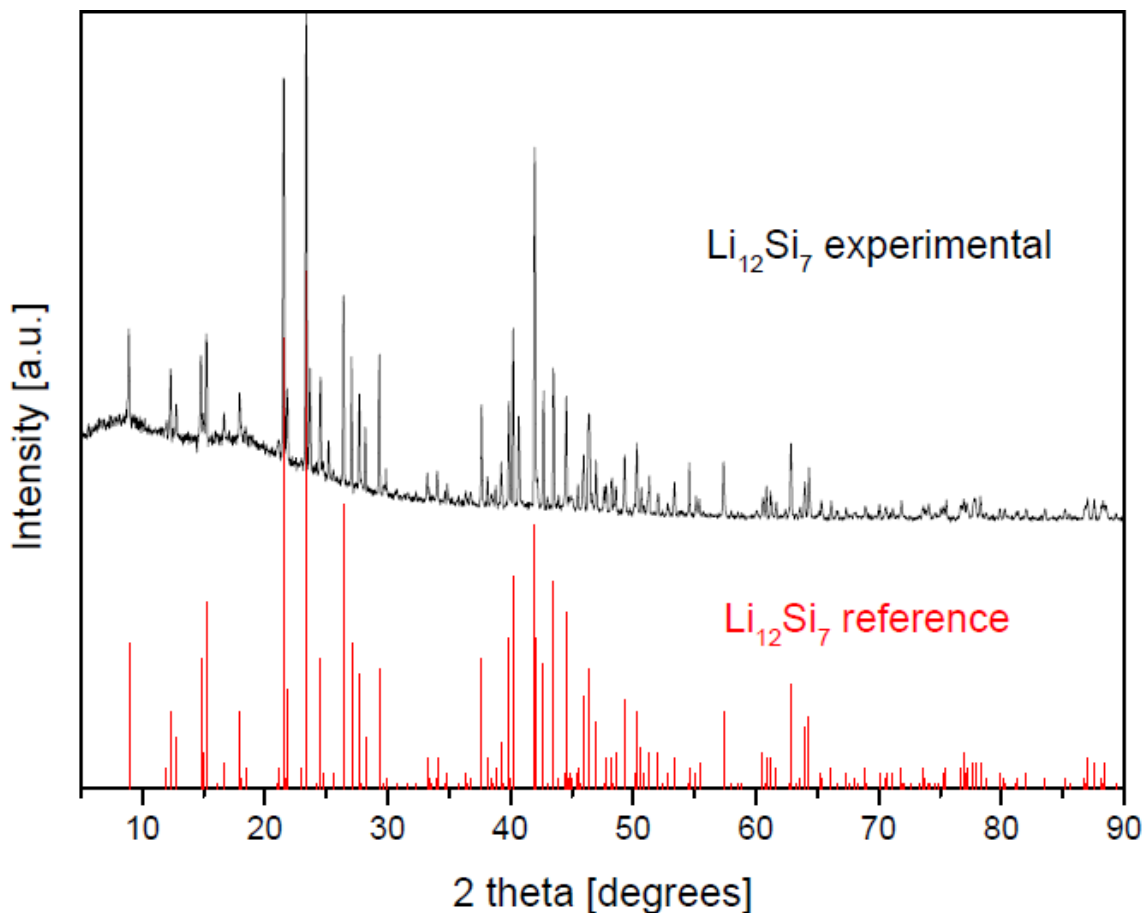
Fig. 2.3: Experimental XRD powder pattern of $Li_{12}Si_7$ (black curve) and theoretically calculated pattern (red lines). $Li_{12}Si_7$ was obtained as a pure and highly crystalline phase.

Electrochemical performance

Before electrochemical testing, $Li_{12}Si_7$ was ball milled in argon to a fine black powder. The electrode was prepared in a glove box under Ar atmosphere; Carbon Black (7 wt. %) and graphite (21 wt. %) were added as conductive additives. PVDF was used as a binder (12 wt. %) and 1 M $LiPF_6$ in ethylenecarbonate / dimethylcarbonate (1:1) was used as electrolyte. The sample was cycled between 10 mV and 2.0 V vs Li/Li^+ with a rate of 50 mA g^{-1}.
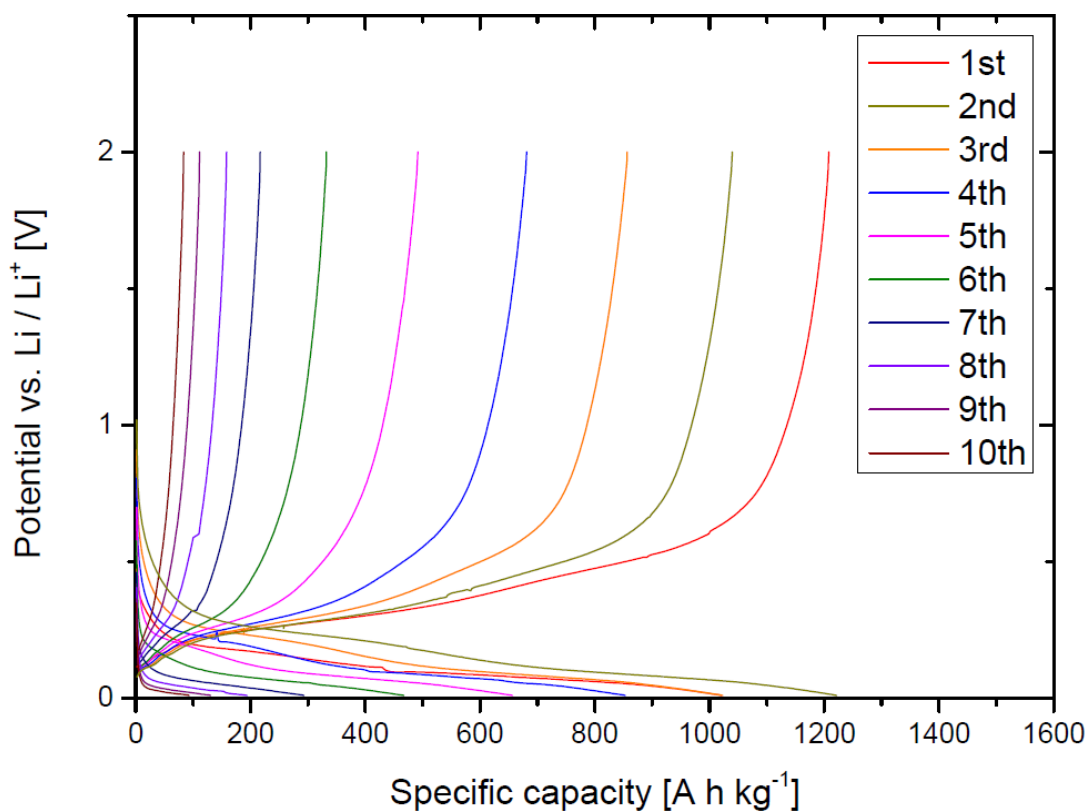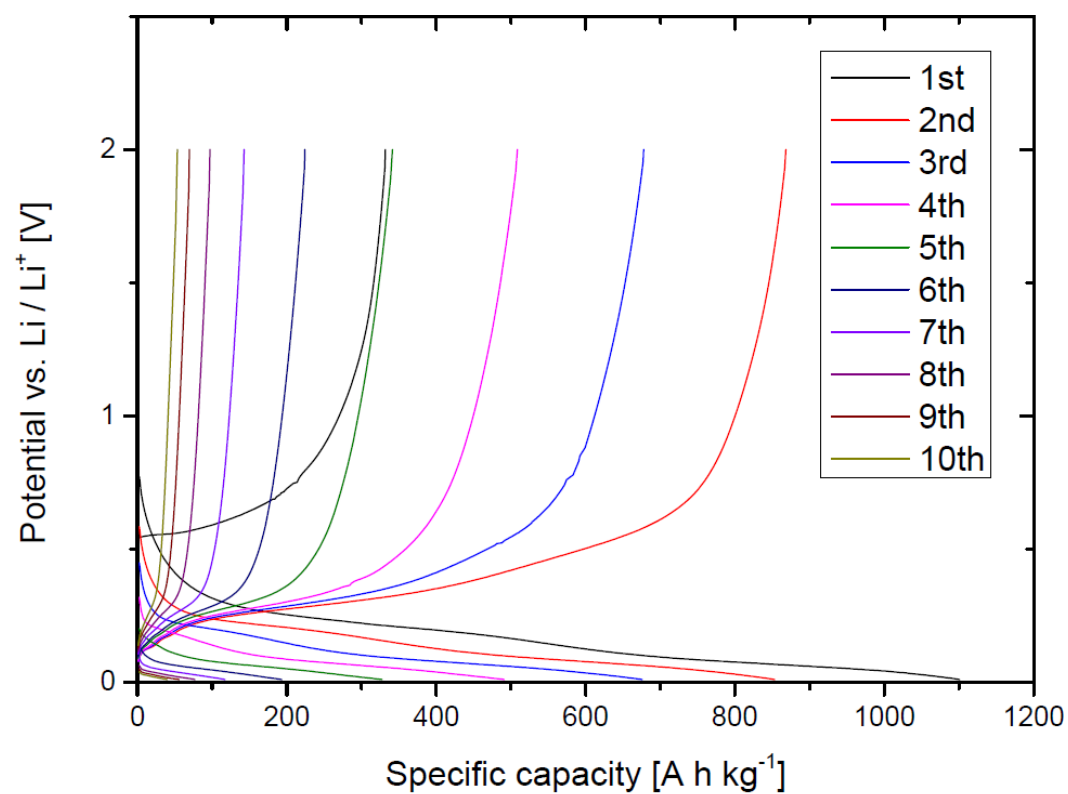
Fig. 2.4: Galvanostatic measurement of ball milled $Li_{12}Si_7$ (only the first 10 cycles are shown). The measurement on top was started by charging (delithiation) and the measurement on the bottom by discharging (lithiation).

When Li is extracted first from $Li_{12}Si_7$, a capacity of 330 mAh g^{-1} was obtained indicating that not the full amount of Li could be extracted from starting phase (full extraction of Li from $Li_{12}Si_7$ corresponds to a capacity of 1150 mAh g^{-1}). During the following discharge a capacity of 1100 mAh g^{-1} was obtained. If Li was inserted first into $Li_{12}Si_7$, a capacity of 1000 mAh g^{-1} was obtained. The theoretical capacity for the insertion of Li into $Li_{12}Si_7$ to form $Li_{15}Si_4$ corresponds to 1365 mAh g^{-1}. The experimental capacity is therefore a little lower. The following charge leads to a capacity of 1200 mAh g^{-1}, which is higher than the first discharge capacity. This observation is congruent with the expected results. However, independent of the first step – charging or discharging – the capacity drops down very quickly and only 95 mAh g^{-1} (from discharge) and 55 mAh g^{-1} (from charge), respectively, could be retained after 10 cycles.
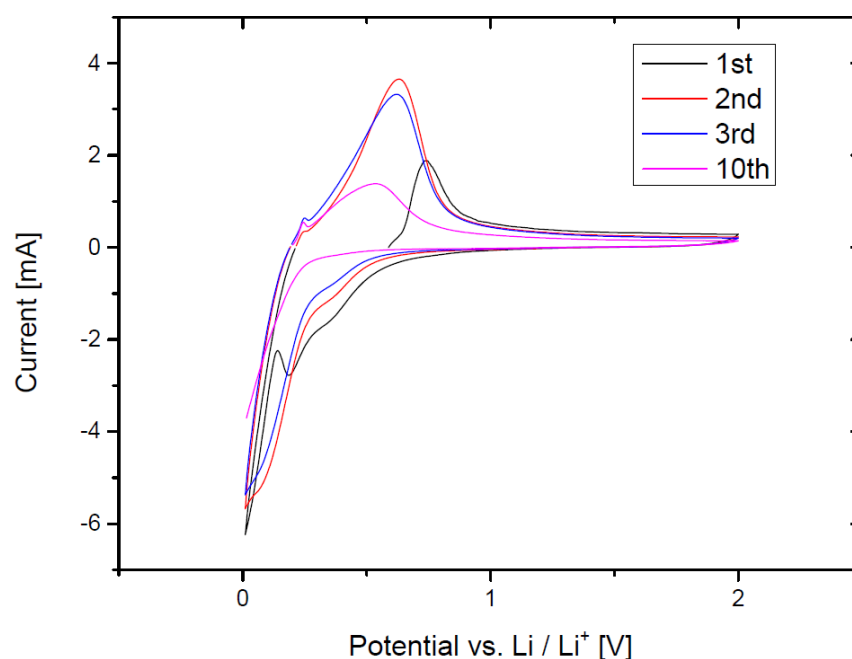
Fig. 2.5: Cyclic Voltammetry measurement of ball milled $Li_{12}Si_7$. The sample was cycled between 10 mV and 2.0 V vs Li/Li$^+$ with a rate of 50 µV s^{-1}. The first step was charging (delithiation). During first discharge, there is a distinct reduction peak at 0.2 V, which is no longer present in the subsequent cycles.

This observed behavior is also manifested in the cyclic voltammetry measurement of $Li_{12}Si_7$. With increasing cycle number, the oxidation peaks at 0.25 V and 0.6 V, respectively, become less intense and broader. Additionally, there is a small shift to the left (lower potential).

2.2.1. $Li_{12}Si_7$ / carbon composite

To prevent the rapid capacity decay of $Li_{12}Si_7$ during cycling in Li ion battery, carbon was used as an active matrix material, since it is a good electronic and ionic conductor (for Li^+), forms a more stable SEI layer than Si and is soft enough to accommodate volume changes of Si during cycling.[78-79] In this work, carbon was directly ball milled with $Li_{12}Si_7$ in argon to form a composite material. The optimal C to $Li_{12}Si_7$ ratio was determined and the effects of the ball milling speed were examined. Additionally, three different type of carbon (graphite, Super P and Carbon Black) were tested.

2.2.1.1. Examination of C to $Li_{12}Si_7$ ratio

Graphite (KS 6, TIMCAL, particle size: 6.5 μm) and $Li_{12}Si_7$ are ball milled in argon for 3 h at a speed of 350 rpm to a fine black powder. The examined mixtures are listed in Table 1 below.

Tab. 1: $Li_{12}Si_7$ / graphite mixtures

Li : C (molar ratio)	$Li_{12}Si_7$: C (weight ratio)
1 : 12	14 : 86
1 : 6	24 : 76
1 : 2	50 : 50
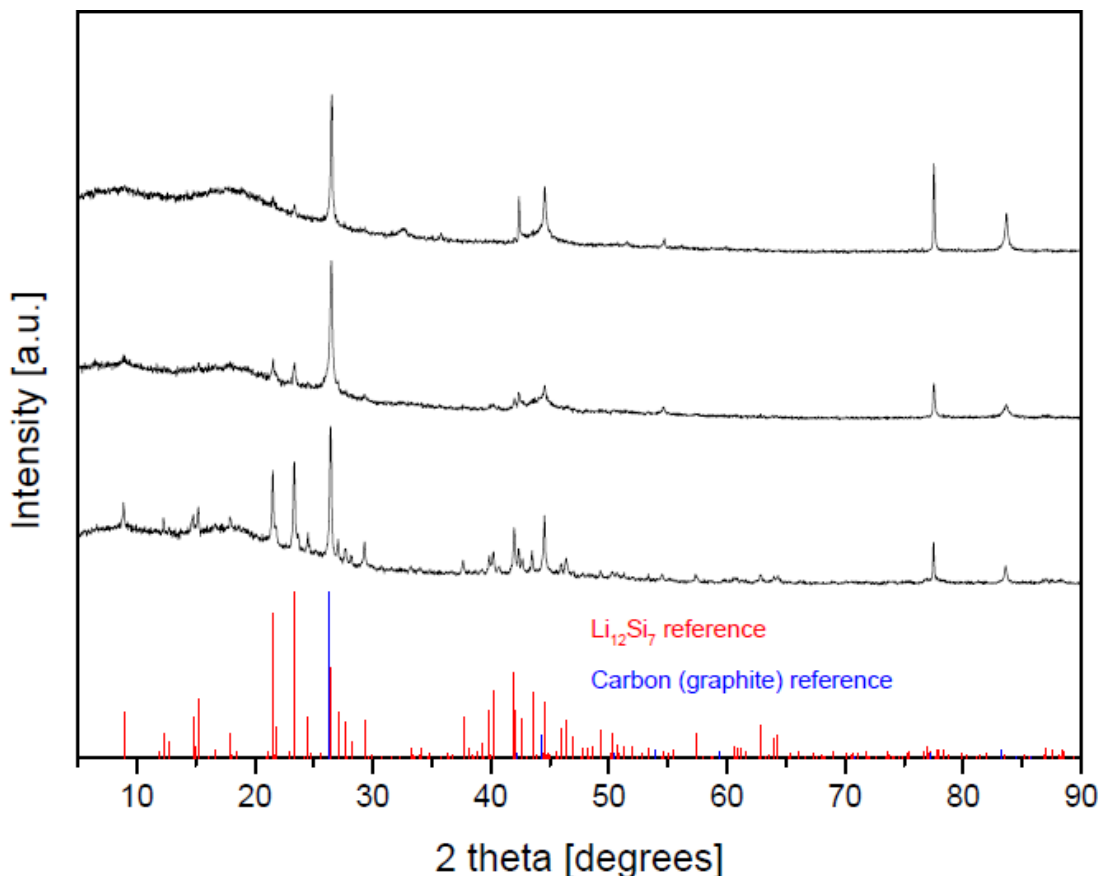
Fig. 2.6: XRD Powder patterns of $Li_{12}Si_7$ + graphite, ball milling in Ar for 3 h at a speed of 350 rpm. From top to bottom: (1) Li to C = 1:12, (2) Li to C = 1:6 and (3) Li to C = 1:2. All samples contain amorphous material as well as graphite and $Li_{12}Si_7$ (increasing intensity from top to bottom as expected due to higher lithium silicide content).

Electrochemical performance

The electrodes were prepared in a glove box under Ar atmosphere; Super P was added as conductive additive (15 - 20 wt. %) and PVDF was used as a binder (10 wt. %). 1 M $LiPF_6$ in ethylenecarbonate / dimethylcarbonate (1:1) was used as electrolyte. The samples were cycled between 10 mV and 2.0 V vs Li/Li$^+$ with a rate of 20 mA g^{-1}. The initial step was charging (delithiation) and values for specific capacity refer to the composite material.
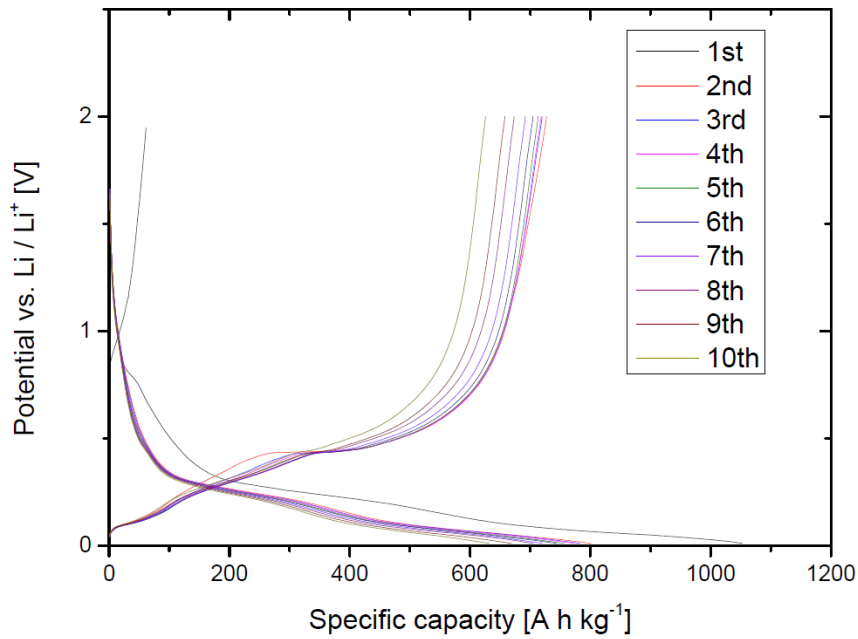
Fig. 2.7: Galvanostatic measurement of ball milled $Li_{12}Si_7$ and graphite with a Li to C ratio of 1:6; the first 10 cycles are shown.
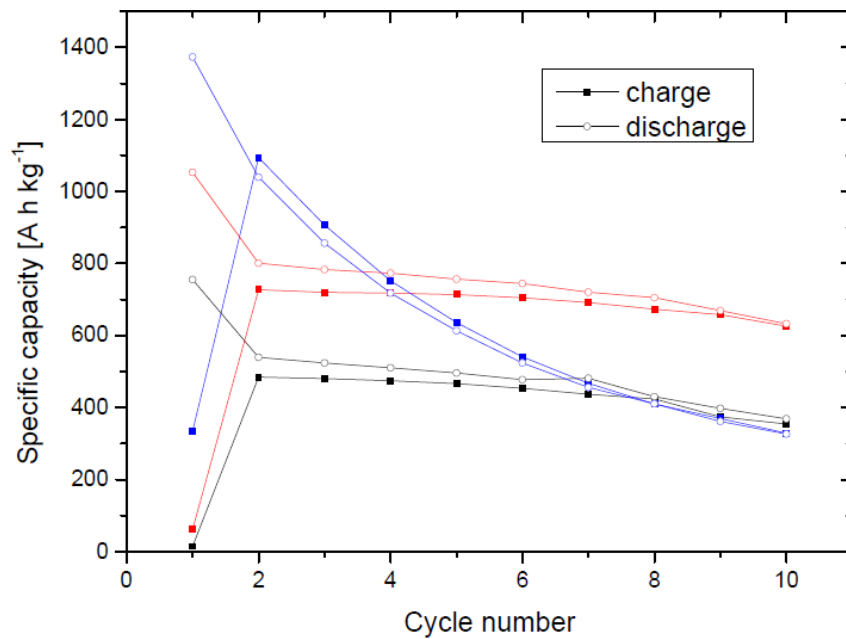

Fig. 2.8: Cycle number vs. specific capacity for ball milled $Li_{12}Si_7$ and graphite. The performance of a mixture with a Li to C ratio of 1:2 is shown in blue, the one with a ratio of 1:6 in red and the one with a ratio of 1:12 in black, respectively.

When looking at the cycling behavior of $Li_{12}Si_7$ with different C content, the maximum achievable capacity increases with lower carbon content. At the same time, however, the capacity drop is much faster. In terms of achievable capacities and capacity retention, mixtures with a Li to C ratio of 1:6 were found to deliver the best performance in the Li ion battery. Therefore, the Li to C ratio was kept at this value for further experiments with these materials.

2.2.1.2. Effects of ball milling speed

Mixtures of $Li_{12}Si_7$ and graphite with a Li to C ratio of 1:6 were treated in argon for 3 h at different ball milling speed of 350, 450 and 550 rpm, respectively. Figure 2.9 shows the obtained XRD powder patterns for these mixtures.
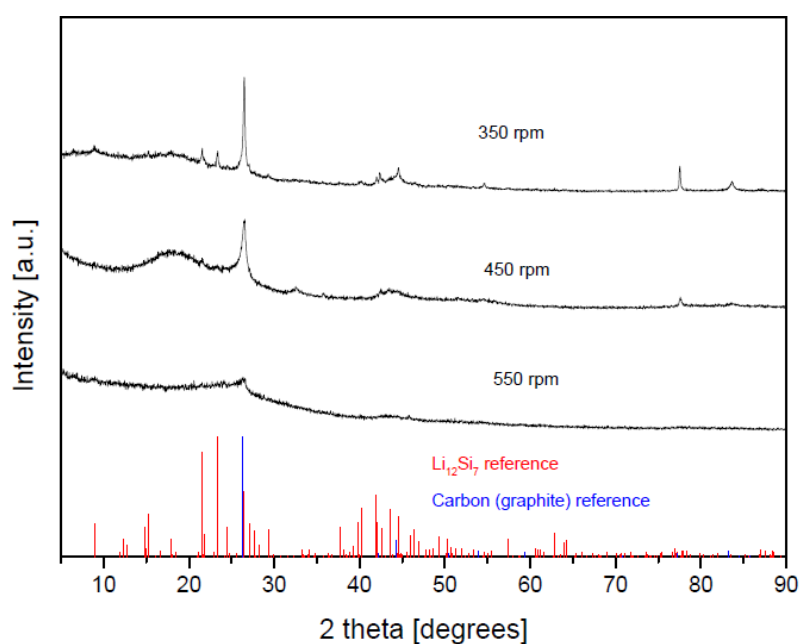
Fig. 2.9: XRD Powder patterns of a $Li_{12}Si_7$ + graphite mixture with a Li to C ratio of 1:6, ball milled in argon for 3 h at different ball milling speed (black curves). From top to bottom: (1) 350 rpm, (2) 450 rpm and (3) 550 rpm. The red and blue lines correspond to calculated patterns of $Li_{12}Si_7$ and graphite, respectively.

As expected, samples have an increasing amorphous character with higher ball milling speed. Note that especially at a ball milling speed of 550 rpm, even the reflections of graphite are very broad and small. This effect can also be seen in the SEM micrographs shown in Figure 2.10.
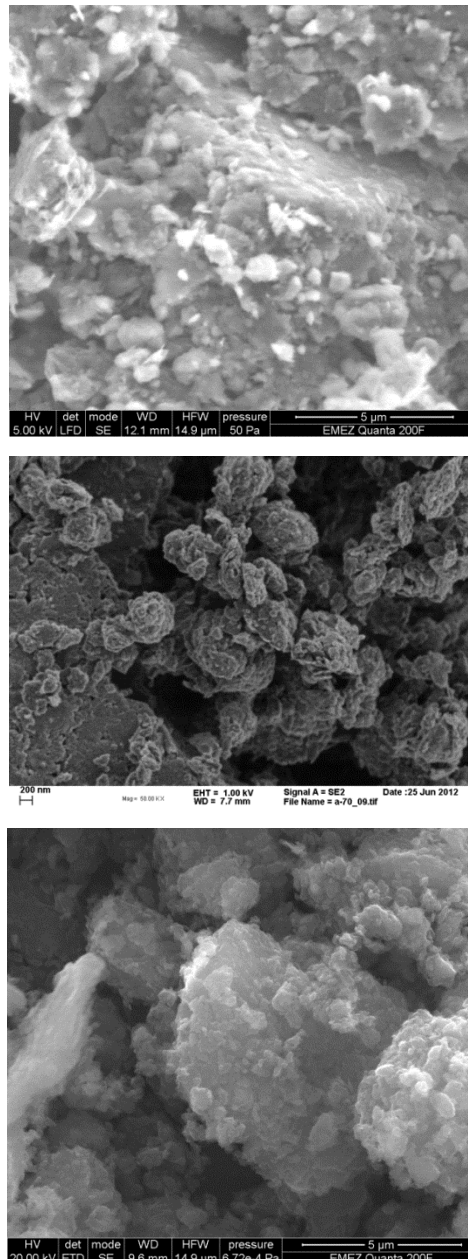

Fig. 2.10: SEM micrographs of a $Li_{12}Si_7$ + graphite mixture, ball milled in argon for 3 h at different ball milling speed. From top to bottom: (1) 350 rpm, (2) 450rpm and (3) 550 rpm.

All samples consist of plate-like particles (graphite) with smaller aggregated particles on their surface ($Li_{12}Si_7$ with a particle size in the range of 100 nm).

Electrochemical performance

The electrodes were prepared in a glove box under Ar atmosphere; Super P was added as conductive additive (22 wt. %) and PVDF was used as a binder (12 wt. %). 1 M $LiPF_6$ in ethylenecarbonate / dimethylcarbonate (1:1) was used as electrolyte. The samples were cycled between 10 mV and 2.0 V vs Li/Li^+ with a rate of 20 mA g^{-1}. The initial step was charging (delithiation) and values for specific capacity refer to the composite material.
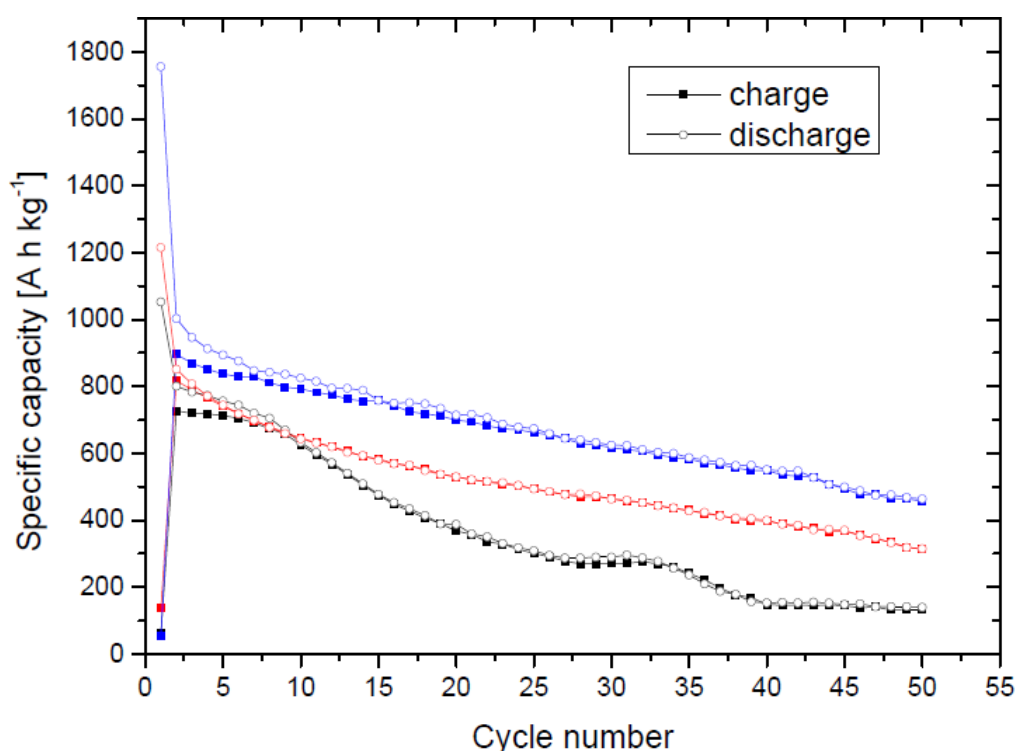

Fig. 2.11: Cycle number vs. specific capacity for ball milled $Li_{12}Si_7$ and graphite with a Li to C ratio of 1:6; 50 cycles are shown. The performance of a mixture ball milled at 350 rpm is shown in black, the one ball milled at 450 rpm in blue and the one ball milled at 550 rpm in red, respectively.

The best performance in the Li ion battery was obtained with a sample ball milled at a speed of 450 rpm; roughly 830 mAh g^{-1} (discharge) and 800 mAh g^{-1} (charge), respectively, were retained after 10 cycles (see Fig. 2.12). Note that for all samples a very low initial charge capacity was observed indicating that only a small amount of Li was extracted.
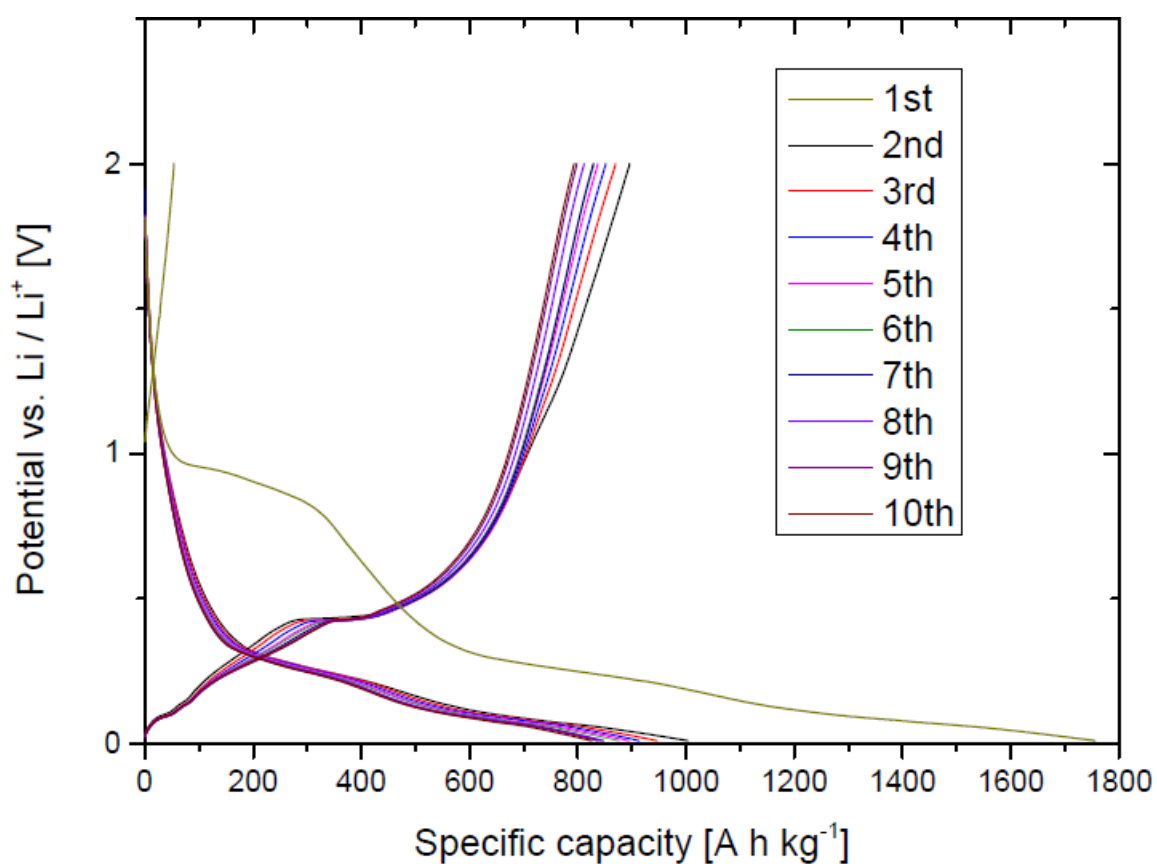
Fig. 2.12: Galvanostatic measurement of Li$_{12}$Si$_7$ and graphite with a Li to C ratio of 1:6, ball milled in argon for 3 h at a speed of 450 rpm. Only the first 10 cycles are shown.
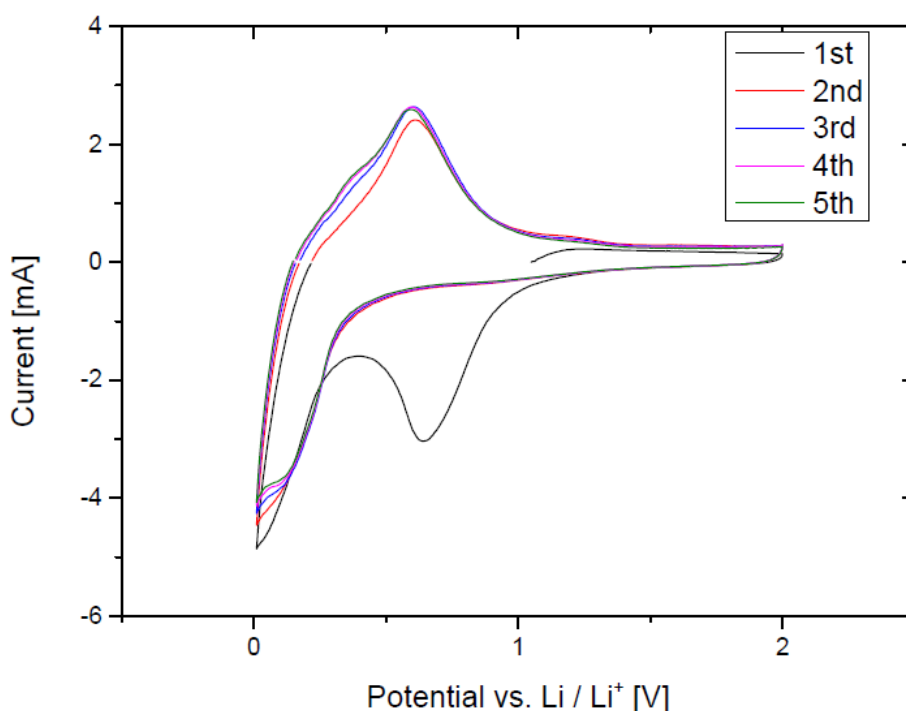
Fig. 2.13: Cyclic Voltammetry measurement of $Li_{12}Si_7$ and graphite with a Li to C ratio of 1:6, ball milled in argon for 3 h at a speed of 450 rpm. The sample was cycled between 10 mV and 2.0 V vs Li/Li$^+$ at a rate of 50 µV s^{-1}. The initial step was charging (delithiation). During first discharge, there is a reduction peak at 0.7 V, which is no longer present in the subsequent cycles. This peak is addressed to the initial SEI formation.

Although cycling behavior was improved by far regarding pure $Li_{12}Si_7$, capacity fading is still a big issue. Additionally, when multiple batteries were running with the same sample, a slightly different cycling behavior (faster decay of capacity) can be observed. This observation can be addressed to a topological effect of the sample, e.g. inhomogeneity. Possible reasons for capacity fading are examined in the following section using post mortem analysis.

Post mortem analysis

A sample of $Li_{12}Si_7$ and graphite with an Li to C ratio of 1:6, ball milled at 450 rpm for 3 h in argon, was examined after 20 cycles in a Li ion battery:

The electrode was prepared in a glove box under Ar atmosphere; Super P was added as conductive additive (14 wt. %) and PVDF was used as a binder (16 wt. %). 1 M $LiPF_6$ in ethylenecarbonate / dimethylcarbonate (1:1) was used as electrolyte. The sample was cycled between 10 mV and 2.0 V vs Li/Li^+ with a rate of 50 mA g^{-1}. The initial step was charging (delithiation). The sample was cycled for 20 full charge / discharge cycles and then charged. The battery cell was opened inside an argon filled glove box and the electrode material was washed multiple times with dry THF (99.5%) to remove the remaining electrolyte. The sample was ground afterwards to a black powder. Figure 2.14 shows the obtained XRD powder pattern of this material.
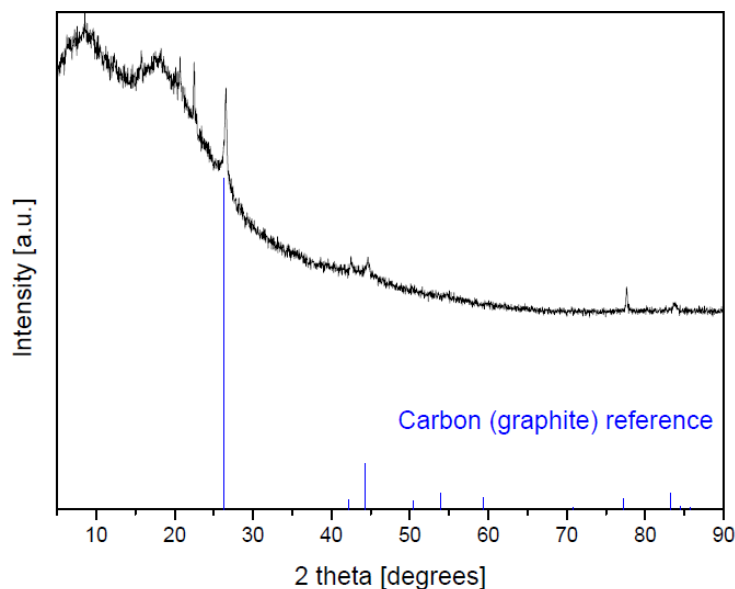
Fig. 2.14: XRD powder pattern of a $Li_{12}Si_7$ and graphite mixture with a Li to C ratio of 1:6, ball milled in argon for 3 h at a speed of 450 rpm after 20 cycles in a Li ion battery (black curve).

The sample is highly amorphous and contains graphite. The absence of crystalline Si in the powder pattern leads to the assumption that Si has become amorphous during cycling in battery which is in accordance with literature. There are three intense unindexed peaks in the low 2θ range at a 2θ = 15.7 °, 20.7 ° and 22.4 °, respectively. These reflections are believed to be caused by the SEI formed on the surface of the active material. An important indication supporting this theory is delivered by SEM analysis shown in Figure 2.15.
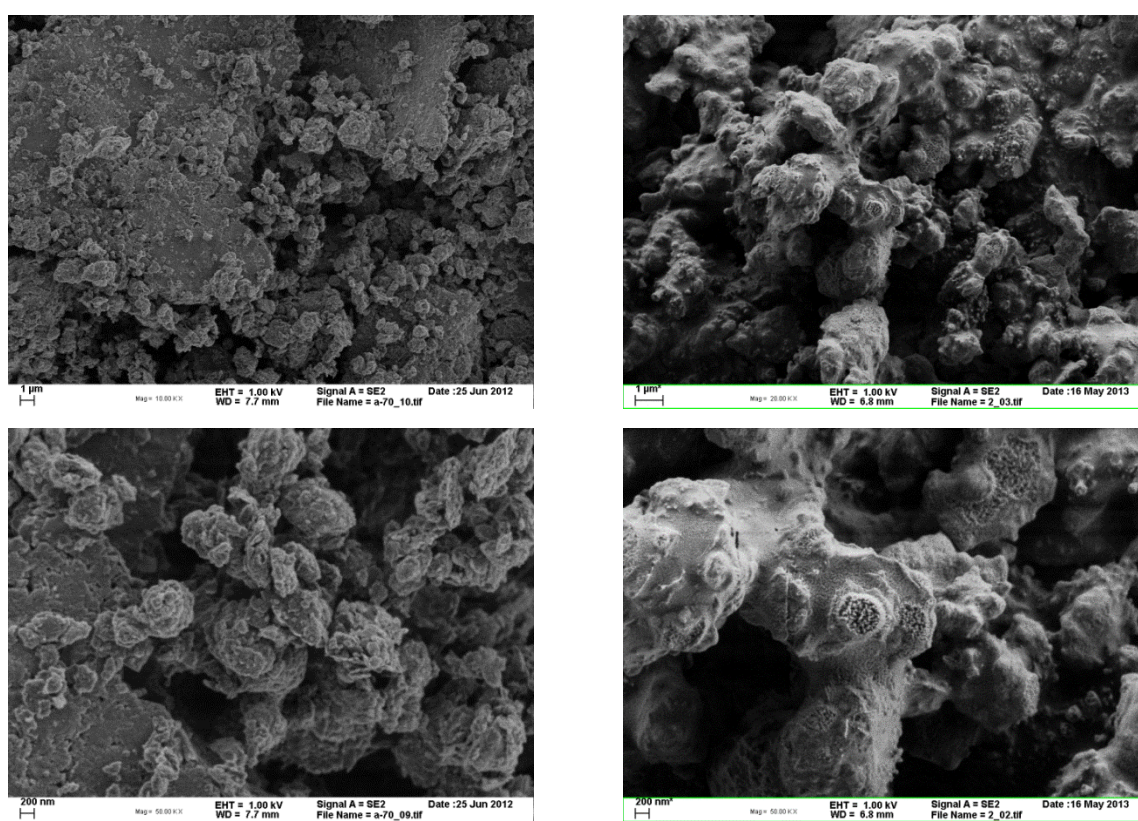
Fig. 2.15: SEM analysis of a $Li_{12}Si_7$ and graphite mixture with a Li to C ratio of 1:6, ball milled in argon for 3 h at a speed of 450 rpm before electrochemical testing (left) and after 20 cycles in a Li ion battery (right).

After 20 cycles in Li ion battery, the sample looks highly amorphous and all particles are coated completely by a thin film, which is believed to be a steadily growing SEI layer. This conjecture is manifested by TEM analysis shown in

Figure 2.16; it can be seen that the particles are wrapped completely inside multiple thin layers.
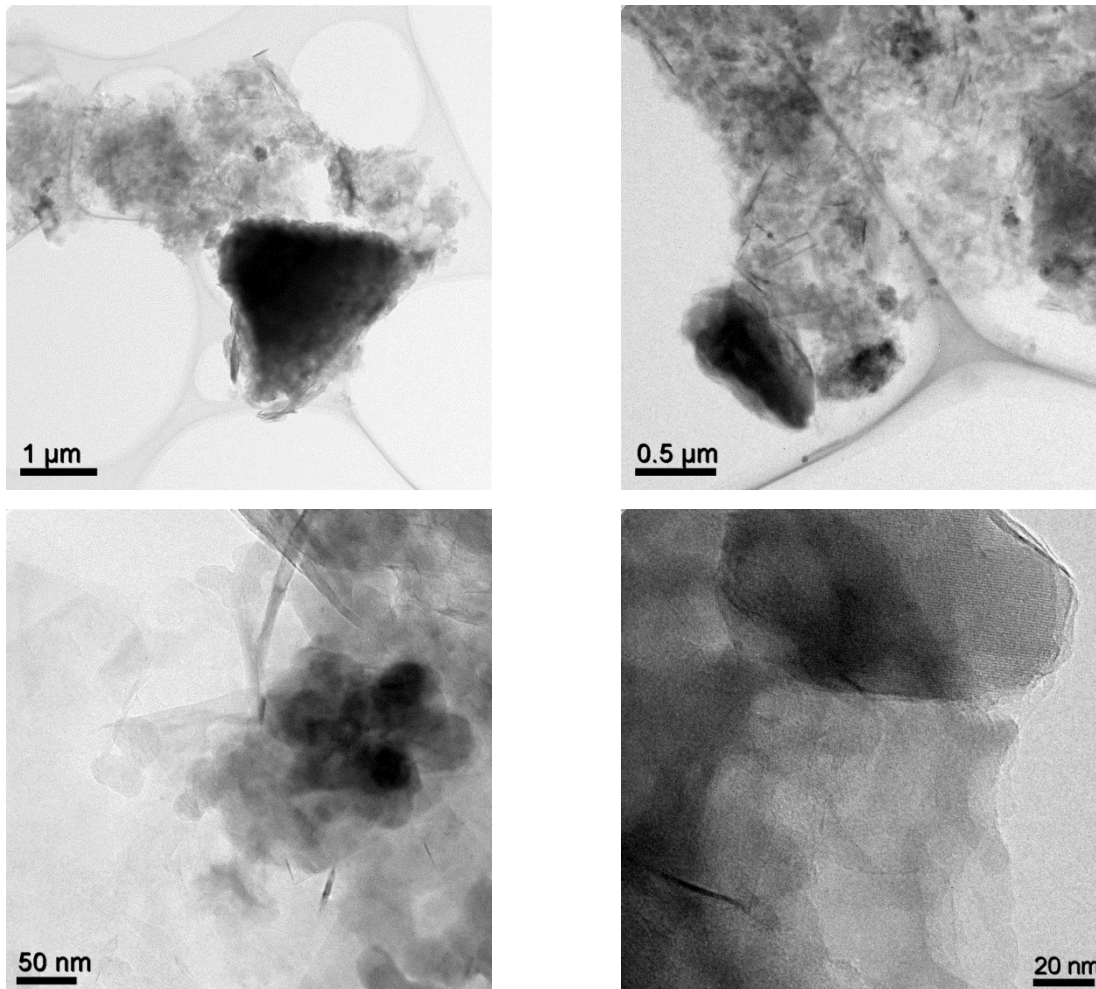
Fig. 2.16: TEM analysis of a $Li_{12}Si_7$ and graphite mixture with a Li to C ratio of 1:6, ball milled in argon for 3 h at a speed of 450 rpm after 20 cycles in a Li ion battery.

As a conclusion, capacity fading is caused mainly by the growing SEI layer on the surface of particles. With increasing cycle number, this layer becomes thicker leading to a slower Li ion transport and therefore to an overall worse kinetic behavior for lithiation and delithiation processes. For a successful implementation of this material in a Li ion battery, some further modifications would be necessary.

2.2.1.3. Examination of different types of carbon

In this chapter, three different sources of carbon were examined: Graphite KS6 (produced by TIMCAL, particle size: 6.5 µm), Super P Li (produced by TIMCAL, spheres of Carbon Black with a diameter of 40 nm) and Carbon Black XC 72 (amorphous particles with size in µm range with a slight graphite character). All carbon additives were ball milled with $Li_{12}Si_7$ in argon for 3 h at a speed of 450 and 500 rpm, respectively. The Li to C ratio was kept at 1:6 (e.g. $Li_{12}Si_7$ + 72 C). The examined mixtures are listed in Table 2 below.

Tab. 2: Examined mixtures of different carbon sources

Mixture	Carbon additives	Ratio
1	Carbon Black	-
2	Graphite and Super P	2:1
3	Graphite and Carbon Black	2:1

The obtained XRD powder patterns of these mixtures can be seen in Figure 2.17. All samples are highly amorphous and contain graphite as well as $Li_{12}Si_7$.
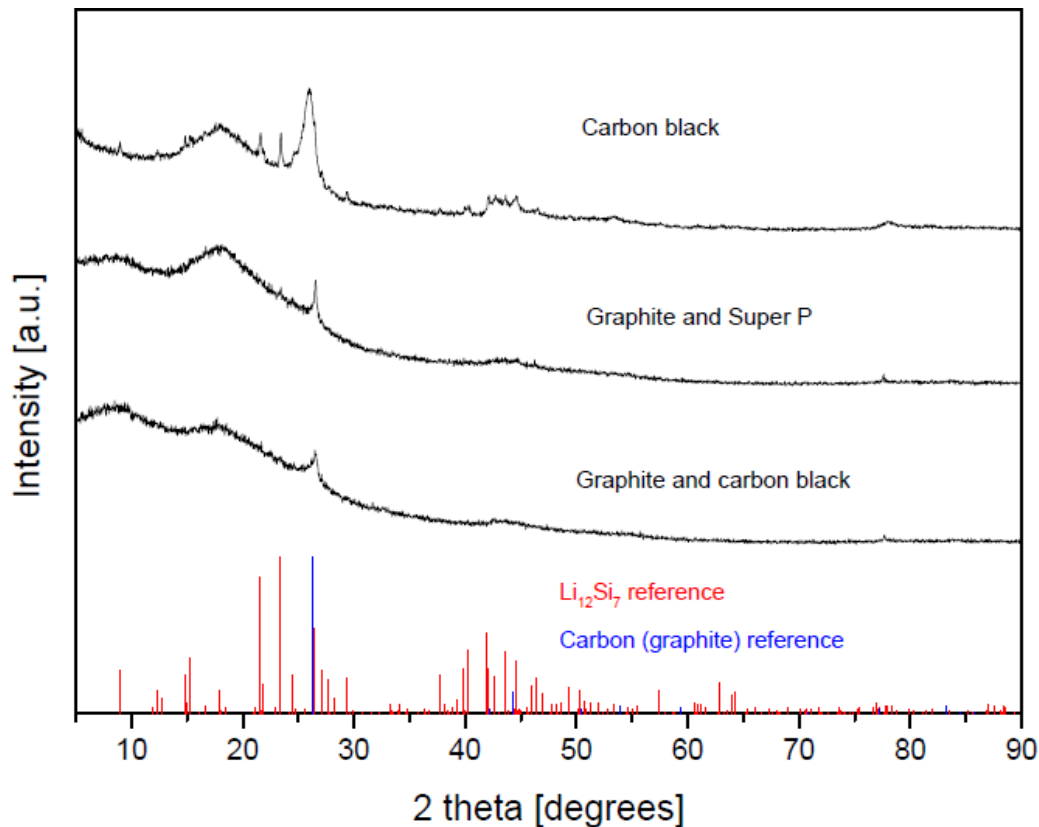
Fig. 2.17: XRD powder patterns of $Li_{12}Si_7$ and carbon additive mixtures with a Li to C ratio of 1:6, which were ball milled in argon for 3 h at a speed of 450 or 500 rpm, respectively (black curves). From top to bottom: (1) Carbon Black, (2) graphite and Super P in 2:1 weight ratio and (3) graphite and Carbon Black in 2:1 weight ratio. The red and blue lines correspond to calculated patterns of $Li_{12}Si_7$ and graphite, respectively.

Note that the samples containing graphite show very broad and weak reflections of $Li_{12}Si_7$, indicating a more efficient ball milling process despite same conditions in terms of time and speed. It is believed that the soft nature of Carbon Black prevents an efficient milling of the lithiumsilicide compound. On the other hand, the sample which contains only Carbon black shows much broader peaks of graphite indicating a smaller particle size of the latter. This observation is congruent with the SEM analysis shown in Figure 2.18.
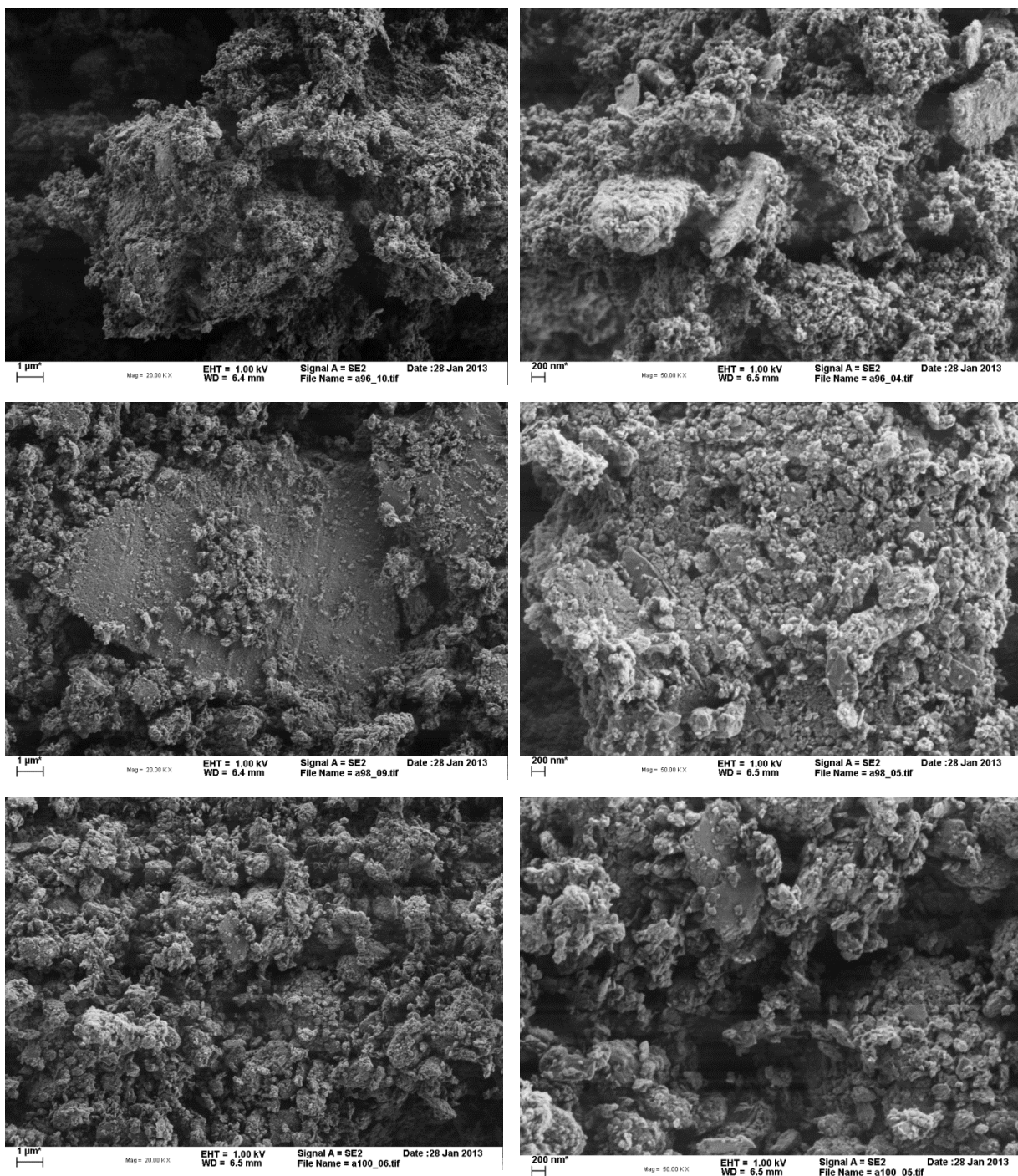
Fig. 2.18: SEM analysis of $Li_{12}Si_7$ and carbon additive mixtures with a Li to C ratio of 1:6, which were ball milled in argon for 3 h at a speed of 450 or 500 rpm, respectively. From top to bottom: (1) Carbon Black, (2) graphite and Super P in 2:1 weight ratio and (3) graphite and Carbon Black in 2:1 weight ratio.

All samples consist of plate-like particles (graphite) with smaller aggregated particles on their surface (submicron sized $Li_{12}Si_7$ particles). Samples with graphite additives contain plates of the latter one with a size between 1 and 50 µm, indicating that ball milling of graphite is not an efficient process. However, this is not the case for Carbon Black, where the average size of the graphite plates is much smaller.

Electrochemical performance

Electrodes were prepared in a glove box in argon atmosphere; PVDF was used as a binder and 1 M $LiPF_6$ in ethylenecarbonate / dimethylcarbonate (1:1) was used as electrolyte. The samples were cycled between 10 mV and 2.0 V vs Li/Li^+ with a rate of 50 mA g^{-1}. The initial step was charging (delithiation). Parameters for the electrode formulation are summarized in Table 3 below.

*Tab.3: Electrode formulation of examined mixtures.*

Mixture	Carbon additives in composite	PVDF [wt.%]	Other C additives for electrode formulation
1	Carbon Black	12	Graphite (18 wt. %)
2	Graphite and Super P (2:1)	6	no
3	Graphite and Carbon Black (2:1)	18	no

Figure 2.19 shows the performance of these mixtures during the galvanostatic measurement. Note that values for specific capacity refer to the composite material.
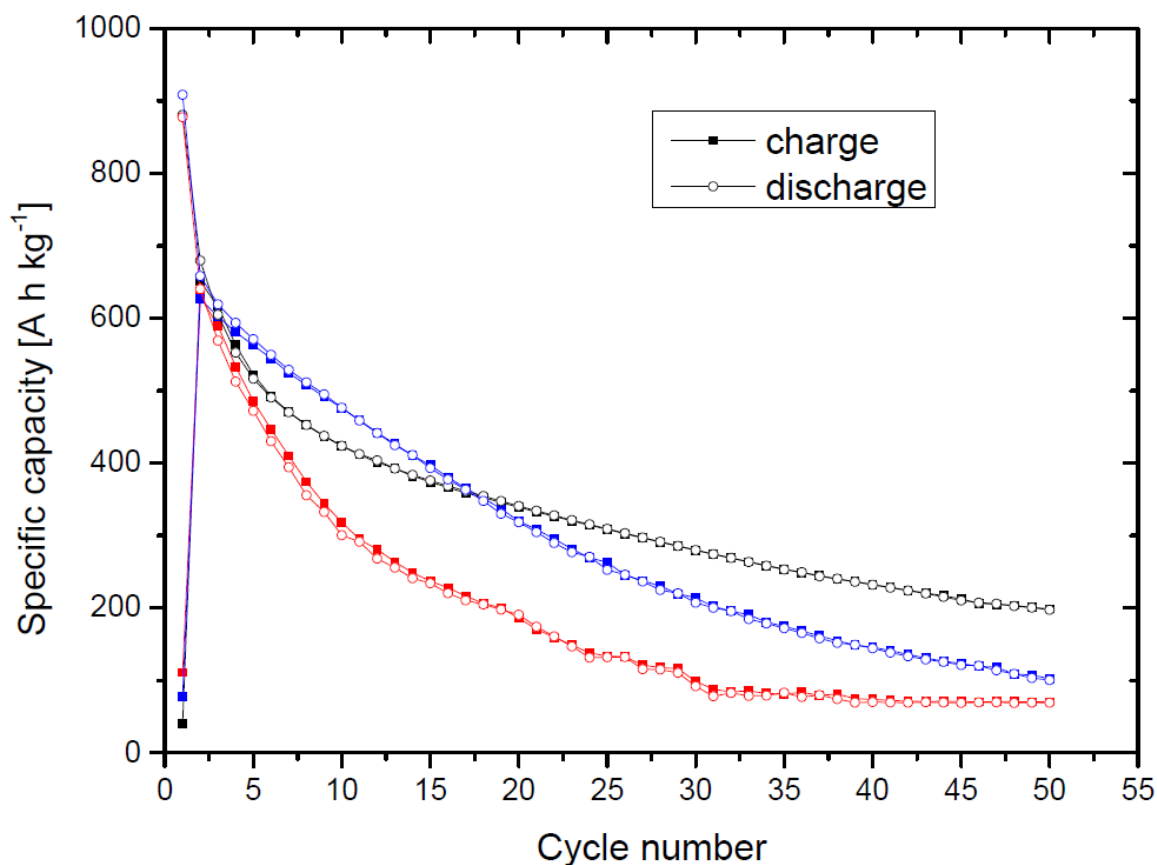
Fig. 2.19: Cycle number vs. specific capacity for ball milled $Li_{12}Si_7$ and carbon with a Li to C ratio of 1:6; 50 cycles are shown. The performance of the composite with Carbon Black is shown in black, the one with graphite and Super P (2:1) in red and the one with graphite and Carbon Black in blue, respectively.

The mixture with Super P showed the worst performance, since capacity decreases the fastest and after 10 cycles only 300 mAh g^{-1} was retained. To compare the performance of these mixtures with the one containing only $Li_{12}Si_7$ and graphite as shown in the previous section, a battery cell was assembled with this material and run at the same rate (50 mA g^{-1} instead of 20 mA g^{-1}). The result of this galvanostatic measurement is shown in Figure 2.20.
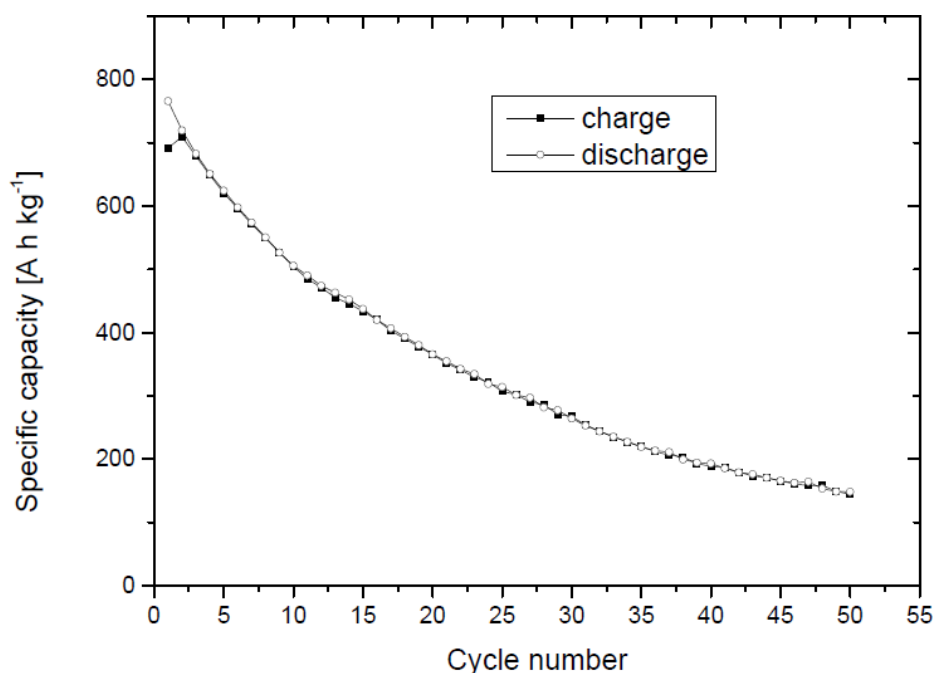
Fig. 2.20: Cycle number vs. specific capacity for ball milled $Li_{12}Si_7$ and graphite with a Li to C ratio of 1:6; 50 cycles are shown. The current rate was 50 mA g^{-1} and the initial step was discharge (lithiation). Values for specific capacity refer to the composite material.

As a conclusion, the best performance was achieved when Carbon Black was used as composite material. The reason for this behavior can be found when looking at the SEM micrographs of these mixtures (Fig. 2.18). First of all, the graphite particles used seem to be too big and ball milling is not an efficient method to significantly decrease their size. In the case of Carbon Black however, resulting carbon particles are much smaller leading to a better distribution of $Li_{12}Si_7$ and C particles, which is believed to enhance cycling stability. Additionally, this experiment shows the massive influence of the current rate on electrochemical performance for this kind of materials. When looking at a $Li_{12}Si_7$ and graphite mixture with a Li to C ratio of 1:6, the maximum achievable capacity as well as capacity retention drops significantly when current rate is changed from 20 mA g^{-1} (Fig. 2. 12) to 50 mA g^{-1} (Fig. 2.20).

2.2.1.4. $Li_{12}Si_7$ and graphite oxide

In this section, the reaction of $Li_{12}Si_7$ with graphite oxide was examined. The reaction of these two components was expected to result in the formation of Li_2O, small Si particles (size in subnano-scale) and partially reduced graphite oxide. This process should be highly exothermic, so Carbon Black was used as a buffer to absorb the heat.

Synthesis

Graphite oxide powder (dried), $Li_{12}Si_7$ and carbon powder (99.999%) in equal weight amounts are ball milled in argon for 3 h at a speed of 350 rpm to a black powder. The resulting XRD powder pattern can be seen in Figure 2.21 below.
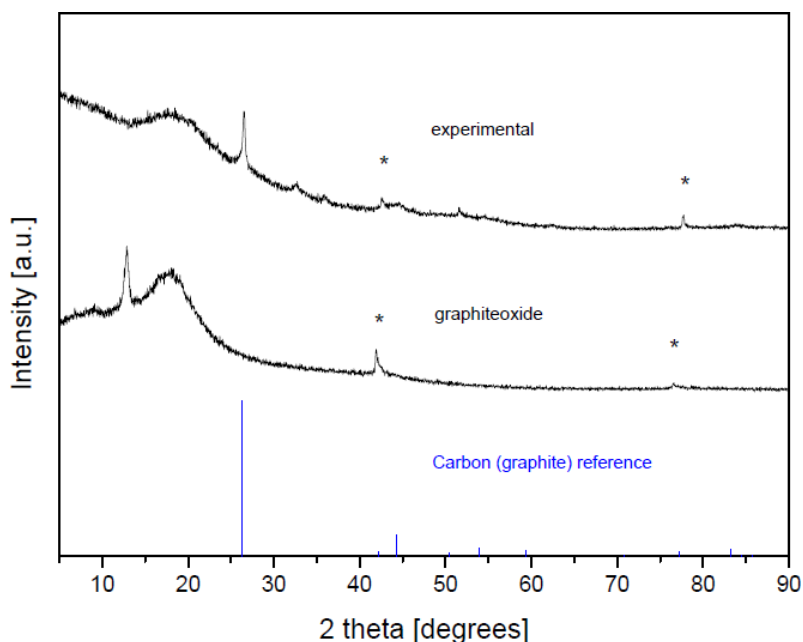

Fig. 2.21: XRD powder pattern of $Li_{12}Si_7$, graphite oxide and carbon, ball milled in argon for 3h at a speed of 350 rpm (black curve on top). An experimental XRD powder pattern of graphite oxide is shown in the middle (black curve) and the blue lines correspond to a calculated pattern of graphite.

48

The sample is highly amorphous and contains carbon. The broad peak at $2\theta =$ 18.1 ° and the two smaller peaks at a $2\theta =$ 42.3 ° and 77.7 °, respectively, match to graphite oxide. However, the most intense peak of graphite oxide at a $2\theta =$ 12.7 ° is missing. Additionally, neither $Li_{12}Si_7$ nor Li_2O could be observed. The absence of the first one indicates a complete oxidation of $Li_{12}Si_7$ to Si; the absence of Li_2O and Si in the powder pattern is caused by their amorphous nature.

Electrochemical performance

The electrode was prepared in a glove box in argon atmosphere; graphite was added as conductive additive (13 wt. %) and PVDF was used as a binder (10 wt. %). 1 M $LiPF_6$ in ethylenecarbonate / dimethylcarbonate (1:1) was used as electrolyte. The sample was cycled between 20 mV and 3.0 V vs Li/Li^+ with a rate of 20 mA g^{-1}. The initial step was discharging (lithiation) and values for specific capacity refer to the composite material.
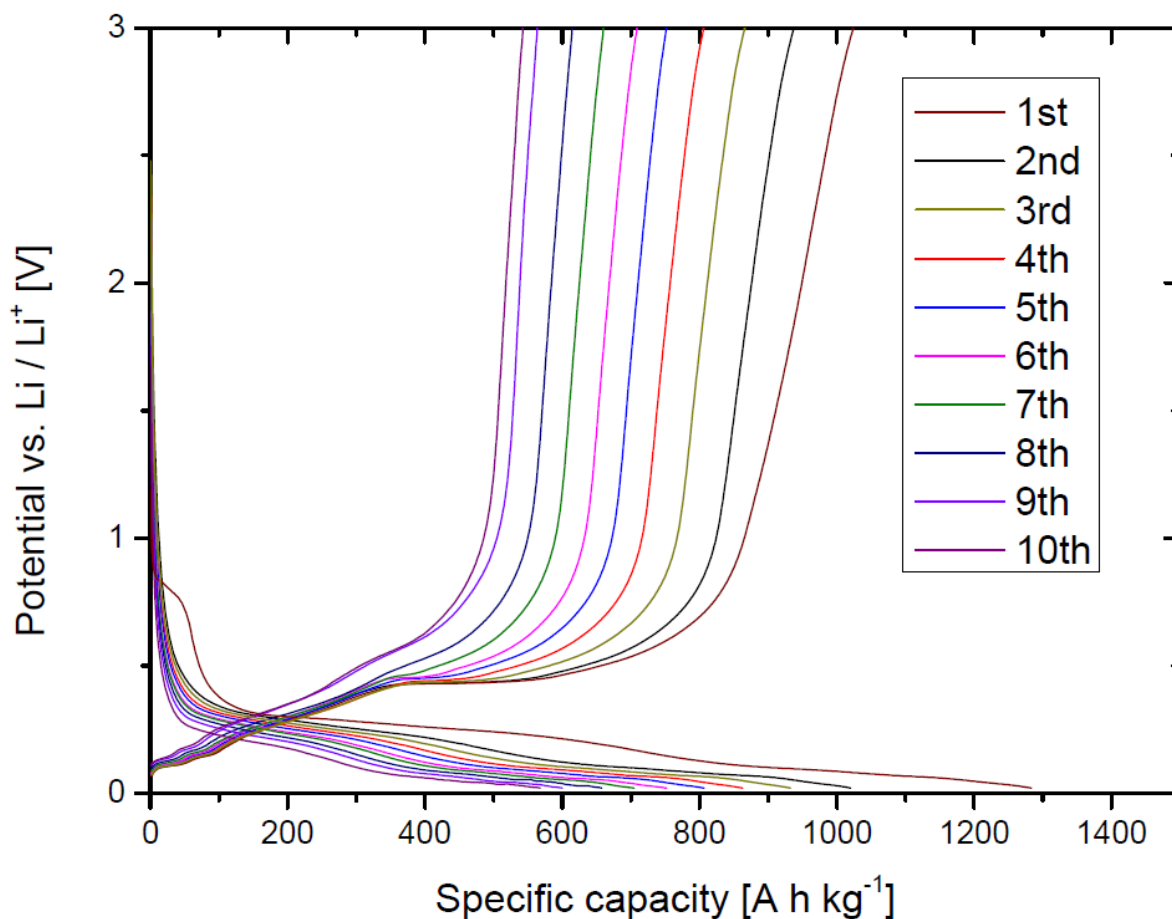
Fig. 2.22: Galvanostatic measurement of a mixture containing $Li_{12}Si_7$, graphiteoxide and carbon, ball milled in argon. Only the first 10 cycles are shown.

There is a fast capacity decay and after 10 cycles only 570 mAh g^{-1} (44%) are retained of the initial 1285 mAh g^{-1}. Additionally, there is no discharge capacity observed in the range between 1 and 2 V, which can be assigned to the irreversible formation of lithiumoxides by the electrochemical reduction of graphite oxide meaning that $Li_{12}Si_7$ and graphite oxide reacted prior to electrochemical testing. This observation is congruent with the cyclic voltammetry measurement shown in Figure 2.23.
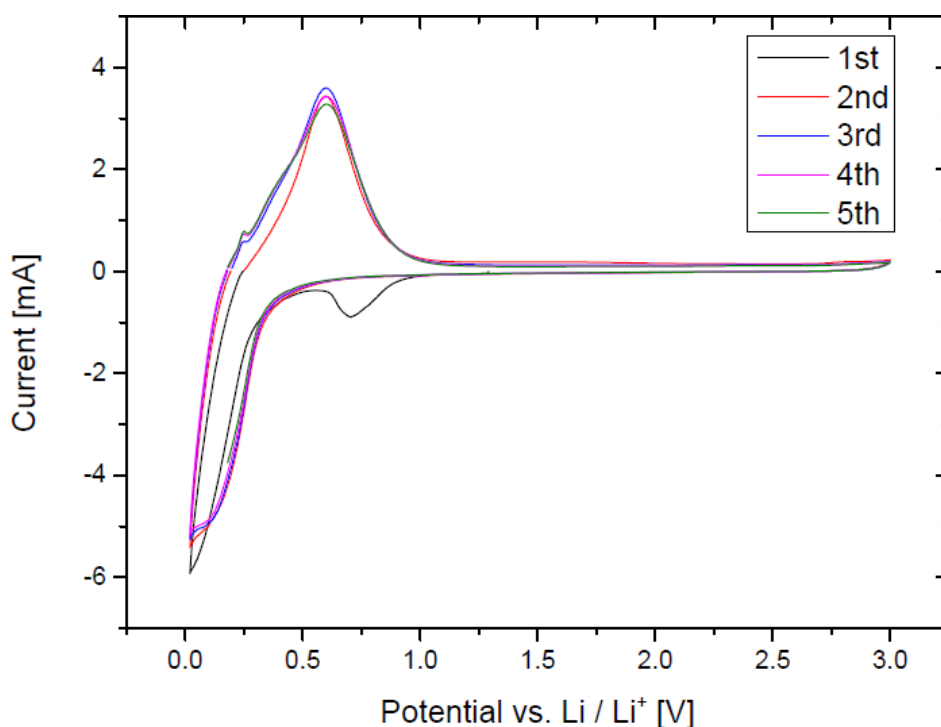
Fig. 2.23: Cyclic Voltammetry measurement of a mixture containing $Li_{12}Si_7$, graphiteoxide and carbon, ball milled in argon. The sample was cycled between 20 mV and 3.0 V vs Li/Li$^+$ with a rate of 50 µV s^{-1}. The initial step was discharging (lithiation).

There are no reduction processes observed above 1 V. During first discharge, there is a reduction peak at 0.7 V, which is no longer present in the subsequent cycles. This peak is addressed to the initial SEI formation.

Further reduction

The sample was tested if further reduction by thermal treatment is possible and if cycling behavior can be improved this way. For this purpose, a mixture of $Li_{12}Si_7$, graphite oxide and carbon powder in equal weight amount was ball milled in argon and then heated at 200 °C for 8 h under nitrogen flow. The resulting XRD powder pattern of the obtained black powder is shown in Figure 2.24.
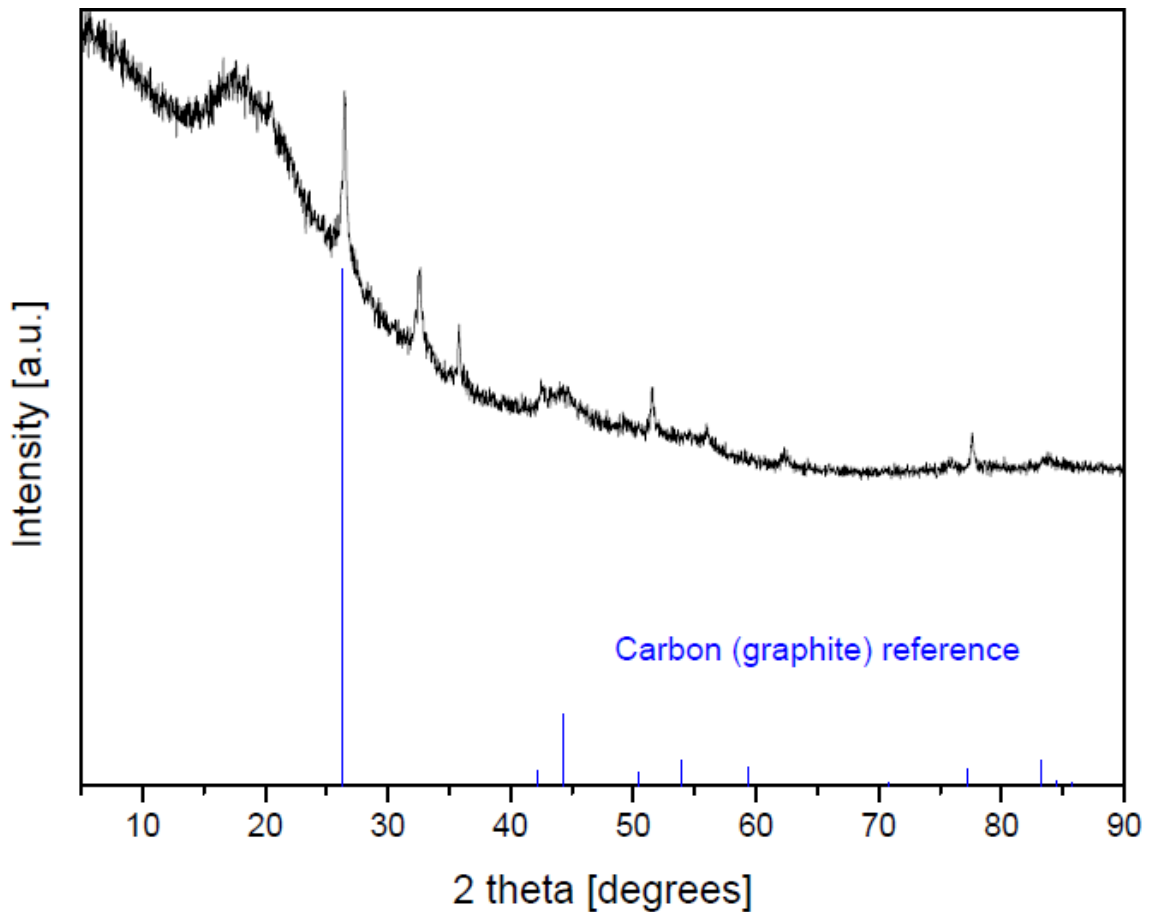
Fig. 2.24: Powder pattern of $Li_{12}Si_7$, graphite oxide and carbon, ball milled in argon for 3h at a speed of 350 rpm and then treated at 200 °C for 8 h under nitrogen flow (black curve).

The sample looks exactly the same as before heat treatment (Fig. 2.21), except that the reflections of graphite are more intense. It can be concluded that a further reduction did not occur. SEM micrographs of the mixture are shown in Figure 2.25.
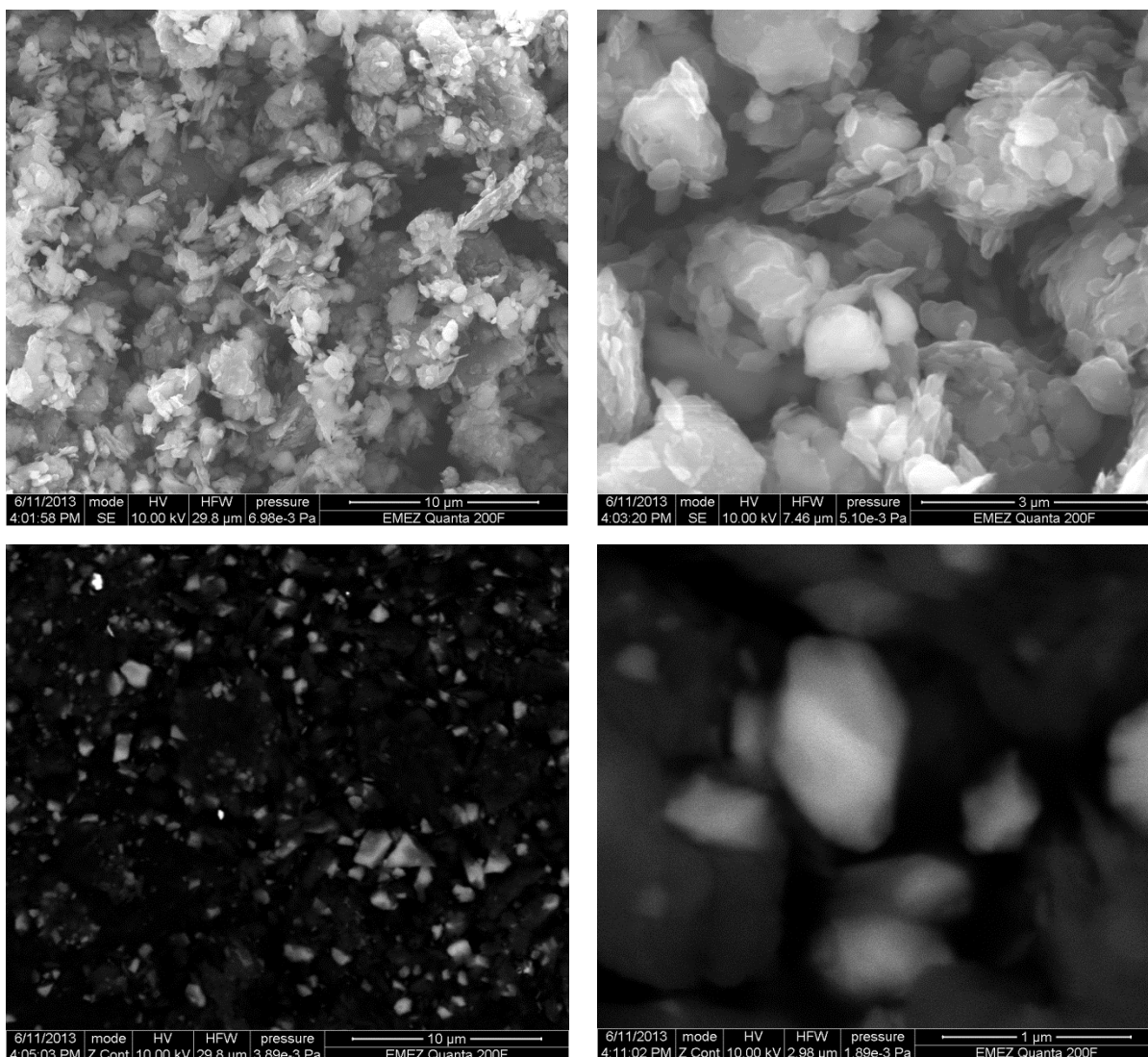
Fig. 2.25: SEM analysis of a mixture containing $Li_{12}Si_7$, graphiteoxide and carbon in equal weight amount, which was ball milled in argon for 3 h and then treated at 200 °C for 8 h in nitrogen. Top: scattered electrons; Bottom: back scattered electrons.

The sample consists of agglomerated Si particles with a diameter of 0.5 to 2 µm, which are dispersed on the surface of graphite oxide plates with a size between 10 and 20 µm. Si particles were identified by back scattered electron pictures (bright spots) as well as EDXS analysis.

53

Electrochemical performance

The electrode was prepared in a glove box in argon atmosphere; graphite was added as conductive additive (12 wt. %) and PVDF was used as a binder (10 wt. %). 1 M $LiPF_6$ in ethylenecarbonate / dimethylcarbonate (1:1) was used as electrolyte. The sample was cycled between 20 mV and 3.0 V vs Li/Li^+ with a rate of 50 mA g^{-1}. The initial step was discharging (lithiation) and values for specific capacity refer to the composite material.
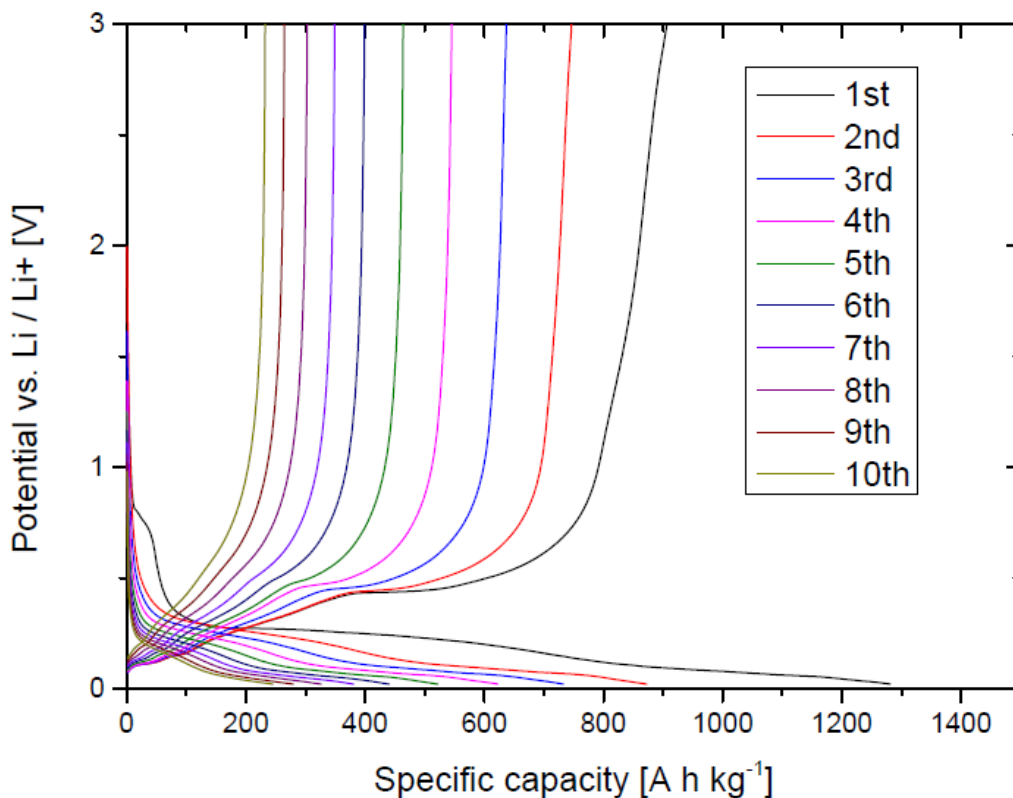
Fig. 2.26: Galvanostatic measurement of a mixture containing $Li_{12}Si_7$, graphite oxide and carbon (ball milled in argon) treated at 200 °C for 8 h under nitrogen flow. Only the first 10 cycles are shown.

Compared to the precursor sample (Fig. 2.22), there is no improvement in cycling behavior visible due to additional heat treatment. Actually, the capacity drop is even faster but this is believed to be caused by the higher current rate

of 50 mA g^{-1} instead of 20 mA g^{-1}. As a conclusion, the reduction of graphite oxide by ball milling with $Li_{12}Si_7$ is possible; Si and Li_2O are formed. Electrochemical testing (galvanostatic measurements as well as cyclic voltammetry) clearly identify Si as the electrochemical active species and no contribution of graphite oxide through formation of lithiumoxides can be observed. However, the resulting composite does not show satisfying cycling properties and needs additional improvement.

2.2.2. Reactions with transition metal chlorides

In this section, synthesis and electrochemical performance of $Li_{12}Si_7$ / carbon / transition metal composite materials are discussed. The main idea was the incorporation of another component into $Li_{12}Si_7$ / carbon composite materials through metal precipitation. This additional component is expected to stabilize the $Li_{12}Si_7$ / carbon pockets and therefore improve their cycling performance. The expected reaction of a transition metal chloride with $Li_{12}Si_7$ is shown in Eq. 2.1.

$$Li_{12}Si_7 + x\ MCl_2 \rightarrow 2\ x\ LiCl + x\ M + ((12 - 2x)\ /\ 12)\ Li_{12}Si_7 + (14x\ /\ 12)\ Si \qquad (2.1)$$
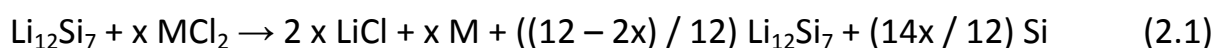
The transition metal M (Cu, Ni) is reduced; LiCl and Si are formed. Additionally, some lithiumsilicide will remain since only a small amount of MCl_2 will be used. The basic synthetic pathway is as following:

A composite material of $Li_{12}Si_7$ and graphite with a Li to C ratio of 1:6 is prepared by ball milling in argon for 3 h at a speed of 450 rpm. Afterwards MCl_2 (dried in high vacuum, ball milled) is added and all components are ball milled in argon for 3 h at a speed of 500 rpm to obtain the final product.

2.2.2.1. CuCl$_2$

The examined mixtures are listed in Table 4 below.
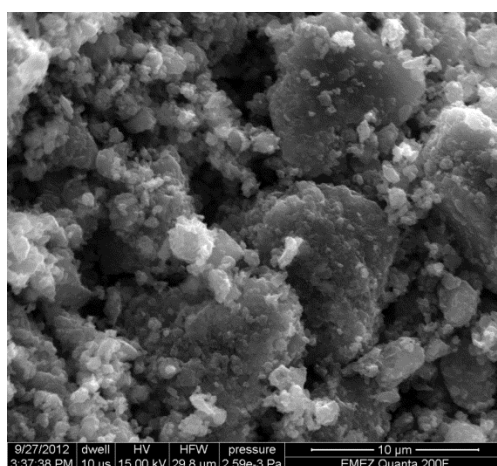
Tab. 4: Li$_{12}$Si$_7$/ graphite/ CuCl$_2$ mixtures

CuCl$_2$ [weight percent]	CuCl$_2$ (equivalents per Li$_{12}$Si$_7$)
5	0.5
12.5	1.2
20	2.1
50	8.5

For a complete reaction of Li$_{12}$Si$_7$ with CuCl$_2$, 6 equivalents of the latter one are needed. For one reaction mixture an excess of CuCl$_2$ was used (50 wt. %), so some unreacted transition metal chloride should be present after ball milling. This expectation is confirmed by the obtained XRD powder patterns of reaction mixtures shown in Figure 2.27.
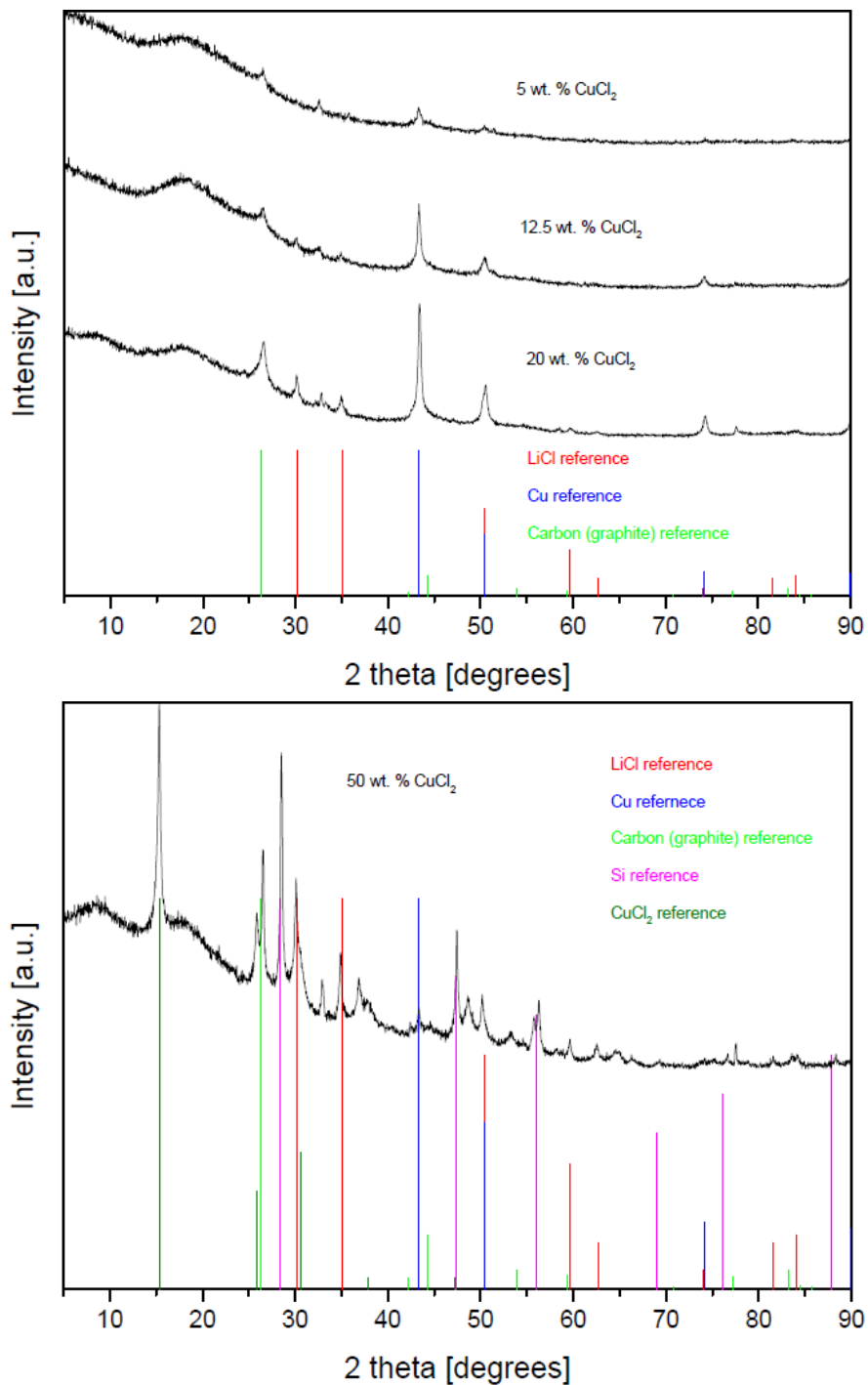
Fig. 2.27: Powder pattern of mixtures containing $Li_{12}Si_7$, graphite and $CuCl_2$, which were ball milled in argon for 3 h at a speed of 500 rpm (black curves). The Li to C ratio was kept at 1:6. Top: 5, 12.5 and 20 wt. % $CuCl_2$. Bottom: 50 wt. % $CuCl_2$.

All samples are highly amorphous and contain graphite. Mixtures containing 5, 12.5 and 20 wt. % $CuCl_2$, respectively, contain Cu as well as LiCl. The intensity of these two phases increases with higher amount of $CuCl_2$ used. The presence of Cu and absence of $CuCl_2$ indicates a complete reaction with $Li_{12}Si_7$. No lithiumsilicide or Si was observed in the powder patterns. This observation is addressed to their amorphous nature. The reaction mixture with an excess $CuCl_2$ (e.g. 50 wt. %) still contains some unreacted $CuCl_2$ besides Cu. Additionally, the formation of crystalline Si can be observed. Note that all samples contain a reflection at a $2\theta = 32.5\,°$ that could not be indexed to a phase. SEM analysis of the reaction mixture containing 12.5 wt. % $CuCl_2$ is shown below in Figure 2.28.

*Fig. 2.28:* SEM analysis of a mixture containing $Li_{12}Si_7$, graphite (with a Li to C ratio of 1:6) and 12.5 wt. % $CuCl_2$. The sample was ball milled for 3 h in argon at a speed of 500 rpm.

The homogeneous reaction mixture contains aggregated particles (micron to submicron size) which are dispersed on the surface of graphite plates (size between 10 to 100 µm). Samples containing other amount of $CuCl_2$ look similar. As a side note, Cu particles could not be distinguished from other particles using EDXS, since EDXS Analysis showed always the same composition of Cu, Si, C and Cl independent of examined area.

Electrochemical performance

Electrodes were prepared in a glove box in argon atmosphere; Super P was added as conductive additive (13 to 18 wt. %) and PVDF was used as binder (13 to 19 wt. %). 1 M LiPF$_6$ in ethylenecarbonate / dimethylcarbonate (1:1) was used as electrolyte. The samples were cycled between 10 mV and 2.0 V vs Li/Li$^+$. All measurements were started from discharge (lithiation) at a current rate of 50 mA g^{-1}. However, the testing material containing 5 wt. % CuCl$_2$ was started from charge (delithiation) with a current rate of 20 mA g^{-1}. Values for specific capacity refer to the composite material.
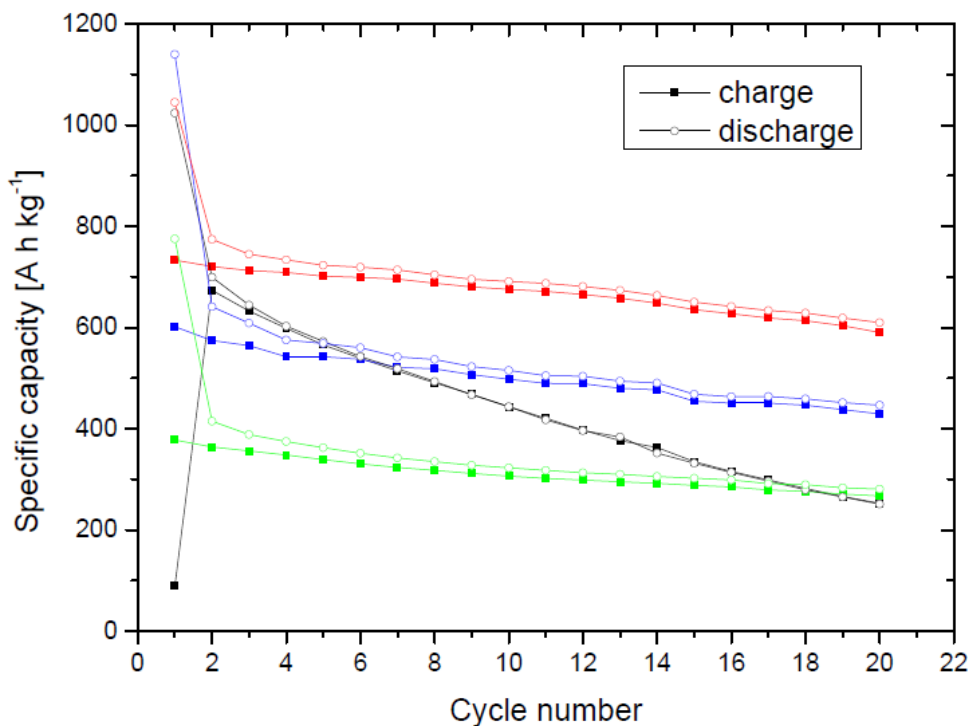
Fig. 2.29: Cycle number vs. specific capacity for ball milled mixtures containing Li$_{12}$Si$_7$, graphite and CuCl$_2$; the Li to C ratio was kept at 1:6. Only the first 20 cycles are shown. The performance of a composite with 5 wt. % CuCl$_2$ is shown in black, the one with 12.5 wt. % in red, the one with 20 wt. % in blue and the one with 50 wt. % in green.

The composite containing only 5 wt. % $CuCl_2$ shows the worst cycling behavior with rapid capacity decay despite the slower current rate. Additionally, when starting from charge, only a small initial charge capacity was observed meaning that Li could not be extracted completely from starting material. Capacity retention of samples containing 12.5, 20 or 50 wt. % $CuCl_2$ is at a comparable level. However, the achievable capacity varies with different $CuCl_2$ content: The more $CuCl_2$ contained in the composite material, the lower the maximum achievable capacity as expected due to the inclusion of additional dead weight in the form of Cu. The best cycling performance was achieved with a mixture containing 12.5 wt. % $CuCl_2$; 600 mAh g^{-1} was retained after 20 cycles. The deposition of Cu metal on the $Li_{12}Si_7$ / graphite pockets has a stabilizing effect in terms of cycling behavior, although the content of Cu should exceed 10 weight percent. The first 10 cycles of a composite material containing 12.5 wt. % $CuCl_2$ are shown in Figure 2.30 below. Si can be identified as the electrochemically active species by the potential profile of the curves. This statement is verified by a cyclic voltammetry measurement shown in Figure 2.31.
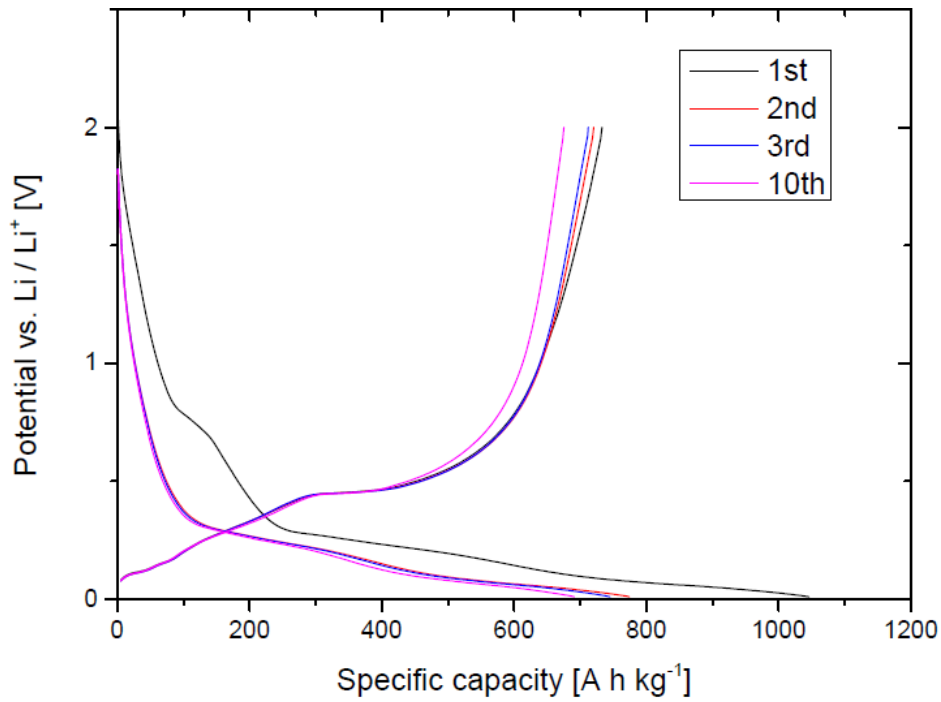
Fig. 2.30: Galvanostatic measurement of a ball milled mixture containing $Li_{12}Si_7$ and graphite with a Li to C ratio of 1:6 as well as 12.5 wt. % $CuCl_2$.
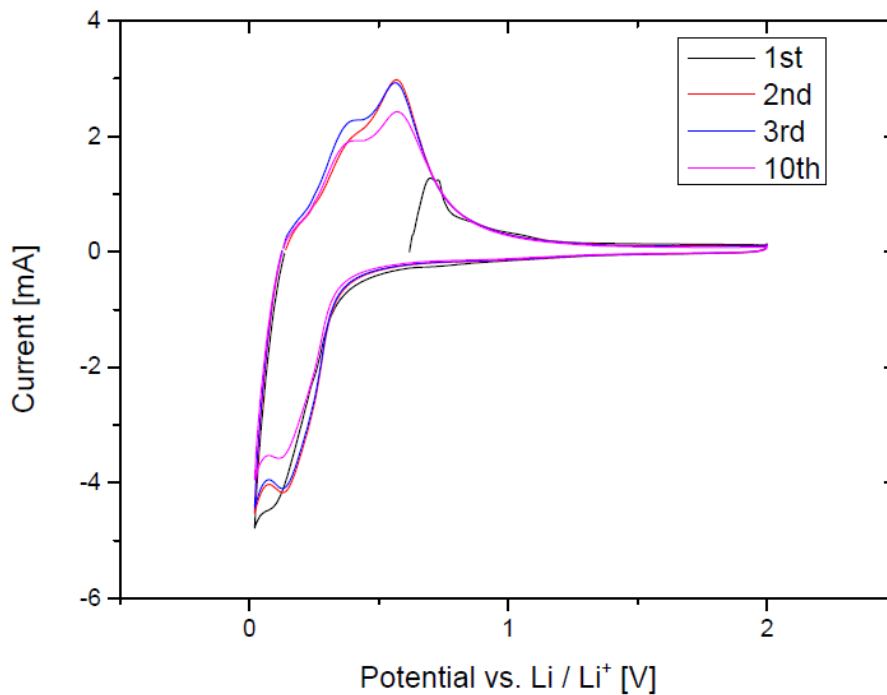

Fig. 2.31: Cyclic voltammetry measurement of a ball milled mixture containing $Li_{12}Si_7$, graphite and $CuCl_2$ in 37.5, 37.5 and 25 wt. %, respectively. The sample was cycled between 20 mV and 2.0 V vs Li/Li$^+$ at a rate of 50 μV s^{-1}. The initial step was charge (delithiation).

To summarize, the introduction of Cu by reaction of $CuCl_2$ and $Li_{12}Si_7$ into lithiumsilicide / graphite pockets was successful. Si was identified as electrochemically active species and the best performance inside Li ion battery was achieved using a composite with 12.5 wt. % $CuCl_2$. Although cycling behavior was improved regarding pure $Li_{12}Si_7$ / carbon composite materials, capacity retention did not prove itself satisfactory. Possible reasons for capacity fading are examined in the following section using post mortem analysis.

Post mortem analysis

A mixture containing $Li_{12}Si_7$, graphite -whereas Li to C ratio was kept at 1:6- and 12.5 wt. % $CuCl_2$, ball milled at 500 rpm for 3 h in argon, was examined after 20 cycles in a Li ion battery:

The electrode was prepared in a glove box under Ar atmosphere; Super P was added as conductive additive (18 wt. %) and PVDF was used as a binder (14 wt. %). 1 M $LiPF_6$ in ethylenecarbonate / dimethylcarbonate (1:1) was used as electrolyte. The sample was cycled between 10 mV and 2.0 V vs Li/Li$^+$ with a rate of 50 mA g^{-1}. The initial step was discharge (lithiation) and the sample was cycled for 20 full charge / discharge cycles. The battery cell was opened inside an argon filled glove box and the electrode material was washed multiple times with dry THF (99.5%) to remove the remaining electrolyte. The sample was ground afterwards to a black powder. Figure 2.32 shows the obtained XRD powder pattern of this material.
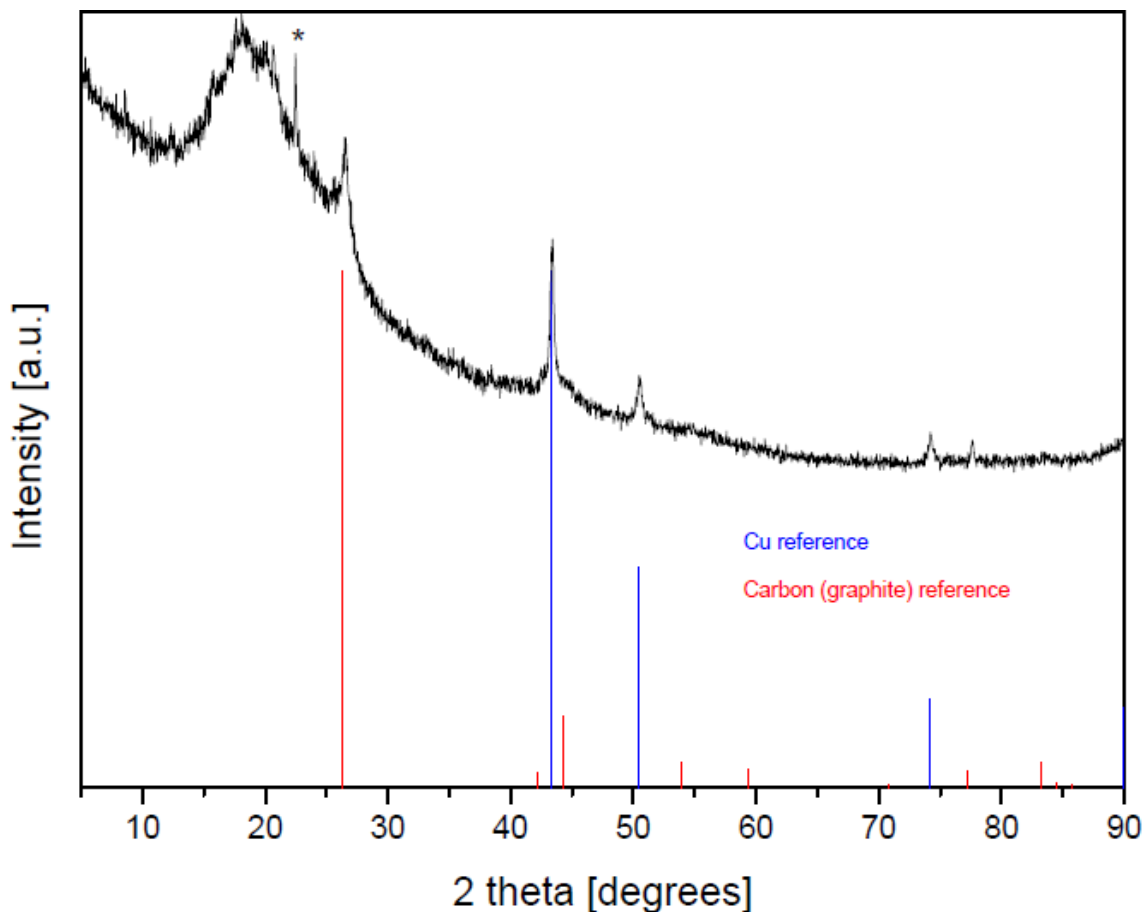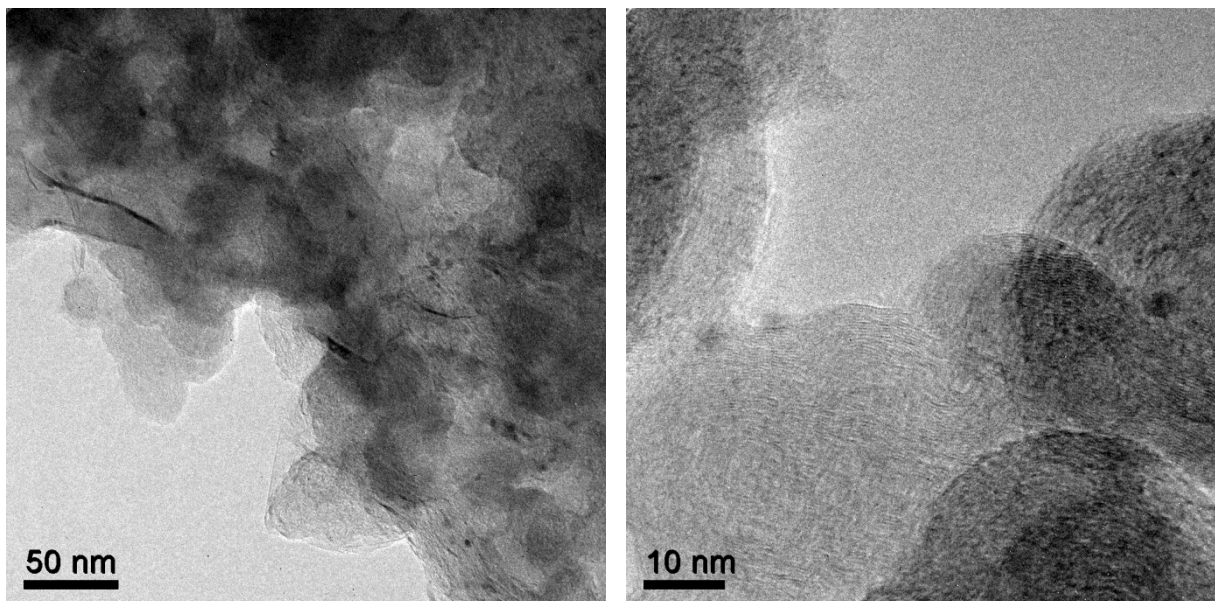
Fig. 2.32: Powder pattern of a mixture containing $Li_{12}Si_7$, graphite and 12.5 wt. % $CuCl_2$, ball milled in argon for 3 h at a speed of 450 rpm after 20 cycles in a Li ion battery (black curve).

The sample is highly amorphous and contains graphite as well as copper. The absence of crystalline Si in the powder pattern leads to the assumption that Si has become amorphous during cycling in the battery which is in accordance with literature. There are multiple unindexed peaks in the low 2θ range; the most intense one appears at a $2\theta = 22.5$ °. These reflections were also observed in the powder pattern of a $Li_{12}Si_7$ and graphite mixture after 20 cycles in a li ion battery (Fig. 2.14) and are believed to be caused by the SEI formed on the surface of the active material. An important indication supporting this theory is delivered by SEM analysis shown in Figure 2.33.

63
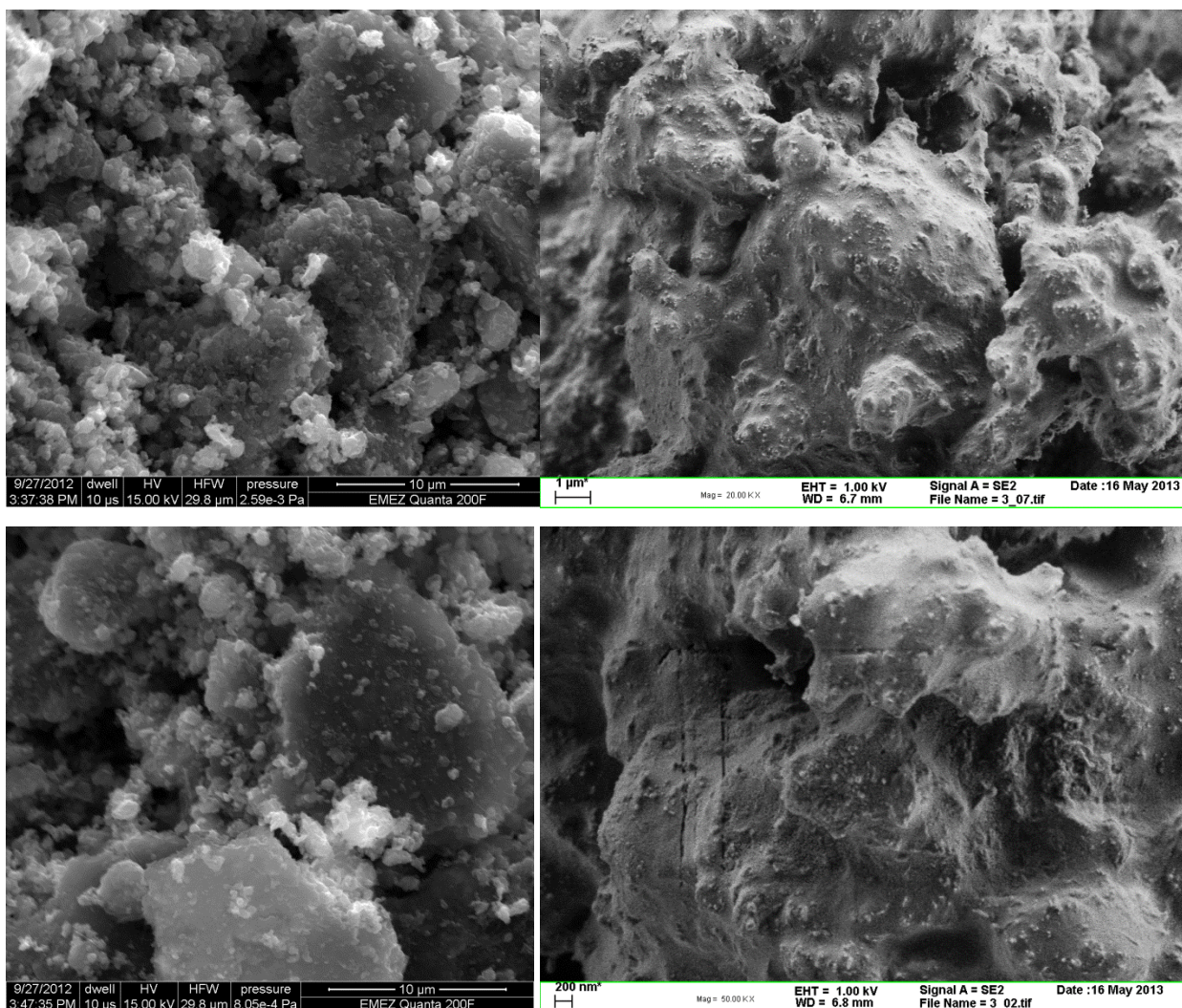
Fig. 2.33: SEM analysis of a mixture containing $Li_{12}Si_7$, graphite and 12.5 wt. % $CuCl_2$, ball milled in argon for 3 h at a speed of 500 rpm before electrochemical testing (left) and after 20 cycles in a Li ion battery (right).

After 20 cycles in Li ion battery, the sample looks highly amorphous and all particles are coated completely by a thin film, which is believed to be caused by a growing SEI layer. This connjecture is manifested by TEM analysis shown in Figure 2.34, where particles wrapped inside multiple thin layers are depicted.
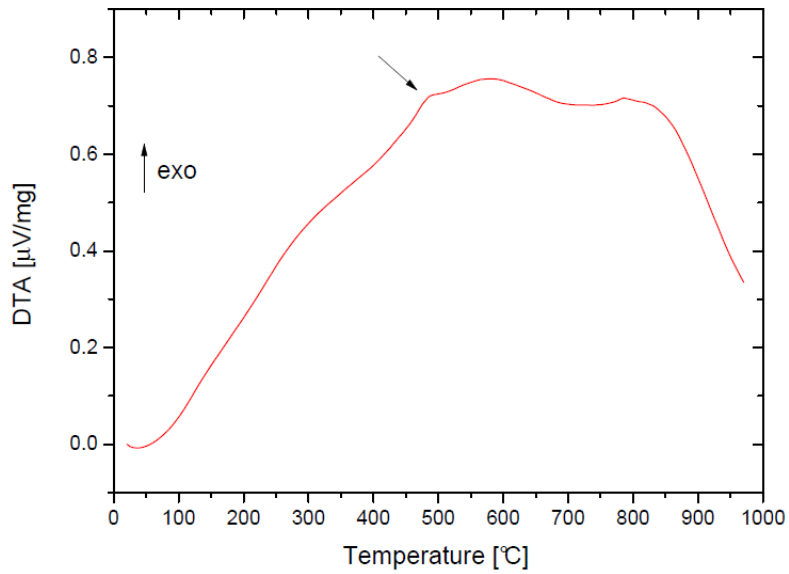
Fig. 2.34: TEM analysis of a mixture containing $Li_{12}Si_7$, graphite and 12.5 wt. % $CuCl_2$, ball milled in argon for 3 h at a speed of 500 rpm after 20 cycles in a Li ion battery.

As a conclusion, capacity fading is believed to be caused mainly by a growing SEI layer on the surface of particles. With increasing cycle number, this layer becomes thicker leading to a slower Li ion transport and therefore to an overall worse kinetic behavior for lithiation and delithiation processes. Additionally, the obtained capacity is too low for a successful implementation of this material in a Li ion battery. Therefore, further modifications are necessary.

TG/DTA

Thermogravimetric (TG) and differential thermal analysis (DTA) of a reaction mixture containing 12.5 wt. % $CuCl_2$ were performed in order to see if there are observable phase transitions at elevated temperatures. 20 mg of the sample were put inside a corundum crucible and heated to 1000 °C at a heating rate of 10 °C min. The measurement was performed at a constant pressure in argon atmosphere. DTA of the reaction mixture is shown in Figure 2.35.

Fig. 2.35: Differential thermal analysis of a mixture containing $Li_{12}Si_7$, graphite and 12.5 wt. % $CuCl_2$, ball milled in argon for 3 h at a speed of 500 rpm.

There is an exothermic peak at 480 °C, indicating to a metastable behavior and consequent unfinished reaction. No weight loss was observed over whole temperature range as shown in Figure2.36.
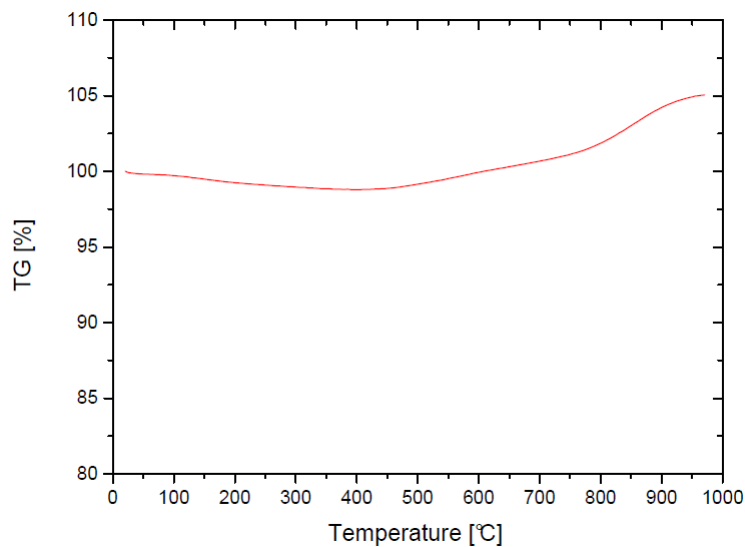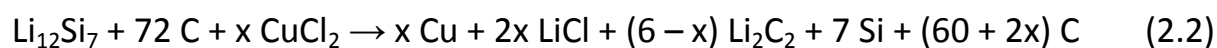

Fig. 2.36: TGA of a mixture containing $Li_{12}Si_7$, graphite and 12.5 wt. % $CuCl_2$, ball milled in argon for 3 h at a speed of 500 rpm.

According to differential thermal analysis, the sample was sealed in a niobium ampoule in argon and then treated at 500 °C for 8 h to see which phases form. The obtained XRD powder pattern of the reaction mixture is shown in Figure 2.37.
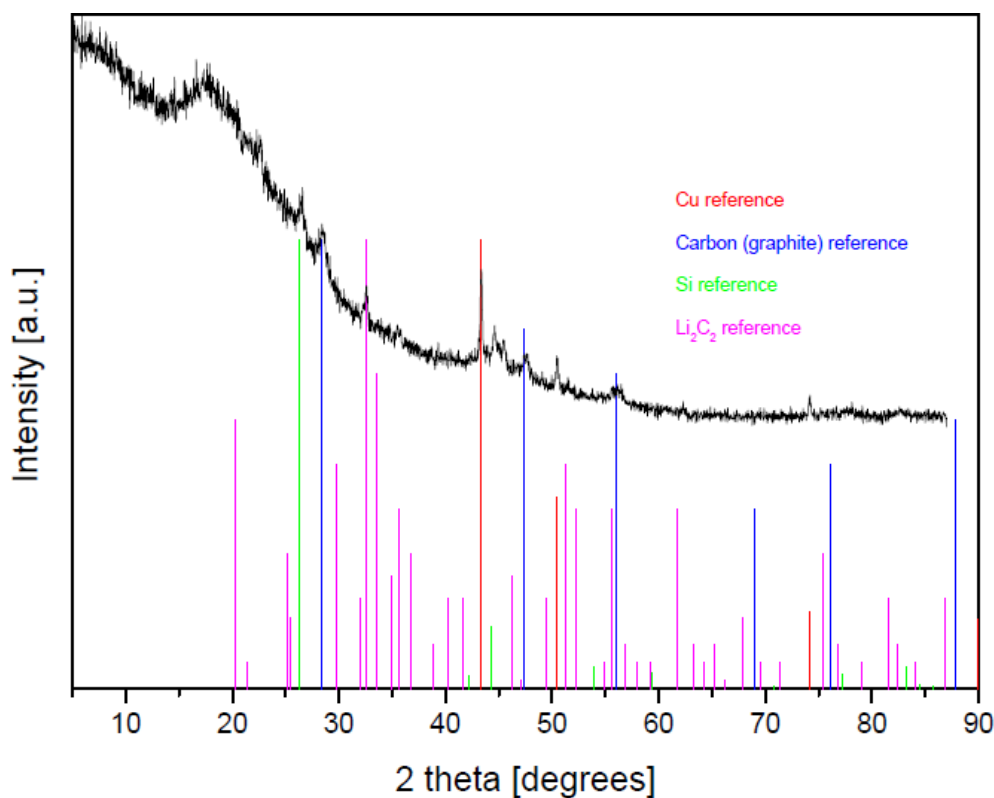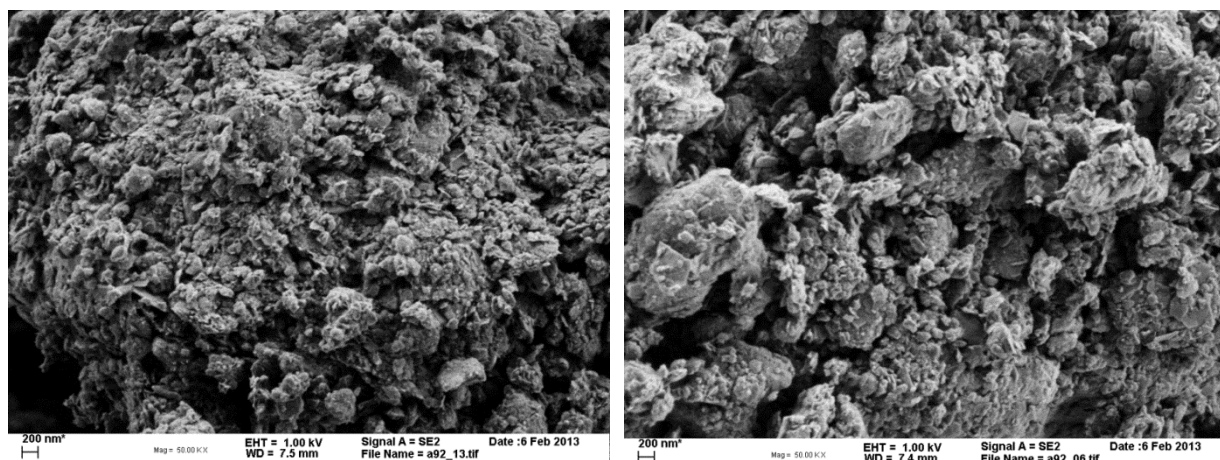

Fig. 2.37: XRD powder pattern of a ball milled mixture containing $Li_{12}Si_7$, graphite and 12.5 wt. % $CuCl_2$, which was treated at 500 °C for 8 h in argon (black curve).

The sample consists of Cu, Si, graphite, some small amount of Li_2C_2 and amorphous material. No LiCl or $Li_{12}Si_7$ was observed. It can be concluded that additional heat treatment at 500 °C leads to the formation of Li_2C_2 as well as the formation of crystalline Si. Taking into account the result of DTA and XRD, the following reaction is suggested:

$$Li_{12}Si_7 + 72\ C + x\ CuCl_2 \rightarrow x\ Cu + 2x\ LiCl + (6-x)\ Li_2C_2 + 7\ Si + (60+2x)\ C \qquad (2.2)$$
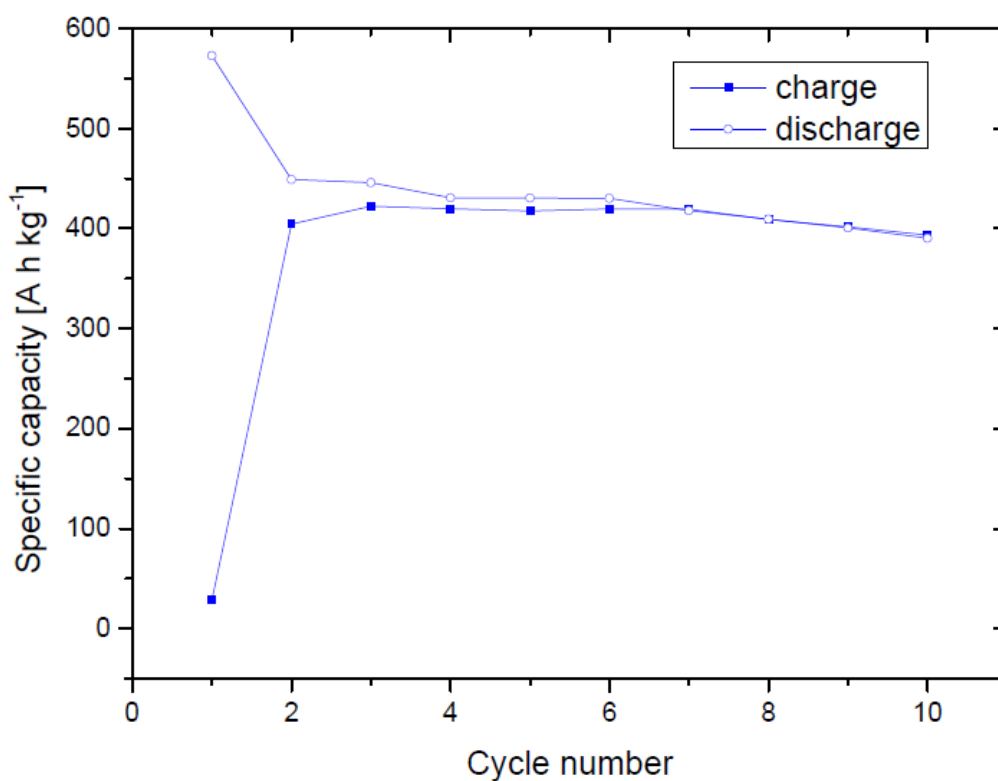
SEM analysis of the reaction mixture is shown in Figure 2.38 below.

Fig. 2.38: SEM analysis of a ball milled mixture containing $Li_{12}Si_7$, graphite and 12.5 wt. % $CuCl_2$, treated at 500 °C for 8 h in argon.

The homogeneous sample consists of agglomerated particles (submicron size) which are dispersed on the surface of graphite plates (size around 10µm). Once again, it was not possible to distinguish Si and Cu particles using EDXS analysis.

Electrochemical performance

The electrode was prepared in a glove box in argon atmosphere; Super P was added as conductive additive (19 wt. %) and PVDF was used as a binder (10wt. %). 1 M $LiPF_6$ in ethylenecarbonate / dimethylcarbonate (1:1) was used as electrolyte. The sample was cycled between 10 mV and 2.0 V vs Li/Li^+ at a current rate of 100 mA g^{-1}. The initial step was charging (delithiation) and values for specific capacity refer to the composite material.

Fig. 2.39: Cycle number vs. specific capacity for a ball milled mixture containing $Li_{12}Si_7$, graphite and 12.5 wt. %$CuCl_2$, treated at 500 °C for 8 h in argon; only the first 10 cycles are shown.

The obtained maximum capacity is significantly smaller than the one achieved with the reaction mixture before heat treatment (Fig. 2.29). However, this effect can be partially addressed to the faster current rate of 100 mA g^{-1} instead of 50 mA g^{-1}. As a summary, there were no visible improvements in cycling behavior observed due to additional heat treatment.

2.2.2.2. NiCl₂

A mixture containing Li₁₂Si₇ and graphite with a Li to C ratio of 1:6 as well as 10 wt. % NiCl₂ was prepared in analog manner to the CuCl₂ containing ones (see section 2.2.2.1). The obtained XRD powder pattern is shown in Figure 2.40.
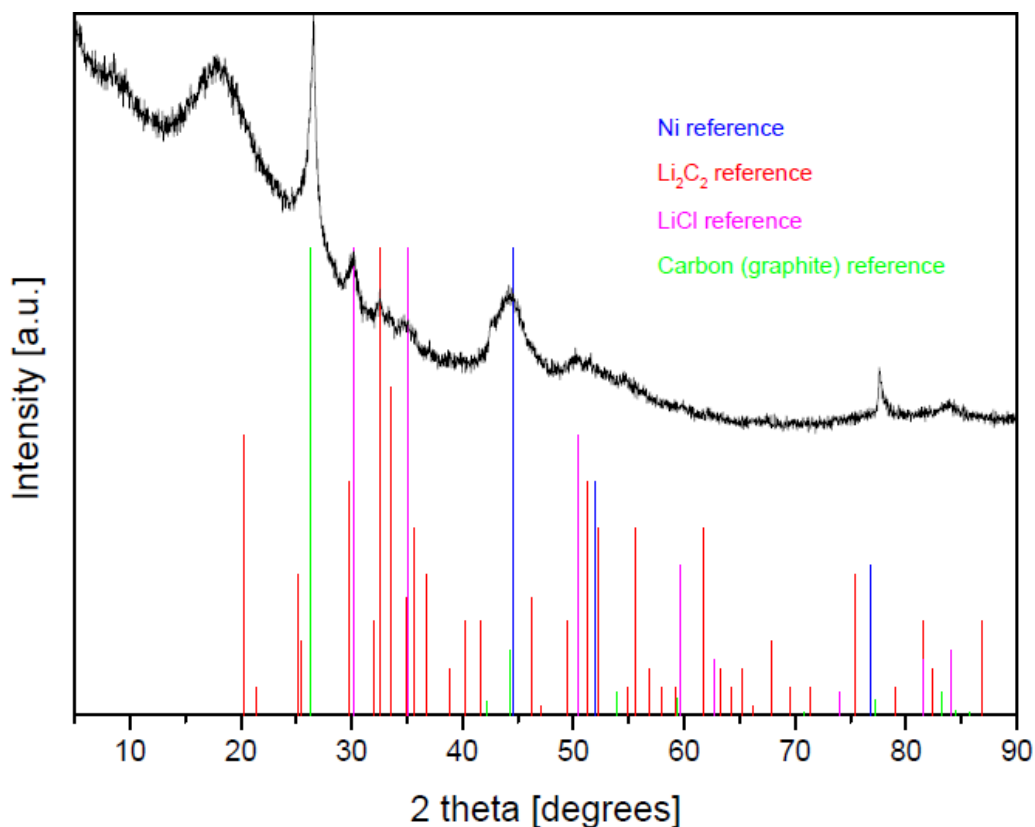

Fig. 2.40: XRD powder pattern of a mixture containing Li₁₂Si₇, graphite and 10 wt. % NiCl₂, which was ball milled in argon for 3 h at a speed of 500 rpm (black curve).

The sample consists of Ni, graphite, LiCl, some small amount of Li₂C₂ and amorphous material. The presence of Ni and the absence of NiCl₂ indicate a complete reaction with Li₁₂Si₇. No lithiumsilicide or Si could be observed in the powder pattern. This observation is addressed to their amorphous nature. SEM analysis of the reaction mixture is shown in Figure 2.41.

70
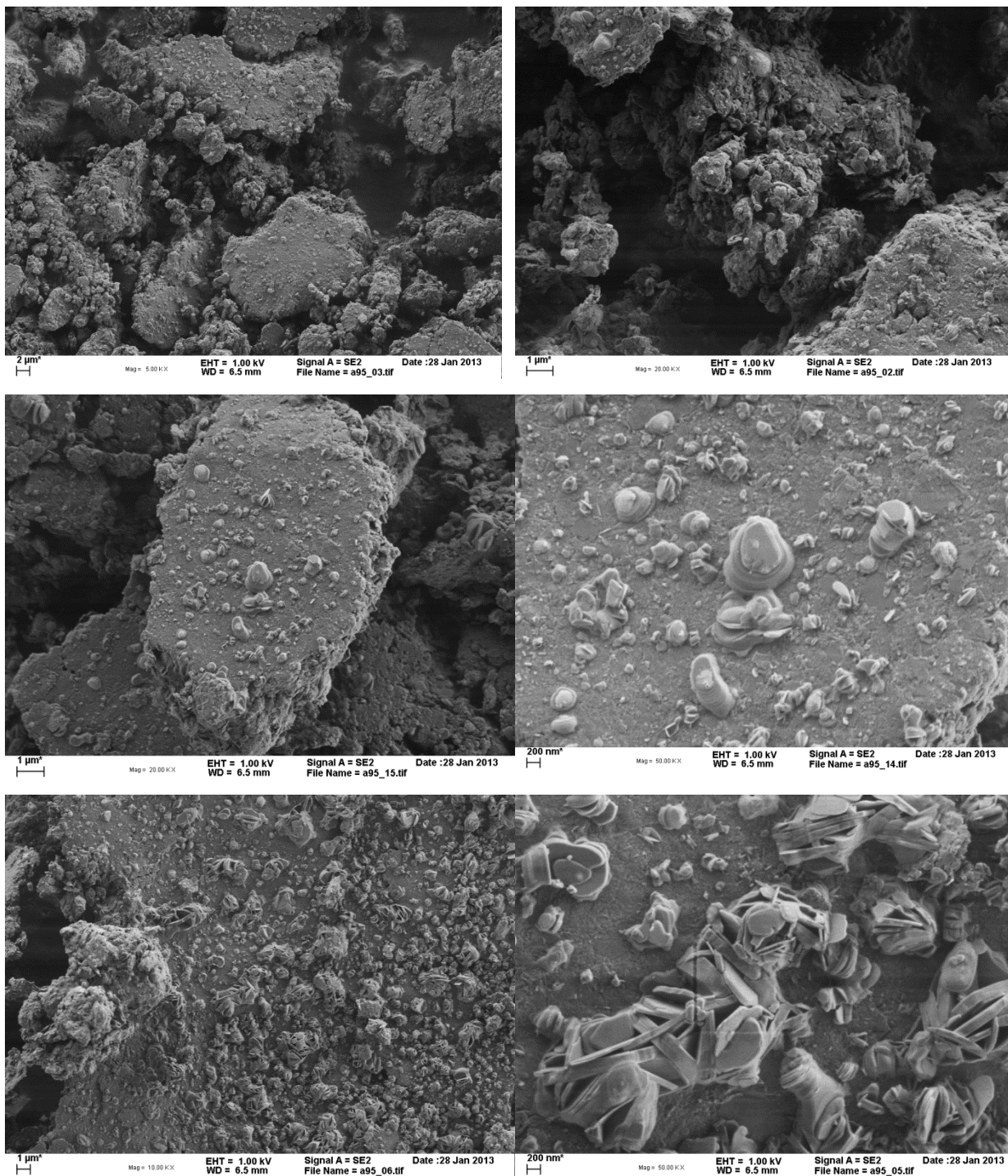
Fig. 2.41: SEM analysis of a mixture containing $Li_{12}Si_7$, graphite (with a Li to C ratio of 1:6) and 10 wt. % $NiCl_2$. The sample was ball milled for 3 h in argon at a speed of 500 rpm.

The sample contains graphite plates with a size of 10 μm; two different type of particles are dispersed on their surface: (1) plate-like particles (size: 200 nm)

which are stacked on each other and (2) other agglomerated particles with no distinct geometry (even smaller in size). The 200 nm plate-like particles are believed to be Ni; the other particles are believed to consist of Si or lithiumsilicides.

Electrochemical performance

The electrode was prepared in a glove box in argon atmosphere; Super P was added as conductive additive (13 wt. %) and PVDF was used as a binder (17 wt. %). 1 M $LiPF_6$ in ethylenecarbonate / dimethylcarbonate (1:1) was used as electrolyte. The sample was cycled between 10 mV and 2.0 V vs Li/Li^+ with a current rate of 50 mA g^{-1}. The initial step was charge (delithiation) and values for specific capacity refer to the composite material.
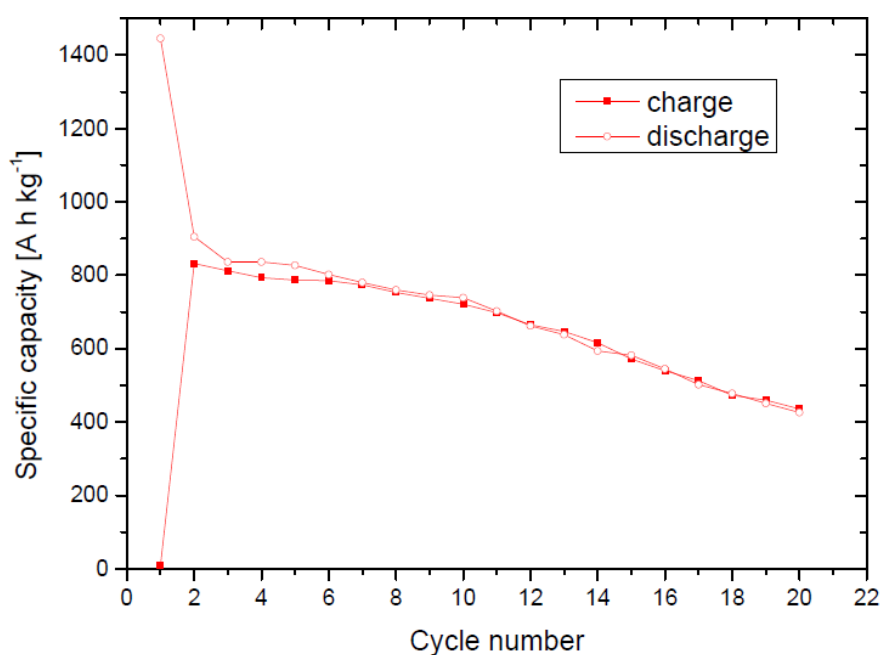
Fig. 2.42: Cycle number vs. specific capacity for a ball milled mixture containing $Li_{12}Si_7$, graphite and 10 wt. % $NiCl_2$; the Li to C ratio was kept at 1:6. Only the first 20 cycles are shown.

During initial charge step, a capacity of 10 mAh g^{-1} was obtained meaning that no Li was extracted from starting material. The following discharge step lead to a capacity of 1450 mAh g^{-1}, which was not retained, however. During next discharge, 900 mAh g^{-1} was obtained. Starting from this point, there is a constant drop of capacity: After 10 cycles, a capacity of 740 mAh g^{-1} and after 20 cycles, a capacity of 440 mAh g^{-1} was retained, respectively.

To summarize, the introduction of Ni by reaction of $NiCl_2$ and $Li_{12}Si_7$ into lithiumsilicide / graphite pockets was successful. However, cycling behavior of this composite material is far worse than the one of its $CuCl_2$ counterparts (Fig. 2.29) and comparable to the one of pure $Li_{12}Si_7$ / carbon composite materials (Fig. 2.20). Possible reasons for capacity fading are examined in the following section using post mortem analysis.

Post mortem analysis

A mixture containing $Li_{12}Si_7$, graphite -whereas Li to C ratio was kept at 1:6- and 10 wt. % $NiCl_2$, ball milled at 500 rpm for 3 h in argon, was examined after 20 cycles in a Li ion battery:

The electrode was prepared in a glove box under Ar atmosphere; Super P was added as conductive additive (14 wt. %) and PVDF was used as a binder (14 wt. %). 1 M $LiPF_6$ in ethylenecarbonate / dimethylcarbonate (1:1) was used as electrolyte. The sample was cycled between 10 mV and 2.0 V vs Li/Li$^+$ at a rate of 50 mA g^{-1}. The initial step was charge (delithiation) and the sample was cycled for 20 full charge / discharge cycles and then charged. The battery cell was opened inside an argon filled glove box and the electrode material was

washed multiple times with dry THF (99.5%) to remove the remaining electrolyte. The sample was ground afterwards to a black powder. Figure 2.43 shows the obtained XRD powder pattern of this material.
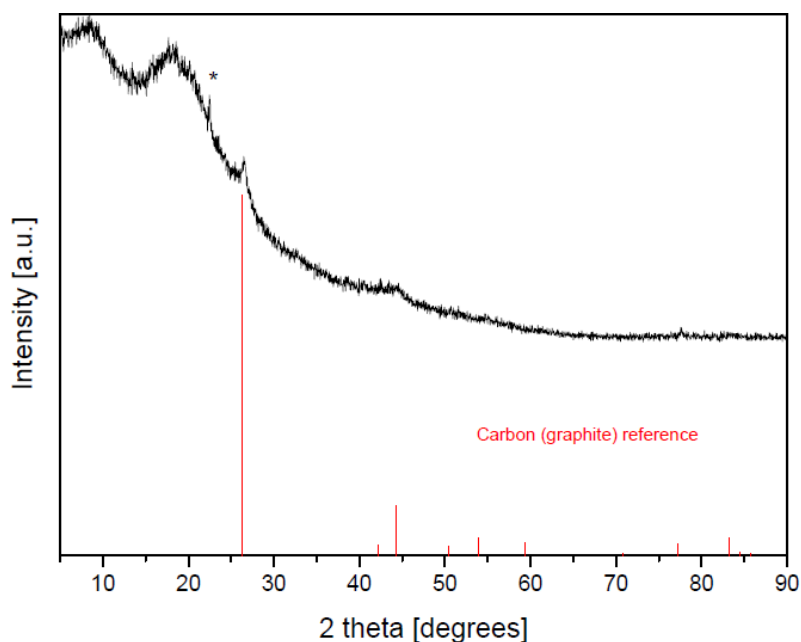
Fig. 2.43: XRD powder pattern of a mixture containing $Li_{12}Si_7$, graphite and 10 wt. % $NiCl_2$, ball milled in argon for 3 h at a speed of 500 rpm after 20 cycles in a Li ion battery (black curve).

The sample is highly amorphous and contains graphite. Ni was not found in the powder pattern which is caused by its amorphous nature. The absence of crystalline Si in the powder pattern leads to the assumption that Si has become amorphous during cycling in battery which is in accordance with literature. There are multiple unindexed peaks in the low 2θ range; the most intense one appears at $2\theta = 22.4$ °. These reflections were also observed in the powder pattern of a $Li_{12}Si_7$ and graphite mixture after 20 cycles in a Li ion battery (Fig. 2.14) and are believed to be caused by the SEI formed on the surface of the active material. An important indication supporting this theory is delivered by SEM analysis shown in Figure 2.44.
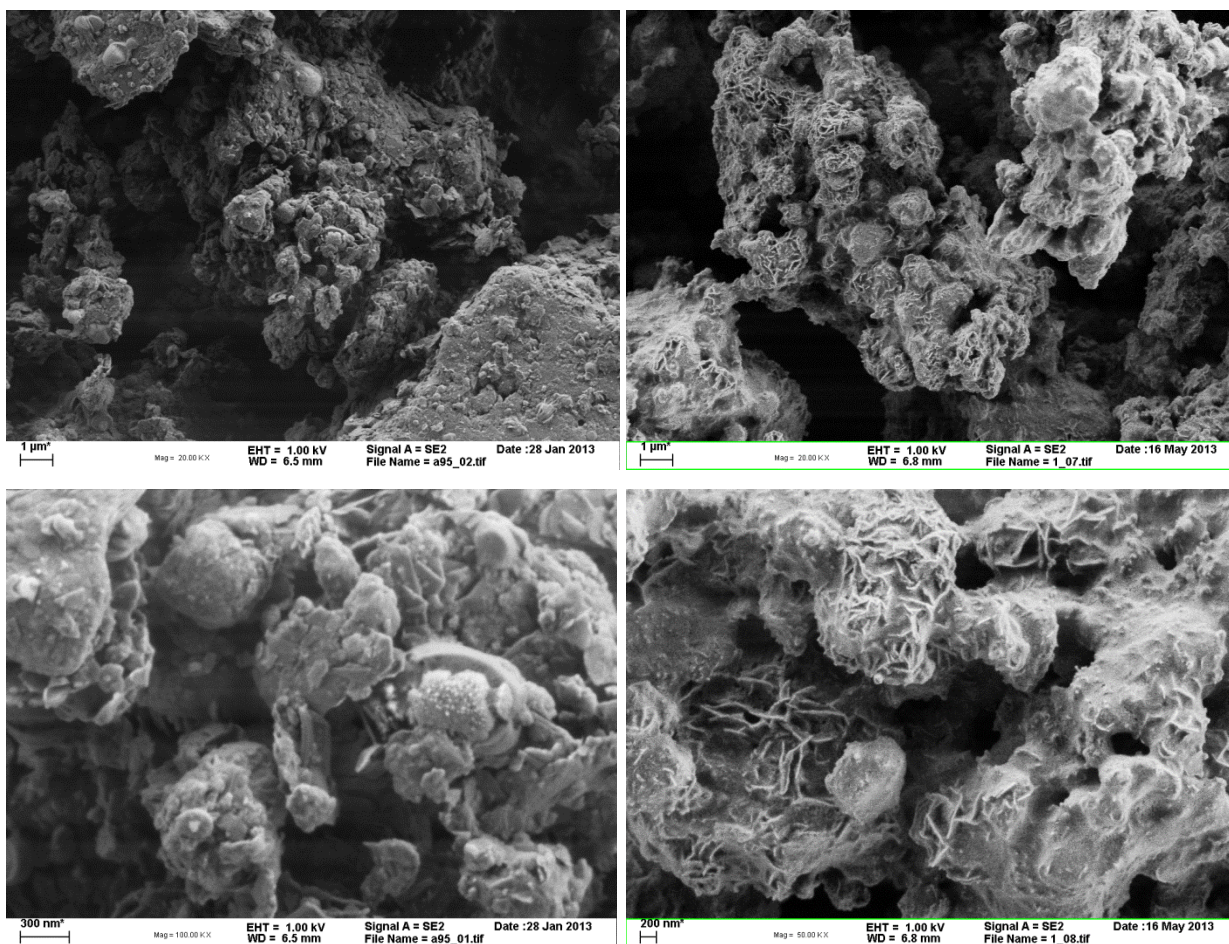
Fig. 2.44: SEM analysis of a mixture containing $Li_{12}Si_7$, graphite and 10 wt. % $NiCl_2$, ball milled in argon for 3 h at a speed of 500 rpm before electrochemical testing (left) and after 20 cycles in a Li ion battery (right).

After 20 cycles in Li ion battery, the sample looks highly amorphous and all particles are coated completely by a thin film, which is believed to be caused by a growing SEI layer. This thesis is manifested by TEM analysis shown in Figure 2.45, where particles wrapped inside multiple thin layers are depicted.
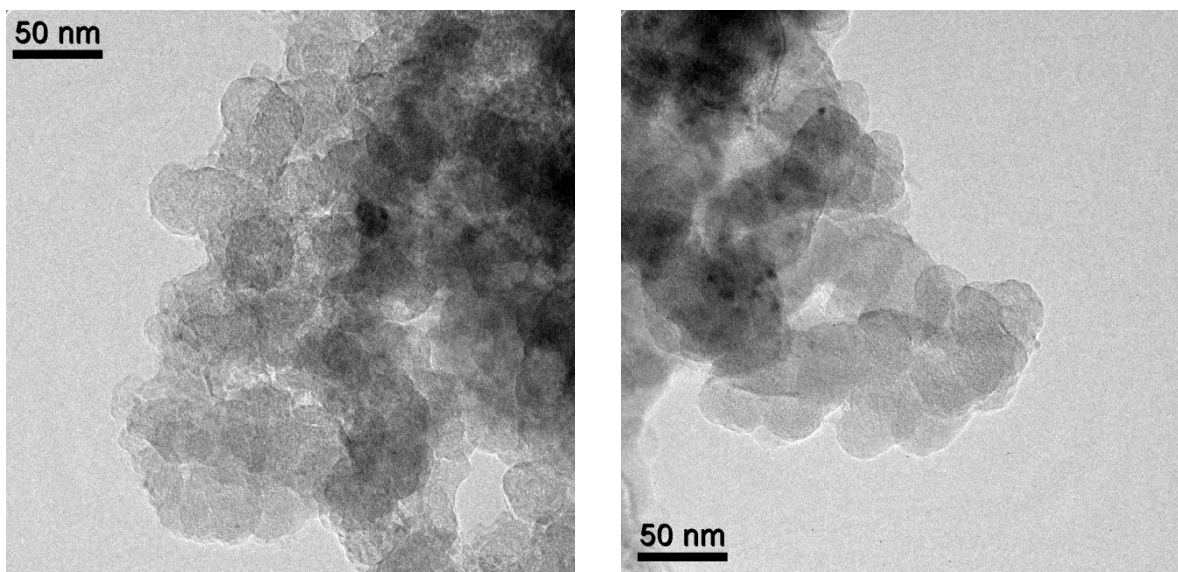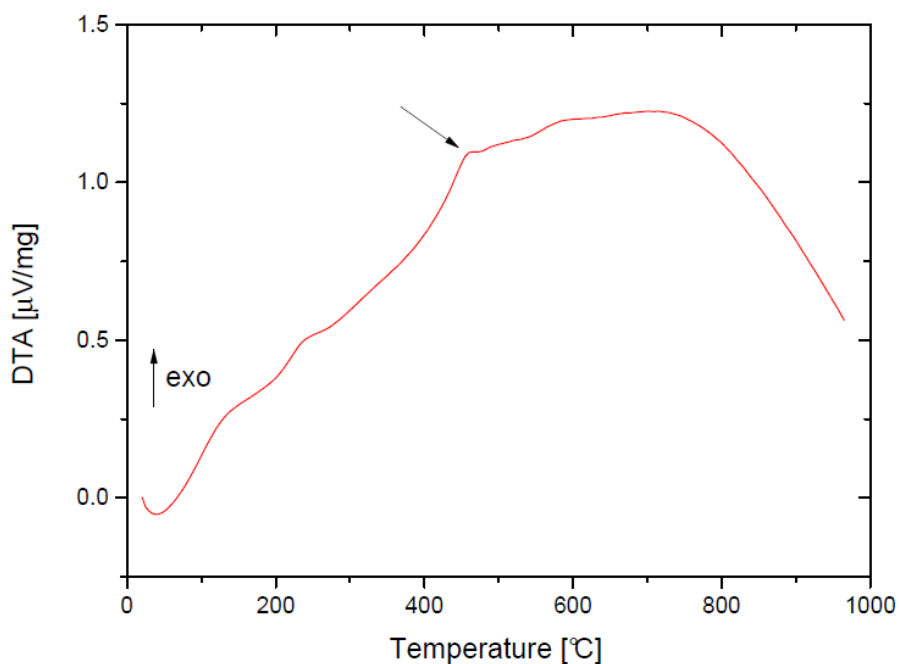
Fig. 2.45: TEM analysis of a mixture containing $Li_{12}Si_7$, graphite and 10 wt. % $NiCl_2$, ball milled in argon for 3 h at a speed of 500 rpm after 20 cycles in a Li ion battery.

As a conclusion, capacity fading is believed to be caused mainly by a growing SEI layer on the surface of particles. With increasing cycle number, this layer becomes thicker leading to a slower Li ion transport and therefore to an overall worse kinetic behavior for lithiation and delithiation processes. Additionally, the obtained capacity is too low for a successful implementation of this material in a Li ion battery. Therefore, further modifications are necessary.

TG/DTA

Thermogravimetric (TG) and differential thermal analysis (DTA) of a reaction mixture containing 10 wt. % $NiCl_2$ were performed in order to see if there are observable phase transitions at elevated temperatures. 20 mg of the sample were put inside a corundum crucible and heated to 1000 °C at a heating rate of 10 °C min. The measurement was performed at a constant pressure in argon atmosphere. DTA of the reaction mixture is shown in Figure 2.46.

Fig. 2.46: Differential thermal analysis of a mixture containing $Li_{12}Si_7$, graphite and 10 wt. % $NiCl_2$, ball milled in argon for 3 h at a speed of 500 rpm.

There is an exothermic peak at 460 °C, indicating to a metastable behavior and consequent unfinished reaction. TG analysis of the reaction mixture is shown in Figure 2.47.
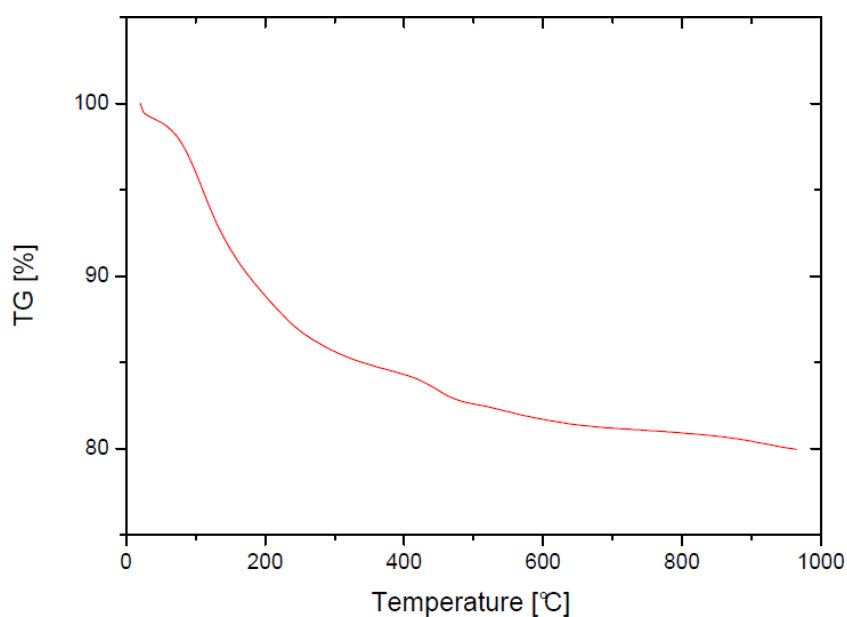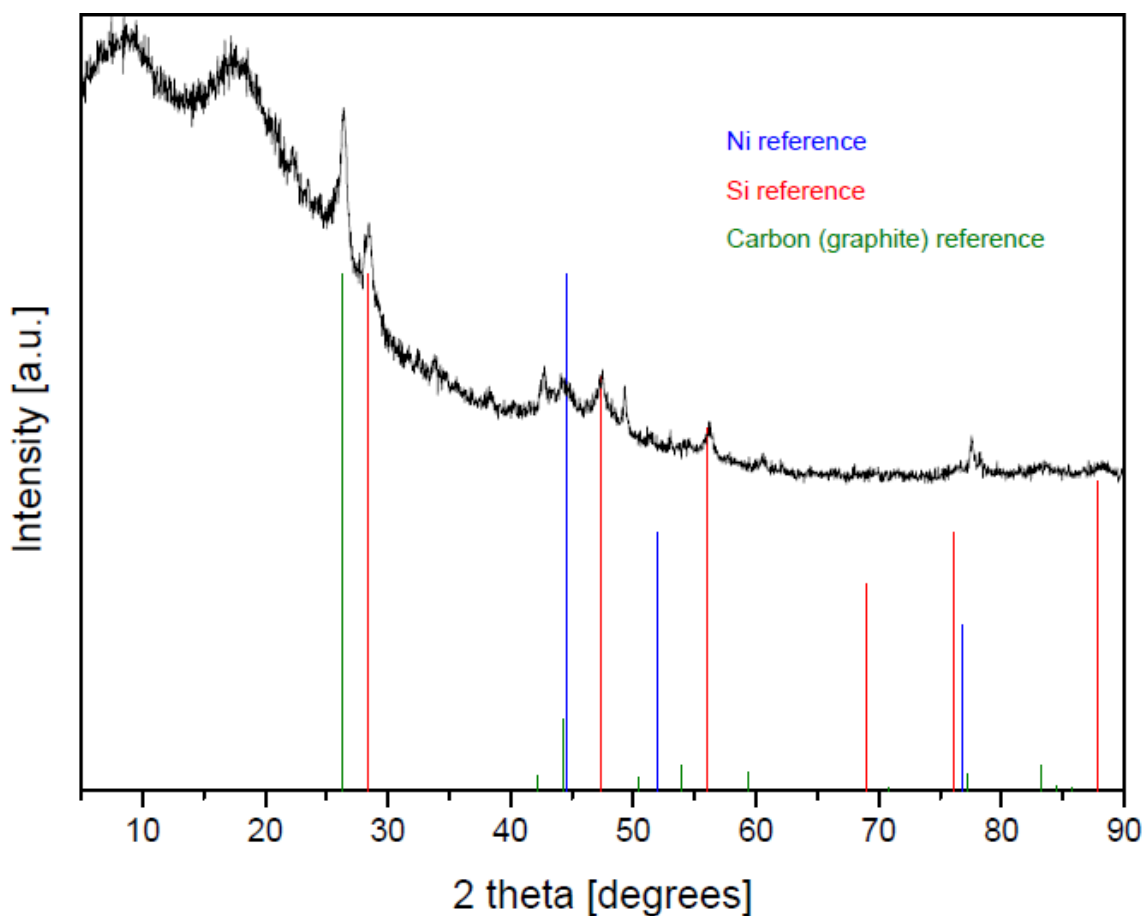

Fig. 2.47: TGA of a mixture containing $Li_{12}Si_7$, graphite and 10 wt. % $NiCl_2$, ball milled in argon for 3 h at a speed of 500 rpm.

There is a weight loss of 15% from room temperature up to 400 °C. This observation could be caused by the loss of water. When $NiCl_2$ was dried before use, the water content was not completely eliminated.

According to differential thermal analysis, the sample was sealed in a niobium ampoule in argon and then treated at 500 °C for 8 h to see which phases form. The obtained XRD powder pattern of the reaction mixture is shown in Figure 2.48.

Fig. 2.48: XRD powder pattern of a ball milled mixture containing $Li_{12}Si_7$, graphite and 10 wt. % $NiCl_2$, which was treated at 500 °C for 8 h in argon.

The sample consists of Ni, Si, graphite and amorphous material. The absence of LiCl and Li_2C_2 in the powder pattern is caused by their amorphous nature. It can

be concluded that additional heat treatment at 500 °C leads to the formation of crystalline Si. Taking into account the result of DTA and XRD, the following reaction is suggested:

$$Li_{12}Si_7 + 72\ C + x\ NiCl_2 \rightarrow x\ Ni + 2x\ LiCl + (6-x)\ Li_2C_2 + 7\ Si + (60+2x)\ C \qquad (2.3)$$
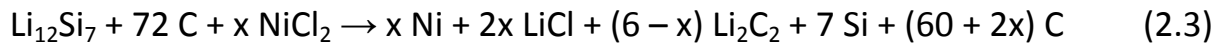
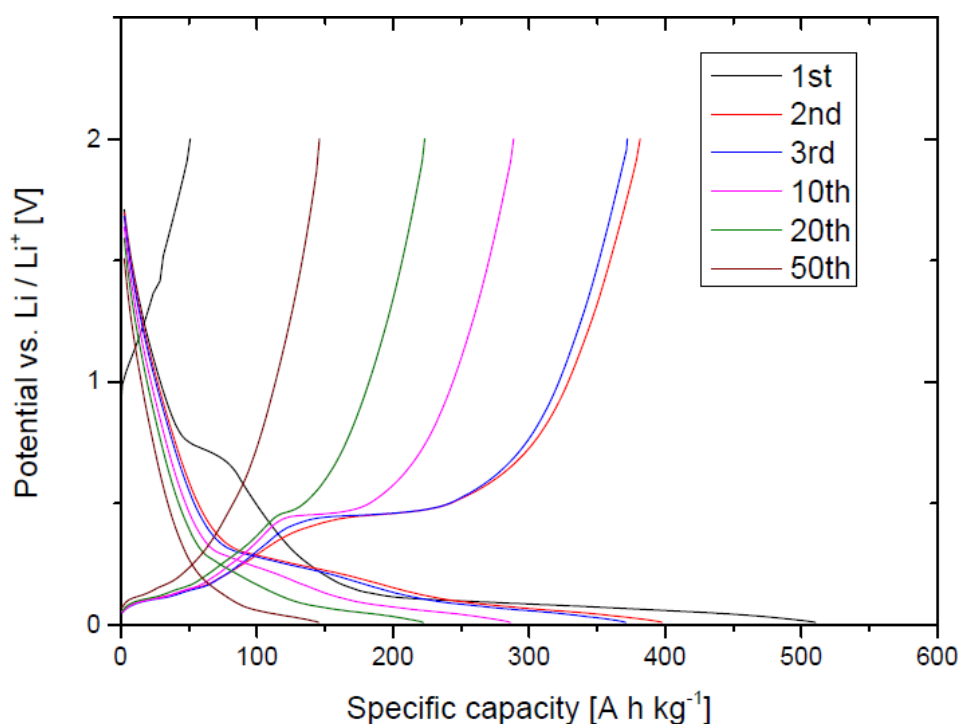SEM analysis of the reaction mixture is shown in Figure 2.49 below.
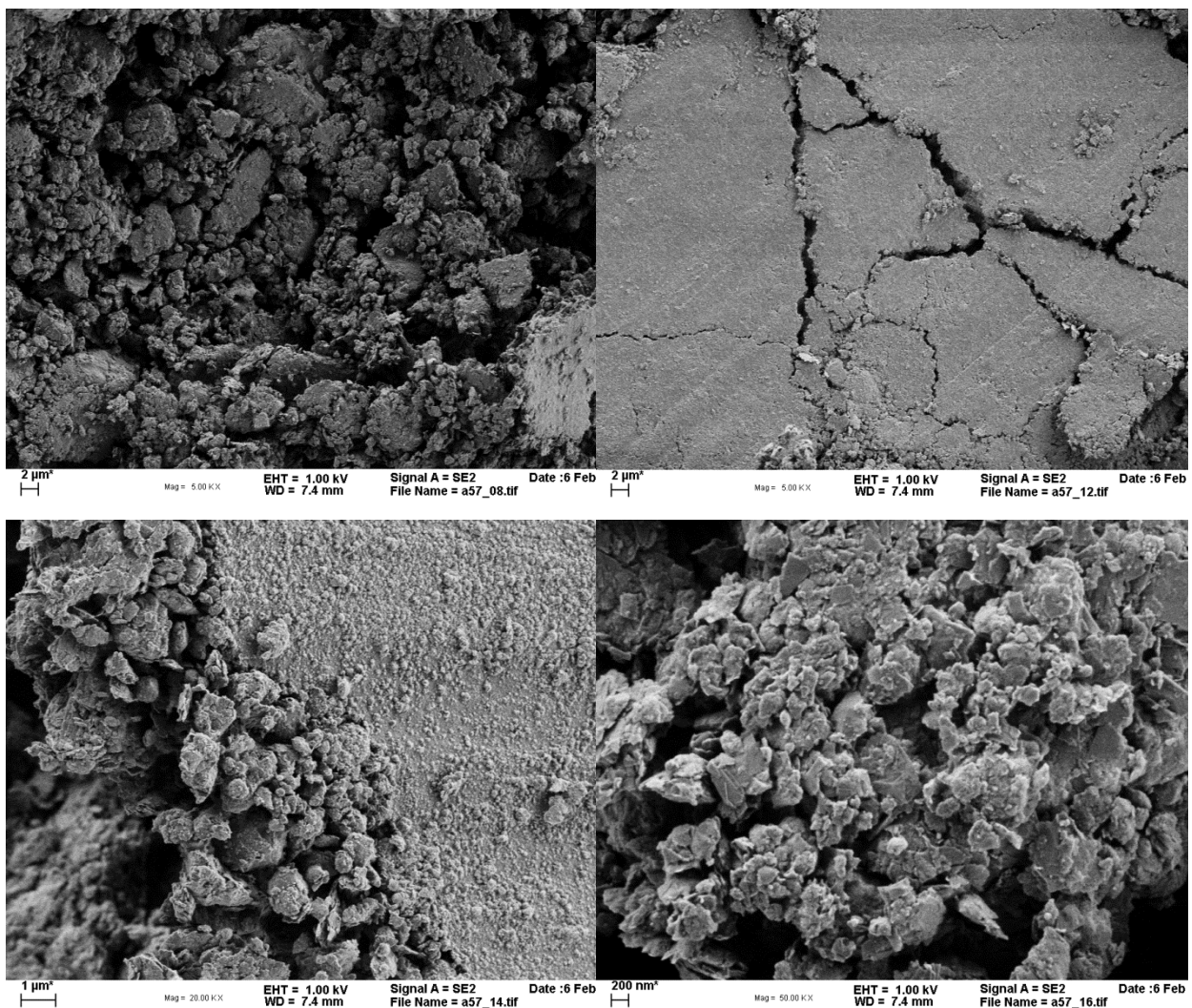
Fig. 2.49: SEM analysis of a ball milled mixture containing $Li_{12}Si_7$, graphite and 10 wt. % $NiCl_2$, treated at 500 °C for 8 h in argon.

Compared to sample before heat treatment, there is only one kind of agglomerated particles on the surface of the graphite plates. The 200 nm plate-like particles stacked on each other disappeared (Fig. 2.41). EDXS analysis was not successful in distinguishing Si and Ni particles.

Electrochemical performance

The electrode was prepared in a glove box in argon atmosphere; Super P was added as conductive additive (12 wt. %) and PVDF was used as a binder (8 wt. %). 1 M $LiPF_6$ in ethylenecarbonate / dimethylcarbonate (1:1) was used as electrolyte. The sample was cycled between 10 mV and 2.0 V vs Li/Li$^+$ at a current rate of 50 mA g^{-1}. The initial step was charging (delithiation) and values for specific capacity refer to the composite material.

Fig. 2.50: Galvanostatic measurement of a ball milled mixture containing $Li_{12}Si_7$ and graphite with a Li to C ratio of 1:6 as well as 10 wt. % $NiCl_2$, treated at 500 °C for 8 h in argon.

Fig. 2.51: Cycle number vs. specific capacity for a ball milled mixture containing Li$_{12}$Si$_7$, graphite and 10 wt. % NiCl$_2$, treated at 500 °C for 8 h in argon; only the first 50 cycles are shown.
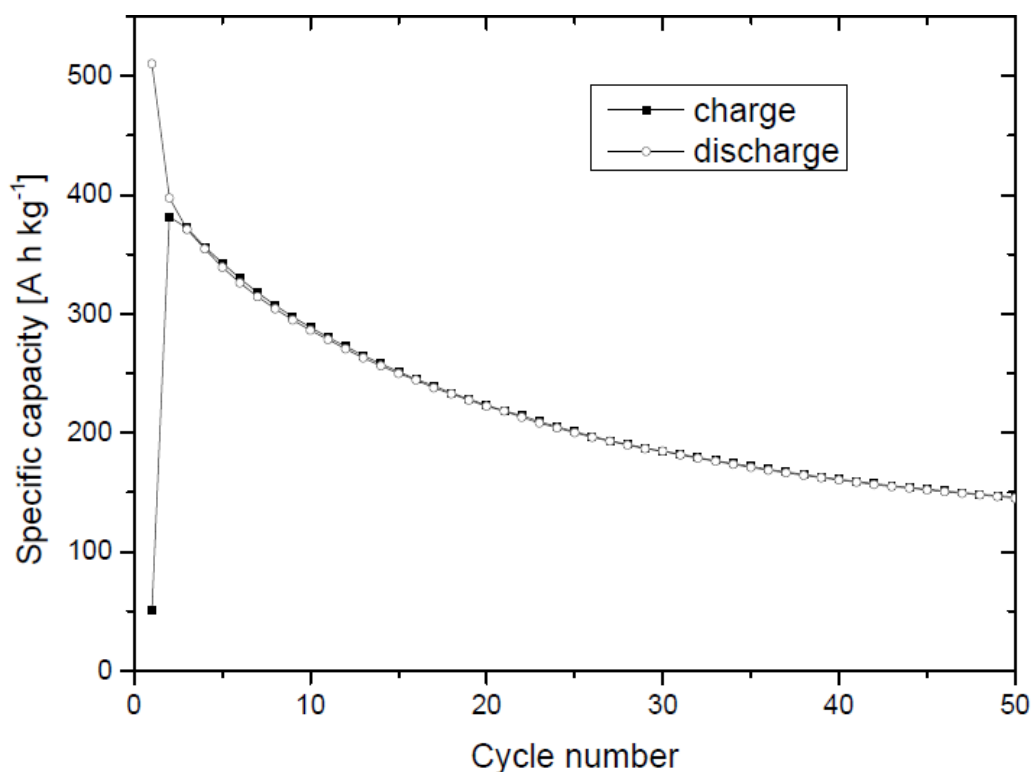
The obtained maximum capacity is significantly smaller than the one achieved with the reaction mixture before heat treatment (Fig. 2.42). Additionally, there is a faster decay of capacity observable. It is believed that heat treatment at 500 °C lead to the formation of bigger Si particles which in return show worse cycling behavior. As a summary, there were no visible improvements in cycling behavior observed due to additional heat treatment.

2.3. $Li_{14}Si_6$

$Li_{14}Si_6$ crystallizes in the trigonal spacegroup *R-3mH* and is a purple semiconductor with a band gap of 0.08 eV. The structure is made up of Si dumbbells representing a double bond between 2 Si atoms. 6 Si atoms form 3 pair of double bonds and each pair of Si atoms receives 4 electrons from 4 Li atoms meaning that 14 Li atoms donate in total 12 electrons; the remaining 2 electrons occupy a cage orbital which is distributed over the surrounding Li atoms.[80] Figure 2.52 shows the primitive cell of $Li_{14}Si_6$; in Figure 2.53, Li atoms surrounding a Si dumbbell are depicted.
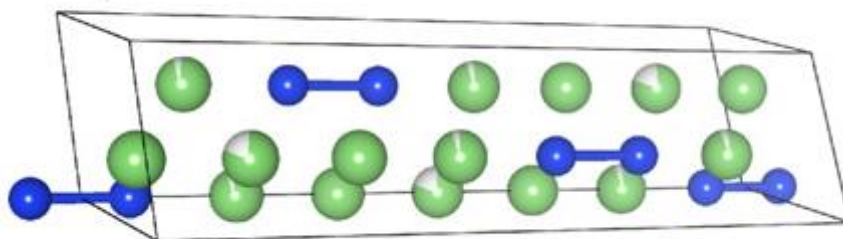
Fig. 2.52: Crystal structure of $Li_{14}Si_6$.[81]
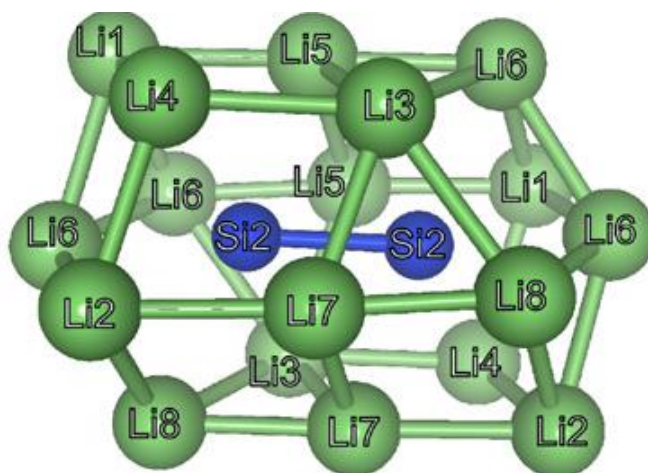
Fig. 2.53: Li atoms surrounding a Si dumbbell in the $Li_{14}Si_6$ structure.[81]

Synthesis

A stoichiometric amount of the elements is sealed in a niobium ampoule in argon and then heated to 800 °C at a heating rate of 400 °C h^{-1}. The sample is kept at this temperature for 3 h and then quenched in cold water. The obtained reaction mixture is ground to a purple powder with a metallic lustre.
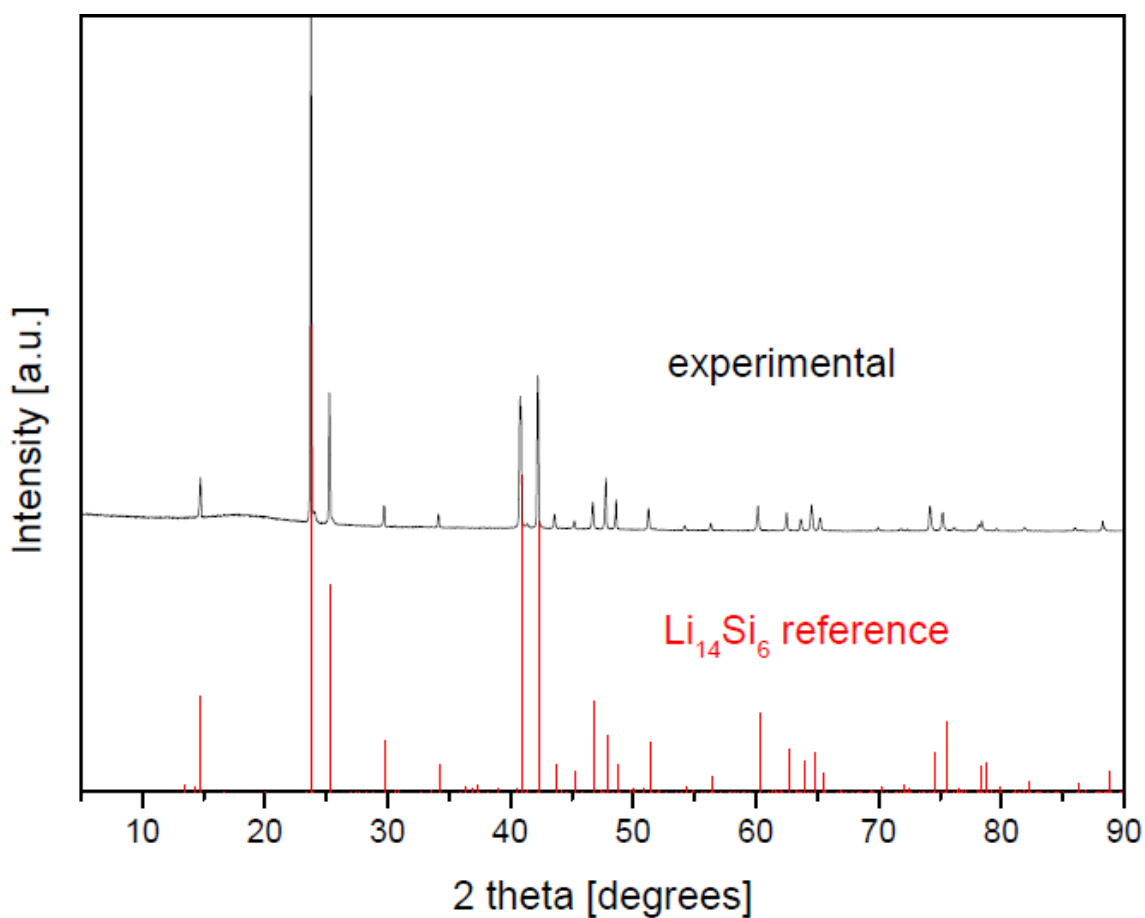
Fig. 2.54: Experimental XRD powder pattern of Li$_{14}$Si$_6$ (black curve) and theoretical one (red lines). Li$_{14}$Si$_6$ was obtained as a pure and highly crystalline phase.

Electrochemical performance

Before electrochemical testing, $Li_{14}Si_6$ was ball milled in argon. The electrode was prepared in a glove box in Ar atmosphere; Carbon black (10 wt. %) and graphite (17 wt. %) were added as conductive additives. PVDF was used as a binder (14 wt. %) and 1 M $LiPF_6$ in ethylenecarbonate / dimethylcarbonate (1:1) was used as electrolyte. The sample was cycled between 10 mV and 2.0 V vs Li/Li$^+$ at a rate of 50 mA g^{-1}. The initial step was charge (delithiation).
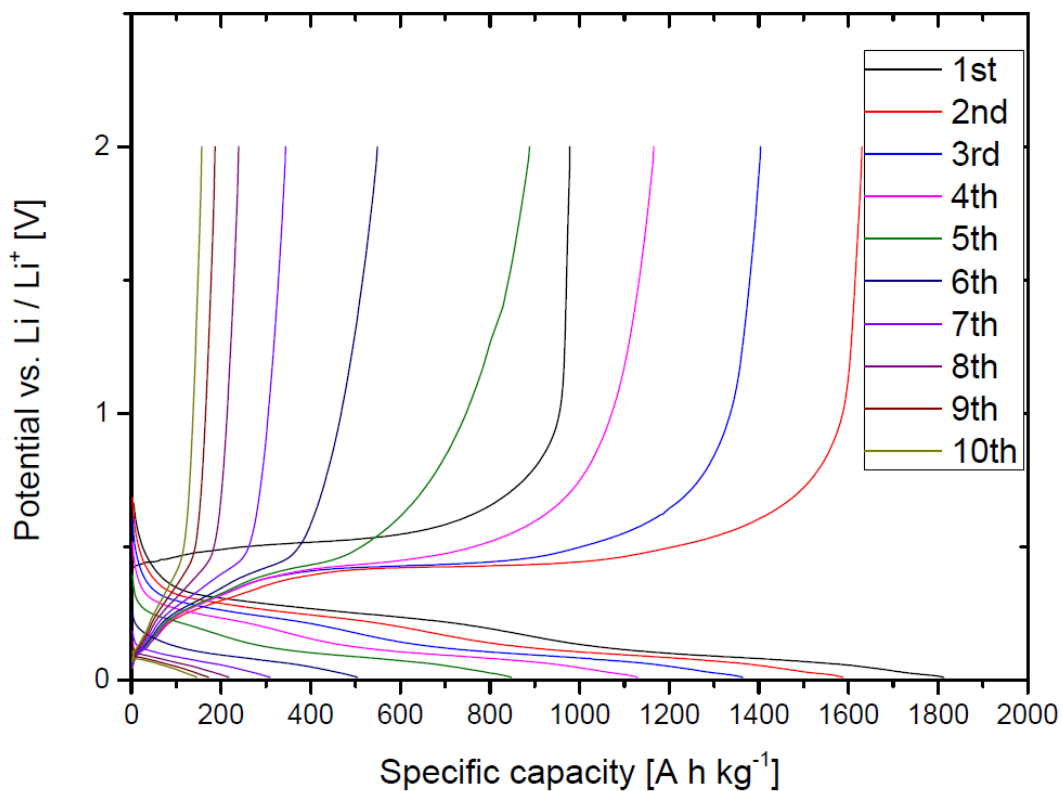
Fig. 2.55: Galvanostatic measurement of ball milled $Li_{14}Si_6$; only the first 10 cycles are shown.
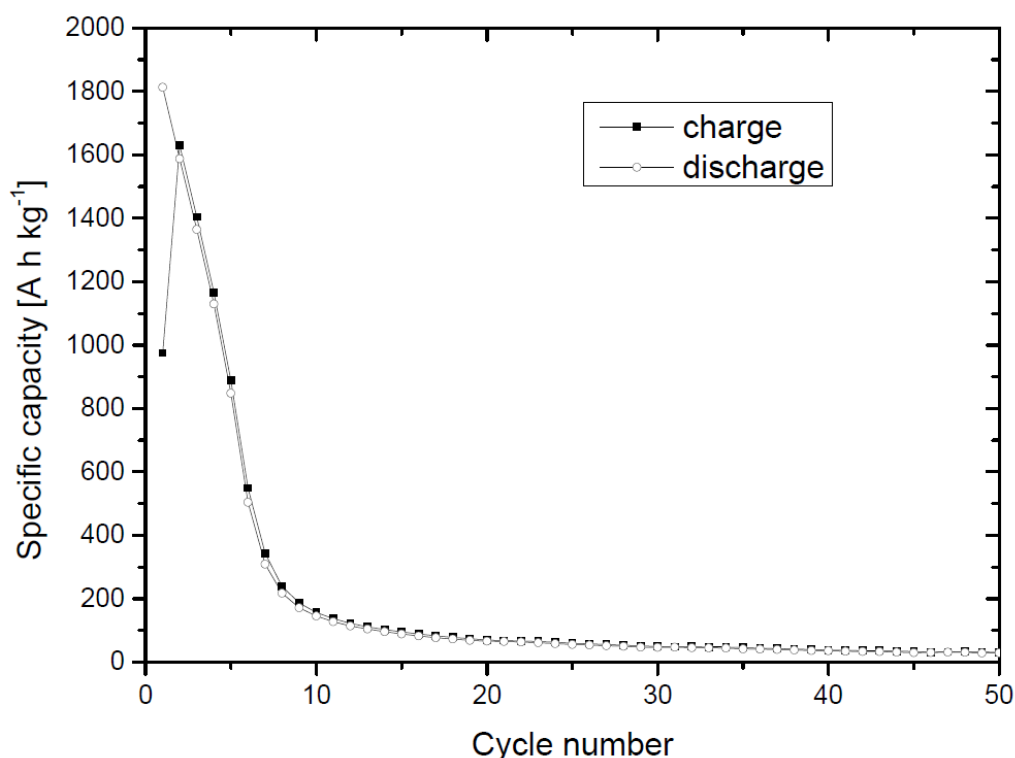
Fig. 2.56: Specific capacity vs. cycle number for ball milled $Li_{14}Si_6$; only the first 50 cycles are shown.

When Li is extracted first from $Li_{14}Si_6$, a capacity of 980 mAh g^{-1} was obtained indicating that not the full amount of Li could be extracted from starting material (full extraction of Li from $Li_{14}Si_6$ corresponds to a capacity of 1410 mAh g^{-1}). During the following discharge a capacity of 1820 mAh g^{-1} was obtained. However, the capacity drops down very quickly and only 160 mAh g^{-1} was retained after 10 cycles.

2.3.1. $Li_{14}Si_6$ / carbon composite

To prevent the rapid capacity decay of $Li_{14}Si_6$ during cycling in Li ion battery, carbon was used as an active matrix material as shown in section 2.2.1 for $Li_{12}Si_7$. In this work, graphite was directly ball milled with $Li_{14}Si_6$ in argon to form a composite material; the Li to C ratio was kept at 1:6 (e.g. $Li_{14}Si_6$ + 84 C).

Synthesis

Graphite (KS 6, TIMCAL, particle size: 6.5 μm) and $Li_{14}Si_6$ are ball milled in argon for 3 h at a speed of 500 rpm to a fine black powder. The obtained XRD powder pattern is shown in Figure 2.57 below.
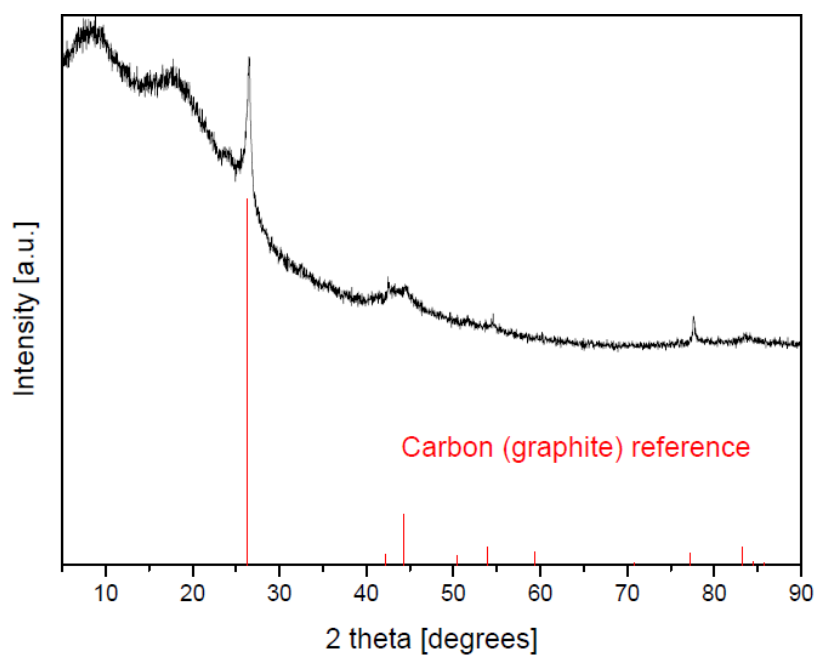
Fig. 2.57: XRD powder pattern of a ball milled mixture containing $Li_{14}Si_6$ and graphite with a Li to C ratio of 1:6 (black curve).

The sample is highly amorphous and contains graphite. $Li_{14}Si_6$ is still present, but the diffraction peaks have become broad and weak.

Electrochemical performance

The electrode was prepared in a glove box in Ar atmosphere; Carbon black was added as conductive additive (16 wt. %) and PVDF was used as a binder (16 wt. %). 1 M $LiPF_6$ in ethylenecarbonate / dimethylcarbonate (1:1) was used as electrolyte. The sample was cycled between 10 mV and 2.0 V vs Li/Li^+ at a rate of 50 mA g^{-1}. The initial step was charge (delithiation) and values for specific capacity refer to the composite material.
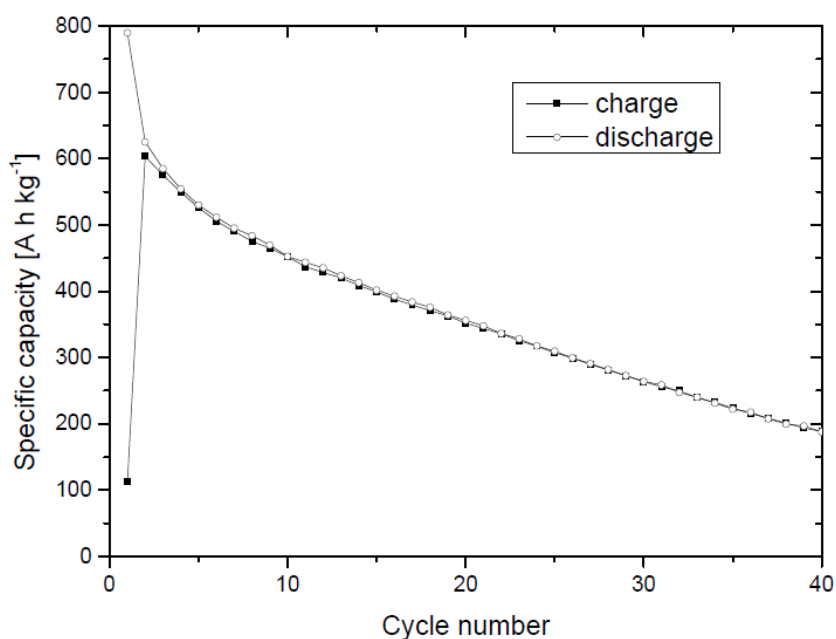
Fig. 2.58: Cycle number vs. specific capacity for a ball milled mixture containing $Li_{14}Si_6$ and graphite with a Li to C ratio of 1:6. Only the first 40 cycles are shown.

During first charge, a capacity of 115 mAh g^{-1} was obtained indicating that Li was not fully extracted from starting material. The following discharge capacity of 800 mAh g^{-1} is much smaller than the one obtained for pure $Li_{14}Si_6$ (Fig. 2.56) which is caused by the additional C content. Although capacity retention is better than the one for the pure lithiumsilicide compound, it is still far from optimal and some further modifications are necessary to improve the cycling behavior.

2.4. $Li_{13}Si_4$

$Li_{13}Si_4$ crystallizes in the orthorhombic spacegroup *Pbam*.[82] No account for a bandgap has been found in literature yet. The structure is made up of one Si dumbbell representing a double bond between 2 Si atoms and 2 isolated Si atoms. 4 electrons are donated to the Si dumbbell from 4 Li atoms (for a total of 12 valence electrons) and each isolated Si atom receives 4 electrons from 4 Lithium atoms (for a total of 8 valence electrons). In total, 12 electrons are donated by 13 Li atoms; the remaining electron occupies a cage orbital which is distributed over the surrounding Li atoms.[81] Figure 2.59 shows the primitive cell of $Li_{13}Si_4$.
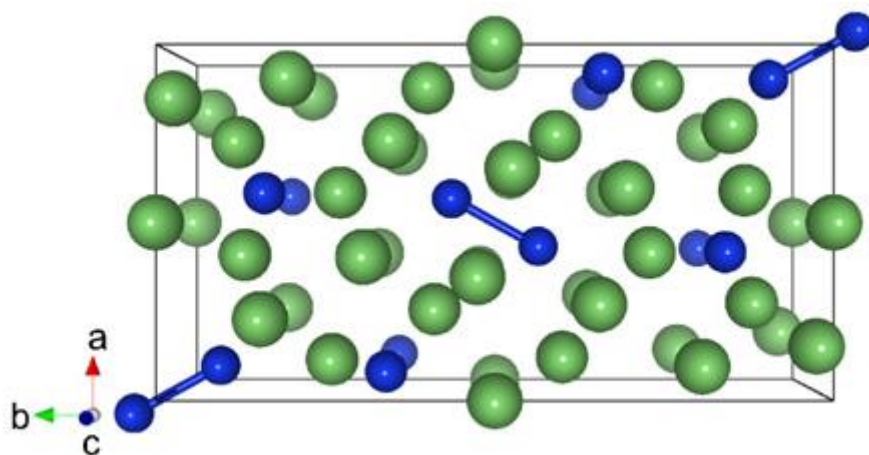
Fig. 2.59: Crystal structure of $Li_{13}Si_4$.[81]

Synthesis

A stoichiometric amount of the elements is sealed in a Niobium ampoule in argon and then heated to 800 °C at a heating rate of 400 °C h^{-1}. The sample is kept at this temperature for 3 h and then quenched in cold water. The obtained reaction mixture is ground to a dark grey powder with a metallic lustre.
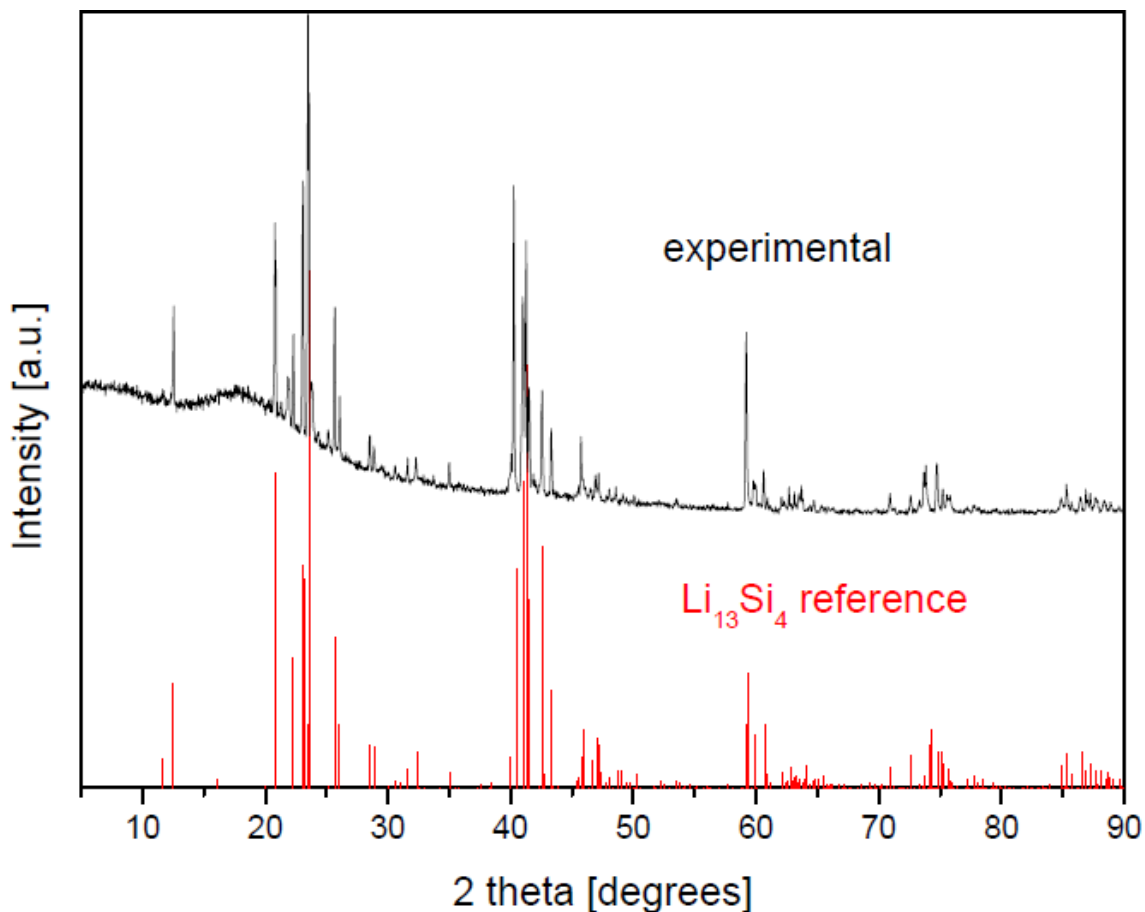
Fig. 2.60: Experimental XRD powder pattern of $Li_{13}Si_4$ (black curve) and theoretical one (red lines). $Li_{13}Si_4$ was obtained as a pure phase.

Electrochemical performance

Before electrochemical testing, $Li_{13}Si_4$ was ball milled in argon to a fine black powder. The electrode was prepared in a glove box in Ar atmosphere; Carbon black (12 wt. %) and graphite (16 wt. %) were added as conductive additives. PVDF was used as a binder (16 wt. %) and 1 M $LiPF_6$ in ethylenecarbonate / dimethylcarbonate (1:1) was used as electrolyte. The sample was cycled between 10 mV and 2.0 V vs Li/Li^+ with a rate of 50 mA g^{-1}. The initial step was charge (delithiation).

Fig. 2.61: Galvanostatic measurement of ball milled $Li_{13}Si_4$; only the first 10 cycles are shown.
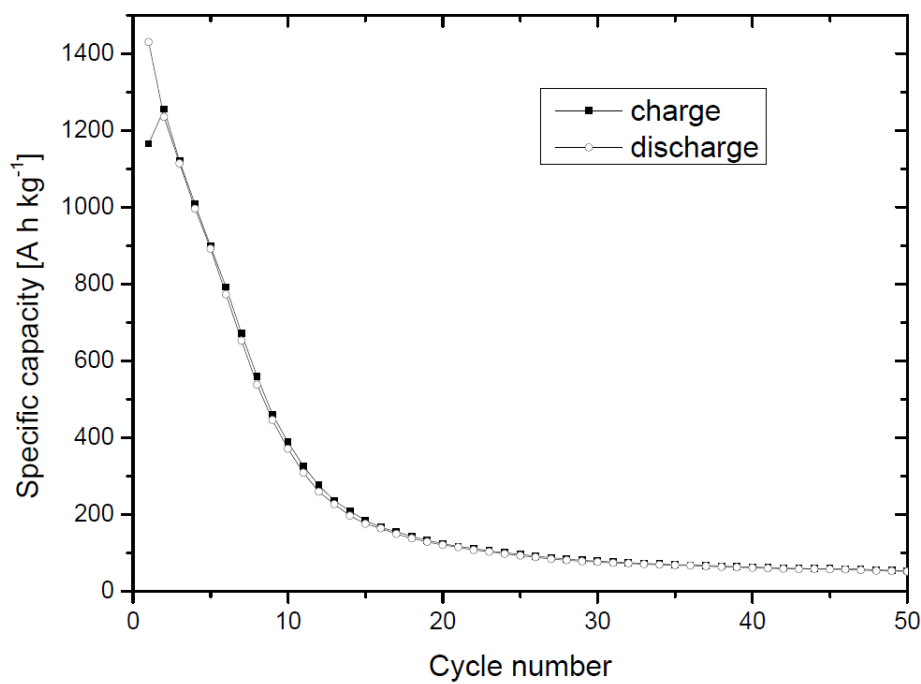
Fig. 2.62: Specific capacity vs. cycle number for ball milled $Li_{13}Si_4$; only the first 50 cycles are shown.

When Li is extracted first from $Li_{13}Si_4$, a capacity of 1170 mAh g^{-1} was obtained indicating that not the full amount of Li could be extracted from starting material (full extraction of Li from $Li_{13}Si_4$ corresponds to a capacity of 1720 mAh g^{-1}). During the following discharge a capacity of 1430 mAh g^{-1} was obtained. However, the capacity drops down very quickly and only 390 mAh g^{-1} was retained after 10 cycles.

2.4.1. $Li_{13}Si_4$ / carbon composite

To prevent the rapid capacity decay of $Li_{13}Si_4$ during cycling in Li ion battery, carbon was used as an active matrix material as shown in section 2.2.1 for $Li_{12}Si_7$. In this work, graphite was directly ball milled with $Li_{13}Si_4$ in argon to form a composite material; the Li to C ratio was kept at 1:6 (e.g. $Li_{13}Si_4$ + 78 C).

Synthesis

Graphite (KS 6, TIMCAL, particle size: 6.5 µm) and $Li_{13}Si_4$ are ball milled in argon for 3 h at a speed of 500 rpm to a fine black powder. The obtained XRD powder pattern is shown in Figure 2.63.
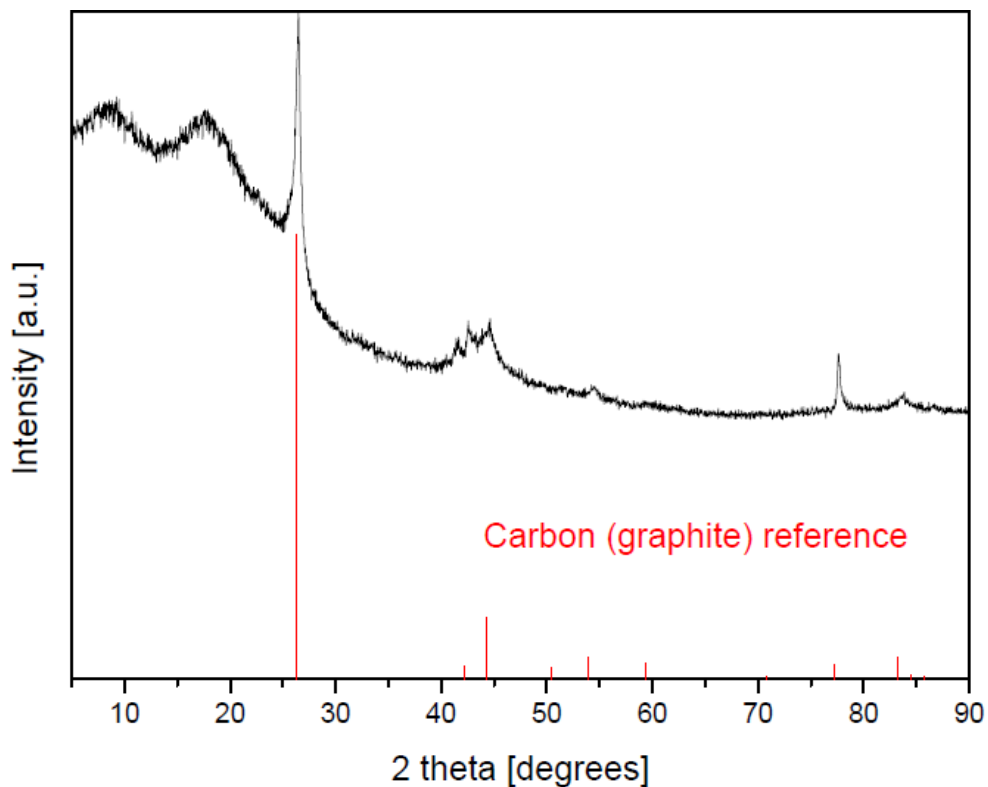
Fig. 2.63: XRD powder pattern of a ball milled mixture containing $Li_{13}Si_4$ and graphite with a Li to C ratio of 1:6 (black curve).

The sample is highly amorphous and contains graphite. $Li_{13}Si_4$ is still present, but the diffraction peaks have become broad and weak.

Electrochemical performance

The electrode was prepared in a glove box in Ar atmosphere; Carbon black was added as conductive additive (15 wt. %) and PVDF was used as a binder (12 wt. %). 1 M $LiPF_6$ in ethylenecarbonate / dimethylcarbonate (1:1) was used as electrolyte. The sample was cycled between 10 mV and 2.0 V vs Li/Li^+ at a rate of 50 mA g^{-1}. The initial step was charge (delithiation) and values for specific capacity refer to the composite material.
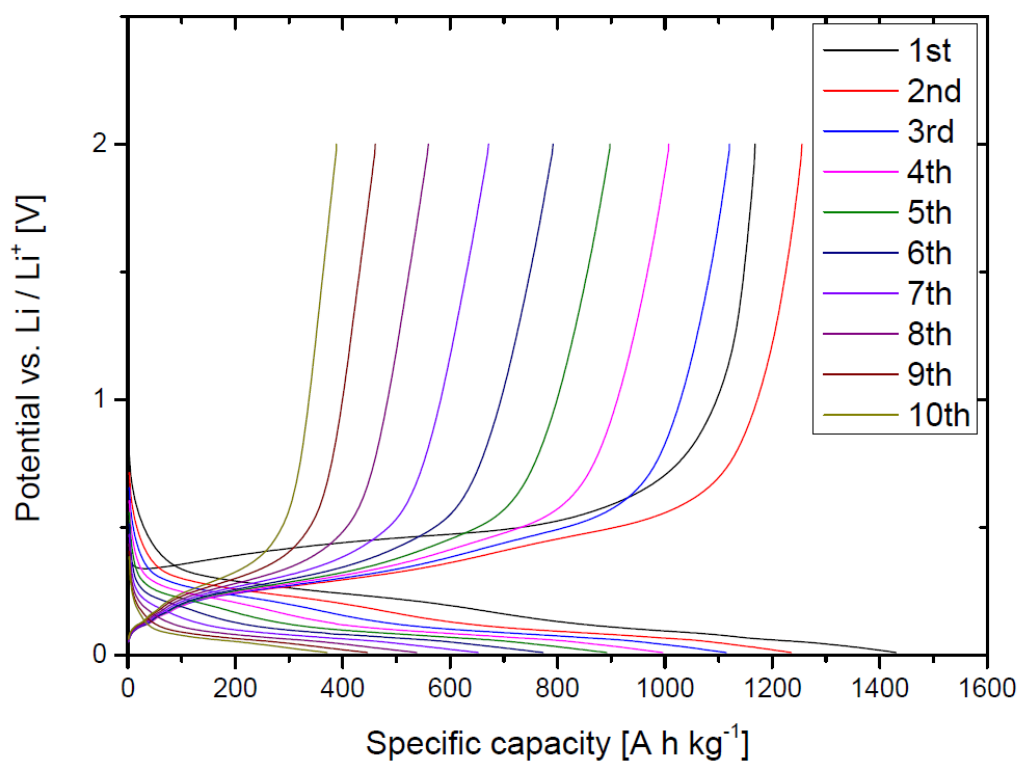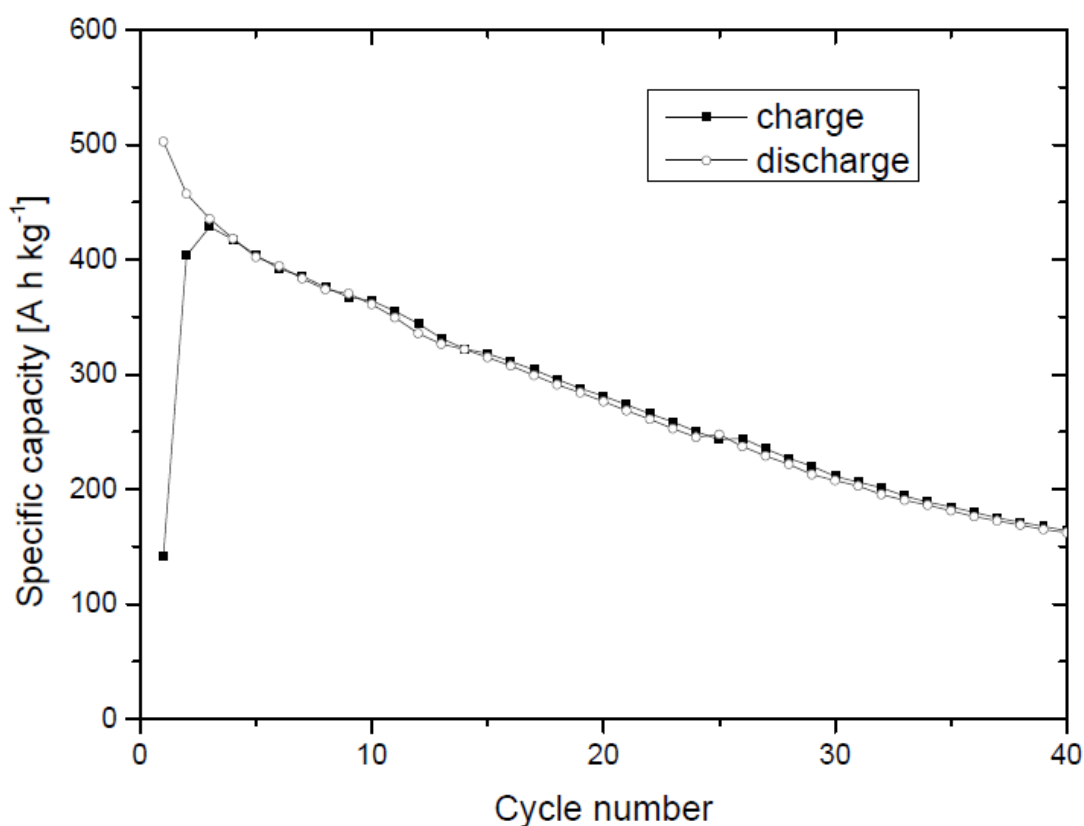
Fig. 2.64: Cycle number vs. specific capacity for a ball milled mixture containing $Li_{13}Si_4$ and graphite with a Li to C ratio of 1:6. Only the first 40 cycles are shown.

During first charge, a capacity of 145 mAh g^{-1} was obtained indicating that Li was not fully extracted from starting material. The following discharge capacity of 500 mAh g^{-1} is much smaller than the one obtained for pure $Li_{13}Si_4$ (Fig. 2.62) which is caused by the additional C content. The capacity retention is comparable to the one of the ball milled mixture of $Li_{14}Si_6$ and graphite (Fig. 2.58), although a lower capacity is obtained due to a lower Si to C ratio. There is a slight improvement in capacity retention compared to the pure lithiumsilicide compound, but it is still far from optimal and some further modifications are necessary.

2.5. Conclusion

$Li_{12}Si_7$, $Li_{14}Si_6$ and $Li_{13}Si_4$ were examined as electrode materials instead of pure Si. The reduced overall relative volume change during cycling did not significantly improve cycling behavior and fast capacity decay occurs. Composite formation with carbon-based materials was examined leading to improvement of cycling behavior at the cost of maximum capacity. Reduction of graphite oxide by ball milling with $Li_{12}Si_7$ was shown to occur, where Si and Li_2O were formed. Electrochemical testing clearly identified Si as the electrochemical active species and no contribution of graphite oxide through formation of lithiumoxides was observed in the battery. Furthermore, composite formation by reaction of $Li_{12}Si_7$ and transition metal chlorides ($CuCl_2$ and $NiCl_2$) was examined leading to the formation of nano-silicon accompanied by metal deposition. The best performance was achieved with a mixture containing $Li_{12}Si_7$, graphite (with a Li to C ratio of 1:6) and 12.5 wt. % $CuCl_2$, where 600 mAh g^{-1} were retained after 20 cycles (80.3 % of initial charge capacity). The deposition of Cu metal upon reaction of $CuCl_2$ with $Li_{12}Si_7$ was shown to have a stabilizing effect in terms of cycling behavior. However, severe capacity fading was still observed for all samples, mainly caused by a growing SEI layer on the surface of particles as shown by post mortem analysis. Consequently, insufficient maximum capacity and insufficient cycle life would make further modifications necessary for a successful implementation of these materials in a Li ion battery.

3. Investigations on alkali- and alkaline earth metal lithium silicides as anode materials for Li ion batteries

3.1. Introduction

In this chapter, different ternary alkali- and alkaline earth metal lithium silicide compounds are examined which all contain oligo- or polymeric silicon units and as such can be thought of as precursors for nano-silicon materials: Li_3NaSi_6, $CaAl_2Si_2$ and Ca_2LiSi_3. Their structures can be described by an arrangement of layered silicon, e.g. polyanionic tubes of Si in Li_3NaSi_6, puckered double layers of $Al_2Si_2^{2-}$ in $CaAl_2Si_2$ and planar anionic chains of silicon in Ca_2LiSi_3. The trigger for such an approach was the idea that nanoscopic silicon may not undergo the disastrous cracking destruction which has been recorded by many researchers since the first investigation in the 1970th.[83] Not long ago, another paper appeared proving that nanosilicon wires do show stable cycling.[60] The disadvantage of this most successful proof of concept was the extraordinary synthetical difficulties and costs of the nanowire preparation. For long, specific Zintl phases are known to undergo topochemical reactions which lead to new forms of silicon.[84] As Zintl phases of silicon are relatively easy to prepare, the here proposed route was estimated to be a very attractive one.

Consequently, it was tested whether the topochemically prepared nanoscopic forms of Si would exhibit better electrochemical behaviour upon cycling in Li ion batteries. Another possible effect employing nanosilicon sample would be the formation of thin oxidic surface layers which might stabilize the nanosilicon even further. As a rule of thumb, topochemical decomposition of the chosen compounds is achieved through reaction with selected oxidation agents. A low-dimensional structure is believed to accommodate the volume changes

between the electrochemically active species by the free interparticle spaces and provide for fast Li-diffusion path.

Synthesis procedures are described for all three compounds and electro-chemical behaviors in a Li ion battery setup were analyzed. Furthermore, composite materials upon treatment with various reagents (e.g. $CuCl_2$, graphite, graphite-oxide and reduced graphene oxide) were synthesized and electrochemically tested.

3.2. Li_3NaSi_6

Li_3NaSi_6 crystallizes in the orthorhombic space group *Pnma(no. 62)* and is a diamagnetic semiconductor.[84] The structure can be described by 2-dimensional infinite $[Si_6]^{4-}$ polyanions with tube- like fivefold channels. The alkali metal cations are inserted between these polyanionic layers and can topochemically be exchanged [allo-Si]. The structure of Li_3NaSi_6 is shown in Figure 3.1 below.
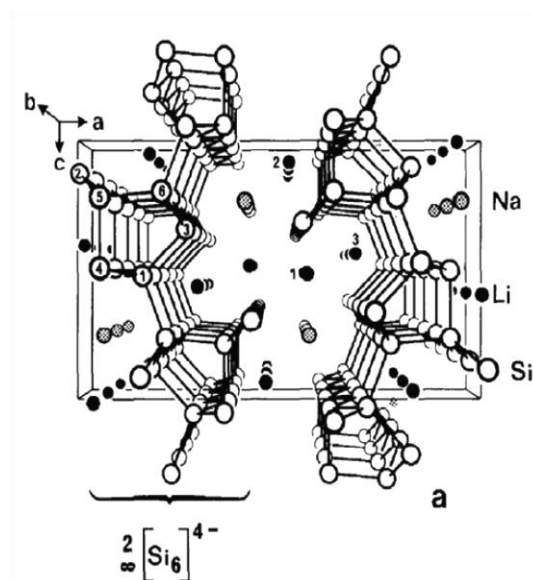
Fig. 3.1: Crystal structure of Li_3NaSi_6.[84]

96

Reaction of Li_3NaSi_6 with alcohols lead to the formation of allo-silicon, a new modification of the element, under evolution of hydrogen gas as shown in equation 3.1 below. Allo-Si has only a slightly modified structure compared to Li_3NaSi_6 where the $_{\infty}^{2}[Si_6]^{4-}$ Zintl anions are decharged and mutually linked, thus forming a fairly open network. Clearly, this is a topochemical reaction which results in a special kind of 3D-nano-silicon. [84]

$$Li_3NaSi_6 + 4\ ROH \rightarrow 6\ allo\text{-}Si^0 + 2\ H_2\ (g) + NaOR + 3\ LiOR \qquad (3.1)$$

Oxidation: $Si_6^{4-} \rightarrow 6\ allo\text{-}Si^0 + 4\ e^-$

Reduction: $4\ H^+ + 4\ e^- \rightarrow 2\ H_2$
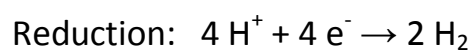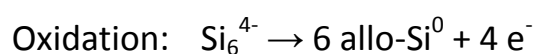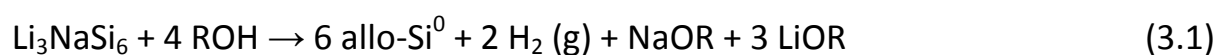
Allo-silicon is a metastable modification of silicon which transforms under heat treatment first into 4H-Si and thereafter to the diamond form, the 3C-phase. The structure can be described by a three- dimensional network of silicon, where the Si atoms are arranged in parallel layers which derive from the original ones by small distortions because of inter-layer linking. This layered structure is of high interest for implementation in Li ion battery, since the free interspace volume between the Si layers is expected to buffer the volume changes of silicon during cycling. In the following section, it is reported how Li_3NaSi_6 was treated with various reagents like $CuCl_2$ and graphite oxide in order to evaluate whether a decomposition reaction takes place in analogy to treatment with a protic alcohol leading to the nanoscopic form of allo-Si.

Synthesis

Stoichiometric amounts of the elements are sealed in a niobium ampoule under dry argon gas. The ampoule is placed into an argon filled corundum tube and transferred into a preheated furnace at 550 °C. This temperature is kept for 24 h and afterwards cooled down to room temperature at a rate of 60 °C h^{-1}. The

reaction mixture is ground to a dark grey powder, pressed into a pellet and sealed inside a tantalum ampoule under argon. This sample is treated at 550 °C for 1 week (heating rate = cooling rate = 100 °C h^{-1}) until a dark grey powder is obtained. The XRD powder pattern of this reaction product is shown Figure 3.2 below.
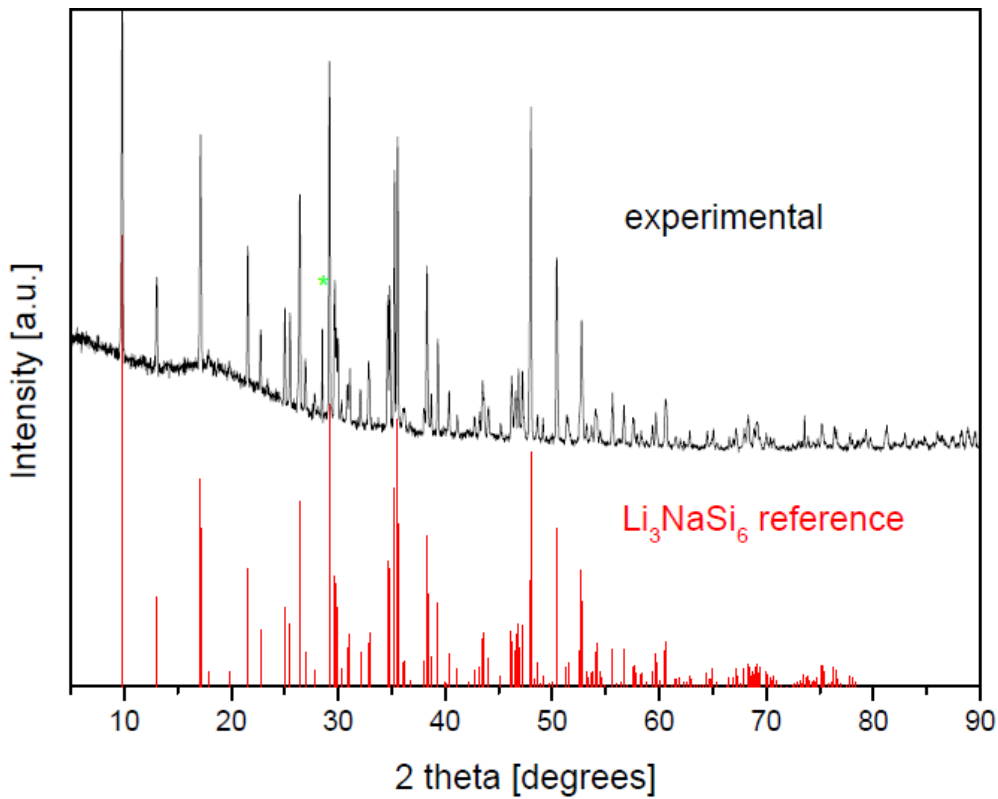
Fig. 3.2: XRD powder pattern of Li_3NaSi_6 treated at 550 °C for 1 week (black curve). The red lines correspond to a calculated pattern.

XRD analysis reveals that the sample contains highly crystalline Li_3NaSi_6. There is a small impurity of Si denoted with a green star at the peak location of 2θ = 28.5°. In addition, an amorphous background shows up in the low angle regime which may be due to an intermediate decomposition state of lower sodium content.

Electrochemical performance

Before electrochemical testing, Li_3NaSi_6 was ball-milled under argon atmosphere to a fine powder. Electrodes were prepared in an argon filled glovebox with graphite (6 wt. %) and Super P (10 wt. %) added as conductive additives. PVDF was used as binder (10 wt. %). 1 M $LiPF_6$ in ethylenecarbonate / dimethylcarbonate (1:1) was used as electrolyte. The sample was cycled between 10 mV and either 2.0 or 2.5 V vs. Li/Li^+ at a rate of 20 mA g^{-1}.
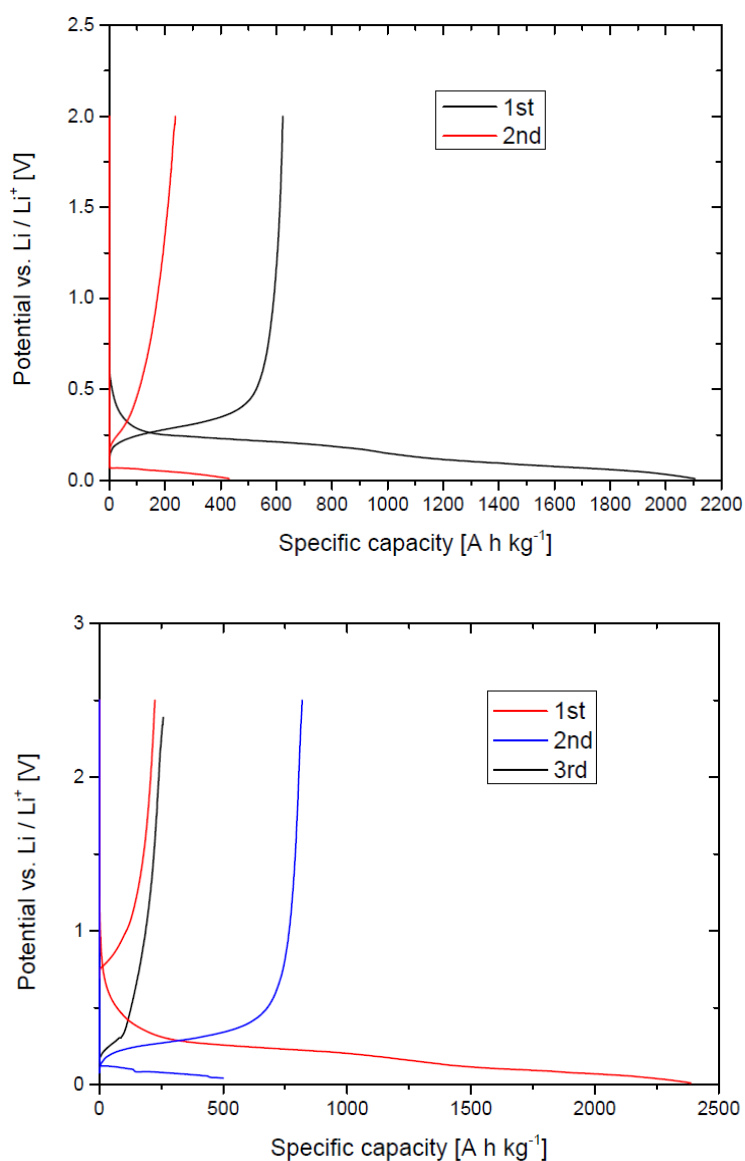
Fig. 3.3: Galvanostatic measurements of ball-milled Li_3NaSi_6. Top: from discharge (lithiation), bottom: from charge (delithiation).

99

For delithiation as the first step, an initial charge capacity of 225 mAh g^{-1} was obtained, indicating that 1.77 equivalents of Li were extracted. Full extraction of Li from Li$_3$NaSi$_6$ would have to lead to a capacity of 380 mAh g^{-1} (3 equivalents) meaning Li was only partially extracted from starting material. First discharge yields a high capacity of 2100 or 2400 mAh g^{-1}, respectively. Independent of first step, capacity drops down very quickly afterwards and after 2 cycles the battery is already dead. It can be concluded that the compound was transferred into Si which lost contact to the electrode during first discharge as indicated by the high obtained capacity as well as by the fast capacity drop. This leads to the conclusion that topochemically reacted Li$_3$NaSi$_6$ is not stable in the Li ion battery without further treatment.

3.2.1. Li$_3$NaSi$_6$ and CuCl$_2$

In this section, the reaction of Li$_3$NaSi$_6$ with CuCl$_2$ is being examined. The idea was that eventually forming binary nano Cu-silicides or elementary nano copper may form conductive pockets for hosting the silicon in a stable way. Recently, inertness of copper silicides against Li and the battery media has been proven in our group.[85]

The desired reaction is formulated in equation 3.2:

Li$_3$NaSi$_6$ + 2 CuCl$_2$ → 2 Cu / 6 allo-Si + NaCl + 3 LiCl   (3.2)

Oxidation: Si$_6^{4-}$ → 6 allo-Si^0 + 4 e$^-$

Reduction: 2 Cu^{2+} + 4 e$^-$ → 2 Cu^0
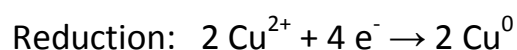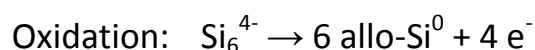
Cu was expected to be inserted between the layers of allo-Si, covering and encapsulating the nano-silicon and eventually connecting it to the copper

current collector foil, thus stabilizing cycling behavior of the composite. The reaction products LiCl and NaCl can be washed out of the reaction mixture prior to the electrochemistry.

Synthesis

Li₃NaSi₆ (1 Eq.) and CuCl₂ (dried at high vacuum, 2 Eq.) are ball milled under argon atmosphere (350 rpm, 2 h). The sample is placed into a 100 ml Schlenk, 20 ml of dry NMP are added and then mixture is treated at 100 °C for 100 min under argon while stirring vigorously to dissolve LiCl. The reaction mixture is washed twice with dry NMP and afterwards washed twice with dry THF (to wash away NMP). The resulting black powder is dried under vacuum (RT, 10⁻¹ mbar, 5 h). The obtained XRD powder pattern is shown in Figure 3.4.
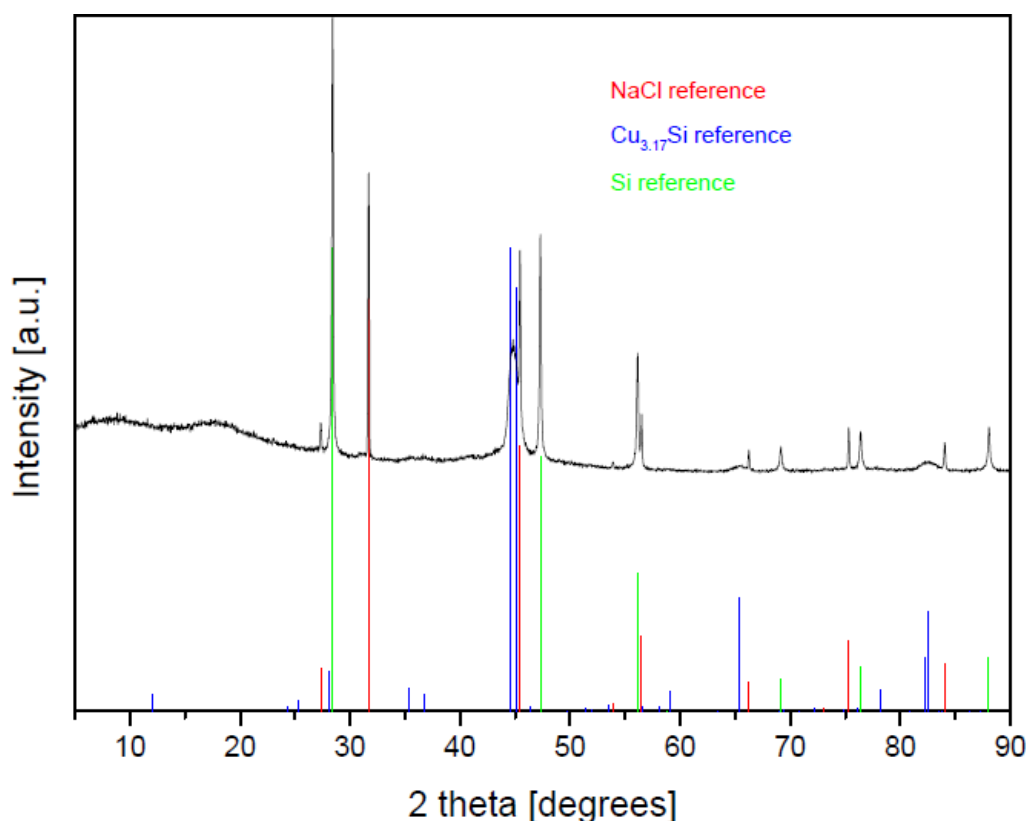
Fig. 3.4: XRD powder pattern of Li_3NaSi_6 + 2 $CuCl_2$ (black curve). The red, blue and green lines correspond to calculated patterns.

The sample contains NaCl, Si, $Cu_{19}Si_6$ ($Cu_{3.17}Si$) as well as amorphous components. Additionally, washing of LiCl was successful because it is not visible in the final XRD powder pattern. Taking into account the result of the XRD analysis, the following reaction is suggested:

$$19\ Li_3NaSi_6 + 38\ CuCl_2 \rightarrow 57\ LiCl + 19\ NaCl + 2\ Cu_{19}Si_6 + 102\ Si \qquad (3.3)$$

Treatment of Li_3NaSi_6 with $CuCl_2$ leads to the decomposition of the ternary Zintl silicide into NaCl, LiCl and Si. The copper chloride is quantitatively transformed into the coppersilicide $Cu_{19}Si_6$. The precipitation of elementary Cu was not observed. SEM micrographs of this sample are shown in Figure 3.5.
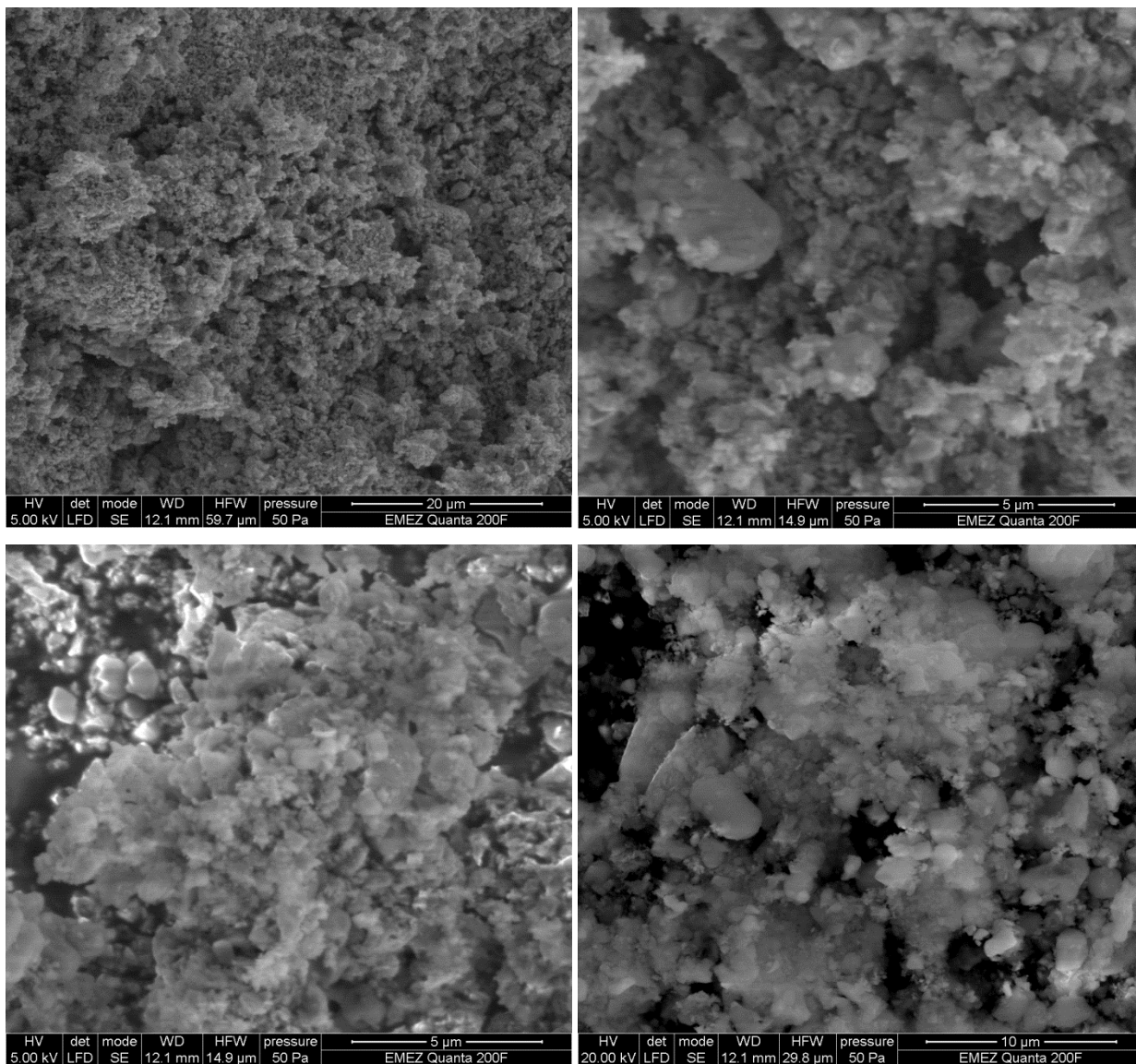
Fig. 3.5: SEM micrographs of the reaction product of Li_3NaSi_6 + 2 $CuCl_2$.

The sample is a mixture of different phases in form of small agglomerated particles with diameters in the submicron range. Additionally, there are a few larger plate-like particles with diameters around 5 µm. EDXS analysis confirms that the sample contains Si, Cu, Na and Cl. However, due to homogeneity on the micron scale, it was not possible to assign individual particles to their respective phases.

103

Electrochemical performance

The electrode was prepared in an argon filled glove box. Graphite (4 wt. %) and Super P (12 wt. %) were added as conductive additives and PVDF was used as binder (8 wt. %). 1 M $LiPF_6$ in ethylenecarbonate / dimethylcarbonate (1:1) was used as electrolyte. The sample was cycled between 10 mV and 3.0 V vs Li/Li^+ with a rate of 20 mA g^{-1}. The initial step was discharge (lithiation) and values for specific capacity refer to the composite material.
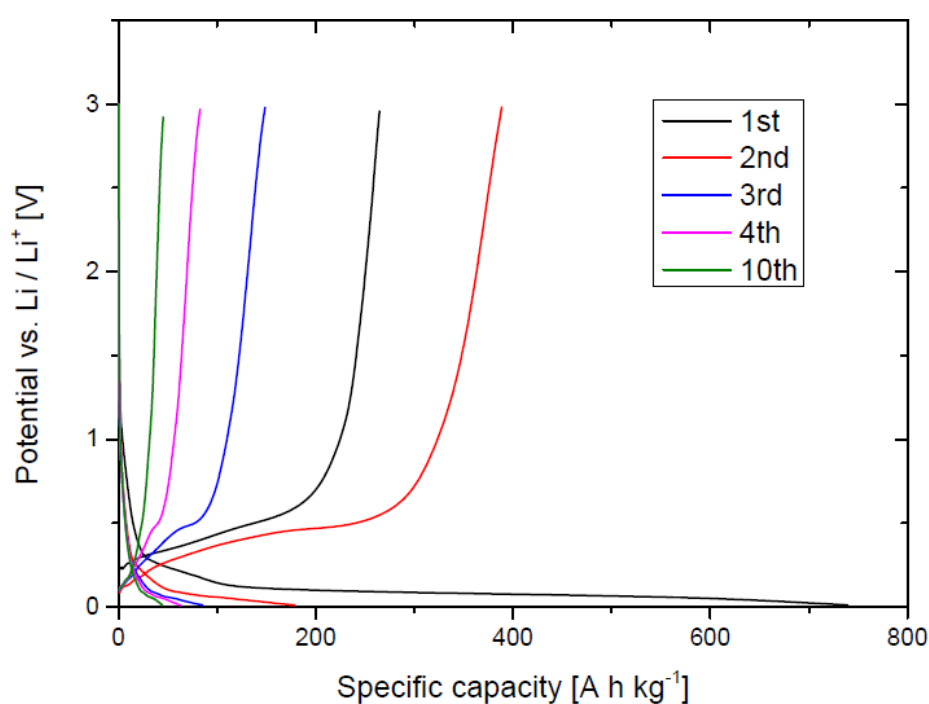
Fig. 3.6: Galvanostatic measurement of the reaction product of Li_3NaSi_6 + 2 $CuCl_2$. Only the first 10 cycles are shown.

There is a high irreversible capacity loss of 47.4 % after the first cycle followed by further rapid capacity decay in subsequent cycles. After 4 cycles, a low capacity of 85 mAh g^{-1} is retained. Compared to pure Li_3NaSi_6, there is a lower maximum capacity as expected due to the incorporation of additional inactive weight in form of copper. Silicon can be identified as electrochemically active species regarding the potential profile of the measurement, i.e. a plateau

below 0.5 V against Li metal. Obviously, his composite material of silicon is not able exhibit stable cycling behavior of the produced silicon.

3.2.2. Li_3NaSi_6 and graphite oxide

In this section, the reaction of graphite oxide and Li_3NaSi_6 is examined. The expected outcome for this reaction is a partial reduction of graphite oxide $C_8O_4H_2$ in combination with oxidation of Li_3NaSi_6, which is believed to be decomposed to Li_2O, Na_2O and Si. In other words, the $C_8O_4H_2$ loses water and oxygen while Li_3NaSi_6 deintercalates the alkaline metals while the Zintl polyanion loses its negative charge.

$$4\ Li_3NaSi_6\ +\ 3\ C_8O_4H_2 \rightarrow 2\ LiOH + 4\ NaOH + 5\ Li_2O + 24\ Si + 24\ C{:}O \qquad (3.4)$$

It was expected, that silicon particles would be embedded in flexible reduced graphite oxide pockets which are believed to accommodate the volume changes of Si during cycling and eventually linked to C via oxygen bridges.

Synthesis

A mixture containing Li_3NaSi_6 and graphite oxide powder (dried at high vacuum) in equal weight ratio is ball-milled in argon (2 h, 350 rpm) to a fine black powder. The obtained XRD powder pattern is shown in Figure 3.7.
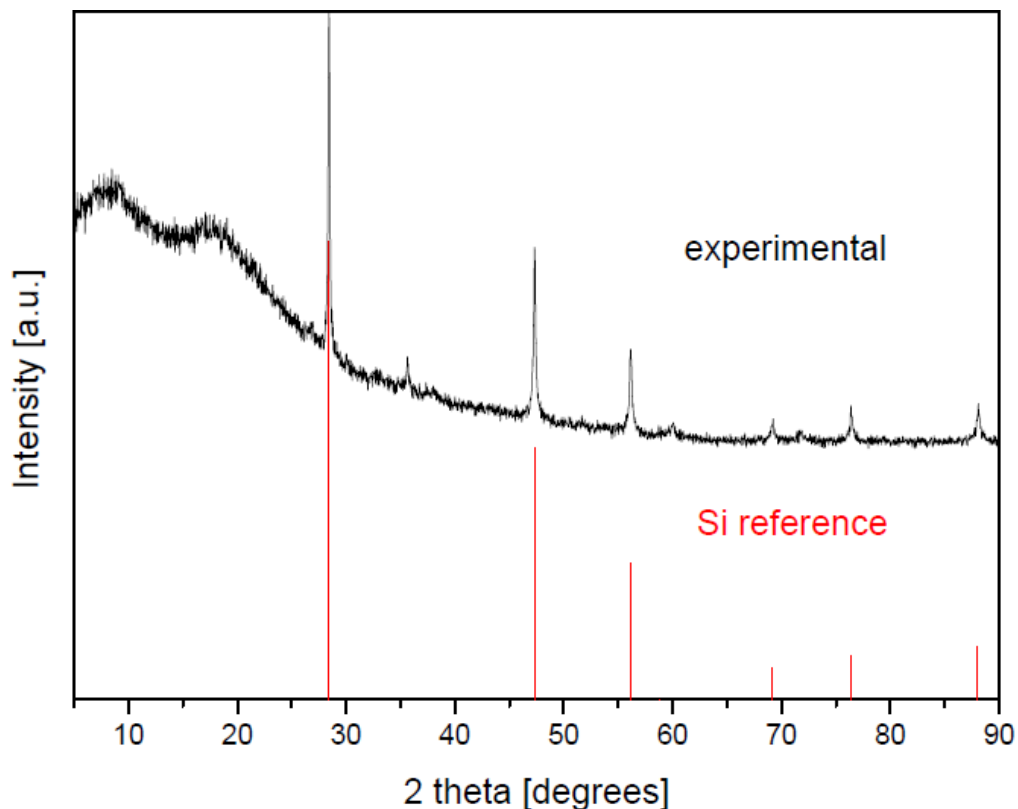
Fig. 3.7: XRD powder pattern of the reaction product of ball-milled Li_3NaSi_6 and graphite oxide powder (1:1 weight ratio, black curve). The red lines correspond to a calculated pattern of α-Si.

Most of the sample is highly amorphous (high background) and the Si reflections are believed to be caused by Si impurities in the starting material (Li_3NaSi_6). Additionally, there are two small unindexed peaks at $2\theta = 35.5$ ° and $2\theta = 71.6$ °, respectively. These peaks do not fit to Li_3NaSi_6, Li_2O or Na_2O. The absence of Li_3NaSi_6 in the XRD powder pattern leads to the conclusion that the ternary Zintl silicide compound was completely decomposed to amorphous products. SEM micrographs of this product are shown in Figure 3.8.
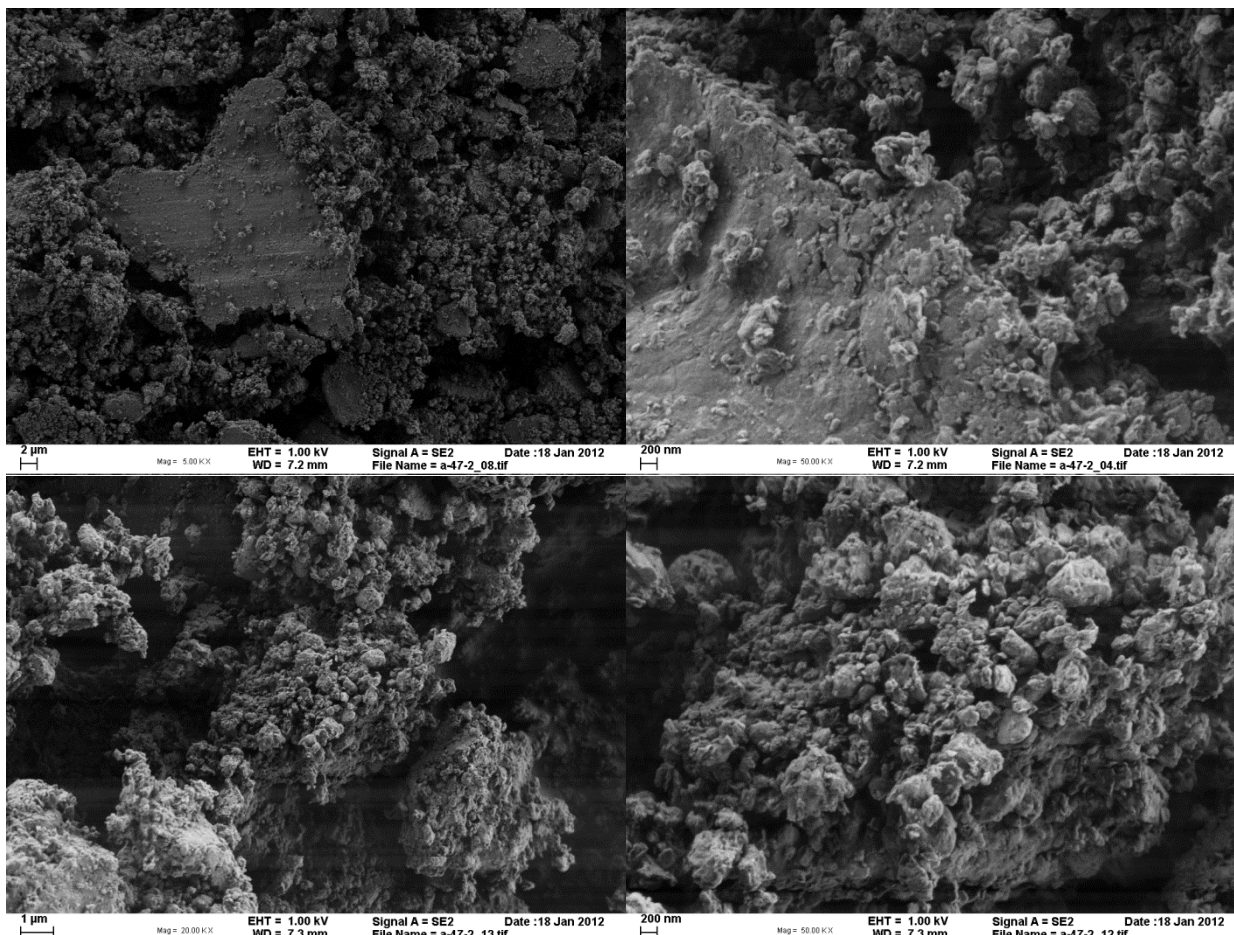
Fig. 3.8: SEM micrographs of the reaction product of Li_3NaSi_6 with graphite oxide (1:1 weight ratio) at different magnification scales.

The sample consists of graphite oxide platelets with an average diameter of 10 μm, which are covered on their surfaces by smaller agglomerated particles (submicron range).

Electrochemical performance

The electrode was prepared in an argon filled glovebox. Graphite (4 wt. %) and Super P (12 wt. %) were added as conductive additives and PVDF was used as binder (8 wt. %). 1 M $LiPF_6$ in ethylenecarbonate / dimethylcarbonate (1:1) was used as electrolyte. The sample was cycled between 10 mV and 3.0 V vs Li/Li^+ with a rate of 20 mA g^{-1}. The initial step was discharge (lithiation) and values for specific capacity refer to the composite material.
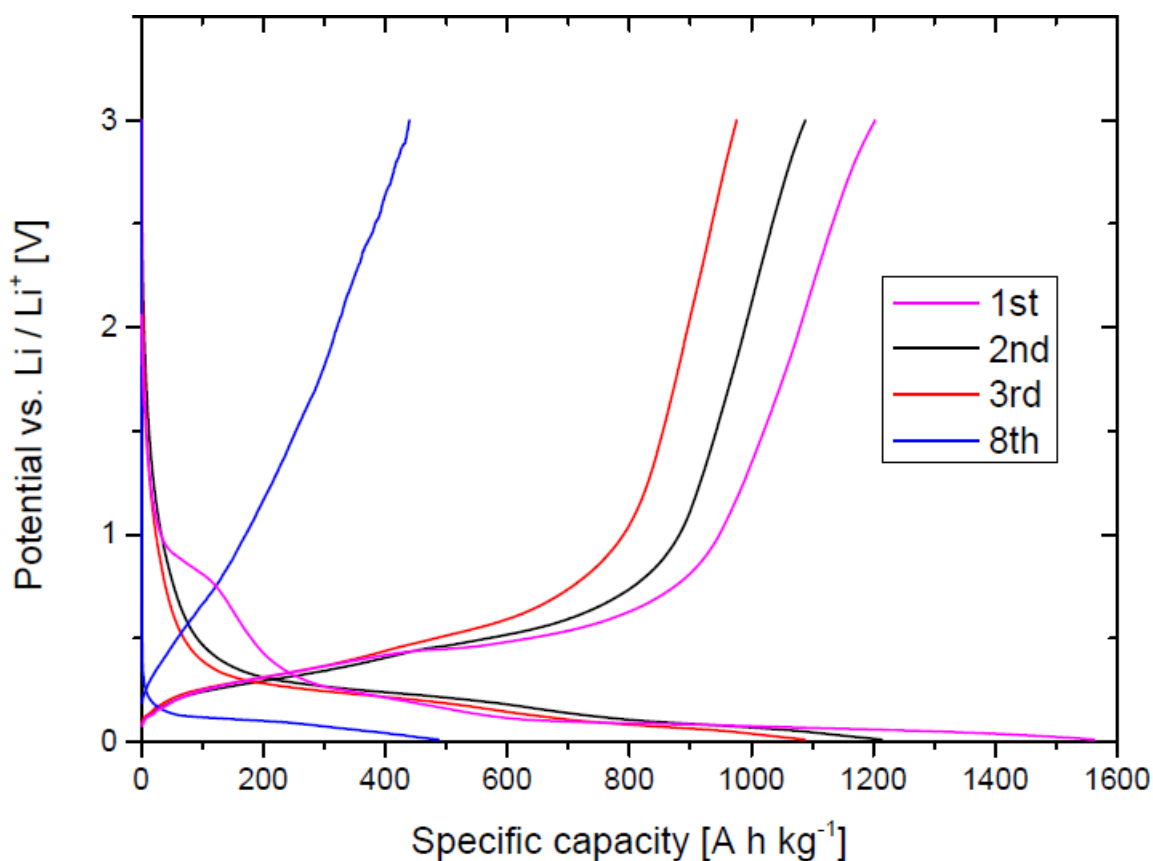
Fig. 3.9: Galvanostatic measurement of the reaction product of ball-milled
Li_3NaSi_6 and graphite oxide (1:1 weight ratio, the first 8 cycles are shown).

The initial capacity of 1550 mAh g^{-1} is quite large and corresponds to 74 % of
the maximal expected value (2090 mAh kg^{-1}). There is no (irreversible)
formation of Li_2O observed during first discharge indicating that Li_3NaSi_6 and
graphite oxide reacted already prior to the electrochemical experiment. There
is an irreversible capacity loss after the first cycle of 23% followed by
continuous capacity losses during subsequent cycles. After the 8th cycle, only
31% of the initial capacity is retained (485 mAh g^{-1}). Compared to pure Li_3NaSi_6
(Fig. 3.3), the cycling behavior has been improved but is far from a reasonable
target performance. The capacity plateau below 0.5 V is significant for active
silicon; the maximum capacity is by a factor of three larger than for experiment
1.1 but by a factor of three smaller than the theoretical one.

3.2.3. Li_3NaSi_6 and graphite

In this section, the reaction between Li_3NaSi_6 and graphite is examined. The expected reaction is given in equation 3.5 below:

$$Li_3NaSi_6 + (x+6)\ C \rightarrow 3\ LiC_6 + 6\ Si + NaC_x \qquad\qquad (3.5)$$
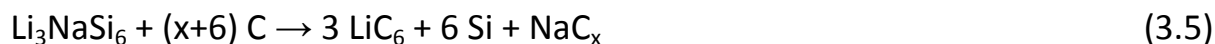
Li_3NaSi_6 is supposed to be decomposed into the elements, whereas Li and Na will be intercalated between the graphite layers and Si enveloped by (soft) graphite pockets which may act as a conductive matrix helping to stabilize the cycling behavior of silicon. For a complete decomposition of Li_3NaSi_6, at least 24 equivalents of C are necessary. Since Na cannot be intercalated in graphite (Na_8C) to the same extent as Li, an excess of graphite was used.

Synthesis

Li_3NaSi_6 (99.9 mg, 0.5 mmol, 1 Eq.) and graphite (dried, 200.1 mg, 16.7 mmol, 35.7 Eq.) are ball-milled in argon for 2 h at a speed of 350 rounds per minute to a fine black powder containing a few small shiny particles. The obtained XRD powder pattern is shown in Figure 3.10.
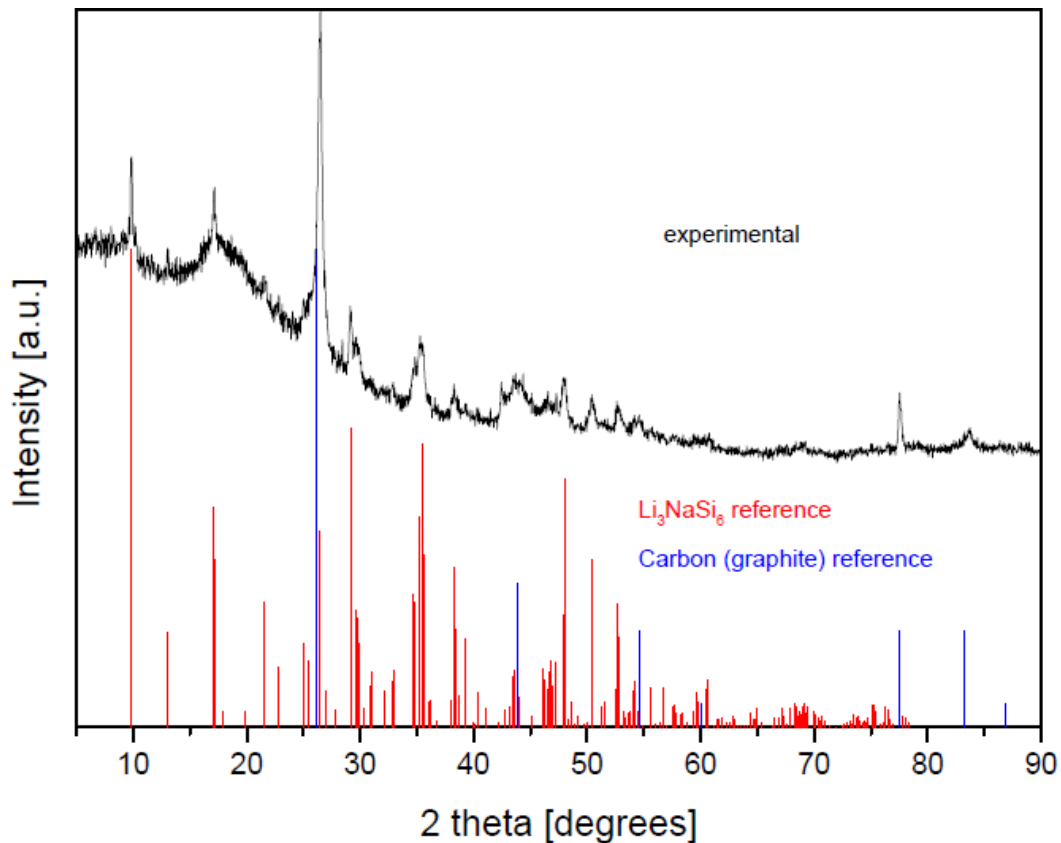
Fig. 3.10: XRD powder pattern of the reaction product of ball-milled Li_3NaSi_6 and graphite (1:2 weight ratio, black curve). The red and blue lines correspond to calculated patterns.

The sample is highly amorphous (high background) and contains graphite flakes as well as very small particles of Li_3NaSi_6. Since the educt phases are still present, it is concluded that this sample is to some extent a mixture between the educt and product phases. Li_3NaSi_6 is only partially decomposed to amorphous silicon. SEM micrographs of this mixture are shown in Figure 3.11.
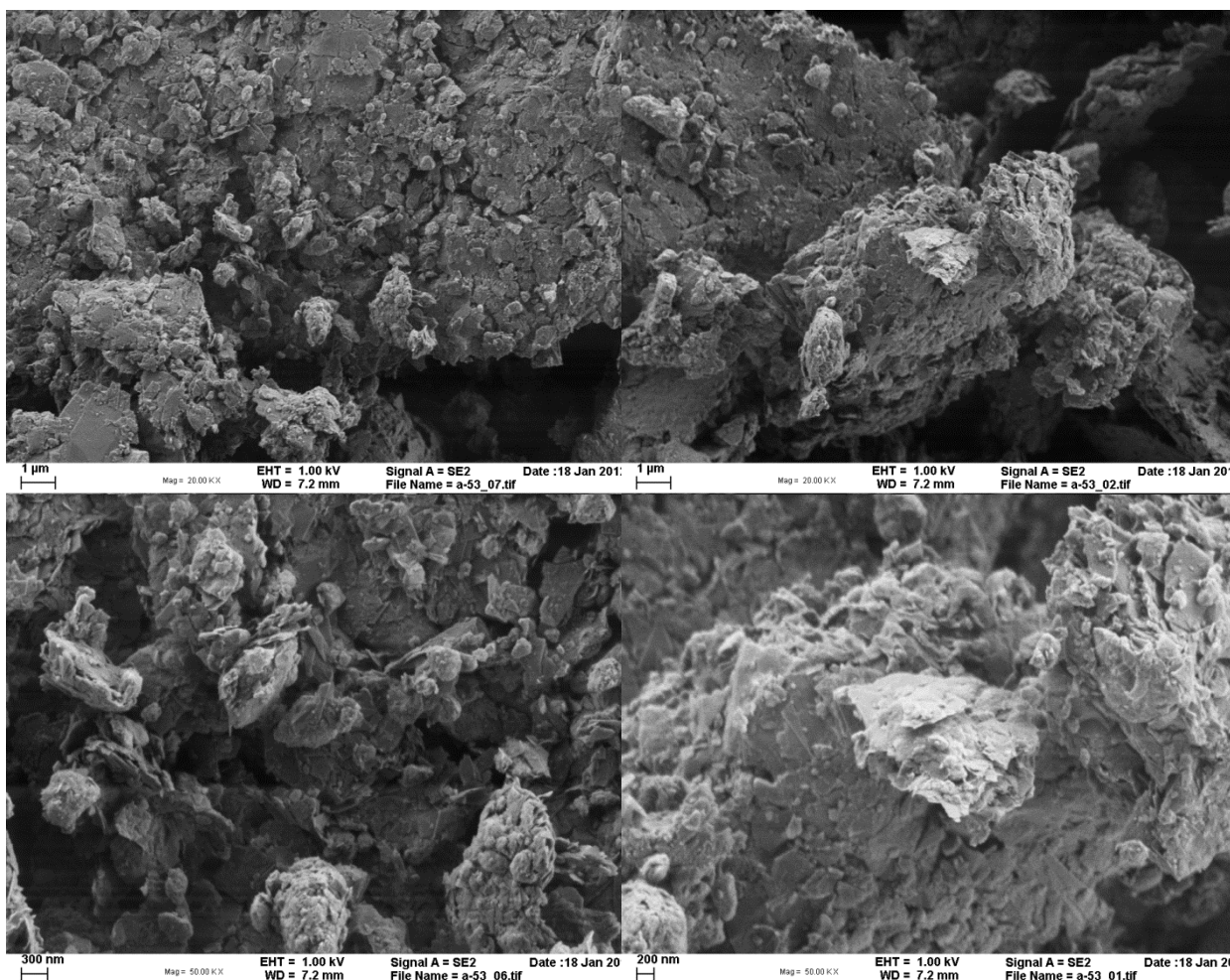
Fig. 3.11: SEM micrographs of the reaction product of ball-milled Li$_3$NaSi$_6$ and graphite (1:2 weight ratio) at different magnification scales.

The sample contains graphite plates with smaller agglomerated particles at submicron size on the surfaces of the platelets, probably of Li$_3$NaSi$_6$ and of amorphous silicon.

Electrochemical performance

Electrodes were prepared in an argon filled glovebox. Super P was added as conductive additive (12 wt. %) and PVDF was used as binder (8 wt. %). 1 M LiPF$_6$ in ethylenecarbonate / dimethylcarbonate (1:1) was used as electrolyte. The sample was cycled between 10 mV and 2.0 V vs. Li/Li$^+$ at a rate of 20 mA g$^-$^{1}. The initial step was charging (delithiation) and values for specific capacity refer to the composite material.

111
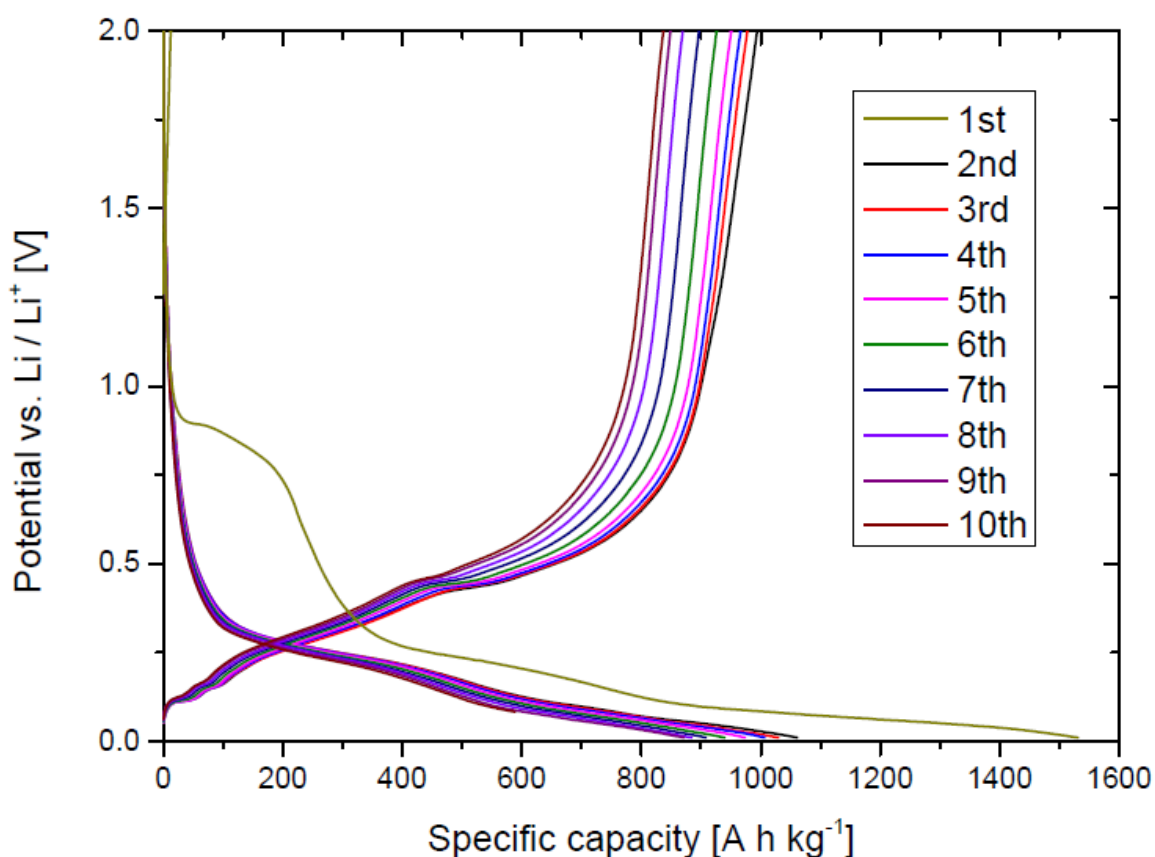
Fig. 3.12: Galvanostatic measurement of the product of ball-milled Li_3NaSi_6 and graphite (1:2 weight ratio); the first 10 cycles are shown.

During first charge, a negligible capacity of 10 mAh g^{-1} is obtained indicating that no Li was extracted from the starting material. The following discharge leads to a capacity of 1530 mAh g^{-1} accompanied by an irreversible capacity loss of 35% in the next loop. During subsequent cycles, capacity is slowly decreasing and after 10 cycles, a capacity of 840 mAh g^{-1} is retained (55% of initial capacity). Compared to pure Li_3NaSi_6 (Fig. 3.3), the cycling behavior has been improved to a large amount. Although it is still far from optimal, it is the best working approach for Li_3NaSi_6 so far and would be a good starting point for further investigations.

3.3. CaAl$_2$Si$_2$

CaAl$_2$Si$_2$ can be described by layered crystal structure where Ca^{2+} ions are intercalated between hexagonal Al$_2$Si$_2$$^{2-}$ layers. This layer can be described as $^2_{oo}$[AlSi]$^-$ double layers, whereas in each layer a two-dimensional net of chair-like 6-membered rings occurs.[86] The structure of CaAl$_2$Si$_2$ is shown in Figure 3.13 below.

○ Ca   ○ Al   ● Si

Fig. 3.13: Crystal structure of CaAl$_2$Si$_2$.[86]

A tentative reaction could be

$$Li + CaAl_2Si_2 \rightarrow Li_2Ca + 2\ Li_xAl + 2\ Li_ySi \qquad (3.6).$$

The expected lithiation sequence would be from right to left according to the relative electro-negativities (first Si, then Al and then Ca). Corresponding phases are known in literature with x_{max} = 2.25 (Li$_9$Al$_4$) and y_{max} = 4.2 (Li$_{21}$Si$_5$). The total theoretical capacity thus could be 14.9 Li or 2662 mAh g^{-1}. If only lithiation of silicon would occur a maximum capacity of 1500 mAhg^{-1} is expected and for $(x+y)_{max}$ = 6.45 a capacity of 2305 mAh g^{-1} would result. It is not likely that the ternary compound would form back under delithiation

because aluminum and silicon do not have a common binary compound which would have to be a quite likely intermediate on this route. There is however the binary $CaAl_2$ which is a Laves phase just as Li_2Ca is. As such Laves phases are known to undergo hydrogenation reactions (hydrogen storage) it seems to be a valuable attempt to test their Li exchange behavior. According to these considerations it was conjectured that reaction of $CaAl_2Si_2$ could establish a nano composite system quite different from the pure silicides.

Synthesis

A stoichiometric amount of the elements is molten to a metallic bulk material using an arc welder furnace in an argon filled glove box. The product is ground and the obtained XRD powder pattern is shown in Figure 3.14 below.

Fig. 3.14: XRD powder pattern of $CaAl_2Si_2$ synthesized from the elements by arc melting (black curve). The red lines correspond to a calculated pattern.

Additionally, the reactivity of $CaAl_2Si_2$ in different solvents was examined. Interestingly and different from most alkaline earth silicide Zintl phases, $CaAl_2Si_2$ is stable in distilled water, ethanol and diluted NH_3 (pH = 11). However, an exothermic decomposition reaction occurs upon treatment with diluted HCl (pH = 2). It is believed that formation of silanes (Si_2H_6) occurs under acidic conditions due to an increased H^+ concentration.

Electrochemical performance

$CaAl_2Si_2$ was ball-milled to a fine powder prior to electrochemical testing and electrodes were prepared in air. Carbon black (10 wt. %) and graphite (5 wt. %) were added as conductive additives and PVDF was used as binder (11 wt. %). 1 M $LiPF_6$ in ethylenecarbonate / dimethylcarbonate (1:1) was used as electrolyte. The sample was cycled between 10 mV and 3.0 V vs. Li/Li^+ with a rate of 20 mA g^{-1}. The initial step was a discharge (lithiation).

Fig. 3.15: Galvanostatic measurement of the $CaAl_2Si_2$ electode; the first four cycles are shown.

The initial reduction capacity is close to 500 mAh g^{-1} and there is a large irreversible capacity loss of 68% after first cycle followed by rapid capacity decay in subsequent cycles. The initial capacity indicates to a reaction between Li and Si only, thus there was no reason to further investigate pure $CaAl_2Si_2$.

3.3.1. $CaAl_2Si_2$ and $CuCl_2$

In this section, the reaction of $CaAl_2Si_2$ and $CuCl_2$ is examined and the expected reaction is formulated in equation 3.7 below.

$$CaAl_2Si_2 + CuCl_2 \rightarrow Cu / Al / Si + CaCl_2 \tag{3.7}$$

One scenario is that Cu^{2+} would be reduced to Cu^0, whereas $Al_2Si_2^{2-}$ might be oxidized to the elements leading to a distribution of aluminium and silicon in a copper matrix. This, however, is pretty unlikely for aluminum. Alloying of Cu and Al is more probable. Since both Al and Si can be lithiated accompanied by drastic volume changes, a $CuAl_x$ matrix might accommodate the active material such as to improve the cycling behavior. There are at least 5 Cu-Al compounds known.[87] $CaCl_2$ which is formed as side product can be washed out of the reaction mixture using a convenient solvent (NMP).

Synthesis

$CaAl_2Si_2$ (1 Eq.) and $CuCl_2$ (anhydrous, dried at high vacuum, 1 Eq.) are ball-milled for 2 h at a speed of 350 rpm in argon. The reaction mixture is suspended in dry NMP (anhydrous, 99.5%) in a Schlenk round flask in argon and stirred for 90 min at 50 °C to dissolve $CaCl_2$. The material is centrifuged followed by removal of the brown NMP phase containing dissolved $CaCl_2$. The sample is washed twice with 20.0 ml dry NMP, washed twice with 20.0 ml dry THF (99.5%) to remove NMP followed by drying under vacuum (0.6 mbar, 3 h, RT). The obtained XRD powder pattern is shown in Figure 3.16.

Fig. 3.16: XRD powder pattern of the reaction product of $CaAl_2Si_2$ treated with $CuCl_2$ (black curve). The red and blue lines correspond to calculated patterns; green starred = unindexed.

The product contains amorphous material as well as Si and $CuAl_2$. There are some unindexed peaks denoted with green stars, which do especially not fit to $CaCl_2$, $CuCl_2$, Al, Cu, $CaAl_2Si_2$ or any known coppersilicide. As these peaks are especially broad one can infer that this phase has nanoparticular morphology. The absence of $CaCl_2$ in the final product leads to the conclusion that it was successfully washed out of reaction mixture using NMP. Taking into account the result of the XRD analysis, the following reaction is suggested:

$$CaAl_2Si_2 + CuCl_2 \rightarrow CuAl_2 + Si + CaCl_2 \tag{3.8}$$
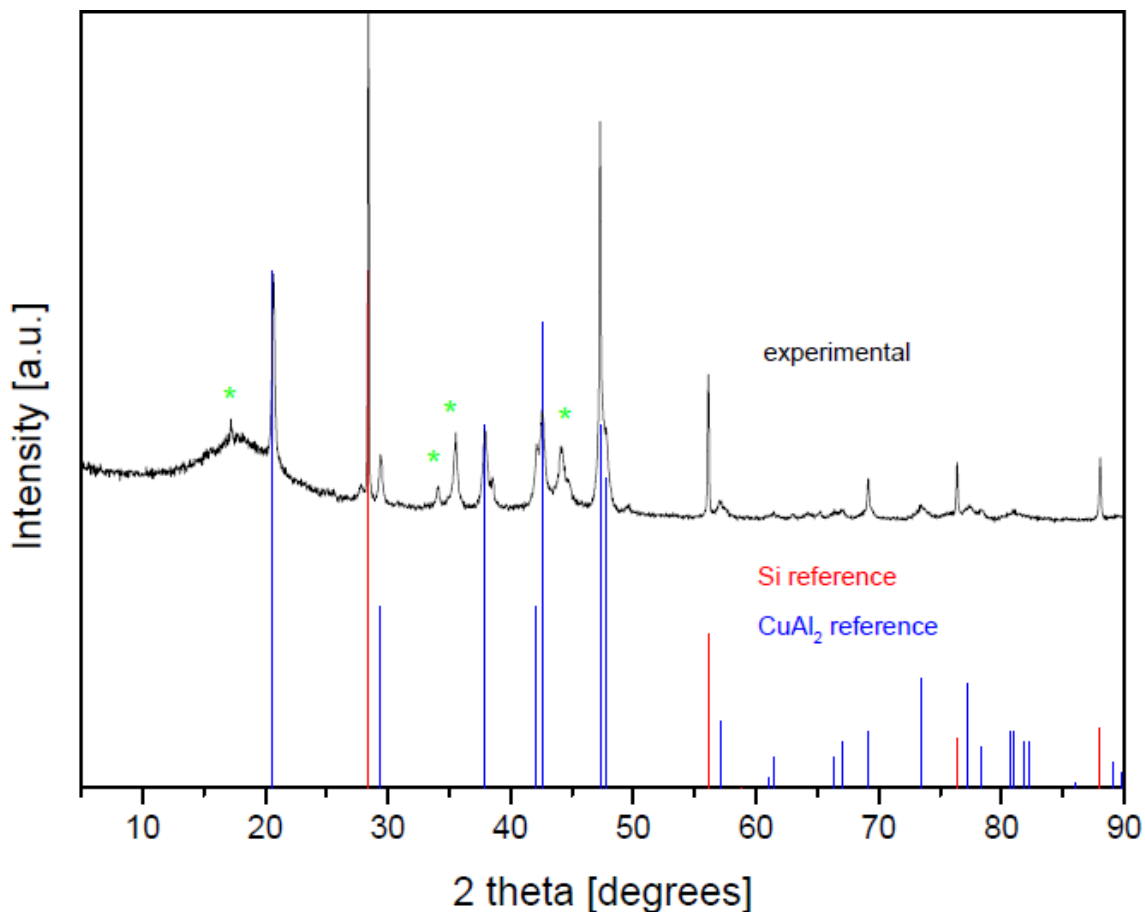
SEM micrographs of the reaction material are shown in Figure 3.17 below.
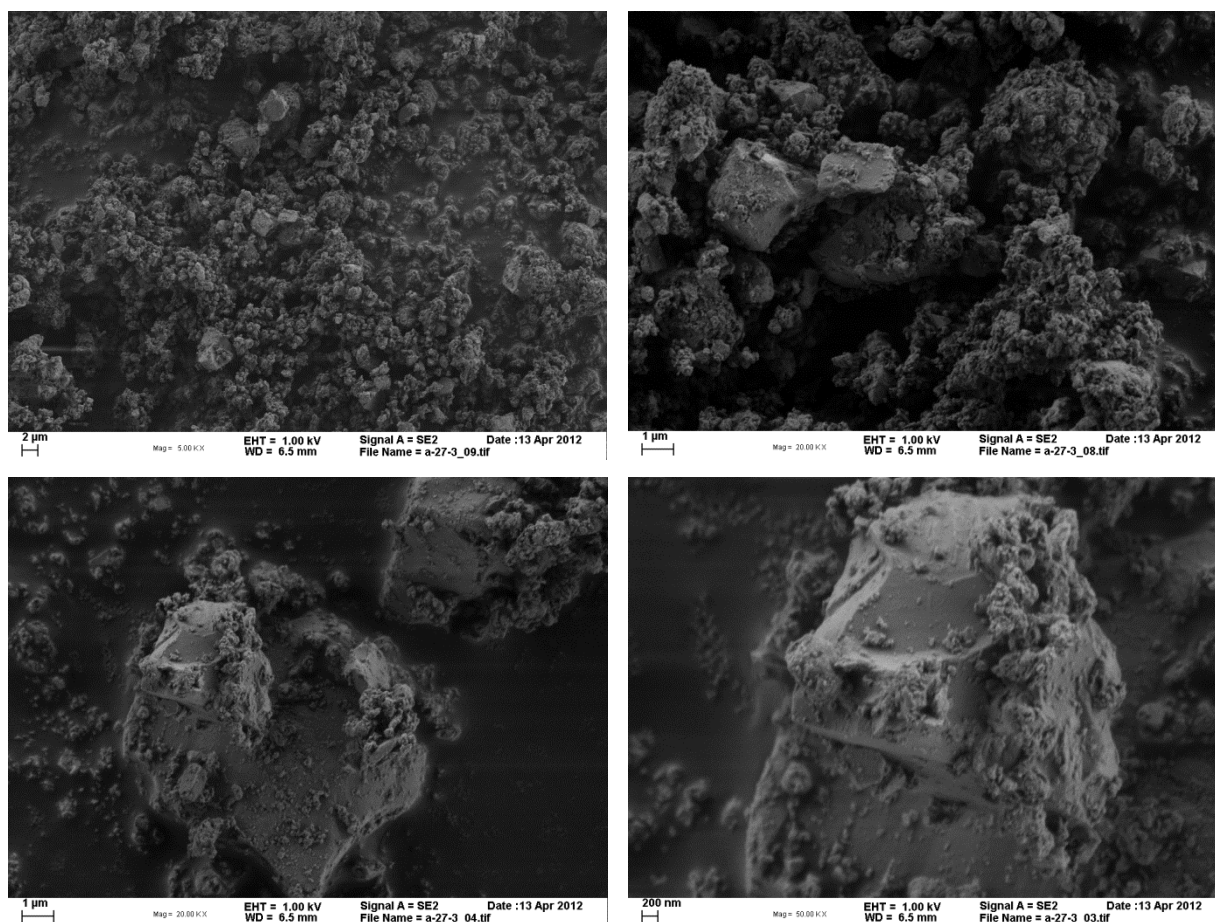
Fig. 3.17: SEM analysis of the reaction product of $CaAl_2Si_2$ and $CuCl_2$.

The sample contains larger compact particles with sizes between 1 and 3 μm, which contain smaller agglomerated particles of about 100 nm size on their surfaces. EDXS analysis was not able to assign particles to their respective phases due to homogeneity of sample.

Electrochemical performance

Electrodes were prepared in air, whereas Carbon black (22 wt. %) and graphite (5 wt. %) were added as conductive additives. PVDF was used as binder (6 wt. %) and 1 M $LiPF_6$ in ethylenecarbonate / dimethylcarbonate (1:1) used as electrolyte. The sample was cycled between 10 mV and 3.0 V vs. Li/Li^+ with a

118

rate of 20 mA g^{-1}. The initial step was discharge (lithiation) and values for specific capacity refer to the composite material.
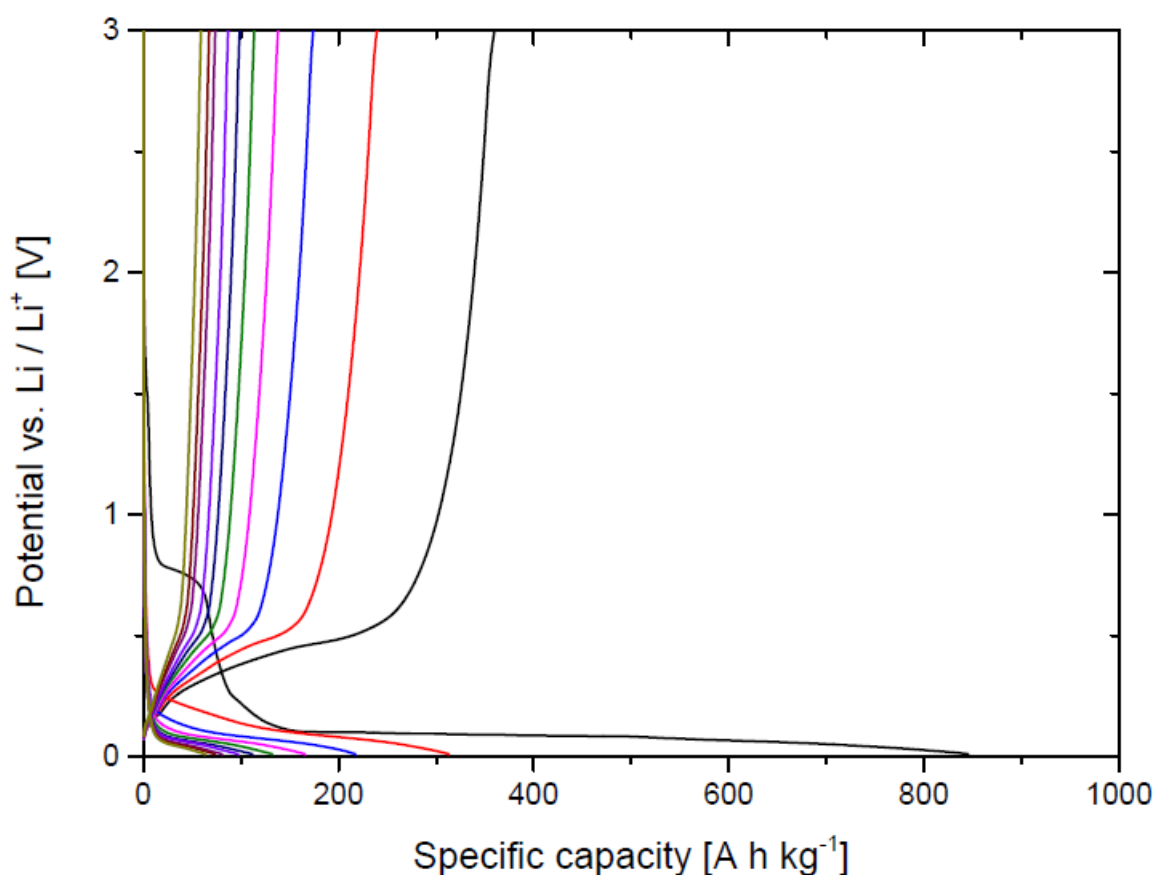
Fig. 3.18: Galvanostatic measurement of the reaction product of CaAl$_2$Si$_2$ and CuCl$_2$, whereas the first ten cycles are shown.

The initial lithiation capacity corresponds practically to full lithiation of the silicon part at a low initial Coulombic efficiency of 43% followed by rapid capacity decay in subsequent cycles. After 10 cycles, only 60 mAh g^{-1} is retained. Compared to pure CaAl$_2$Si$_2$ (Fig. 3.15), a higher capacity is obtained accompanied by slightly improved cycling behavior. However, capacity is not reversible leading to the conclusion that the as-formed CuAl$_2$ is not able to accommodate the volume changes of Si during cycling in this composite.

3.3.2. CaAl$_2$Si$_2$ and graphite oxide

In this section, the reaction of CaAl$_2$Si$_2$ and graphite oxide is examined. The expected result is a partial reduction of graphite oxide accompanied by oxidation of CaAl$_2$Si$_2$, which is decomposed to CaO, Al and Si. As a result, aluminium and silicon might be embedded in graphite oxide pockets therefore acting as a soft matrix to accommodate for the volume changes of electrochemically active species and improving cycling behavior.

Synthesis

CaAl$_2$Si$_2$ (ball-milled) and graphite oxide powder in equal amounts of weight are ball-milled in air (3 h, 350 rpm) to a fine black powder. The obtained XRD powder pattern is shown in Figure 3.19 below.

Fig. 3.19: XRD powder pattern of the reaction product of CaAl$_2$Si$_2$ and graphite oxide (1:1 weight ratio, black curve). The red lines correspond to a calculated pattern.

After ball milling the sample is highly amorphous with some $CaAl_2Si_2$ in a nanoscopic form leading to the conclusion that the ternary Zintl silicide compound was only partially transformed into amorphous products.

Electrochemical performance

Electrodes were prepared in air, whereas Carbon black (12 wt. %) and graphite (4 wt. %) were added as conductive additives. PVDF was used as binder (19 wt. %) and 1 M $LiPF_6$ in ethylenecarbonate / dimethylcarbonate (1:1) used as electrolyte. The sample was cycled between 10 mV and 3.0 V vs. Li/Li^+ with a rate of 20 mA g^{-1}. The initial step was discharge (lithiation) and values for specific capacity refer to the composite material.
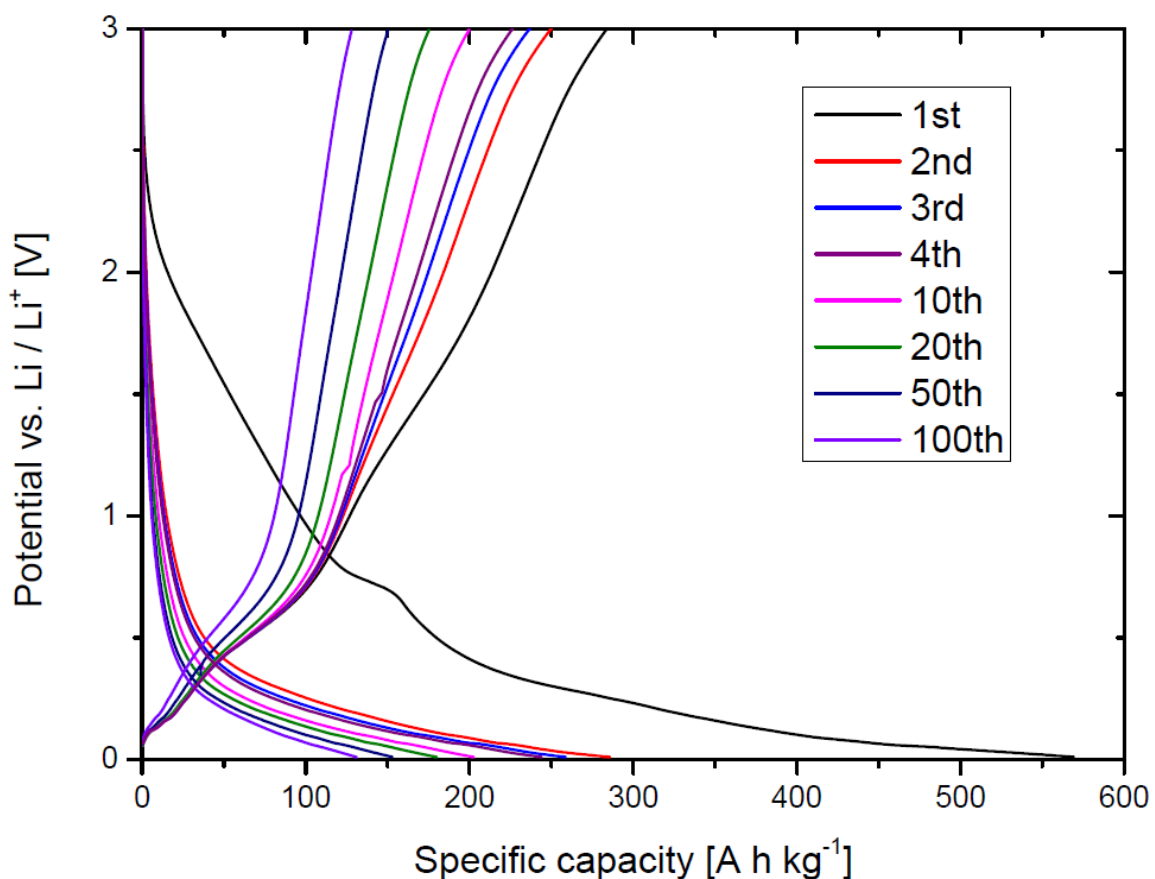
Fig. 3.20: Galvanostatic measurement of the reaction product of $CaAl_2Si_2$ and graphite oxide (1:1 weight ratio), whereas the first 100 cycles are shown.

There is an initial capacity of 570 mAh g^{-1} which can only account for active silicon at a Coulombic efficiency of 50%. This result may be caused by graphite oxide due to an irreversible formation of Li_2O which explains the obtained capacity of about 100 mAh g^{-1} between 1.0 – 2.0 V that is only observable during first discharge. One may further guess that there is no elementary aluminum but formation of Al-C bonds; as aluminumcarbide is extremely hard it is not expected to grow to diffraction sized particles under the reaction conditions. After the first cycle, there is a continuous loss of capacity during subsequent cycles, where 130 mAh g^{-1} are restored after 100 cycles (23% of initial capacity). Compared to pure $CaAl_2Si_2$ (Fig. 3.15), the obtained capacity as well as the cycling behavior is improved. However, the overall cycling behavior is still insufficient and would need serious improvement. Nevertheless, this may be a good starting point for future experiments.

3.3.3. $CaAl_2Si_2$ and graphene oxide

In analogy to treatment with graphite oxide (section 3.2), the reaction of $CaAl_2Si_2$ with graphene oxide is examined. As in the previous section, a partial reduction of graphene oxide accompanied by oxidation and decomposition of $CaAl_2Si_2$ is expected. The main difference to treatment with graphite oxide is an improved packing of the electrochemically active species due to the huge surface area of graphene oxide. Silicon is expected to be better embedded in the resultant pockets.

Synthesis

Deionized water (60 ml) is added to CaAl$_2$Si$_2$ (ball-milled, 100 mg) and dispersed in an ultrasonication bath for 90 min (T = 20 °C). The resulting black dispersion is added to 100 ml of a graphene oxide dispersion in H$_2$O / NH$_3$ (c = 1 g l^{-1}) followed by additional ultrasonication for 120 min at room temperature. Diluted HCl is added to the black mixture to lower pH to 8 and then diluted AlCl$_3$ solution in H$_2$O is added dropwise while stirring until some brown flakes precipitate. The sample is filtrated overnight, washed with deionized water and dried in the oven for 1 h at 80 °C. The resulting black plates (highly elastic and electrostatically charged) are dried in vacuum for 5 h at 50 °C. These plates cannot be ground effectively, but cutting them with a knife to smaller pieces works. Therefore, a single black plate was used for the following XRD analysis shown in Figure 3.21.
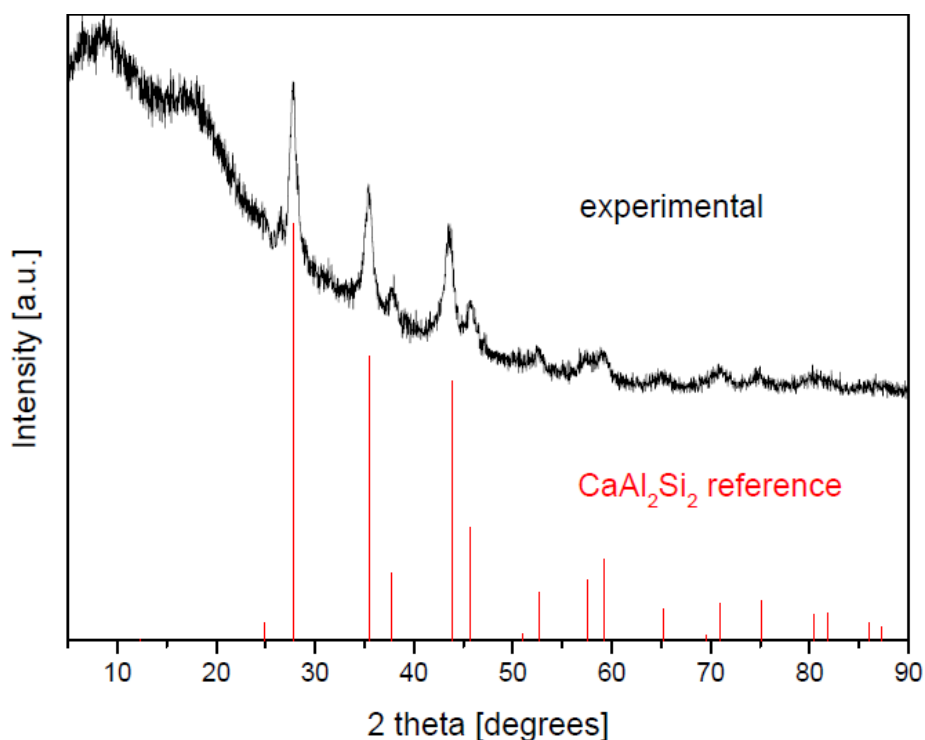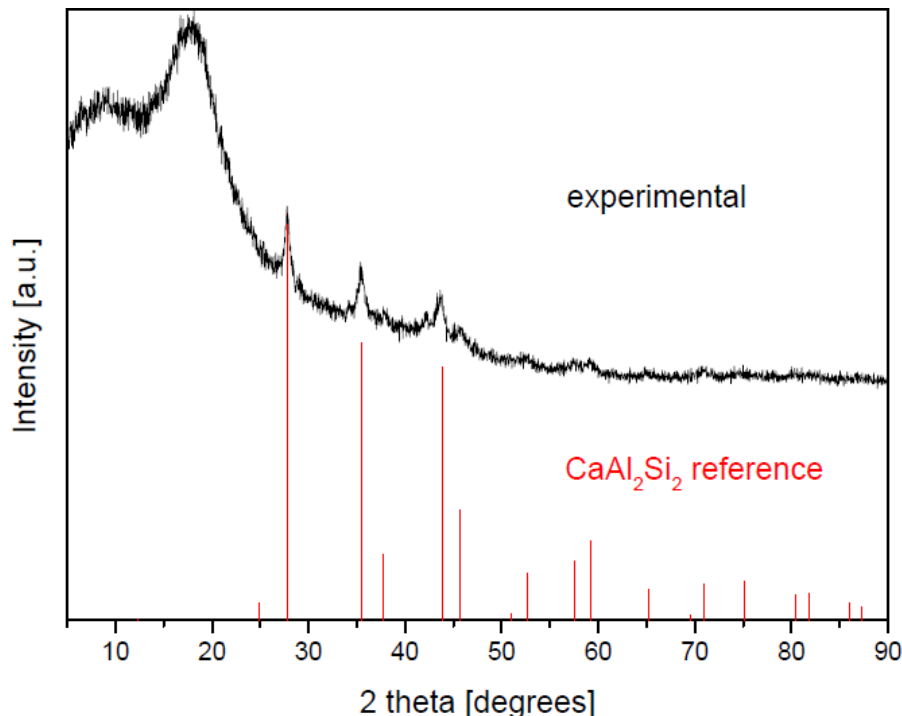

Fig. 3.21: XRD powder pattern of the reaction product of CaAl$_2$Si$_2$ and graphene oxide (1:1 weight ratio, black curve). The red lines correspond to a calculated pattern.

123

The sample is highly amorphous and contains residual nanoscopic $CaAl_2Si_2$ leading to the assumption that this compound was only partially reacted. SEM micrographs of the product are shown in Figure 3.22.
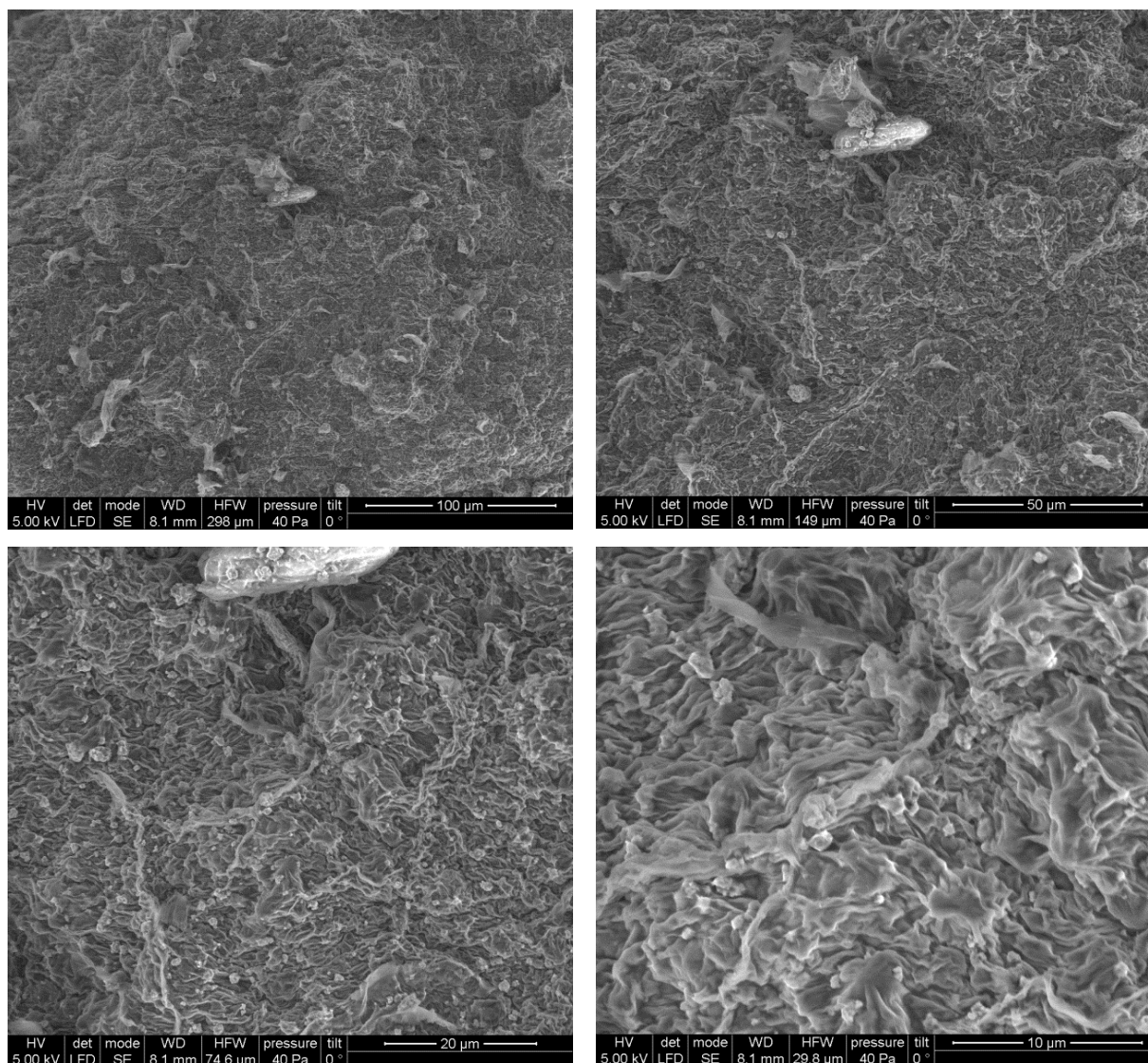
Fig. 3.22: SEM analysis of the reaction product of $CaAl_2Si_2$ and graphene oxide (1:1 weight ratio) at different magnification scales.

Bulk particles of $CaAl_2Si_2$ with different size ranging from submicron to 30 µm are distributed on the surface of graphite oxide. TEM micrographs of the product are shown in Figure 3.23.
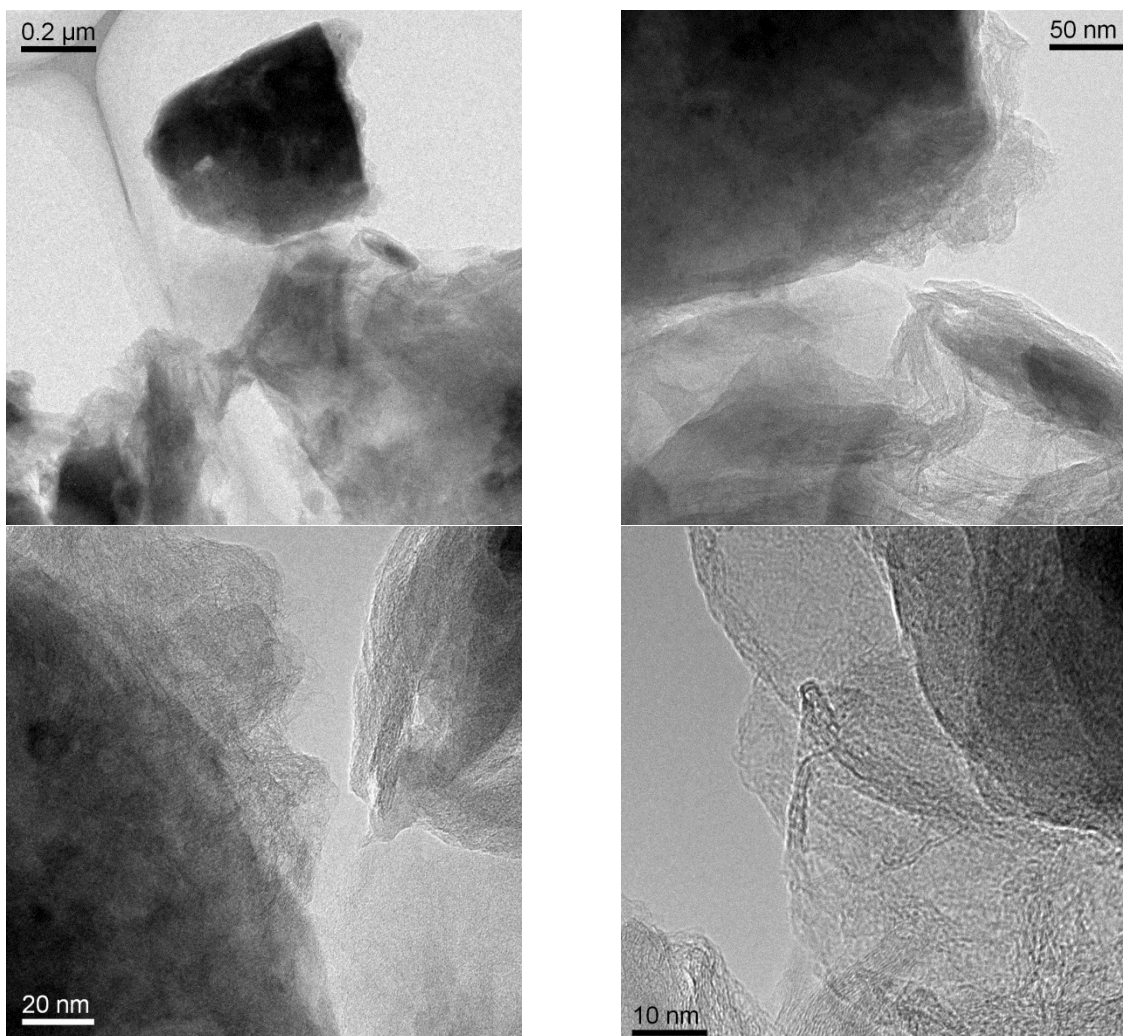
Fig. 3.23: TEM analysis of the reaction product of $CaAl_2Si_2$ and graphene oxide (1:1 weight ratio) at different magnification scales.

Single layers of graphene oxide which are partially stacked can be clearly seen. In between these layers, $CaAl_2Si_2$ particles with diameters between 200 and 500 nm (dark spots, confirmed by EDXS) are embedded.

Electrochemical performance

Plates of the composite material were cut to smaller pieces using a knife prior to electrochemical testing and electrodes prepared in air. Carbon black (11 wt. %) and graphite (4 wt. %) were added as conductivity providers and PVDF was used as a binder (13 wt. %). 1 M $LiPF_6$ in ethylenecarbonate / dimethyl-carbonate (1:1) was used as electrolyte. The sample was cycled between 10 mV

and 3.0 V vs. Li/Li$^+$ with a rate of 20 mA g^{-1}. The initial step was discharge (lithiation) and values for specific capacity refer to the composite material.
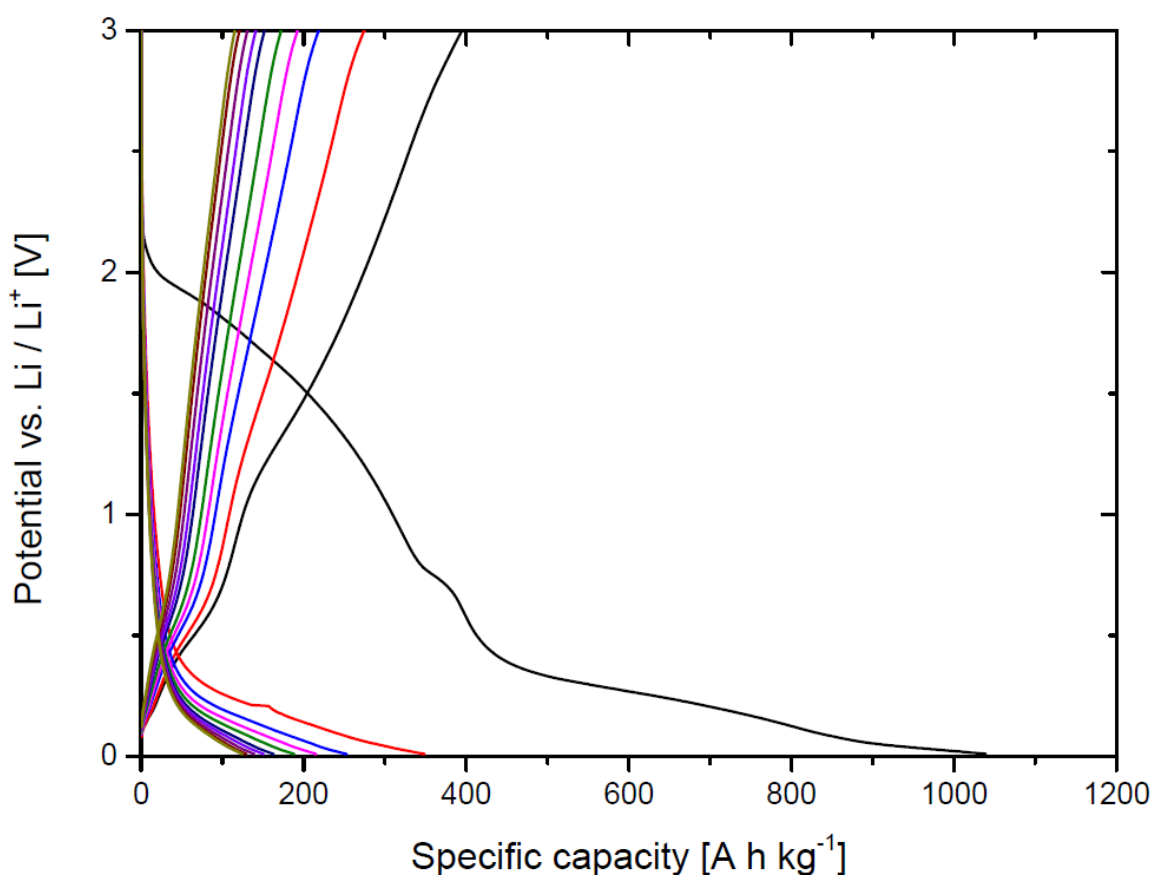
Fig. 3.24: Galvanostatic measurement of the reaction product of CaAl$_2$Si$_2$ and graphene oxide (1:1 weight ratio); the first 10 cycles are shown.

The low initial Coulombic efficiency of 35% is most likely caused by reaction of graphene oxide with lithium due to irreversible formation of Li$_2$O during first discharge in the potential range of 1.0 and 2.0 V. After first cycle, there is continuous decay of capacity and only 120 mAh g^{-1} are retained after 10 cycles. Compared to pure CaAl$_2$Si$_2$ (Fig. 3.15), the cycling behavior was slightly improved but is still insufficient. However, the formation of an elastic matrix made of CaAl$_2$Si$_2$ and graphene oxide was observed. Therefore, it was tested how silicon can be stored inside this promising elastic material which is discussed in the following section.

3.3.3.1. Composite of silicon and the "CaAl$_2$Si$_2$ / graphene oxide" elastomer

3.3.3.1.1. Nano Si

Synthesis

Deionized water (80 ml) is added to a mixture of CaAl$_2$Si$_2$ (ball-milled, 100.0 mg) and Si nanopowder (98%, particle size: 50 nm, 98.9 mg). The sample is dispersed in an ultrasonication bath for 2 h at room temperature and 100 ml of a grapheme oxide dispersion in H$_2$O / NH$_3$ (c = 1 g l^{-1}) is added to the brown dispersion followed by additional ultrasonication for 210 min (T = 20 °C). Diluted HCl is added to the black mixture to lower pH to 8 and then diluted AlCl$_3$ solution in H$_2$O is added dropwise while stirring until grey-brown flakes precipitate. The sample is filtrated overnight, washed with deionized water and dried in the oven for 90 min at 80 °C. The resulting dark green plates were dried in vacuum for 5 h (50 °C, 10^{-1} mbar). The obtained XRD powder pattern of the ground plates is shown in Figure 3.25 below.

Fig. 3.25: XRD powder pattern of the reaction product of CaAl$_2$Si$_2$, graphene oxide and nano Si in 1:1:1 weight ratio (black curve). The red and blue lines correspond to calculated patterns.

The product is highly amorphous and contains nanoscopic $CaAl_2Si_2$ as well as nano-Si. The size of silicon particles is estimated to roughly 50 nm using the Scherrer equation regarding the [220] diffraction peak. TEM micrographs of this sample are shown in Figure 3.26 below.
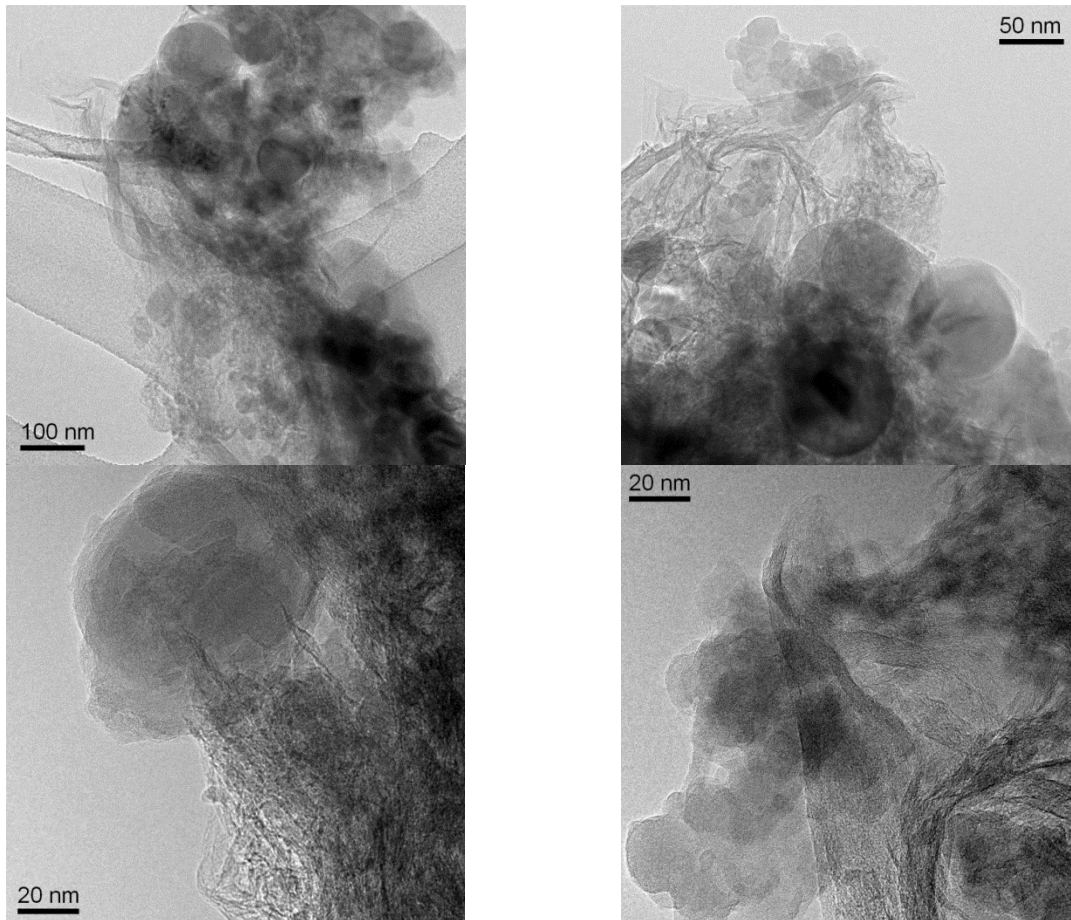
Fig. 3.26: TEM analysis of the reaction product of $CaAl_2Si_2$, graphene oxide and nano Si in 1:1:1 weight ratio.

$CaAl_2Si_2$ particles with a diameter between 200 and 500 nm (dark spots) as well as Si particles with a diameter of 50 nm (dark grey spheres) are wrapped inside layers of grapheme oxide. A HAADF image of this composite material was acquired and the composition for the $CaAl_2Si_2$ as well as for the Si particles is confirmed by EDXS analysis as shown in Figure 3.27.
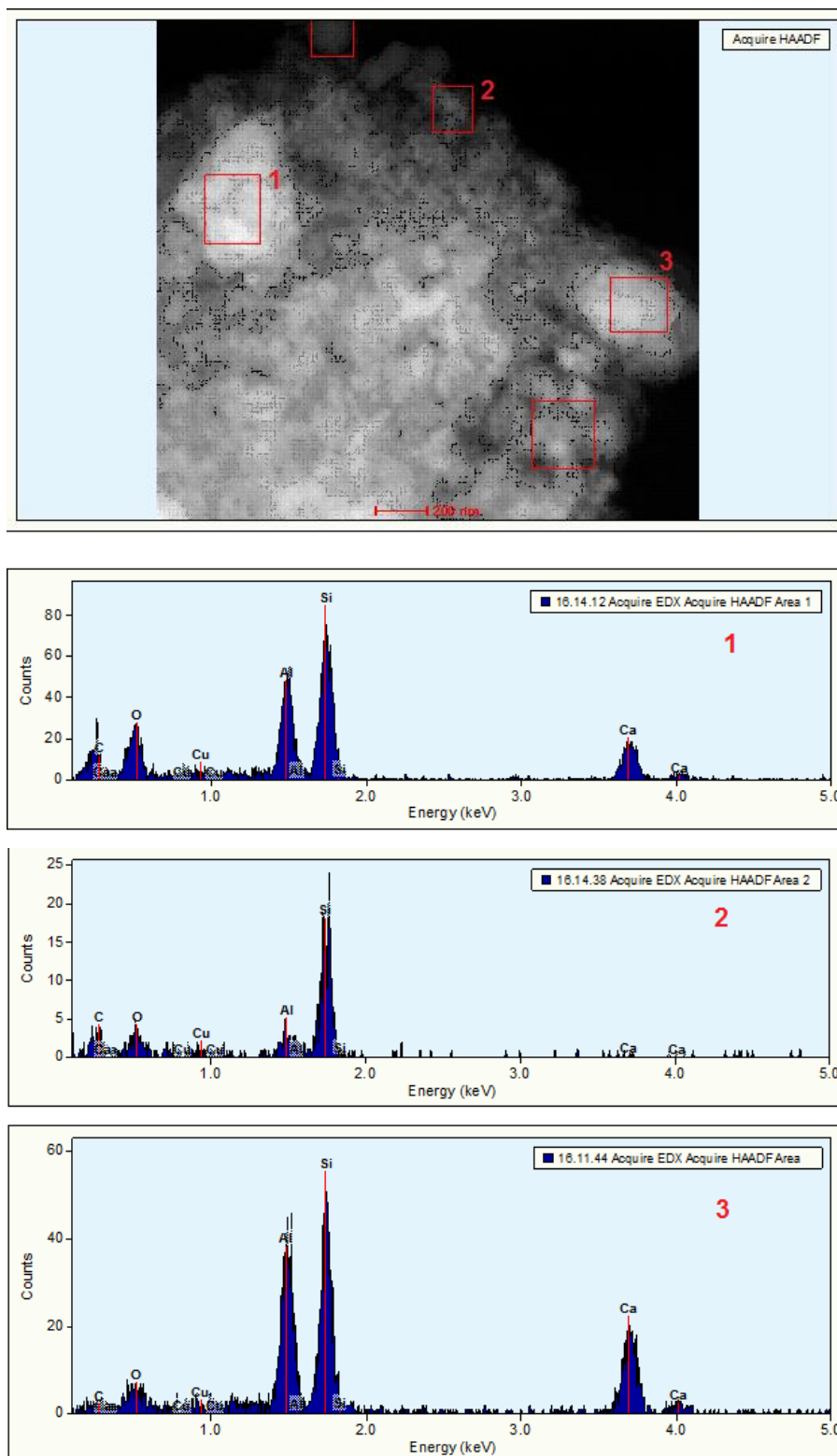
Fig. 3.27: High angle annular dark field (HAADF) scanning transmission electron microscopy (STEM) imaging of the reaction product of $CaAl_2Si_2$, graphene oxide and nano silicon in 1:1:1 weight ratio; energy dispersive X-ray (EDX) spectra of marked regions are shown.

Electrochemical performance

The sample was ground to a dark green powder prior to electrochemical testing and electrodes were prepared in air. Carbon black (16 wt. %) and graphite (5 wt. %) were added as conductive additives and PVDF was used as binder (14 wt. %). 1 M $LiPF_6$ in ethylenecarbonate / dimethylcarbonate (1:1) was used as electrolyte. The sample was cycled between 10 mV and 3.0 V vs. Li/Li$^+$ with a rate of 20 mA g^{-1}. The initial step was discharge (lithiation) and values for specific capacity refer to the composite material.
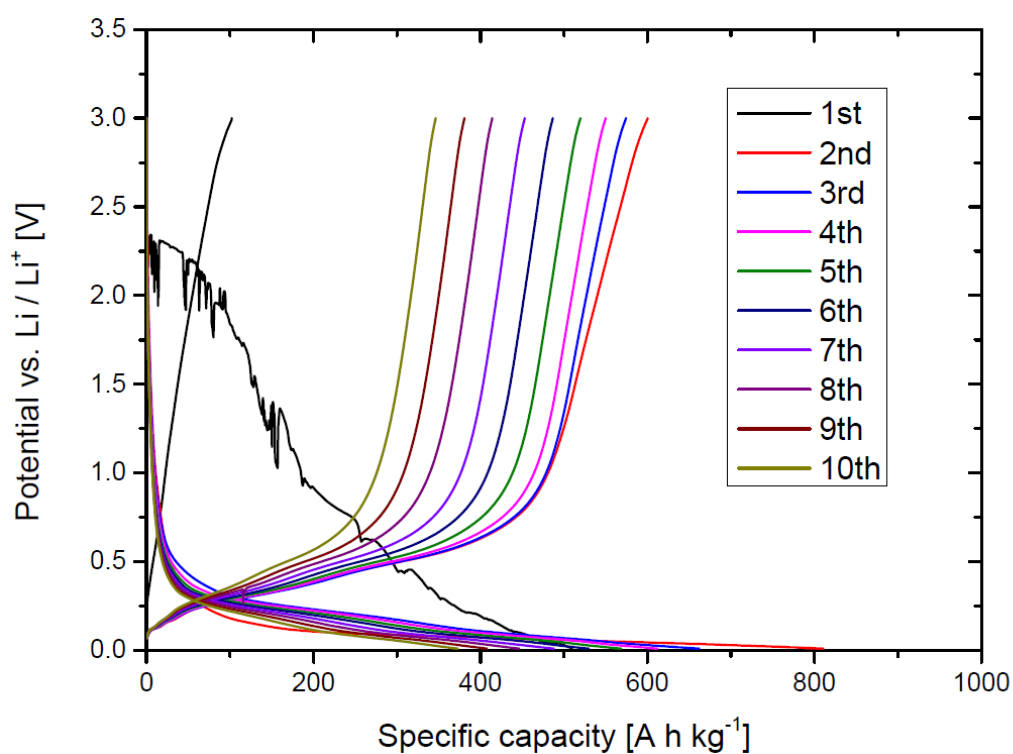
Fig. 3.28: Galvanostatic measurement of the reaction product of $CaAl_2Si_2$, graphene oxide and nano Si in 1:1:1 weight ratio; the first 10 cycles are shown.

Regarding first discharge, the electrode material is still reactive: Instead of a smooth potential curve, there are many peaks indicating an ongoing reaction. The following charge is quite small with a capacity of 100 mAh g^{-1} indicating to no exchangeable cations at this point. Discharge during the second cycle leads to a high capacity of 810 mAh g^{-1} which again may be attributed to the silicon

130

part of the electrode. During subsequent cycles, there is continuous capacity fading. After 10th cycle, only 375 mAh g^{-1} is retained (46% of the maximum discharge capacity). To improve the cycling behavior of this sample, a reduction process was examined (e.g. reduction of graphene oxide) which is described below.

Synthesis

The reaction product of CaAl2Si2, graphene oxide and nano silicon in 1:1:1 weight ratio is ground to a dark green powder, put into a carbon crucible and treated at 250 °C for 8 h under nitrogen flow. The obtained XRD powder pattern of the resulting black powder is shown in Figure 3.29 below.
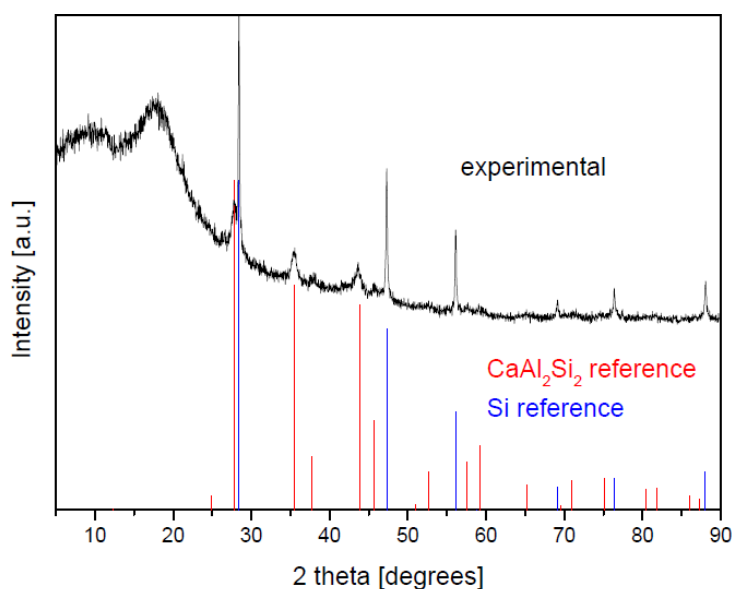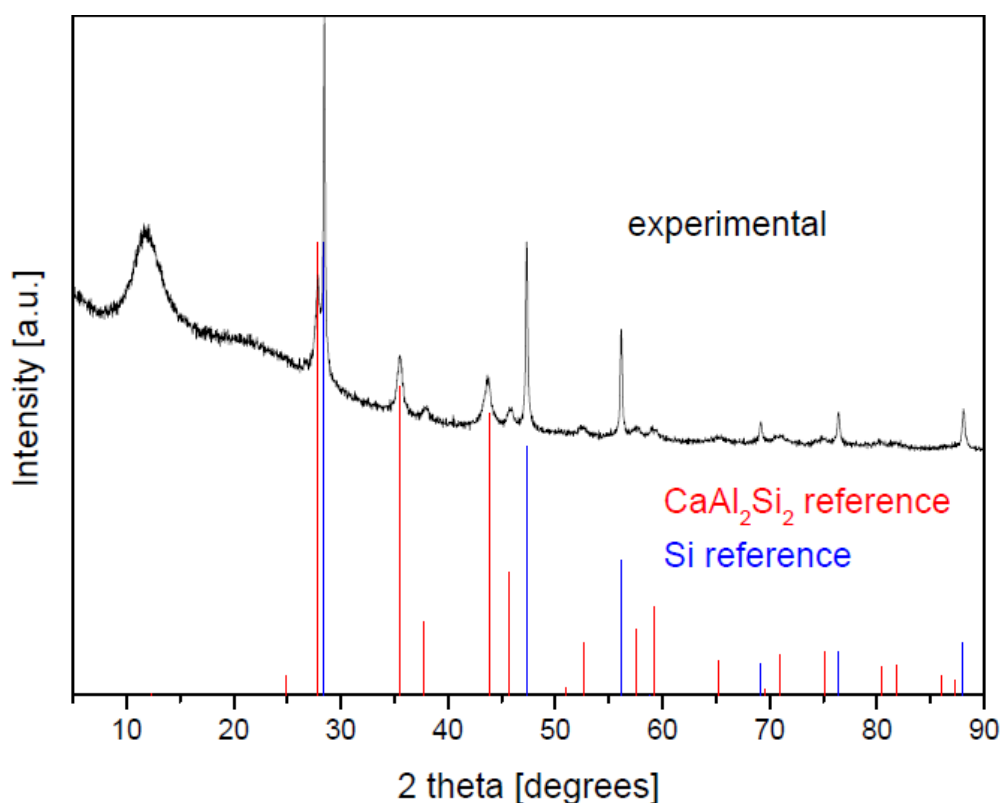

*Fig. 3.29:* XRD powder pattern of the reaction product of CaAl$_2$Si$_2$, graphene oxide and nano Si in 1:1:1 weight ratio, treated at 250 °C for 8 h in nitrogen (black curve). The red and blue lines correspond to calculated patterns of CaAl$_2$Si$_2$ and alpha-Si, respectively.

Compared to the precursor sample (Fig. 3.25), amorphous character of the sample was decreased due to heat treatment. The size of silicon particles is estimated to roughly 50 nm using the Scherrer equation regarding the [220] diffraction peak. A broad peak at 2 theta = 12 ° which is typical for graphene oxide, is still present indicating only partially reduction.

Electrochemical performance

Electrodes were prepared in air, with Carbon Black (13 wt. %) and graphite (5 wt. %) added as conductive additives. PVDF was used as binder (11 wt. %) and 1 M $LiPF_6$ in ethylenecarbonate / dimethylcarbonate (1:1) was used as electrolyte. The sample was cycled between 10 mV and 3.0V vs. Li/Li$^+$ with a rate of 20 mA g^{-1}. The initial step was discharge (lithiation) and values for specific capacity refer to the composite material.
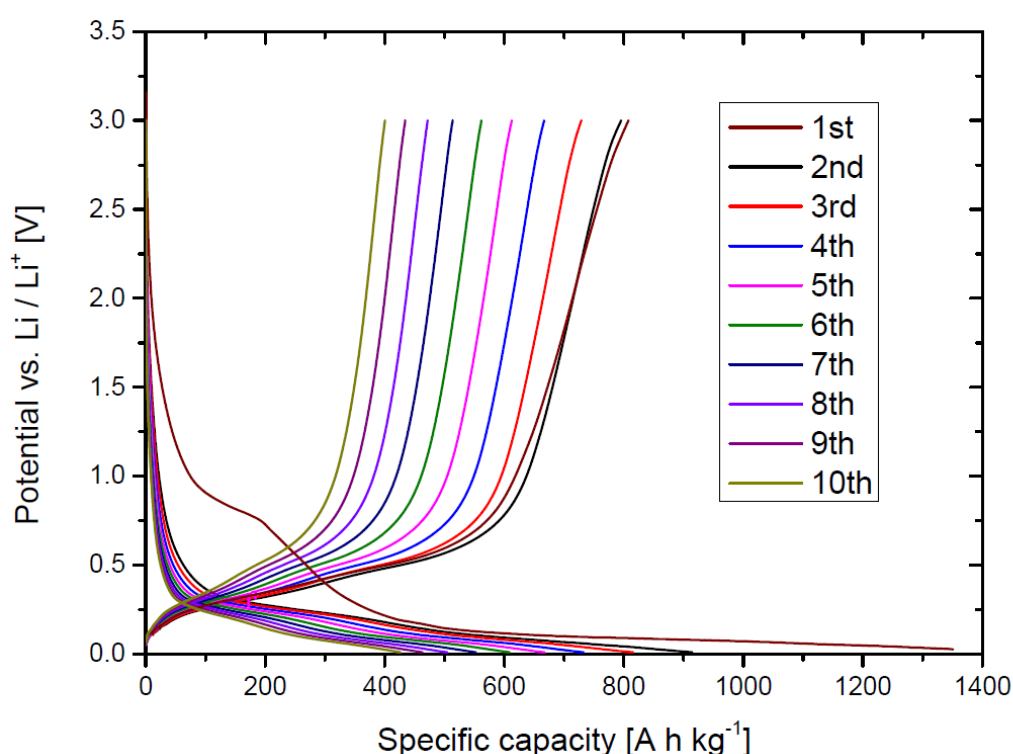
Fig. 3.30: Galvanostatic measurement of the reaction product of $CaAl_2Si_2$, graphene oxide and nano Si in 1:1:1 weight ratio, treated at 250 °C for 8 h in nitrogen. The first 10 cycles are shown.

Compared to precursor sample (Fig. 3.28), there is a higher maximum capacity as well as a lower contribution to first discharge capacity by irreversible formation of Li_2O, indicating partial reduction of graphene oxide. Additionally, there are no observed irregularities during cycling due to a reaction of electrode material and capacity retention is slightly improved. Still, cycling behavior is insufficient for an application and calls for further modifications.

3.3.3.1.2. Ball-milled Si

Synthesis

Deionized water (80 ml) is added to $CaAl_2Si_2$ (ball-milled, 100.0 mg) and Si (99.9999%, ball-milled to a fine black powder, 100.4 mg). The mixture is dispersed in an ultrasonication bath for 90 min (T = 20 °C) and 100 ml of a graphene oxide dispersion in H_2O / NH_3 (c = 1 g l^{-1}) is added to the black dispersion followed by additional ultrasonication for 2 h (T = 20 °C). Diluted HCl is added to black mixture to lower pH to 8 and then diluted $AlCl_3$ solution in H_2O is added dropwise while stirring until brown flakes precipitate. The sample is filtrated overnight, washed with deionized water and dried in the oven for 90 min at 80 °C. The resulting black plates are dried under vacuum for 5 h (50 °C, 10^{-1} mbar). The XRD powder pattern of this composite is shown in Figure 3.31.
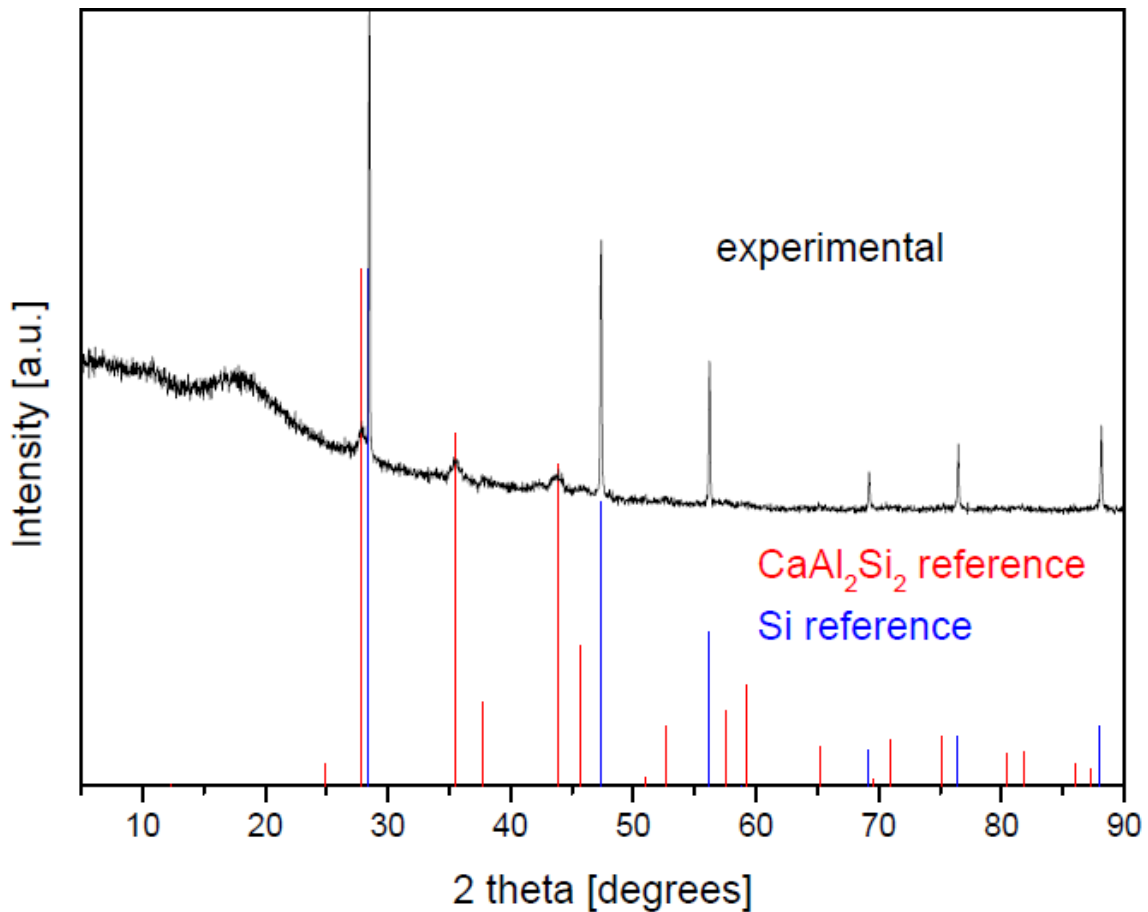
Fig. 3.31: Powder pattern of the reaction product of $CaAl_2Si_2$, graphene oxide and ball-milled Si in 1:1:1 weight ratio (black curve). The red and blue lines correspond to calculated patterns of $CaAl_2Si_2$ and alpha-Si, respectively. For XRD analysis, the black plates were ground to a black powder.

The sample contains amorphous material as well as $CaAl_2Si_2$ (broad peaks) and Si (sharp, intense peaks). The sample looks similar to the one using nano silicon (Fig. 3.25), except that the peaks for Si are sharper here, indicating to larger overall particle size. However, the size of silicon particles is estimated to roughly 70 nm using the Scherrer equation regarding the [220] diffraction peak. TEM micrographs of the composite material are shown in Figure 3.32.
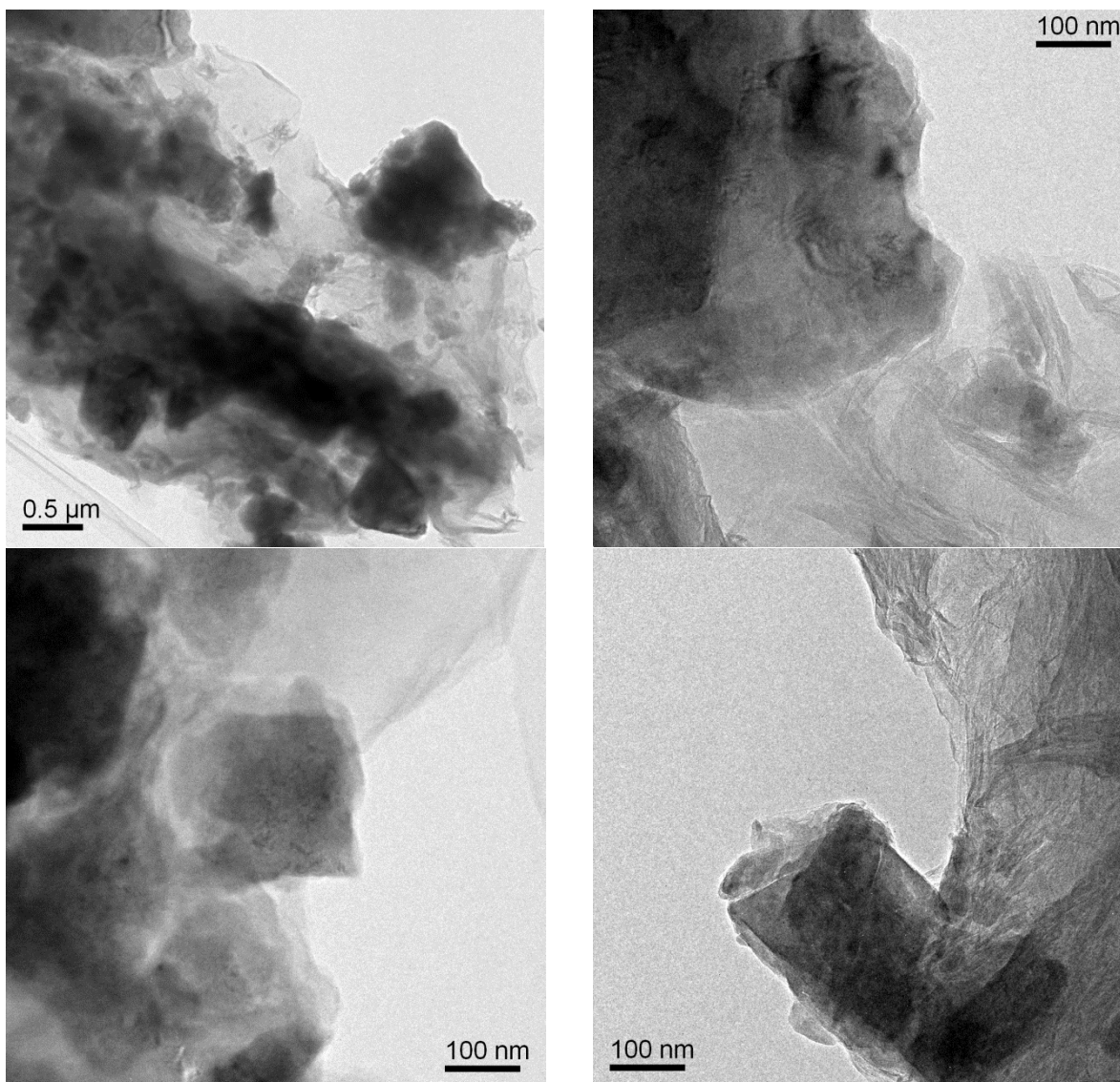
Fig. 3.32: TEM micrographs of the reaction product of $CaAl_2Si_2$, graphene oxide and ball-milled Si in 1:1:1 weight ratio.

Particles with diameters between 100 and 500 nm are wrapped inside graphene oxide layers. EDXS analysis of particles shows a high content of silicon as well as lower content of Ca and Al, whereas the layers contain C and O. However, it was not possible to distinguish Si from $CaAl_2Si_2$ particles.

Electrochemical performance

The sample was ground to a black powder prior to electrochemical testing and electrodes were prepared in air. Carbon black (15 wt. %) and graphite (6 wt. %)

were added as conductive additives and PVDF was used as binder (10 wt. %). 1 M $LiPF_6$ in ethylenecarbonate / dimethylcarbonate (1:1) was used as electrolyte. The sample was cycled between 10 mV and 3.0 V vs. Li/Li^+ at a rate of 20 mA g^{-1}. The initial step was discharge (lithiation) and values of specific capacity refer to the composite material.
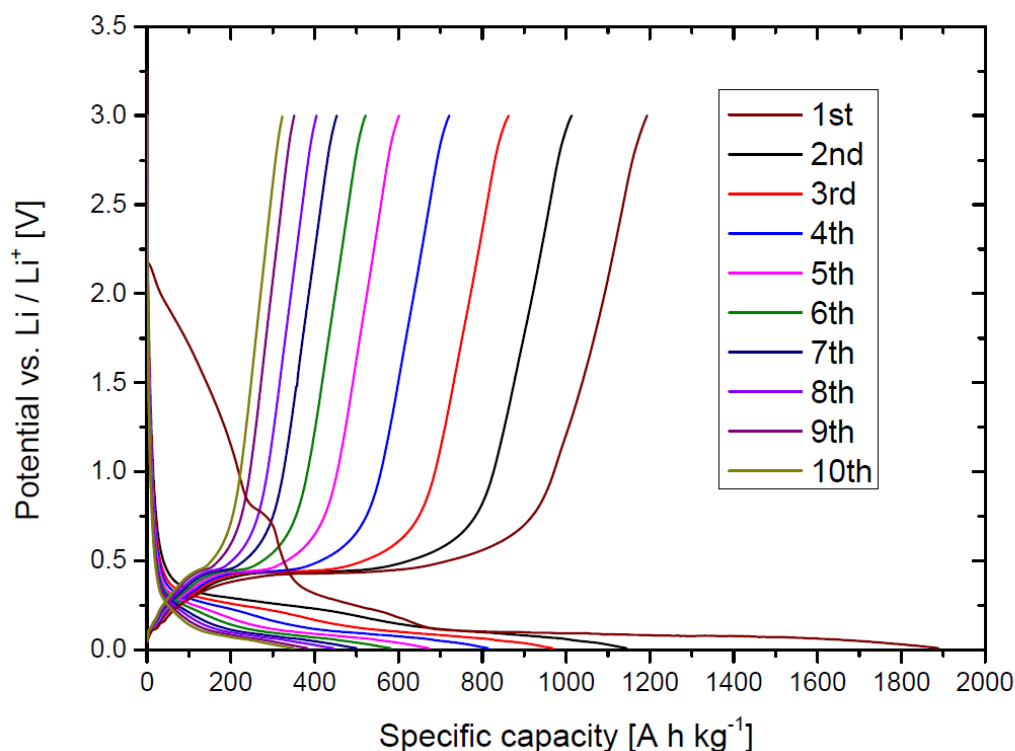

Fig. 3.33: Galvanostatic measurement of the reaction product of $CaAl_2Si_2$, graphene oxide and ball-milled Si in 1:1:1 weight ratio; the first 10 cycles are shown.

There is a high capacity of 1890 mAh g^{-1} during first discharge accompanied by a low initial Coulombic efficiency of 63%. These observations can be partially addressed to the irreversible formation of Li_2O from graphene oxide which is manifested in the cyclovoltammogram shown in Figure 34. During subsequent cycles, there is rapid decay of capacity and after 10 cycles 350 mAh g^{-1} is retained (19% of initial capacity).
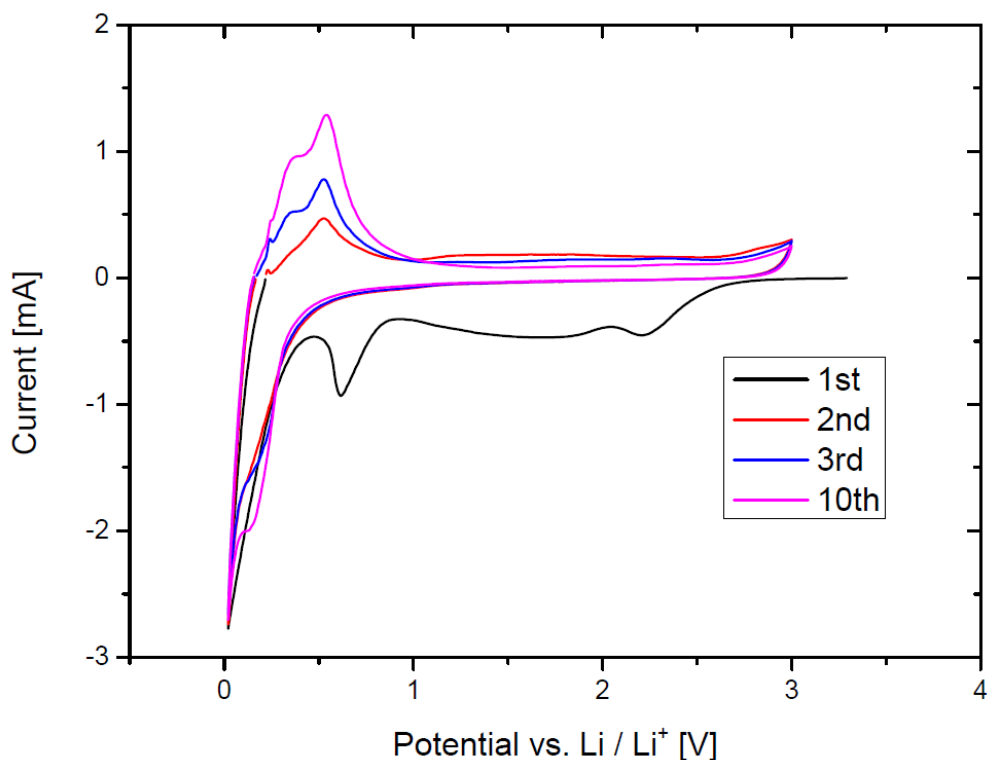
Fig. 3.34: Cyclovoltammogram of the reaction product of $CaAl_2Si_2$, graphene oxide and ball-milled Si in 1:1:1 weight ratio, whereas the first 10 cycles are shown. . The sample was cycled between 20 mV and 3.0 V vs. Li/Li^+ with a rate of 0.05 mV / s. The initial step was discharge (lithiation).

During first discharge, there are two reduction peaks which are no longer present in subsequent cycles: a broad peak at 2.2 V and another one at 0.6 V, respectively. The latter one is addressed to the initial SEI formation whereas the first one indicates the reduction of graphene oxide by irreversible formation of Li_2O. For oxidation, there are three clearly defined peaks at 0.25, 0.35 and 0.55 V which identify silicon as electrochemically active species. The rapid capacity decay is believed to be caused by Si particles which are too large and therefore not properly enveloped by graphene oxide layers. In accordance with previous section (3.3.3.1.1), a reduction process was examined (e.g. reduction of graphene oxide) to improve cycling behavior of this composite material.

Synthesis

The reaction product of CaAl$_2$Si$_2$, graphene oxide and ball-milled Si in 1.1:1 weight ratio is put into a carbon crucible and treated at 210 °C for 8 h under nitrogen flow and the resulting black plates are ground to a black powder. The obtained XRD powder pattern is shown in Figure 3.35.
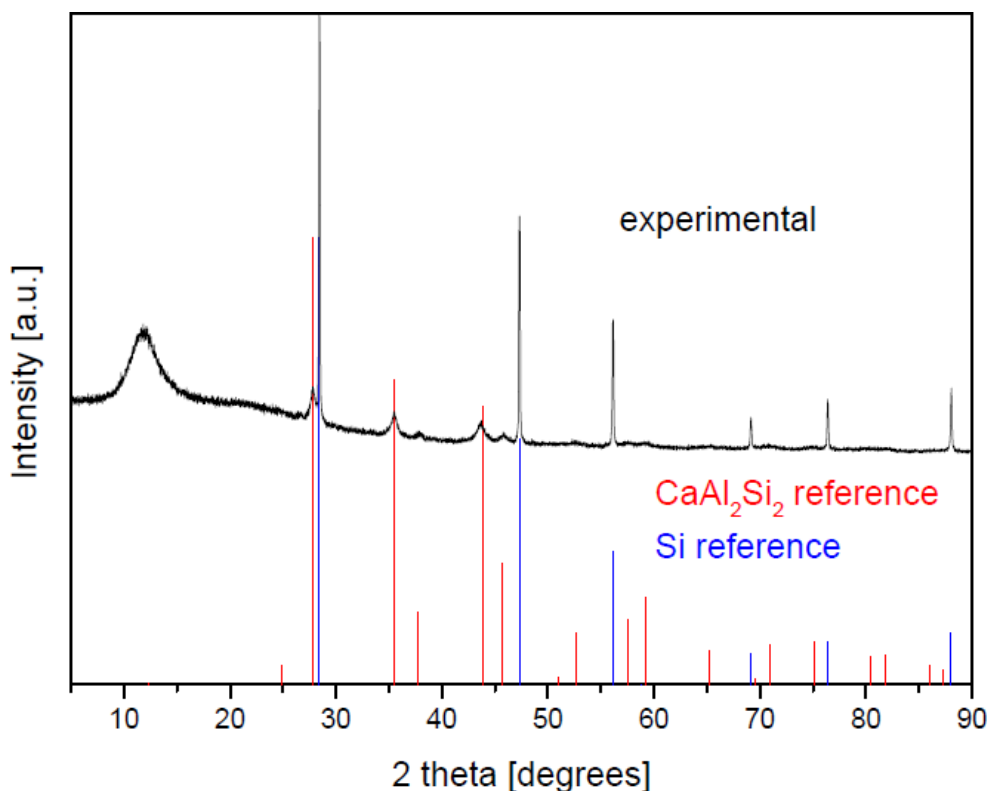
Fig. 3.35: XRD powder pattern of the reaction product of CaAl$_2$Si$_2$, graphene oxide and ball-milled Si in 1:1:1 weight ratio, treated at 210 °C for 8 h in nitrogen (black curve). The red and blue lines correspond to calculated patterns of CaAl$_2$Si$_2$ and alpha-Si, respectively.

Compared to the precursor sample (Fig. 3.31), the amorphous character of the sample was slightly decreased due to heat treatment. The size of silicon particles is estimated to roughly 70 nm using the Scherrer equation regarding the [220] diffraction peak. The broad peak at $2\theta = 12$ °, which is typical for graphene oxide, is still present indicating only partial reduction.

Electrochemical performance

Electrodes were prepared in air, with Carbon Black (13 wt. %) and graphite (5 wt. %) added as conductive additives. PVDF was used as a binder (11 wt. %) and 1 M $LiPF_6$ in ethylenecarbonate / dimethylcarbonate (1:1) was used as electrolyte. The sample was cycled between 10 mV and 3.0V vs. Li/Li$^+$ with a rate of 20 mA g^{-1}. The initial step was discharge (lithiation) and values for specific capacity refer to the composite material.
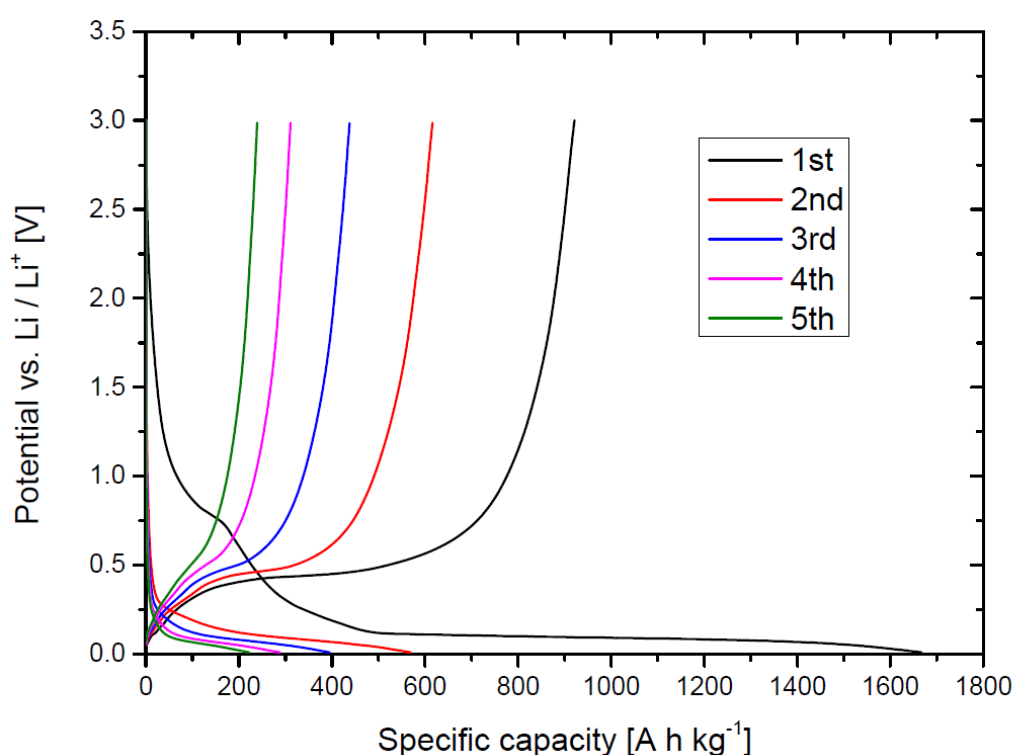
Fig. 3.36: Galvanostatic measurement of the reaction product of $CaAl_2Si_2$, graphene oxide and ball-milled Si in 1:1:1 weight ratio, treated at 210 °C for 8 h in nitrogen, whereas the first 5 cycles are shown.

Compared to precursor sample (Fig. 3.33), the contribution to first discharge capacity by irreversible formation of Li_2O has decreased, indicating to partial reduction of graphene oxide prior to the electrochemistry. However, capacity retention is worse.

139

Summary

CaAl$_2$Si$_2$ and diverse composites thereof were widely investigated with respect to electrochemical lithium exchange. Accidentally, an elastic matrix made of CaAl$_2$Si$_2$ and graphene oxide was formed in which Si particles are embedded. The size of the silicon particles remains an important factor for capacity retention, which is exemplified by the better performance of nanosized particles. The composite material can be reduced by additional heat treatment in nitrogen atmosphere improving the initial Coulombic efficiency. However, the cycling behavior remains insufficient and calls for new ideas and further modifications.

3.4. Ca$_2$LiSi$_3$

Ca$_2$LiSi$_3$ crystallizes in the orthorhombic spacegroup *Pnnm*. The structure can be described as a layered Zintl phase with planar Zintl anions which form a one dimensional chain.[88] The distance between these stacked layers is 4.2 Å. The crystal structure is shown in Figure 3.37 below.
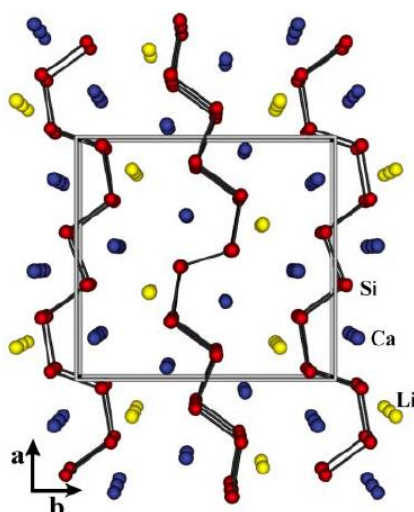
Fig. 3.37: Crystal structure of Ca$_2$LiSi$_3$ in [001] projection.[88]

Ca_2LiSi_3 is obtained although the initial plan had been to synthesize $CaLiSi_2$. It is believed that reaction time and temperature (900 °C for 4 h) were too high, so eventually formed $CaLiSi_2$ transformed into the Li-poorer and more stable Ca_2LiSi_3 by loss of Li vapor. So far, there was no success in preparing Ca_2LiSi_3 from a stoichiometric amount of the elements.

The sample is prepared using a stoichiometric amount of the elements for $CaLiSi_2$: 554.6 mg Si lumps (99.9999%, ground, 19.4 mmol, 2 eq.), 388.9 mg Ca pieces (99%, 9.7 mmol, 1 eq.) and 67.1 mg Li granulate (99.9%, 9.7 mmol, 1 eq.) are sealed in a niobium ampoule in argon, which is sealed afterwards in a steel tube in argon for additional protection. The sample is put inside a vertical furnace and treated at 900 °C for 4 h and the obtained reaction material is ground to a shiny dark grey powder. The XRD powder pattern is shown in Figure 3.38.
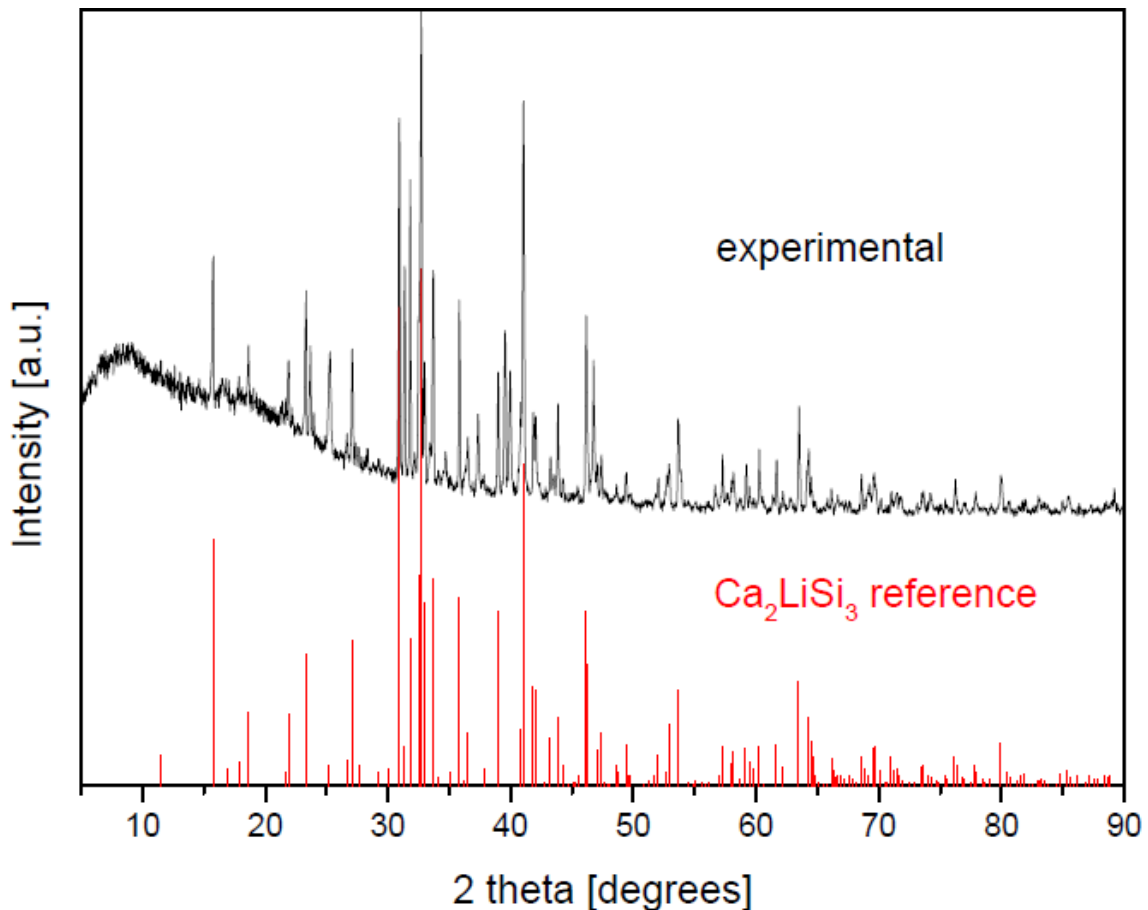
Fig. 3.38: XRD powder pattern of Ca_2LiSi_3 (black curve). The red lines correspond to the calculated pattern.

The sample looks quite pure and well crystalline with only a few small unindexed peaks, however there is a large amorphous background, too.

Electrochemical performance

The sample was ball-milled prior to electrochemical testing and electrodes were prepared in an argon filled glove box. Super P (11 wt. %) and graphite (4 wt. %) were added as conductive additives and PVDF was used as binder (11 wt. %). 1 M $LiPF_6$ in ethylenecarbonate / dimethylcarbonate (1:1) was used as electrolyte. The sample was cycled between 10 mV and 3.0V vs. Li/Li^+ with a rate of 20 mA g^{-1}. The initial step was discharge (lithiation).

142
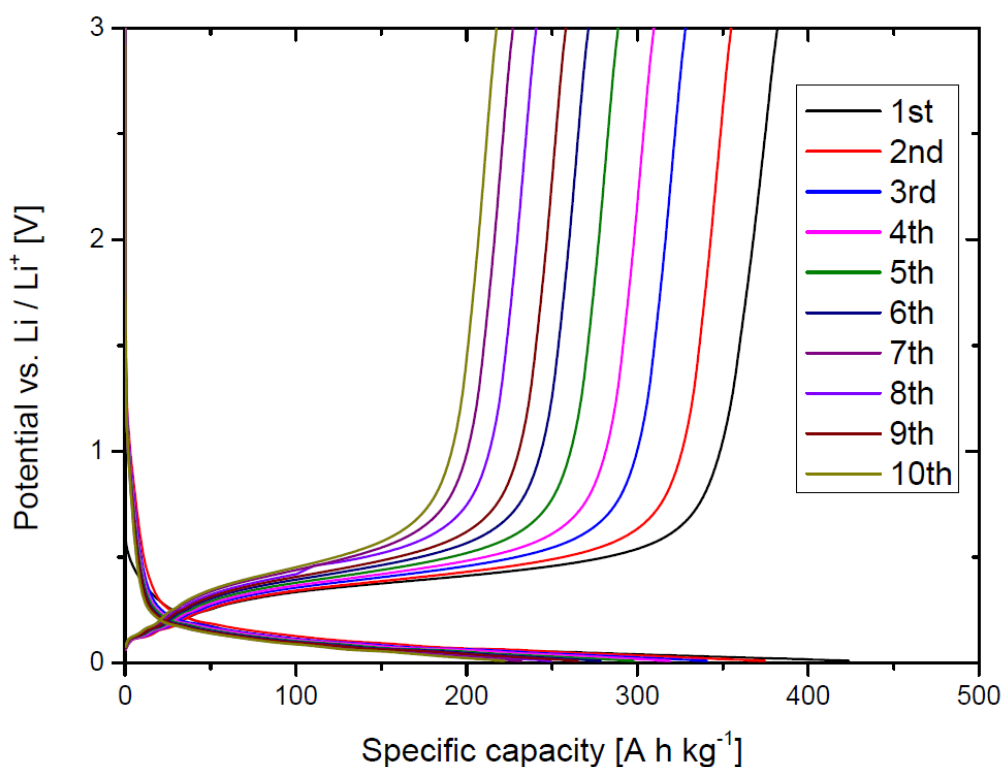
Fig. 3.39: Galvanostatic measurement of ball-milled Ca_2LiSi_3; the first 10 cycles are shown.

There is an initial capacity of 420 mAh g^{-1} which corresponds to 21.8 % of the maximal theoretical silicon capacity of the sample (1925 mAh g^{-1}) and a Coulombic efficiency of 90% followed by a continuous capacity loss during subsequent cycles. After the 10th cycle, 52% of the initial capacity is retained. It is interesting to note the losses seem to be more pronounced during oxidation half cycles.

3.4.1. Ca_2LiSi_3 and graphene oxide

In this section, the reaction of graphene oxide and Ca_2LiSi_3 is examined. The expected outcome for this reaction is a partial reduction of graphene oxide in combination with oxidation of Ca_2LiSi_3, which is decomposed to Li_2O, CaO and Si. As a result, silicon particles are embedded in a soft graphene oxide pocket which is believed to accommodate the volume changes of Si during cycling.

Synthesis

A mixture containing Ca$_2$LiSi$_3$ and graphite oxide powder (dried at high vacuum) in equal weight ratio is ball-milled in argon (2 h, 350 rpm) to a fine black powder. The obtained XRD powder pattern is shown in Figure 3.40.
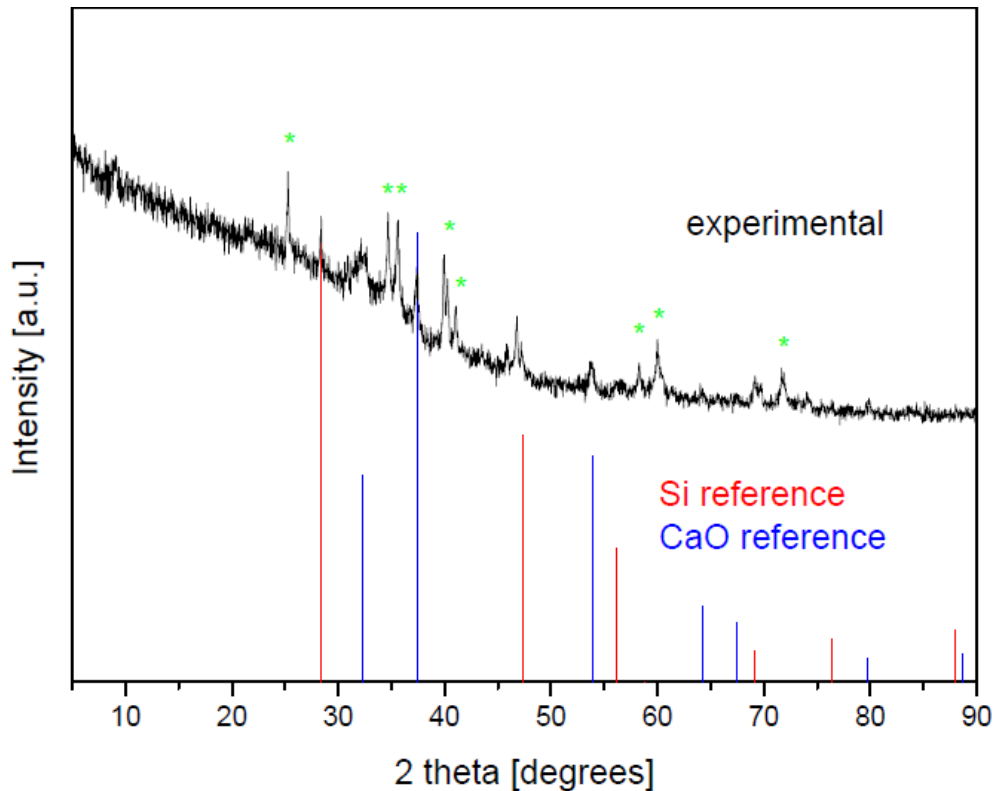
Fig. 3.40: XRD powder pattern of the reaction product of Ca$_2$LiSi$_3$ ball-milled with graphite oxide powder (1:1 weight ratio, black curve). The red and blue lines correspond to calculated patterns of α-Si and CaO, respectively.

The sample is highly amorphous (high background) and contains CaO as well as Si. There are a lot of unindexed peaks denoted with green stars that do especially not fit to Li$_2$O, CaLi$_2$Si$_3$, SiO$_2$ or any lithiumsilicide phase. The formation of CaO and Si as well as the absence of Ca$_2$LiSi$_3$ indicates a reaction with partially unknown products. SEM micrographs of the sample are shown in Figure 3.41.
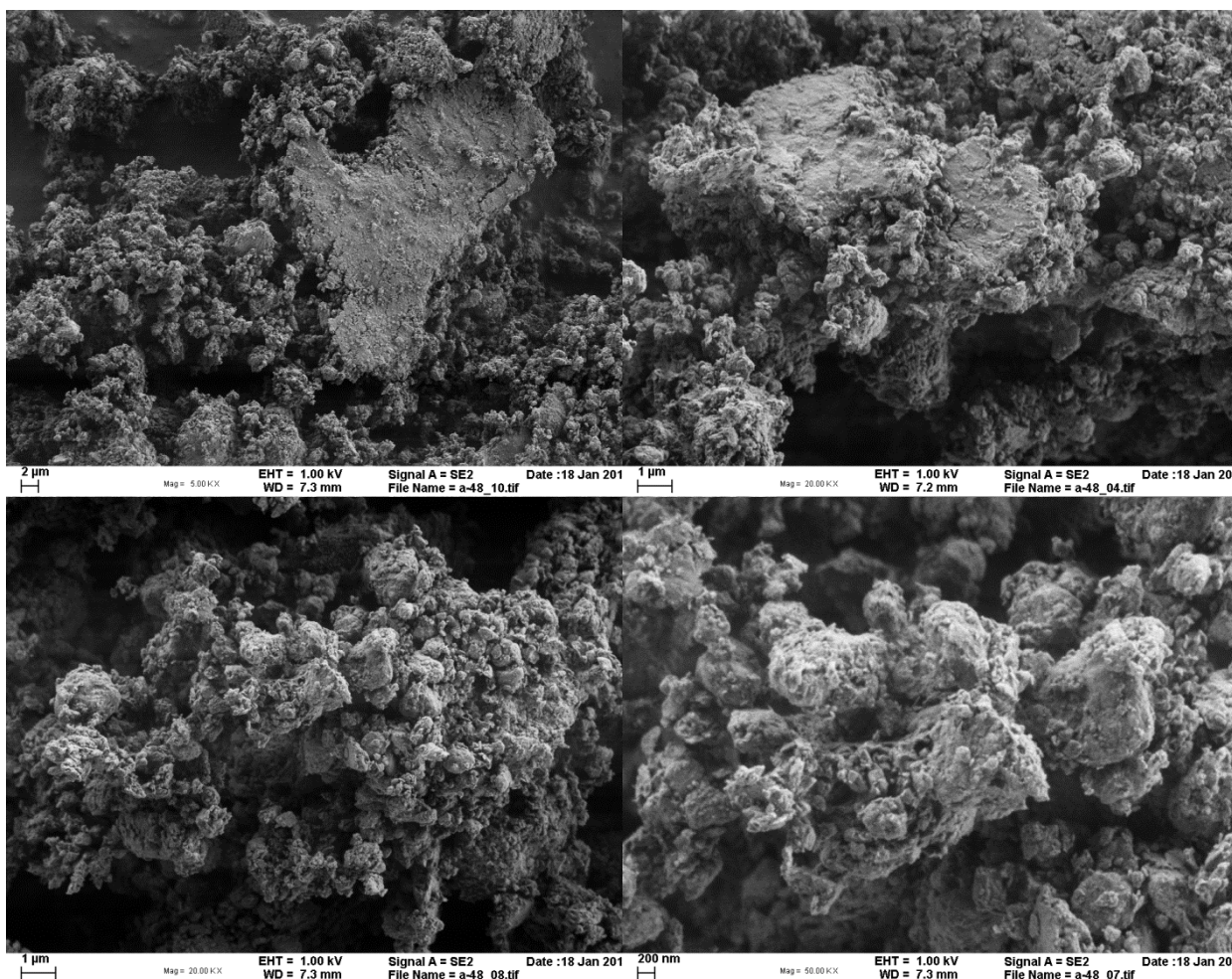
Fig. 3.41: SEM analysis of the reaction product of ball-milled Ca_2LiSi_3 and graphene oxide (1:1 weight ratio).

The sample is homogeneous mixture, whereas plate-like particles (probably graphite oxide) with a size of 10 µm are covered by submicron sized agglomerated particles on their surface.

Electrochemical performance

Electrodes were prepared in an argon filled glove box. Super P (12 wt. %) and graphite (6 wt. %) were added as conductive additives and PVDF was used as binder (8 wt. %). 1 M $LiPF_6$ in ethylenecarbonate / dimethylcarbonate (1:1) was used as electrolyte. The sample was cycled between 10 mV and 3.0 V vs. Li/Li^+

with a rate of 20 mA g^{-1}. The initial step was discharge (lithiation) and values for specific capacity refer to the composite material.
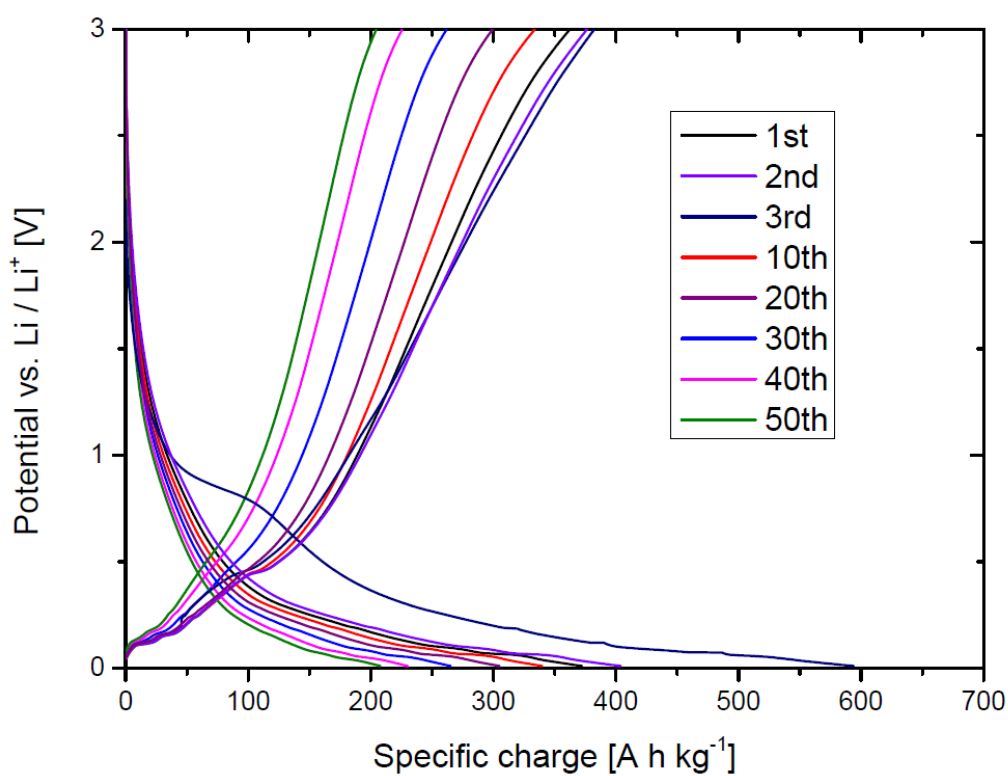
Fig. 3.42: Galvanostatic measurement of the reaction product of ball-milled Ca$_2$LiSi$_3$ and graphite oxide (1:1 weight ratio), whereas the first 50 cycles are shown.

The initial capacity of 600mAh g^{-1} corresponds to 62% of the theoretical capacity of the silicon content (962 mAh g^{-1}); the Coulombic efficiency is only about 64%. Then, starting from 400 mAh g^{-1}, capacity drops slowly during following cycles until it is roughly 200 mAh g^{-1} at 50th cycle. Compared to pure Ca$_2$LiSi$_3$ (Fig. 3.39), the obtained maximum capacity as well as capacity retention is increased. However, initial Coulombic efficiency is decreased which is believed to be caused by the reaction with graphite oxide and the decomposition of Ca$_2$LiSi$_3$ to diverse oxides. However, the contribution to first discharge capacity by irreversible formation of Li$_2$O is low. This observation as well as the formation of CaO leads to the assumption that graphite oxide was

reduced by reaction with Ca_2LiSi_3. However, obtained capacities are too small and capacity retention is insufficient for a direct application.

3.4.2. Ca_2LiSi_3 and graphite

In this section, composite formation of Ca_2LiSi_3 and graphite is tested in order to enhance the performance of the ternary Zintl silicide.

Synthesis

A mixture of Ca_2LiSi_3 and graphite (dried) in equal weight amounts is ball-milled in argon for 3 h at a speed of 450 rounds per minute to a fine black powder. The obtained XRD powder pattern is shown in Figure 3.43 below.
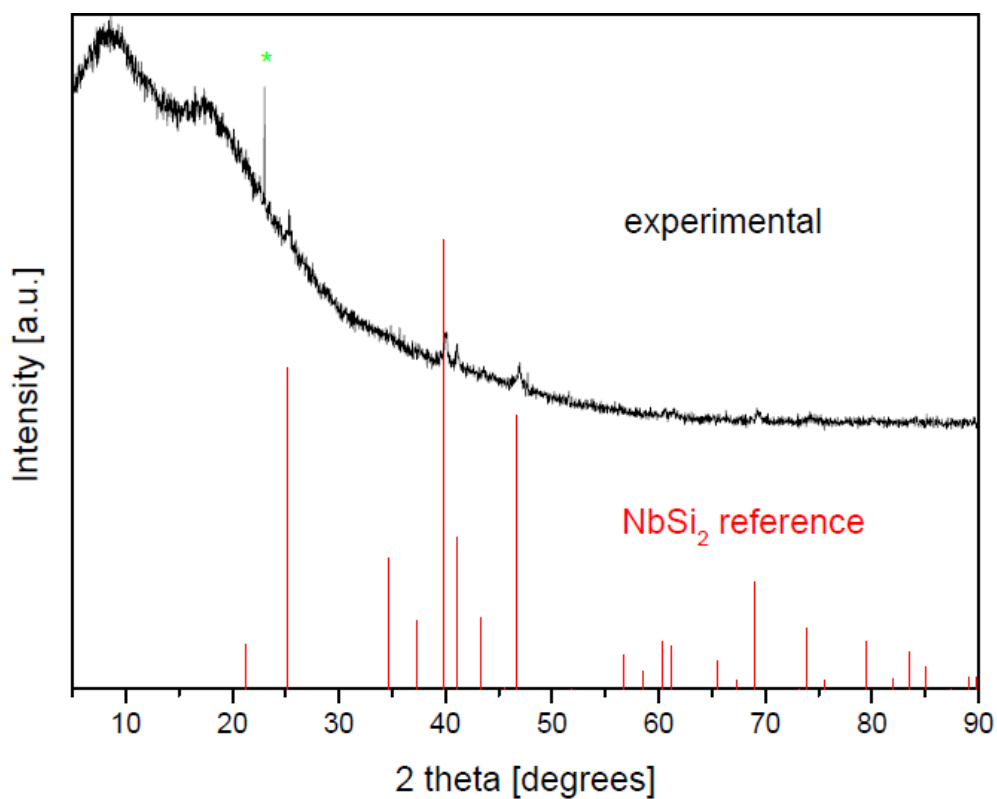
Fig. 3.43: XRD powder pattern of the reaction product of ball-milled Ca_2LiSi_3 and graphite (1:1 weight ratio, black curve). The red lines correspond to the calculated pattern of $NbSi_2$.

147

The sample is highly amorphous and contains traces of NbSi$_2$, which was found as an impurity in the Ca$_2$LiSi$_3$ starting material. Additionally, there is a sharp reflection at a 2θ = 22.8 ° denoted with a green star, which cannot be indexed to a known phase. The absence of Ca$_2$LiSi$_3$ and graphite implies that the educts were mixed to an amorphous composite.

Electrochemical performance

Electrodes were prepared in an argon filled glovebox, whereas Carbon black was added as conductive additive (18 wt. %) and PVDF used as binder (18 wt. %). 1 M LiPF$_6$ in ethylenecarbonate / dimethylcarbonate (1:1) was used as electrolyte. The sample was cycled between 10 mV and 2.0 V vs. Li/Li$^+$ with a rate of 50 mA g^{-1}. The initial step was discharge (lithiation) and values for specific capacity refer to the composite.
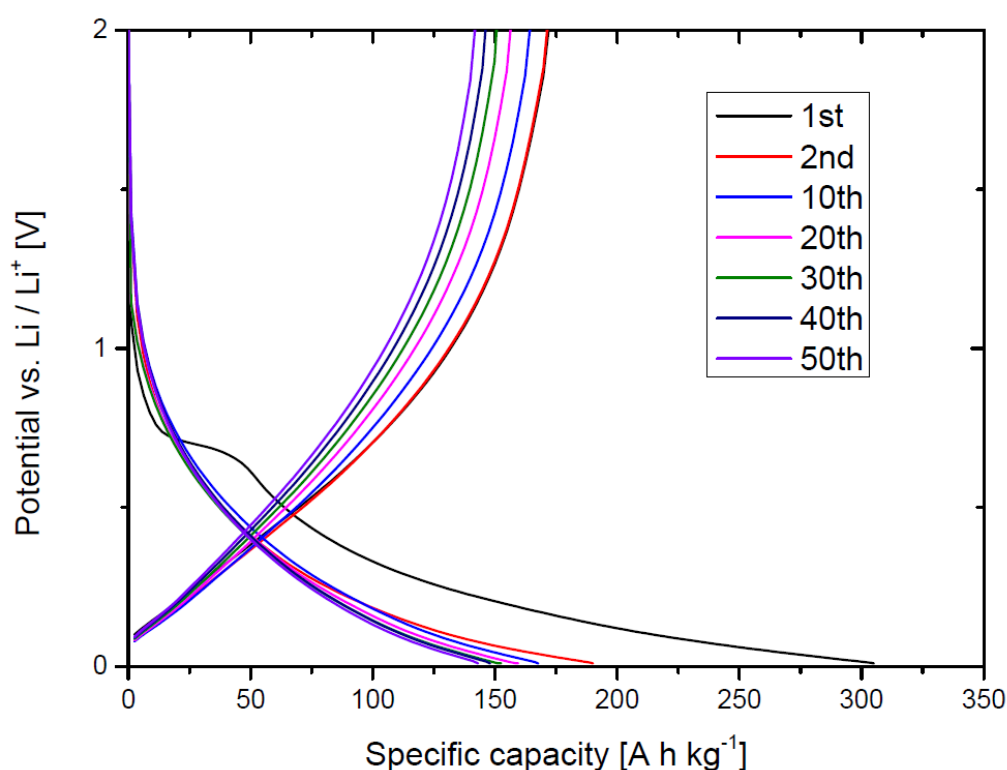
Fig. 3.44: Galvanostatic measurement of the reaction product of ball-milled Ca$_2$LiSi$_3$ and graphite (1:1 weight ratio); the first 50 cycles are shown.

The initial capacity of 300 mAh g^{-1} corresponds to only 31% of the maximum silicon contribution (962 mAh g^{-1}) and the initial Coulombic efficiency is only 57%. Then starting from 190 mAh g^{-1} for discharge and 175 mAh g^{-1} for charge, respectively, there is a slow decay of capacity and after 50 cycles, 145 mAh g^{-1} (48 % of initial discharge capacity) is retained. Coulombic efficiency increases with increasing cycle number up to a maximum of 99.2% at 50th cycle. Compared to pure Ca_2LiSi_3 (Fig. 3.39) and the one treated with graphite oxide (Fig. 3.42), this sample shows slightly better capacity retention at the cost of a lower overall capacity.

Ca_2LiSi exhibits some activity in the Li-ion battery experiments which can be traced back to its silicon content. Composite materials can be formed upon treatment with graphite oxide as well as with graphite leading to some improvements in cycling behavior. However, obtained capacity is too low for all tested variations of this compound which may rule out further exploration of these compounds.

3.5. Summary

The present chapter has proven that silicide Zintl phases can be employed as precursors for nanoisation of silicon by composite formation with graphite oxide (GO) and graphite. Dependent on the actual compound different oxygen exchange reactions occur with graphite oxide which lead mainly to metal oxide formations although partial oxidation of silicon cannot be completely ruled out especially if the initial capacity drops markedly. There was no indication found that the metal components would contribute to the Li-exchange behavior of corresponding electrodes, i.e. of Al and of Ca, respectively. This may be due to preferred reactions of aluminum with active carbon contents of the electrodes and to the extraordinary stability of CaO catching all oxygen contents form the GO composites.

The main result of this chapter is that formation of nano silicon of different kinds has practically no effect on the cycling stabilities of corresponding pristine and composite electrodes. This must be taken as a clear indication that just enveloping of nano silicon products is not sufficient for stable anode formation due to either mechanical deterioration of the composites in question and/or extensive SEI formation separating the initial composite components irreversibly. The low Coulombic efficiencies found in many cases may be interpreted in favor of the latter case.

Nanoisation of silicon and of other tetrel elements or their mixtures through Zintl phase precursors remains a valuable approach for fabrication nanotetrel composites, especially because the preparations of the Zintl phases are straightforward and comparatively cheap methods. However, the clue to successful composite formation has still to be found by other means than those tested in this chapter.

4. Employment of eutectic mixtures of silicon and transition metals for nano silicon / silicide composite formation

4.1. Introduction

In this chapter, various binary phase systems of silicon and a transition metal containing an eutectic on the Si rich side are examined. Melting and afterwards quenching of an eutectic mixture composed of silicon and transition metal leads to the formation of nano-sized Si crystals surrounded by transition metal silicide. It is believed that this transition metal silicide arrangement could act as a stable domain to accommodate volume changes of Si upon cycling in Li ion battery as well as facilitate the diffusion of Li ions to the silicon crystals. Furthermore, transition metal silicides are electronic conductors therefore facilitating electron flow. On the other hand, these silicides are electrochemically inactive in the Li ion battery, thus preventing lithiation and volume conversion of matrix material.

Eutectic mixtures of the following binary systems were explored: Ti/Si, Co/Si, Mn/Si and Cu/Si. Their synthesis as well as electrochemical performance is described in the following sections.

4.2. TiSi$_2$ / Si eutectic mixture

The eutectic mixture on the silicon rich side in this binary system is composed of 14% Ti and 86% Si. The phase diagram is depicted in Figure 4.1. Therefore, the following reaction can be formulated as:

$$14 \text{ Ti} + 86 \text{ Si} \rightarrow 14 \text{ TiSi}_2 + 58 \text{ Si} \tag{4.1}$$

Fig. 4.1: Binary phase diagram of titanium and silicon.[90]

Synthesis

A mixture of the elements in eutectic ratio is pressed to a pellet and melted in an arc welder furnace inside an argon filled glove box. The resulting metallic bulk is ground to a powder. The product XRD powder pattern is shown in Figure 4.2.
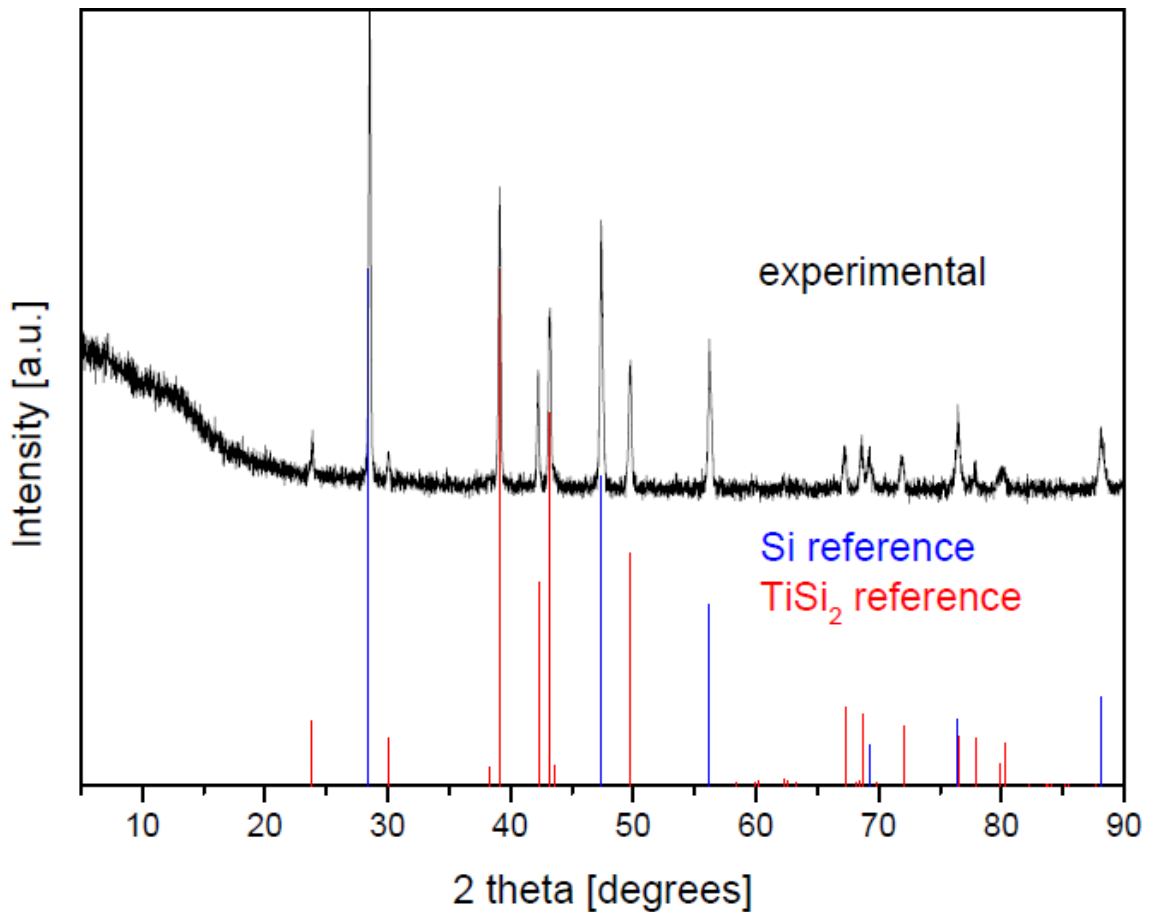
Fig. 4.2: Powder pattern of the eutectic (14 Ti + 86 Si) after treatment in arc welder furnace (black curve). The red and blue lines correspond to calculated patterns of $TiSi_2$ and of α-Si, respectively.

As expected the resulting powder is composed of $TiSi_2$ and Si. The size of silicon particles is estimated to roughly 40 nm using the Scherrer equation regarding the [220] diffraction peak. SEM micrographs of this mixture are shown in Figure 4.3.
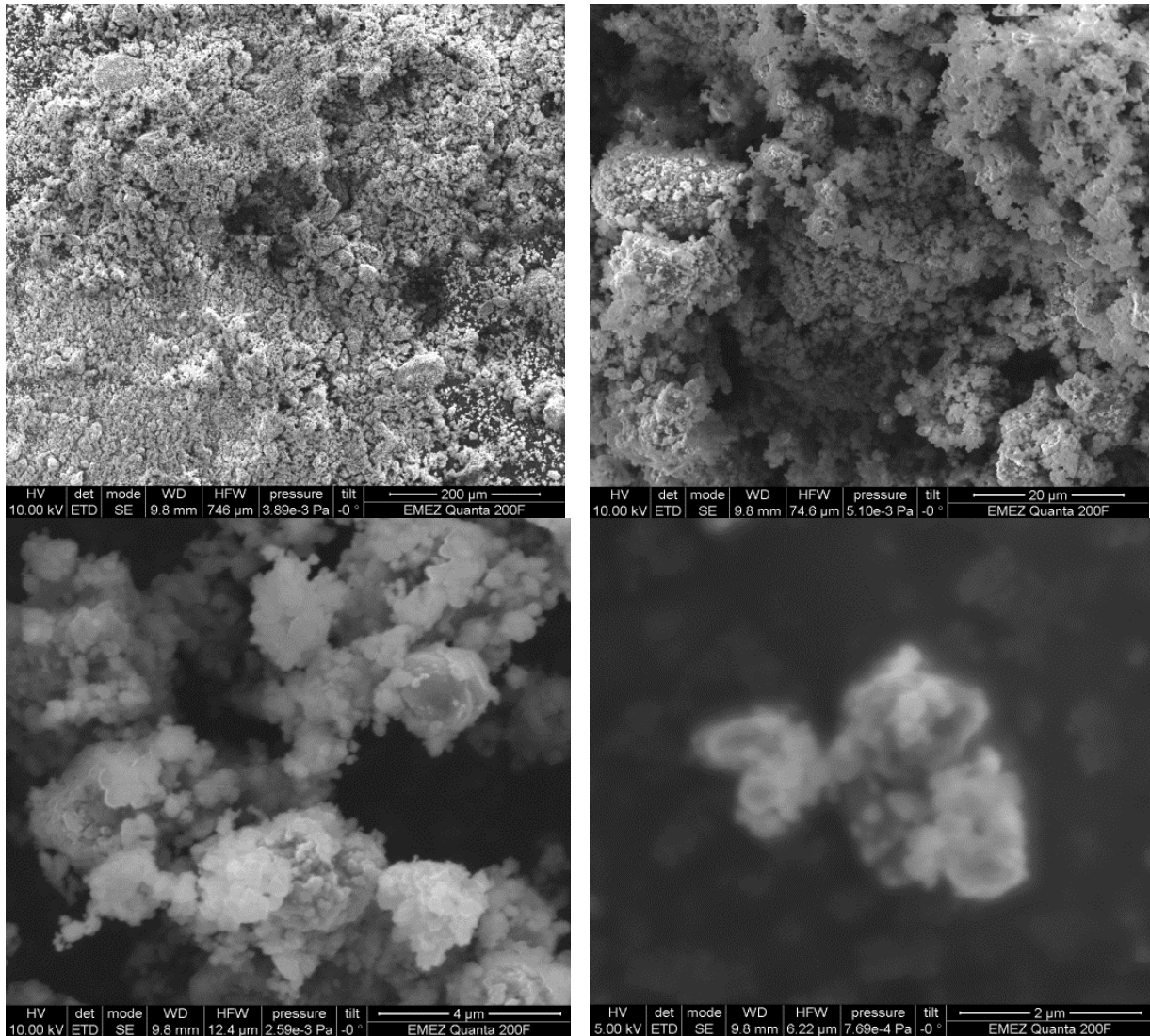
Fig. 4.3: SEM analysis of the eutectic (14 Ti + 0.86 Si) after treatment in arc welder furnace.

The sample is a mixture of agglomerated particles at submicron size. TEM micrographs of this sample are shown in Figure 4.4.
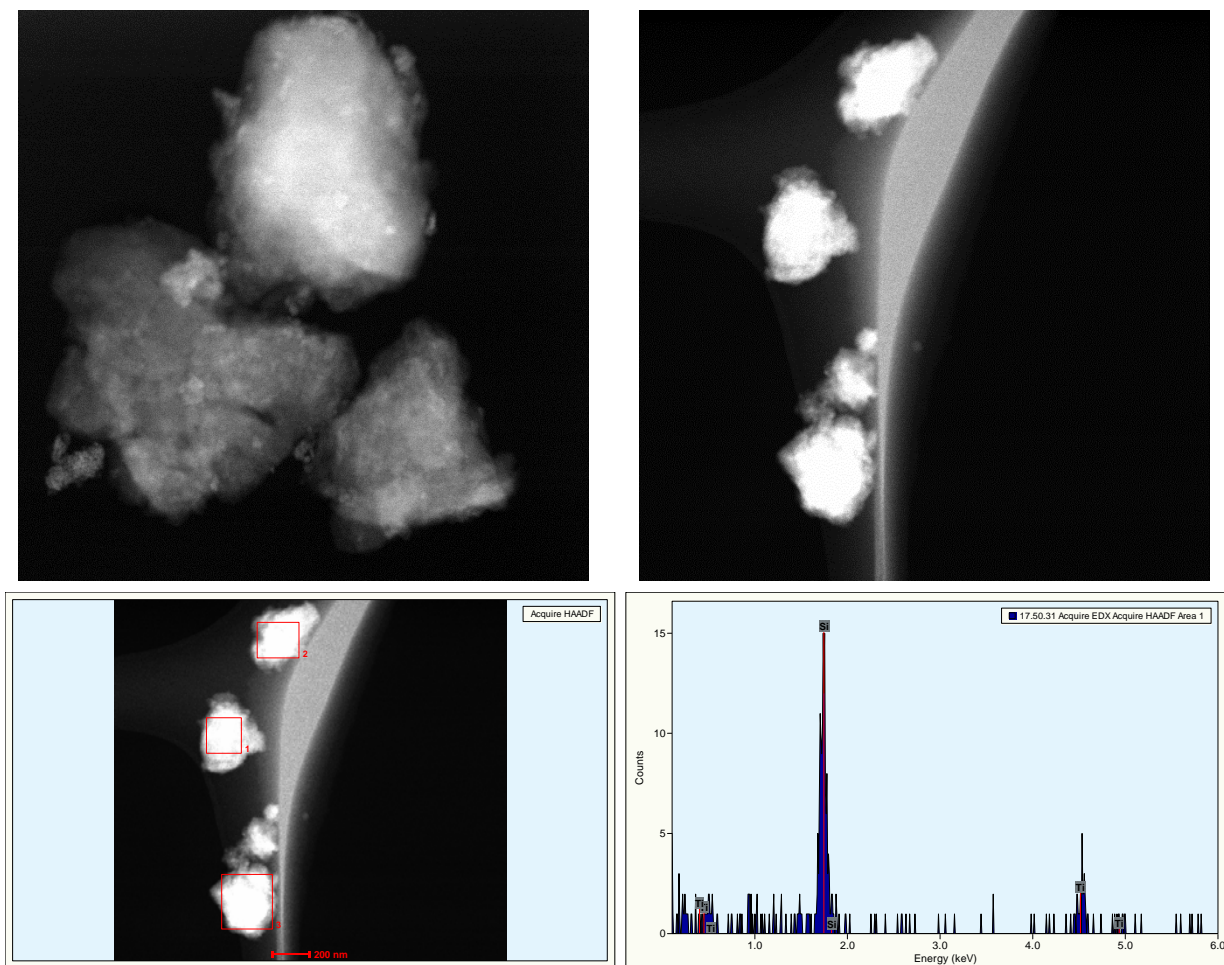
Fig. 4.4: TEM analysis of the eutectic (14 Ti + 86 Si) after treatment in arc welder furnace, where EDXS analysis is shown on the bottom.

Particles of about 200 nm diameter were examined by EDXS analysis. At this size domain, the sample still appears to be homogeneous, so that Si and $TiSi_2$ particles cannot be distinguished.

Additionally, the bulk eutectic mixture of $TiSi_2$ and Si was treated for 150 min in 2 M NaOH. $TiSi_2$ is inert and not attacked, whereas Si is partially dissolved and etched away from the surface of the heterogeneous particles in order to examine the structure of the transition metal silicide matrix. SEM micrographs of the surface of particles after this treatment are shown in Figure 4.5.
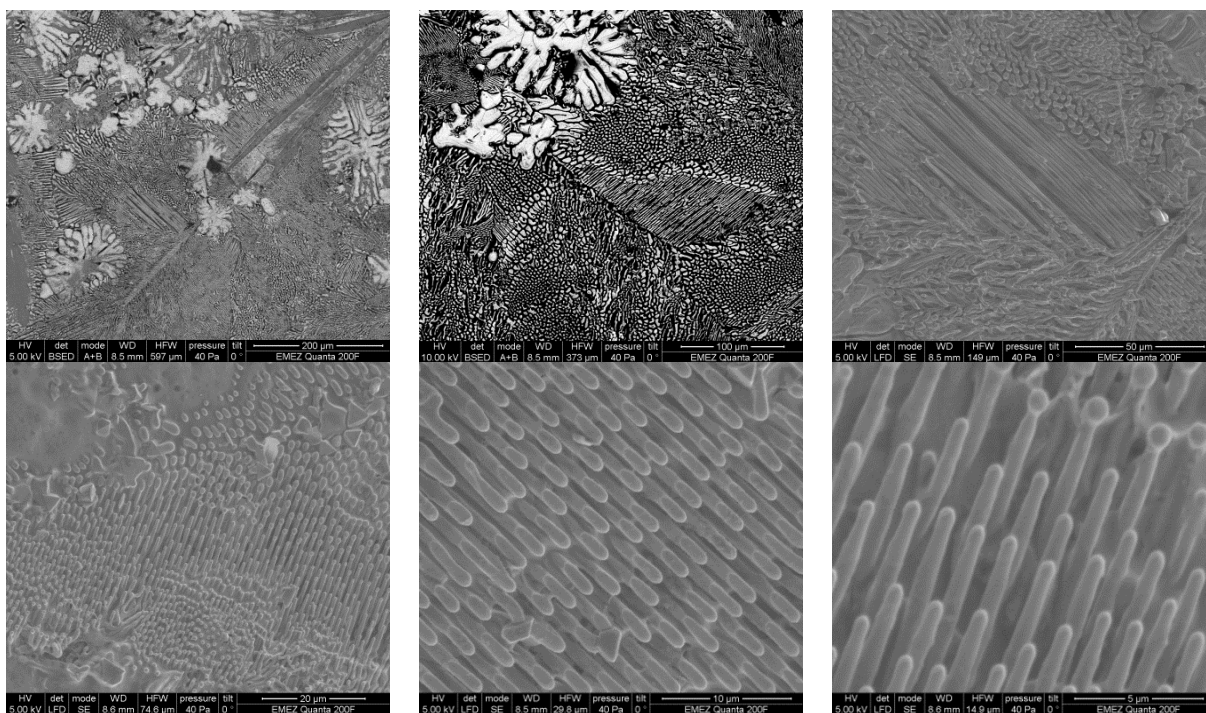
Fig. 4.5: SEM micrographs of the surface of $TiSi_2$ and Si eutectic mixture after etching with 2 M NaOH for 150 min.

The surface of the examined particles is etched and shows domains of nanorods of $TiSi_2$ with different orientations indicating to a submicroscopic mixture of Si and $TiSi_2$, whereas silicon and titanium silicide domains envelope each other mutually. The eutectic segregation leads to fascinating nano structures which should be explored further.[91-92]

Electrochemical performance

The sample was ball milled to a fine powder prior to electrochemical testing and electrodes were prepared in air. Carbon Black (11 wt. %) and graphite (4 wt. %) were added as conductive additives and PVDF used as a binder (7 wt. %). 1 M $LiPF_6$ in ethylenecarbonate / dimethylcarbonate (1:1) was used as electrolyte. The sample was cycled between 10 mV and 3.0 V vs. Li/Li^+ at a rate of 20 mA g^{-1}. The initial step was discharge (lithiation) and values for specific capacity refer to the composite.
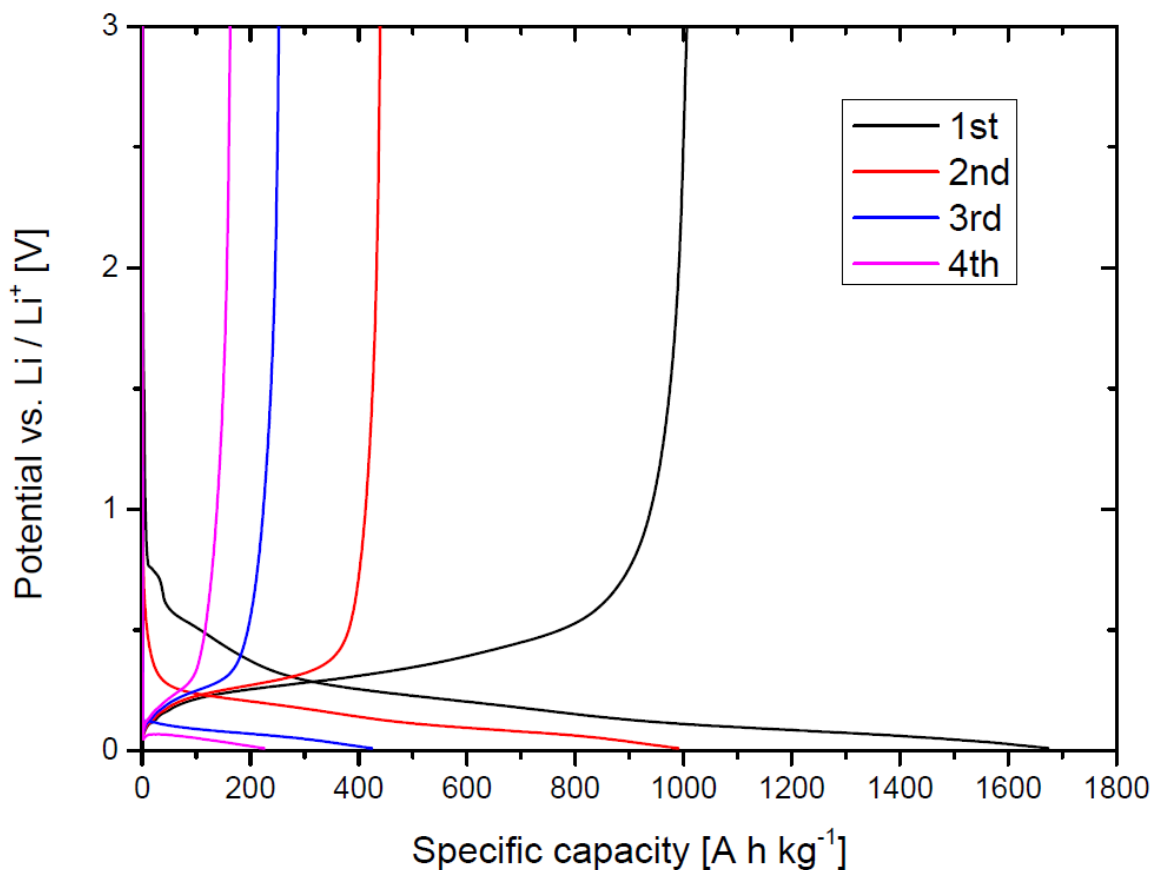
Fig. 4.6: Galvanostatic measurement of the eutectic (14 Ti + 86 Si) after treatment in arc welder furnace, whereas the first 4 cycles are shown.

There is a high initial capacity of 1650 mAh g^{-1} obtained during first discharge which is 78% of the maximum expectation capacity (2116 mAh g^{-1}); it is accompanied by a low initial Coulombic efficiency of 61%. Rapid decay of capacity is observed during subsequent cycles and after the 4th cycle the battery is dead leading to the conclusion that the as formed TiSi$_2$ is not able to stabilize the cycling behavior of the nano silicon.

4.3. CoSi₂ / Si eutectic mixture

There is another eutectic mixture on the silicon rich side of the Co / Si system which is composed of 20% Co and 80% Si. The phase diagram is depicted in Figure 4.7. Starting from the pure elements, the following reaction will happen under thermodynamic control:

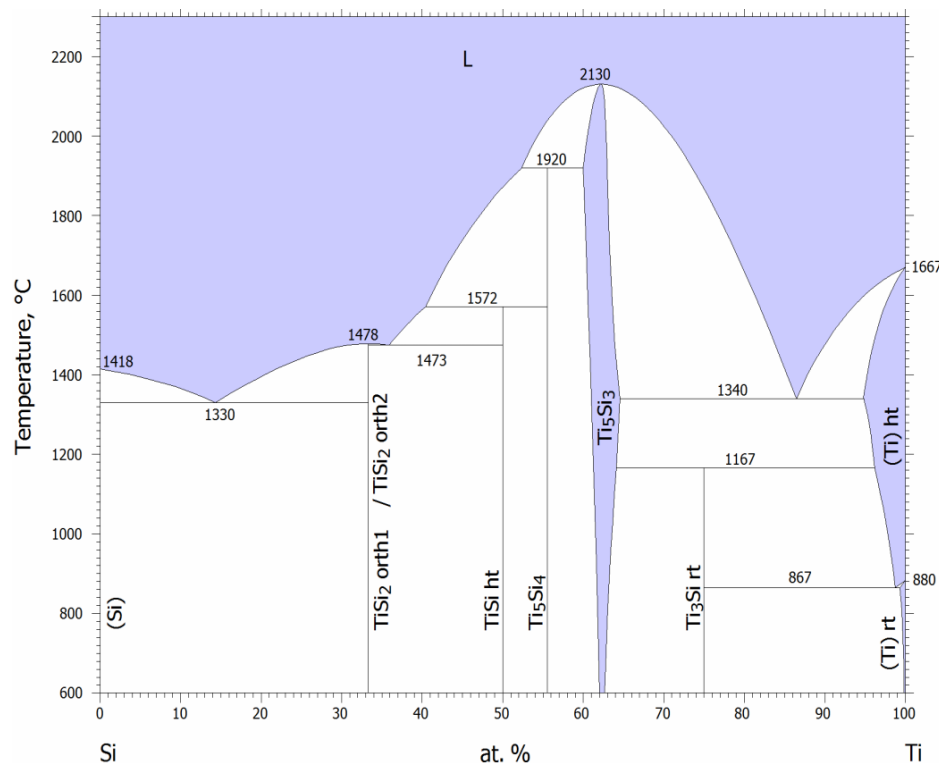$$Co + 4\,Si \rightarrow CoSi_2 + 2\,Si \tag{4.2}$$
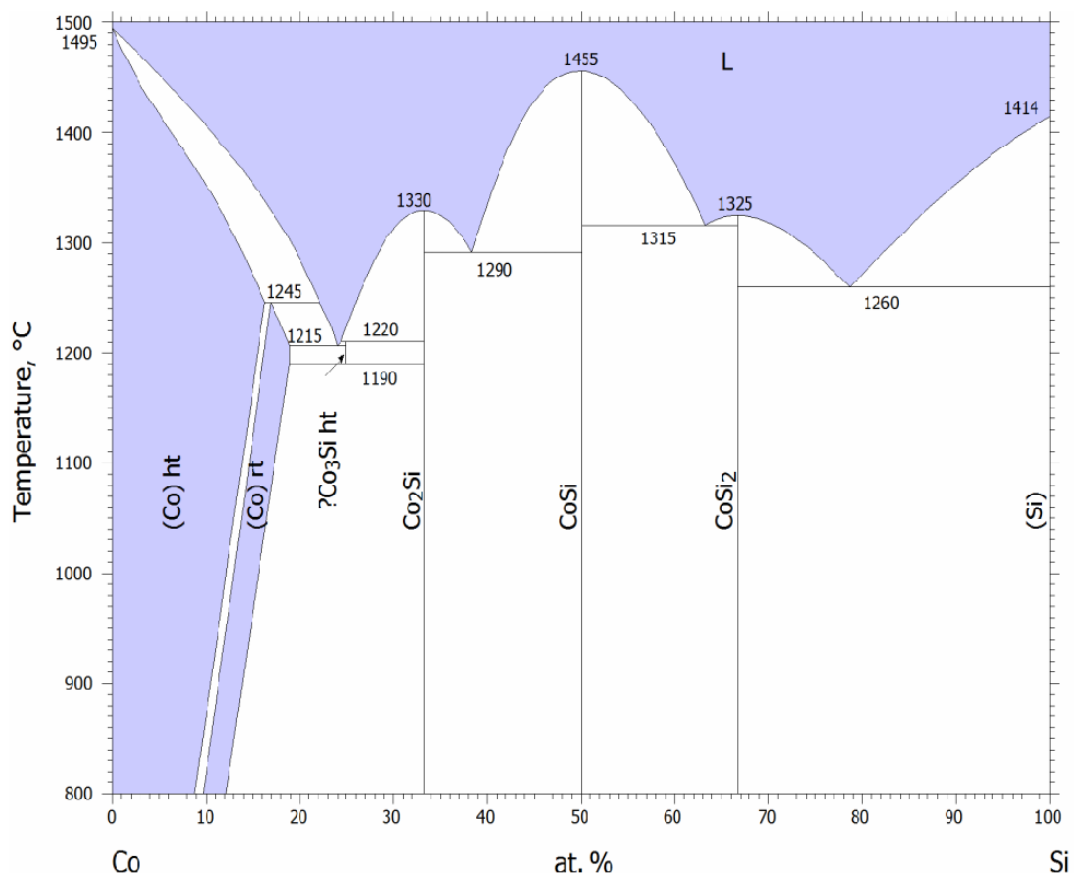
*Fig. 4.7:* Binary phase diagram of cobalt and silicon.[93]

Synthesis

A mixture of the elements in eutectic ratio is pressed to a pellet and melted in an arc welder furnace inside an argon filled glove box. The resulting metallic bulk is ground to a powder. The obtained XRD powder pattern is shown in Figure 4.8.
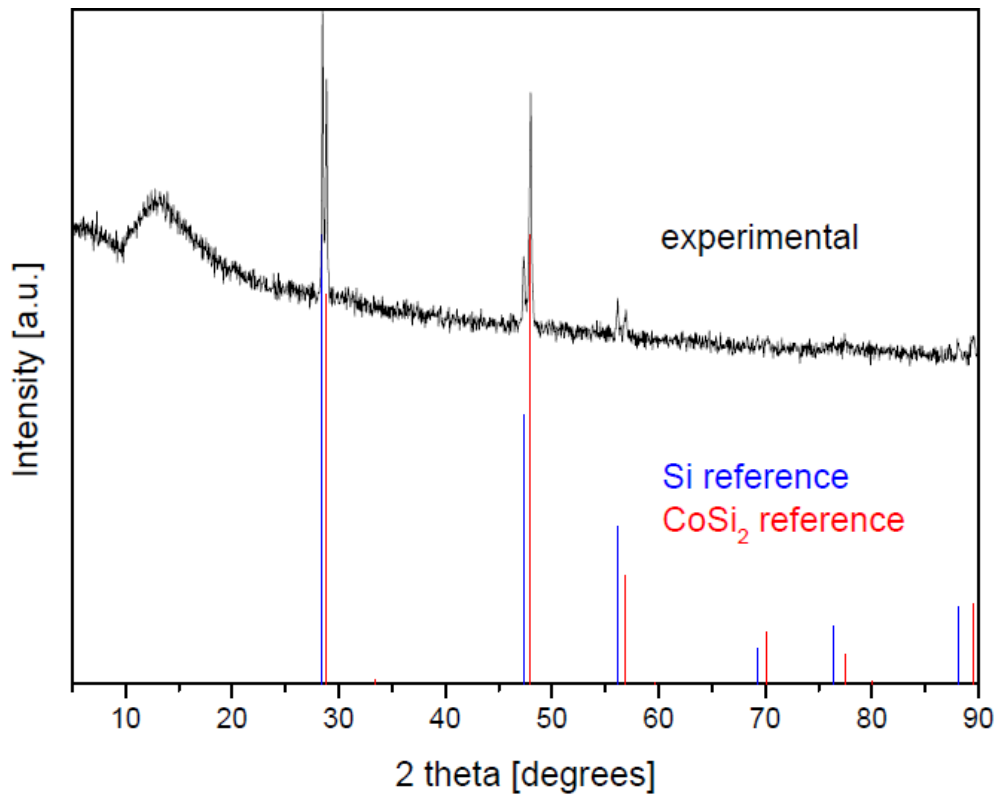

Fig. 4.8: Powder pattern of the eutectic (20 Co + 80 Si) after treatment in an arc welder furnace (black curve). The red and blue lines correspond to calculated patterns of $CoSi_2$ and of α-Si, respectively.

The resulting powder is composed of $CoSi_2$ and Si as expected. The size of silicon particles is estimated to roughly 50 nm using the Scherrer equation regarding the [220] diffraction peak.

Electrochemical performance

The sample was ball milled to a fine powder prior to electrochemical testing and electrodes were prepared in air. Carbon Black (13 wt. %) and graphite (3 wt. %) were added as conductive additives and PVDF used as a binder (14 wt. %). 1 M $LiPF_6$ in ethylenecarbonate / dimethylcarbonate (1:1) was used as electrolyte. The sample was cycled between 10 mV and 3.0 V vs. Li/Li^+ at a rate of 20 mA g^{-1}. The initial step was discharge (lithiation) and values for specific capacity refer to the composite.
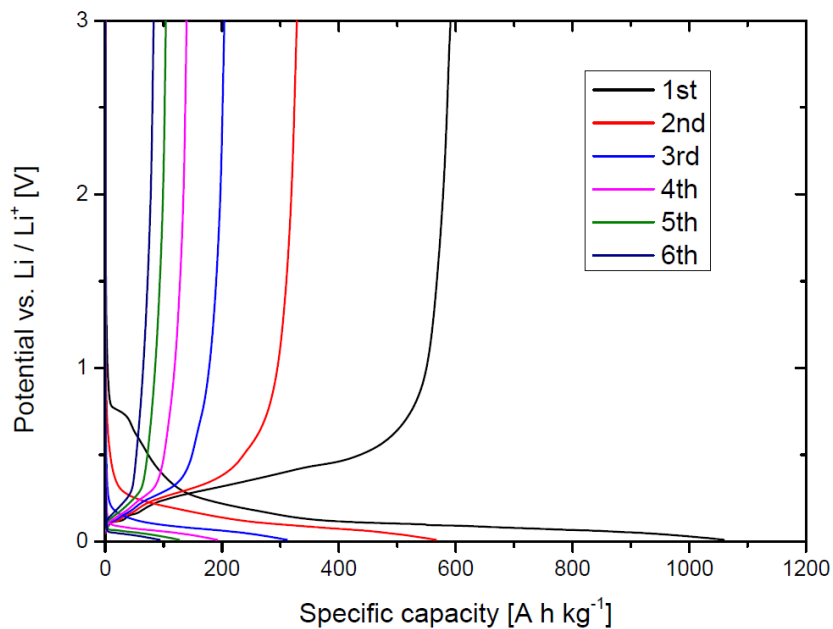
Fig. 4.9: Galvanostatic measurement of the eutectic (20 Co + 80 Si) after treatment in an arc welder furnace; the first 6 cycles are shown.

There is a high initial capacity of 1050 mA h kg^{-1} during first discharge which is 80% of the maximum expectation capacity (1315 mAh g^{-1}); it is accompanied by a low initial Coulombic efficiency of 56%. Rapid decay of the capacity is observed during subsequent cycles and after the 6th cycle the battery is dead. Seemingly, the nano composite of silicon and $CoSi_2$ is not able to stabilize the cycling behavior of Si.

4.4. $Mn_{11}Si_{19}$ / Si eutectic mixture

The eutectic mixture on the silicon rich side in this binary system is composed of 33 Mn and 67 Si as shown in the phase diagram depicted in Figure 4.10 below. Starting from the elements, the following reaction will take place under thermodynamic control:

11 Mn + 22 Si → $Mn_{11}Si_{19}$ + 3 Si   (4.3)
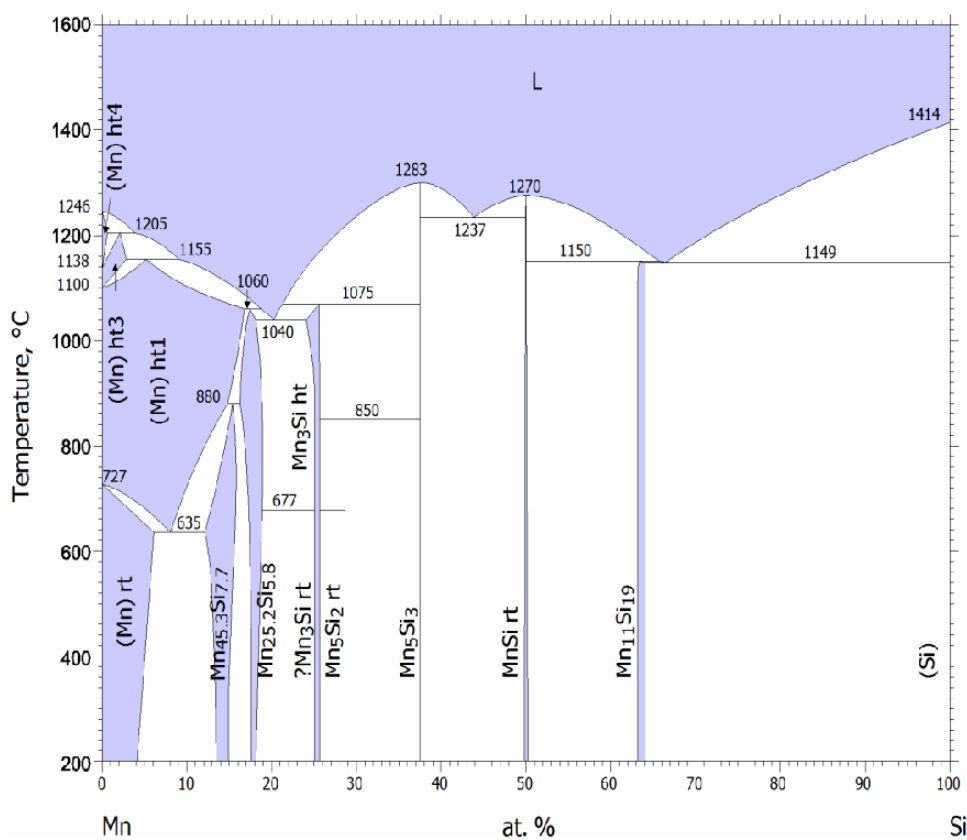
Fig. 4.10: Binary phase diagram of manganese and silicon.[94]

Synthesis

A mixture of the elements in eutectic ratio is pressed to a pellet and melted in an arc welder furnace inside an argon filled glove box. The resulting metallic bulk is ground to a powder. The obtained XRD powder pattern is shown in Figure 4.11.
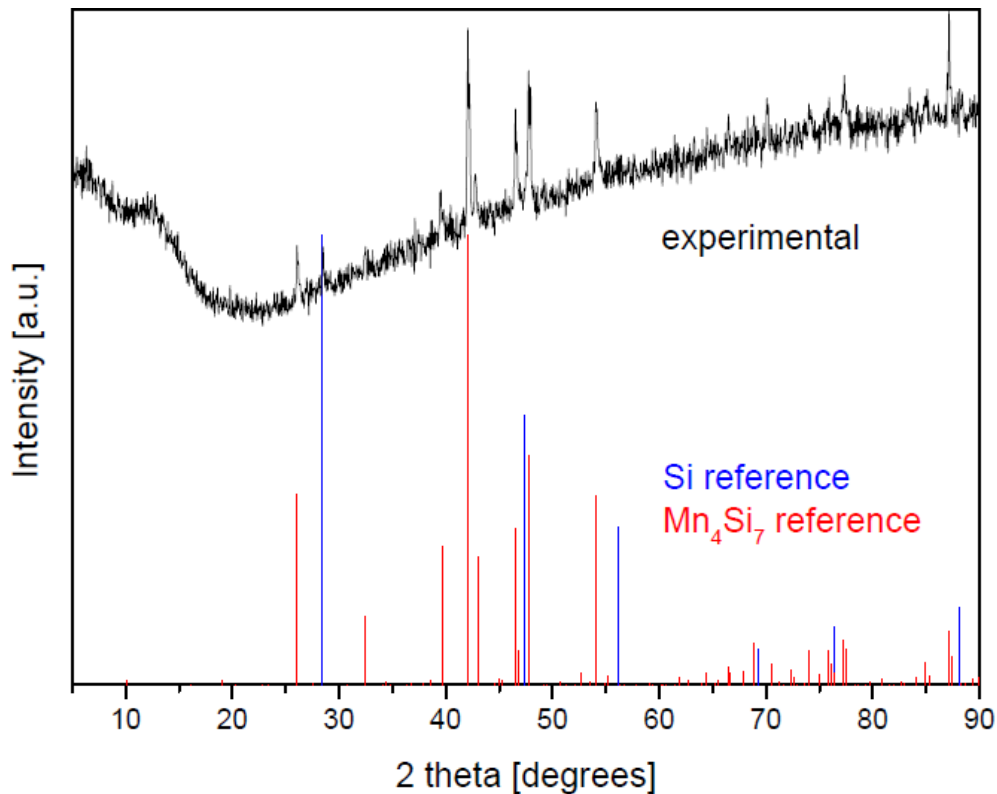
Fig. 4.11: XRD powder pattern of the eutectic (33 Mn + 67 Si) after treatment in arc welder furnace (black curve). The red and blue lines correspond to calculated patterns of Mn_4Si_7 and of α-Si, respectively.

The sample is highly amorphous and contains Mn_4Si_7 which is closely neighboring to $Mn_{11}Si_{19}$ and silicon. The size of silicon particles is estimated to roughly 70 nm using the Scherrer equation regarding the [111] diffraction peak. The nanoscopic nature of such eutectic products was nicely exemplified by She et al.[95]

Electrochemical performance

The sample was ball milled to a fine powder prior to electrochemical testing and electrodes were prepared in air. Carbon Black (12 wt. %) and graphite (4 wt. %) were added as conductive additives and PVDF used as a binder (12 wt. %). 1 M $LiPF_6$ in ethylenecarbonate / dimethylcarbonate (1:1) was used as electrolyte. The sample was cycled between 10 mV and 3.0 V vs. Li/Li$^+$ at a rate

of 20 mA g^{-1}. The initial step was discharge (lithiation) and values for specific capacity refer to the composite.
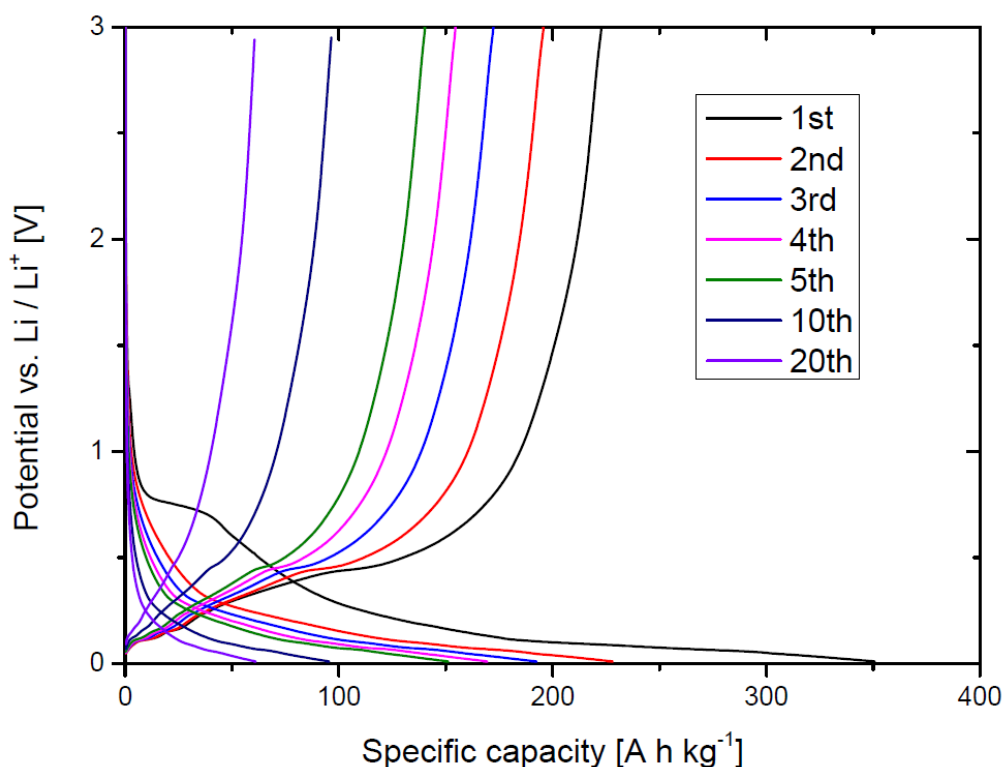
Fig. 4.12: Galvanostatic measurement of the eutectic (33 Mn + 67 Si) after treatment in arc welder furnace; the first 20 cycles are shown.

There is an initial capacity of 350 mAh g^{-1} during first discharge which is 127% of the maximum expectation capacity (276 mAh g^{-1}); it is accompanied by a low initial Coulombic efficiency of just 63%. The obtained initial capacity with a value higher than the theoretical one is believed to be caused by a weighting error during electrode preparation. During subsequent cycles, there is a continuous loss of capacity, such that 95 mAh g^{-1} is retained after the 10th cycle (27% of initial capacity). Compared to the eutectic mixtures containing TiSi$_2$ and CoSi$_2$ (Fig. 4.6 and 4.9), significantly lower capacities are obtained. However, capacity retention is slightly better but still not sufficient for a practical application.

4.5. $Cu_{19}Si_6$ / Si eutectic mixture

The eutectic mixture on the silicon rich side in this binary system is composed of 70% Cu and 30% Si as depicted in the phase diagram in Figure 4.13 below. In order to enter the eutectic, the following reaction was performed:

$$21\ Cu + 9\ Si \rightarrow Cu_{19}Si_6 + 3\ Si \tag{4.4}$$
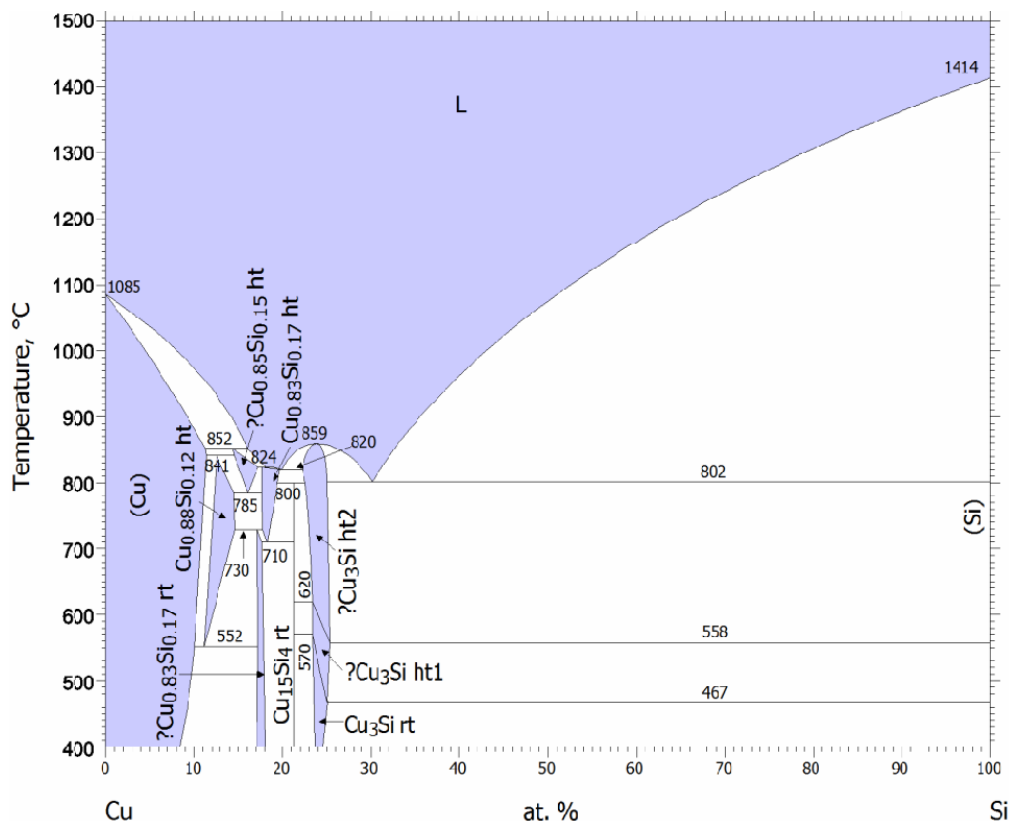
Fig. 4.13: Binary phase diagram of copper and silicon.[94]

Synthesis

The eutectic mixture of the elements is pressed to a pellet and sealed in a quartz tube under vacuum. The sample is treated at 1000 °C for 3 d followed by quenching in cold water. The reaction mixture is ground to a grey powder in air. XRD analysis is shown in Figure 4.14.
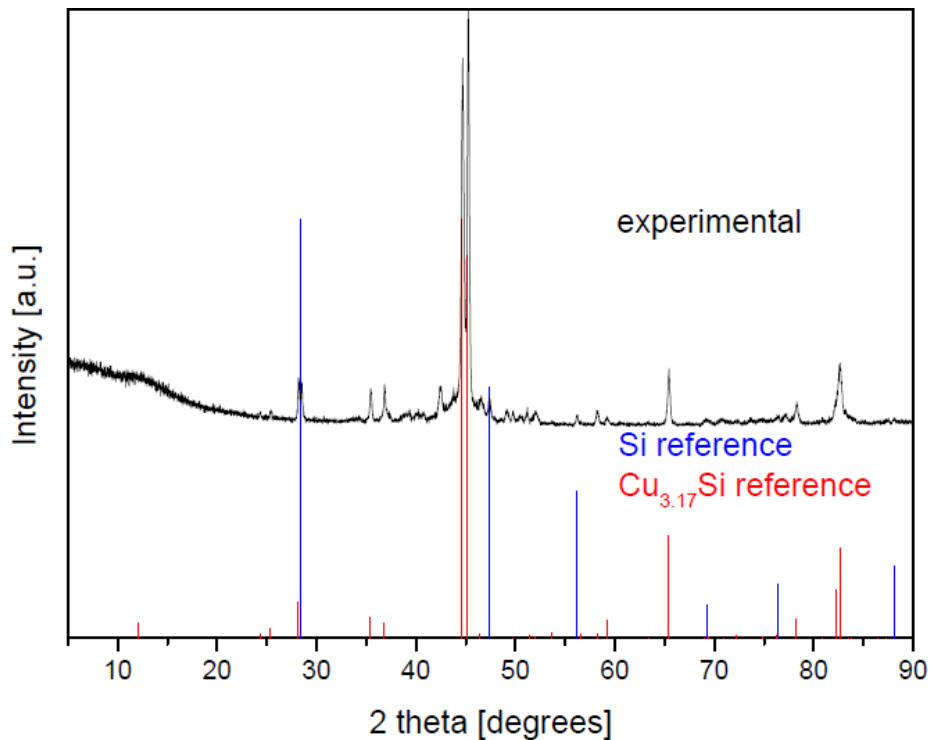
Fig. 4.14: Powder pattern of the eutectic (70 Cu + 30 Si), treated at 1000 °C for 3 d under vacuum (black curve). The red and blue lines correspond to calculated patterns of $Cu_{3.17}Si$ and of α-Si, respectively.

The sample is composed of $Cu_{19}Si_6$ ($Cu_{3.17}Si$) and Si, with only a smaller fraction of silicon regarding intensity of diffraction peaks. The size of silicon particles is estimated to roughly 50 nm using the Scherrer equation regarding the [111] diffraction peak. The morphology of this eutectic was described by Vetter et al.: Si fibers are embedded in a $Cu_{19}Si_6$ matrix phase, where eutectic dendrite growth leads to the formation of branched Si crystallites as found in Al-Si alloys.[96-97]

Electrochemical performance

Electrodes were prepared in air, whereas Carbon Black (10 wt. %) and graphite (4 wt. %) were added as conductive additives. PVDF was used as a binder (9 wt. %) and 1 M $LiPF_6$ in ethylenecarbonate / dimethylcarbonate (1:1) used as

165

electrolyte. The sample was cycled between 10 mV and 3.0 V vs. Li/Li$^+$ with a rate of 20 mA g^{-1}. The initial step was discharge (lithiation) and values for specific capacity refer to the composite.
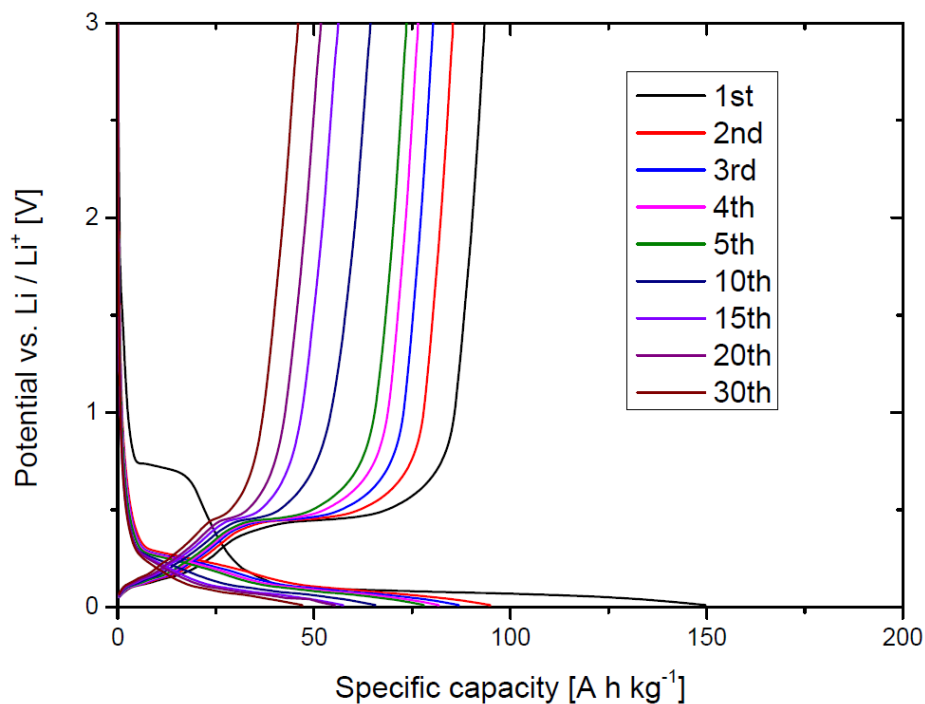
Fig. 4.15: Galvanostatic measurement of the eutectic (70 Cu + 30 Si) after treatment in arc welder furnace; the first 20 cycles are shown.

A low initial capacity of 150 mAh g^{-1} is obtained during first discharge which is 45% of the maximum expectation capacity (330 mAh g^{-1}); it is accompanied by an initial Coulombic efficiency of 62%. There is a continuous loss of capacity during subsequent cycles and after 10th cycle 65 mAh g^{-1} is retained (43% of initial capacity). Obtained capacities are very low as expected due to the low amount of Si in the eutectic mixture. However, potential profiles clearly identify silicon as the electrochemically active species and capacity retention is the best among tested eutectic mixtures in this chapter which is in favor of further more detailed investigations on copper composite anodes with nano silicon.

4.6. Conclusion

It is well known that eutectic systems of metals and silicon can be used to fabricate nano particular two-phase products, i.e metal silicide plus nano silicon. This strategy was employed in this section for the four binary systems Ti/Si, Mn/Si, Co/Si and Cu/Si. The syntheses yield the expected products which were then tested electrochemically. In all cases anodic behavior was found which can be traced back to the elemental silicon parts of the samples. Seemingly, all of the corresponding transition metal silicides are inert with respect to the redox reactions in the battery electrodes. They may be considered as inert electronic conductors which may come into action either as matrix or as coating materials, in some future. All silicon parts are redox-active in the battery without further initial activation, however at quite different capacitive efficiencies. In general, all of the investigated forms of composites cannot stabilize the active silicon parts, thus rapid capacity decays have been recorded. The best capacity retentions have been found for the Mn and Cu systems at comparatively low total capacities, though. This may be taken as an indication for surface stabilization due to larger silicon-to-silicide interphase contacts (due to the low Si fraction).Further attempts in this direction may focus on enhancing the nanoscopic nature of the silicide components, i.e. increasing their surface areas. On the whole, one must admit that such silicide-silicon composites may not bring about a general solution of the silicon stability problem in the Li-ion battery.

5. LiCu$_2$Si for formation of a Cu$_{19}$Si$_6$ based conductive matrix for electrode materials

5.1. Introduction

LiCu$_2$Si crystallizes in the cubic face centered space group *Fm-3m* with lattice parameter a of 5.77(6) Å. [98] The crystal structure of LiCu$_2$Si is shown in Figure 5.1 below; it comprises a complete filling of a basic fcc array, here for example of silicon atoms by filling all octahedral and all tetrahedral holes by cations. In the center of the cell there is a metal cluster formed by a cube of copper atoms and centered by a lithium site. The compound does not fulfil the Zintl-Klemm rules and must be understood as an intermetallic with good electronic conductivity. This will not change on delithiation because binary coppersilicides happen to be excellent electronic conductors.[99]
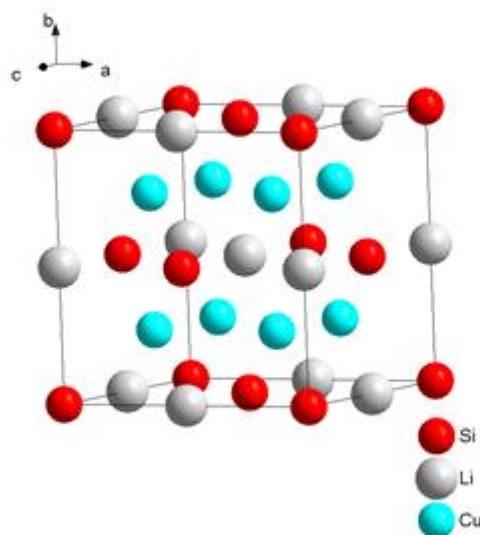
Fig. 5.1: Crystal structure of LiCu$_2$Si (Li – grey, Cu – cyan, Si – red).

LiCu$_2$Si belongs to a special kind of intermetallic compounds which have been called Heusler phases. These are phases of the general composition X$_2$YZ, where X and Y are transition metals and Z is an element of the main groups III

to V (e.g. for $LiCu_2Si$, X=Cu, Y=Li and Z=Si). Heusler phases are known for long especially for being ferromagnetic, even though the individual elements are non-magnetic. Recently, Heusler phases have become a focus of solid state physics in terms of the so-called topological semiconductors.[100]

We did investigate the delithiation product of $LiCu_2Si$ in order to test the developed binary silicide for its inert conducting matrix properties. It is difficult to judge how dense the active material could be packed in an electrode composite but surely denser than in a cubic close packaging with 74% volume filling, however from percolation theory it is known that at least 16% conductive matrix material in spherical form are sufficient for inducing full electronic percolation. It should also be noted that there must be some free space for the electrolyte liquid and the Li^+ ion transport. There are several requirements for a conductive matrix: First of all, it has to be a good electronic conductor and should be electrochemically inert so only the active material will be lithiated and delithiated. Additionally, it should have low volume occupancy like for example a porous metallic foam. $Cu_{19}Si_6$ ($Cu_{3.17}Si$) seems to be a perfect candidate since it is a transition metal silicide with a low resistivity, high thermal stability and good contact properties to copper metal, i.e. the present current collector at the anodic side. [101-104]

Although there is a number of other ternary copper silicides of lithium, $LiCu_2Si$ is the one closest to the atomic composition of the delithiation product and thus used as a precursor for formation of a $Cu_{19}Si_6$ based matrix: A mixture of $LiCu_2Si$ and another lithiated electrode material (for example $LiFePO_4$) are charged in a Li ion battery. During this delithiation process, Li should be extracted from $LiCu_2Si$, in-situ forming a matrix composed of connected amorphous $Cu_{19}Si_6$ particles surrounding the $LiFePO_4$ particles. This process is not reversible. During following discharge (lithiation), $Cu_{19}Si_6$ cannot be

transformed back to a lithiumcoppersilicide compound since it is electrochemically inactive under these reaction conditions.

Synthesis of LiCu₂Si

A stoichiometric amount of the elements is sealed in a Nb ampoule under argon, then treated at 650 °C for 24 h. The resulting reaction mixture is pressed to a pellet, sealed in a Nb ampoule under argon followed by an additional heat treatment at 650 °C for 24 h. The reaction product is ground to a purple powder. The obtained XRD powder pattern is shown in Figure 5.2.
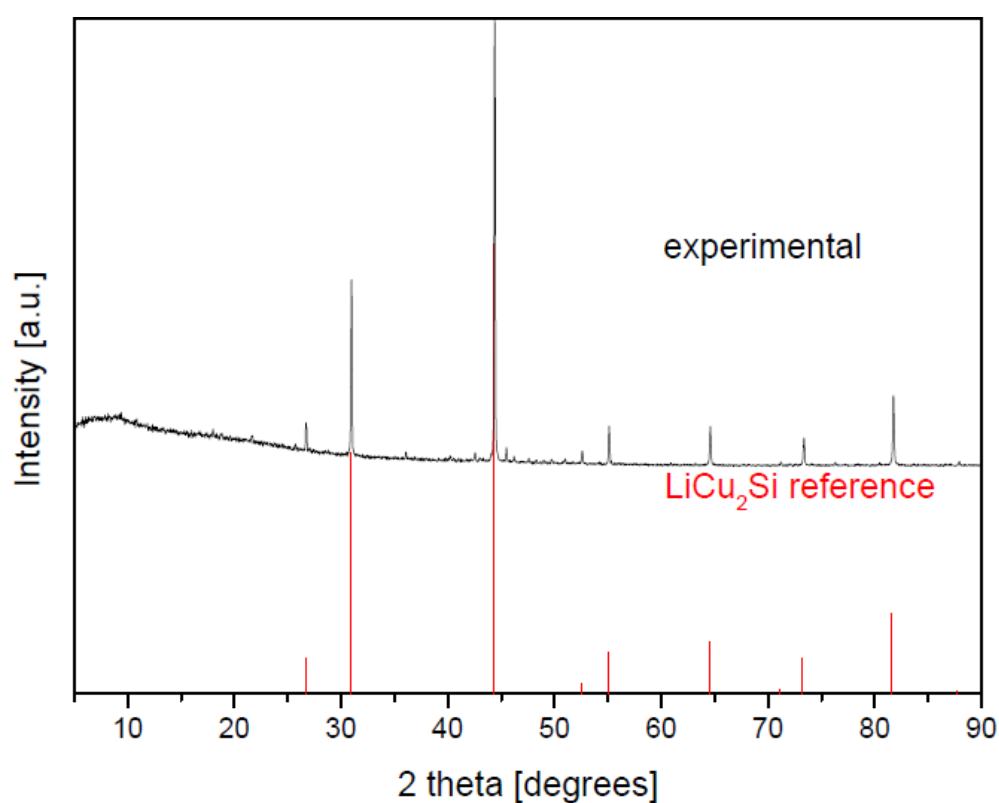
Fig.5.2: XRD powder pattern of LiCu₂Si (black curve). The sample is very pure.

Electrochemical performance

Before electrochemical testing, LiCu₂Si was ball milled in argon to a fine purple powder. The electrode was prepared in a glove box under Ar atmosphere, where Super P (12 wt. %) and graphite (4 wt. %) were added as conductive

additives and PVDF was used as a binder (8 wt. %). 1 M LiPF$_6$ in ethylenecarbonate / dimethylcarbonate (1:1) was used as electrolyte. The sample was cycled between 10 mV and 4.0 V vs Li/Li$^+$ with a rate of 20 mA g^{-1}. The initial step was charging (delithiation).
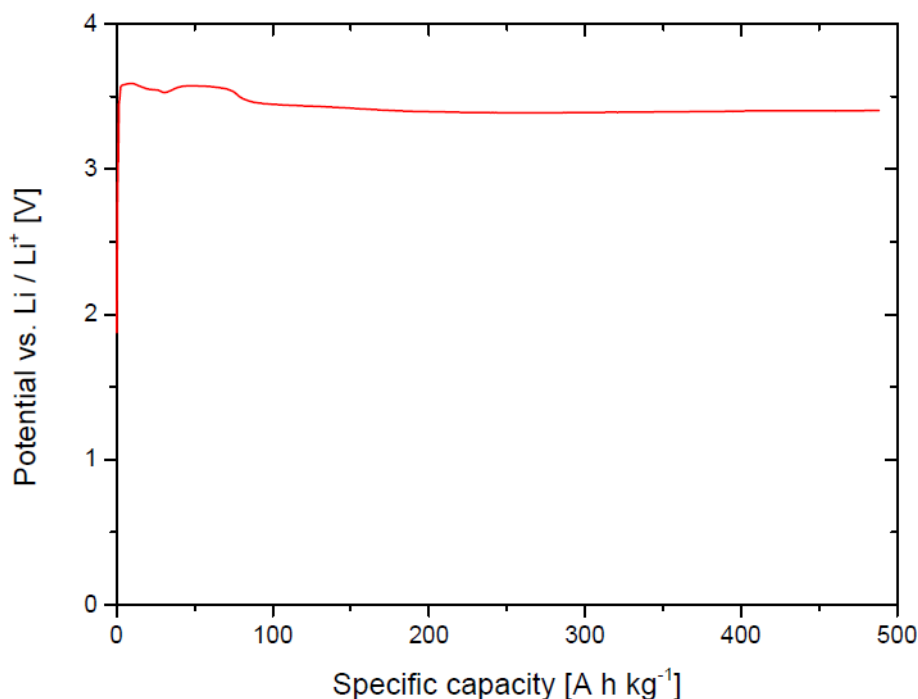
Fig. 5.3: Galvanostatic measurement of LiCu$_2$Si. Only the first charge (delithiation) is shown since it led to an error in the battery. This is just an example of many batteries tested with LiCu$_2$Si all of them giving rise to the same result.

When potential reaches critical value of 3.6 V, there is an ongoing decomposition reaction destroying and/or modifying the electrode. It is believed that electrolyte decomposition with LiCu$_2$Si occurs at 3.6 V as indicated by a droping potential after this point. This finding is manifested by a cyclic voltammetry measurement shown in Figure 5.4.
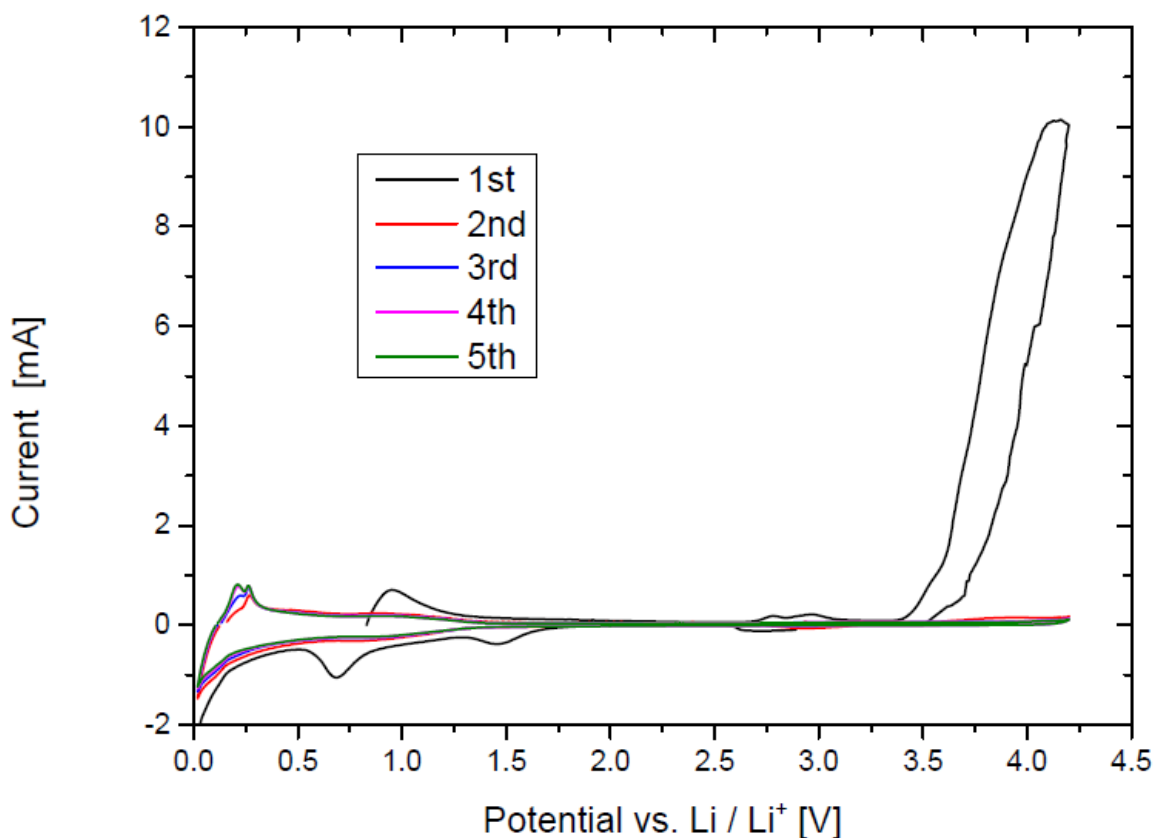
Fig. 5.4: Cyclic voltammetry measurement of ball milled $LiCu_2Si$, where only the first 5 cycles are shown. The electrode was prepared in a glove box under Ar atmosphere. Super P (18 wt. %) and graphite (6 wt. %) were added as conductive additive and PVDF was used as a binder (8 wt. %). 1 M $LiPF_6$ in ethylenecarbonate / dimethylcarbonate (1:1) was used as electrolyte. The sample was cycled between 20 mV and 4.2 V vs Li/Li^+ with a rate of 0.1 mV s^{-1}. The initial step was charging (delithiation).

There is a huge oxidation peak appearing at 3.5 V during first charge which is no longer present in the future cycles. This peak is addressed to electrolyte decomposition with $LiCu_2Si$. Additionally, there are two reduction peaks visible during first discharge at 1.5 V and 0.7 V (SEI-formation), which are not anymore present in consecutive cycles.

Post mortem analysis

Ball-milled $LiCu_2Si$ was examined after 10 cycles in a Li ion battery:

The electrode was prepared in a glove box under Ar atmosphere, where PVDF was used as a binder (8 wt. %). 1 M $LiPF_6$ in ethylenecarbonate / dimethylcarbonate (1:1) as electrolyte. The sample was cycled between 10 mV and 4.0 V vs. Li/Li^+ at a rate of 20 mA g^{-1}. The sample was started from charge (delithiation) and then cycled for 10 cycles. The battery cell was opened in air and the electrode material was washed with 20 ml of THF to remove the remaining electrolyte. Figure 5.5 shows the obtained XRD powder pattern of the black material.
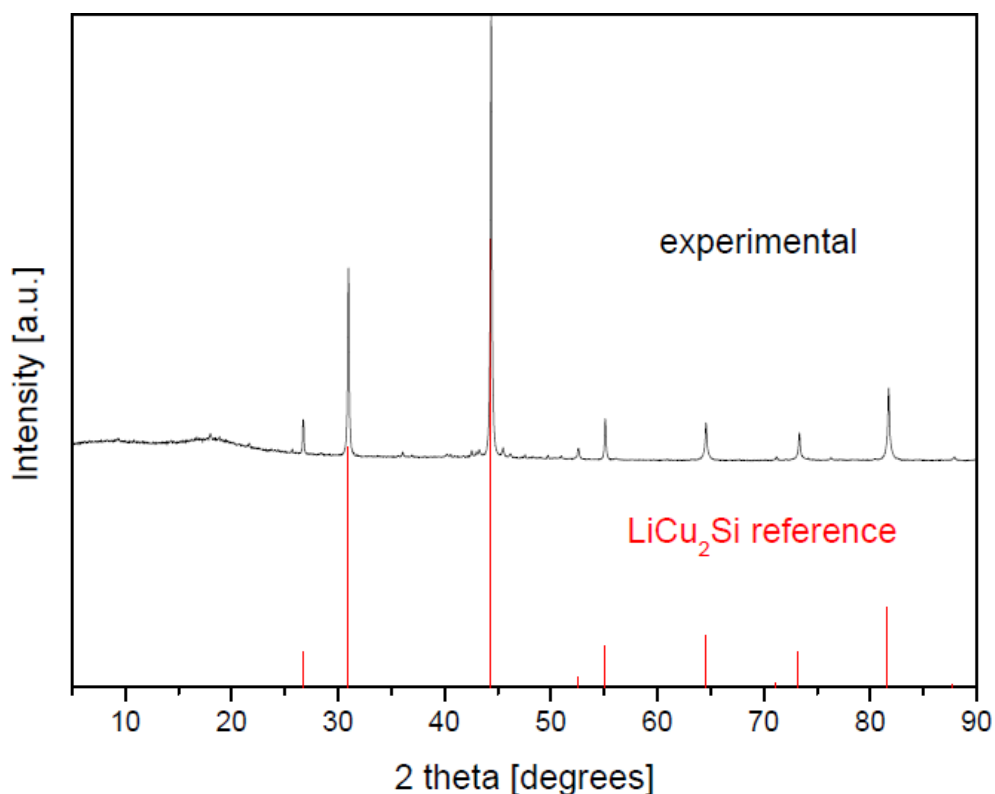
Fig. 5.5: XRD powder pattern of $LiCu_2Si$ after 10 cycles in a Li ion battery (black curve).

After 10 full charge / discharge cycles in the battery, only $LiCu_2Si$ and no $Cu_{19}Si_6$ are observable in the powder pattern. $LiCu_2Si$ is still highly crystalline and the background (caused by eventually formed amorphous products) is very low. Successful extraction of Li from $LiCu_2Si$ leads to the formation of $Cu_{19}Si_6$, this process is not reversible since $Cu_{19}Si_6$ is not electrochemically active in the Li ion battery. However, formation of crystalline $Cu_{19}Si_6$ was not observed.

It is quite unlikely that it is not possible to electrochemically remove Li from $LiCu_2Si$, leading to the following theory: Lithium diffuses from the surface of $LiCu_2Si$ and $Cu_{19}Si_6$ is formed at the interface. This coppersilicide compound is believed to form a compact layer on $LiCu_2Si$. Due to the inertness of $Cu_{19}Si_6$ in the lithium ion battery, passivation of $LiCu_2Si$ occurs upon extraction of lithium rendering the electrode inactive. This finding also explains the apparent stability of $LiCu_2Si$ in air: Formation of $LiOH$ accompanied by the formation of $Cu_{19}Si_6$ occurs at the interface, once again impose self-coating of the lithiumcoppersilicide compound by the latter one, therefore rendering it stable against further oxidation.

5.2. $LiCu_2Si$ and $FePO_4$

In this section, it was tested if Li can be extracted from $LiCu_2Si$ by the following chemical reaction:

$$19\ LiCu_2Si + 19\ FePO_4 \rightarrow 19\ LiFePO_4 + 2\ Cu_{19}Si_6 + 7\ Si \qquad (5.1)$$
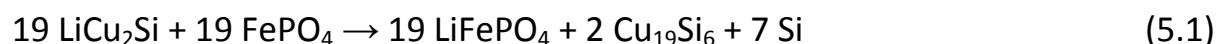
Synthesis

$LiCu_2Si$ (301.8 mg, 1.9 mmol, 1 Eq.) and $FePO_4$ (synthetized from $FeCl_3$ and H_3PO_4, 281.0 mg, 1.9 mmol, 1 Eq.) are ball milled in argon for 3h at a speed of

350 rpm. The resulting black powder is sealed in a Nb ampoule in argon, heated to 300 °C at a rate of 100 °C h⁻¹, kept at 300 °C for 12 h and then cooled down to room temperature at a cooling rate of 100 °C h⁻¹. The obtained XRD powder pattern is shown in Figure 5.6.
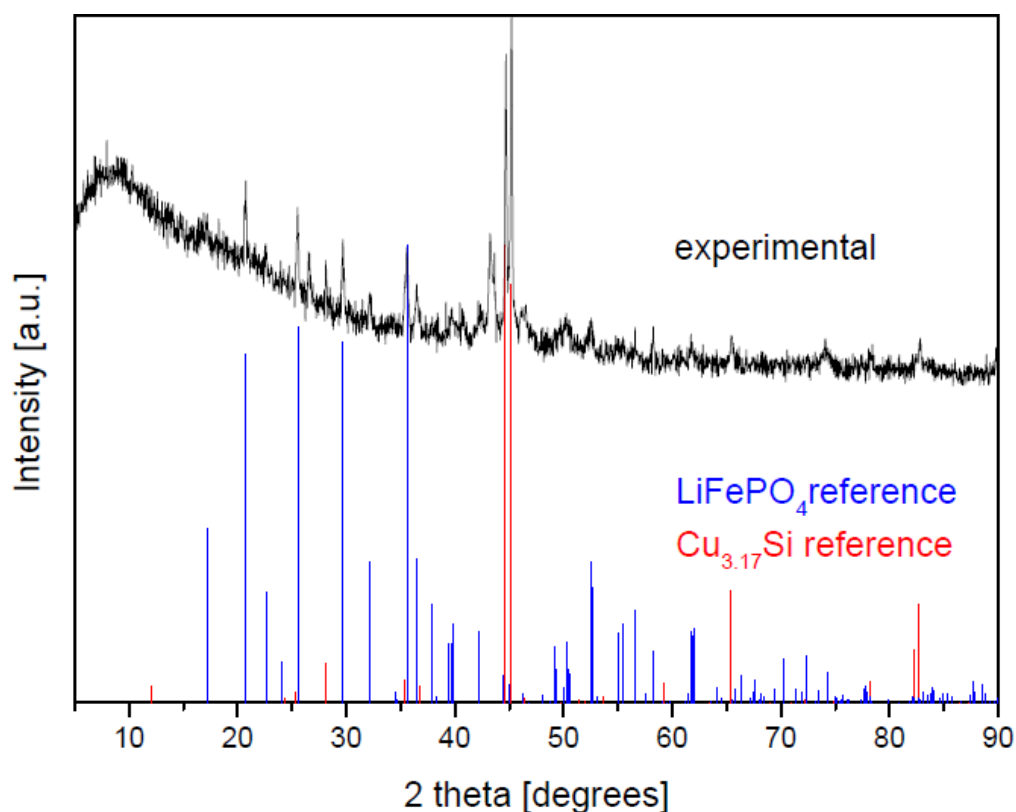
Fig. 5.6: XRD powder pattern of ball milled LiCu$_2$Si + FePO$_4$ after heat treatment at 300 °C for 12 h (black curve).

The sample is quite amorphous and contains the phase LiFePO$_4$ as well as Cu$_{19}$Si$_6$ (Cu$_{3.17}$Si). The presence of the two product phases shows that there is a delithiation reaction. As the highest delithiation potential of LiFePO$_4$ is at about 3.8V an electrochemical oxidation of LiCu$_2$Si should work at least at this potential. SEM analysis of the reaction mixture is shown in Figure 5.7.
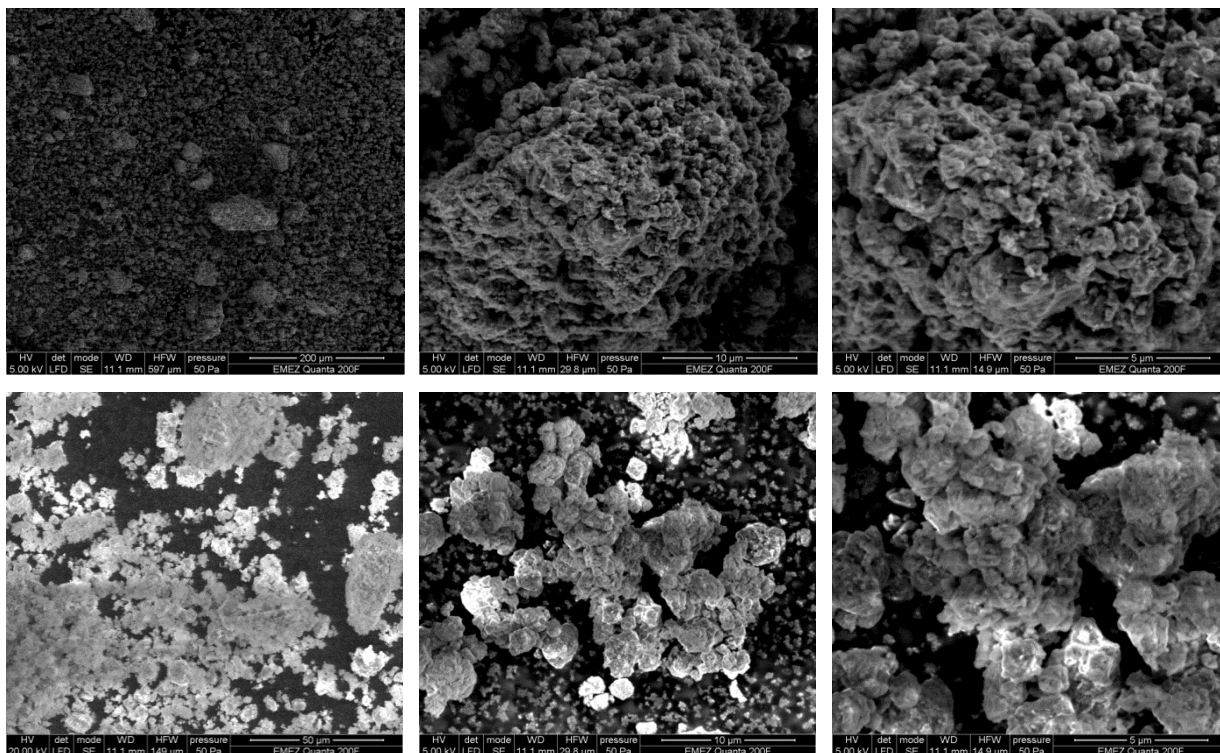
Fig. 5.7: SEM micrographs of LiCu$_2$Si + FePO$_4$ after heat treatment at 300 °C for 12 h at different magnification scales.

The sample looks homogeneous and consists of small aggregated particles. However, it was not possible to assign particles to certain phases using EDXS.

Electrochemical performance

The electrode was prepared in a glove box in argon atmosphere, where Super P (15 wt. %) and graphite (5 wt. %) were added as conductive additives and PVDF was used as a binder (10 wt. %). 1 M LiPF$_6$ in ethylenecarbonate / dimethylcarbonate (1:1) was used as electrolyte. The sample was cycled between 2.0 and 4.3 V vs. Li/Li$^+$ at a rate of 20 mA g^{-1}. The initial step was discharge (lithiation) and values for specific capacity refer to the composite material.
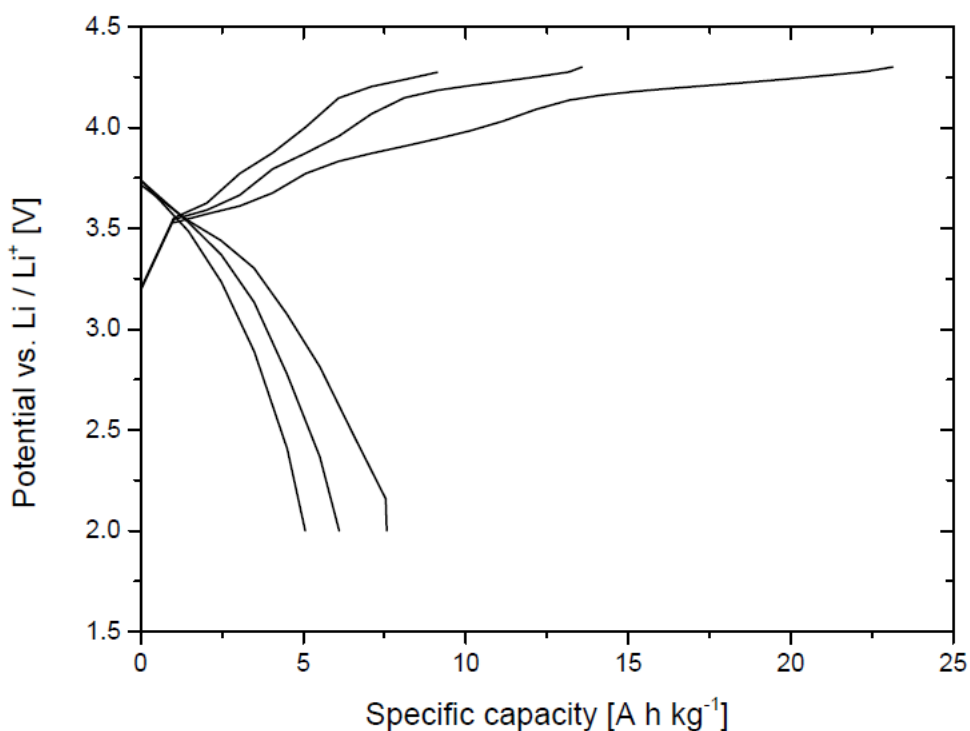
Fig. 5.8: Galvanostatic measurement of ball milled $LiCu_2Si$ + $FePO_4$ after heat treatment at 300 °C for 12 h. Only the first three cycles are shown.

During first charge, a low charge capacity of 23 mAh g^{-1} is obtained starting from 3.6 V. This value is further decreased during the next two cycles. Note that the obtained discharge capacity is significantly smaller than the charge capacity for each cycle. As a conclusion, the cycling behavior of this mixture does not match the expectations for $LiFePO_4$ based cathode materials. It is believed that $LiFePO_4$ is completely coated by $Cu_{19}Si_6$, therefore hindering its electrochemical activity. However, $Cu_{19}Si_6$ should not completely coat the active material: Instead, only the holes of the cubic closest package of the active material have to be filled and the particles connected. Therefore, mixtures with a lower $LiCu_2Si$ content are prepared which are summarized in Table 1.

Tab. 1: Prepared mixtures of $LiCu_2Si$ and $FePO_4$.

$LiCu_2Si$ [Vol. %]	Ratio [$n(FePO_4)$ / $n(LiCu_2Si)$]
5	11.14
10	5.28
15	3.32
20	2.35

For these calculations, a molar mass of 162.12 g mol^{-1} and a density of 5.59 g cm^{-3} were used for $LiCu_2Si$.[98] Respective values for $FePO_4$ are 150.82g mol^{-1} and 3.05 g cm^{-3}, respectively.[105]

Synthesis

For all mixtures, $LiCu_2Si$ and $FePO_4$ in according molar ratios are ground and then sealed in a Nb ampoule in argon. The samples are heated to 300 °C at a rate of 100 °C h^{-1}, kept at 300 °C for 12 h and then cooled down to room temperature at a cooling rate of 100 °C h^{-1}. The resulting brown powder is pressed to a pellet, sealed in a Nb ampoule in argon and then treated again at 300 °C for 12 h. The obtained XRD powder patterns are shown in Figure 5.9.
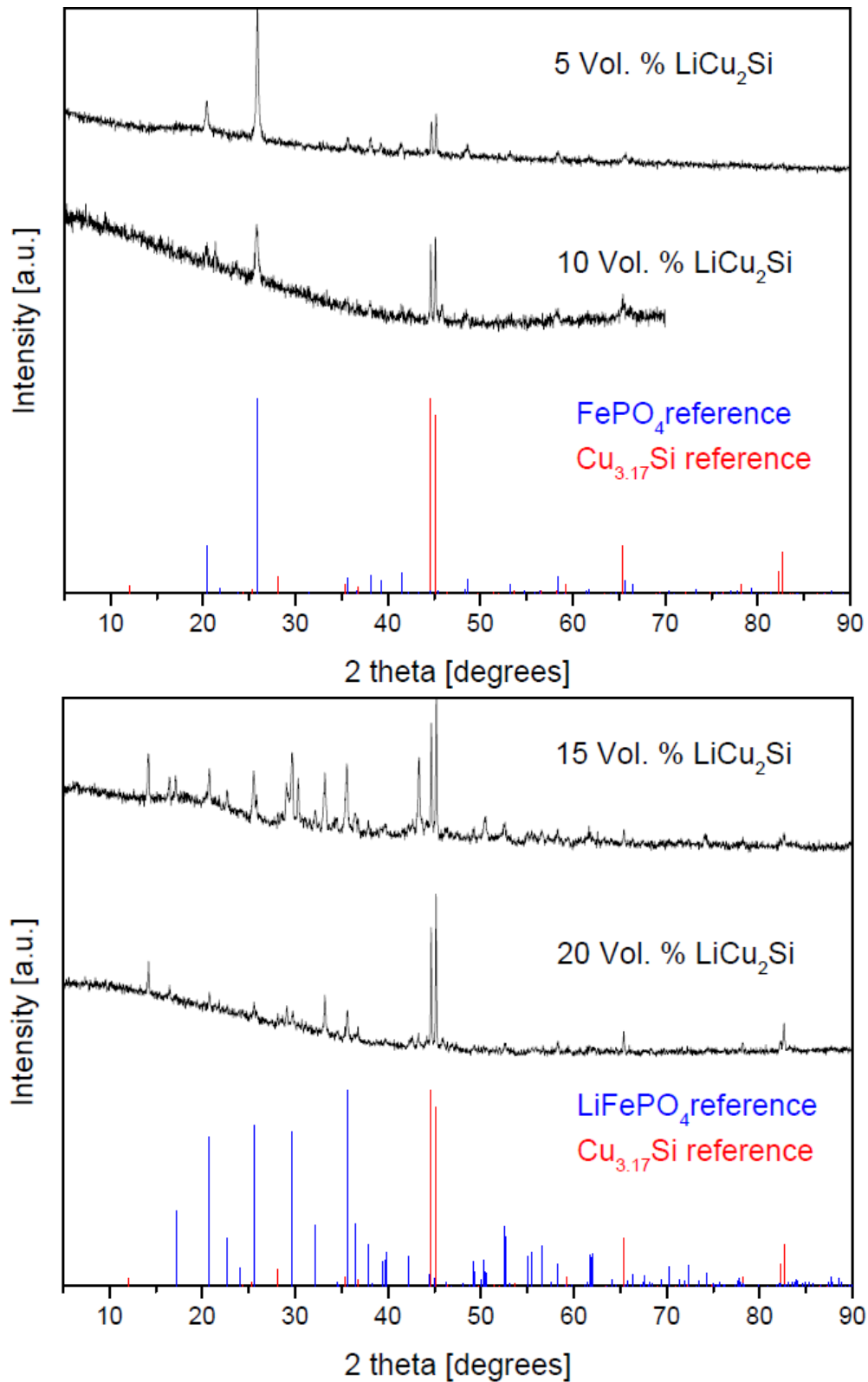
Fig. 5.9: XRD powder patterns of LiCu$_2$Si and FePO$_4$, treated at 300 °C for 12 h in argon containing different amount of LiCu$_2$Si (black curves).

Note that for samples containing 5 and 10 Vol. % of LiCu$_2$Si, only FePO$_4$ and no LiFePO$_4$ is present in the powder pattern. This is due to the low amount of LiCu$_2$Si used, so only a small amount of LiFePO$_4$ was formed. However, the phase Cu$_{19}$Si$_6$ (Cu$_{3.17}$Si) is present in all samples and no LiCu$_2$Si can be observed indicating a complete delithiation reaction of the lithiumcoppersilicide to the binary compound. As a side note, two intense reflections at $2\theta = 14$ ° and 43.2 °, respectively, were observed in the powder pattern of the mixture containing 15 Vol. % LiCu$_2$Si. However, these reflections could not be indexed to a known phase. SEM micrographs of a mixture containing 10 Vol. % LiCu$_2$Si are shown in Figure 5.10 below.
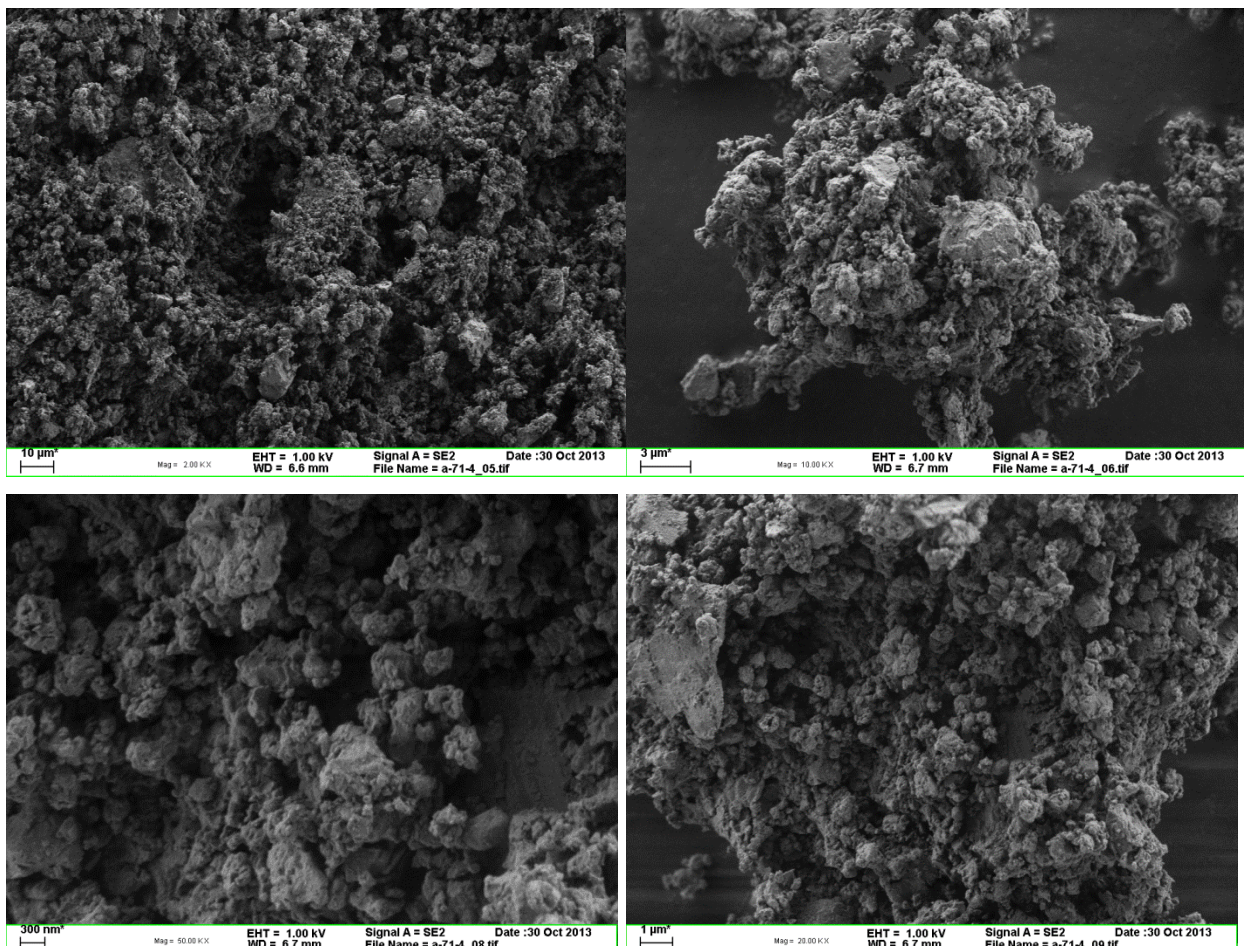
Fig. 5.10: SEM analysis of 10 Vol. % LiCu$_2$Si and FePO$_4$, treated at 300 °C for 12 h.

The sample is a mixture, where primary particles with a size between 2 to 10 μm are partially covered by smaller agglomerated particles at submicron size. Neither EDXS analysis (Fig. 5.11) nor elemental mapping was successful in distinguishing $LiFePO_4$ from $Cu_{19}Si_6$ particles.
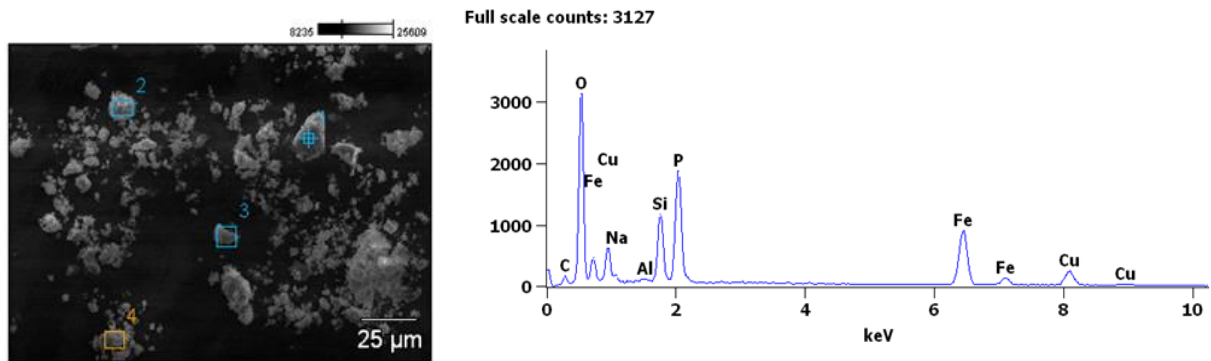
Fig. 5.11: EDXS analysis of 10 Vol. % $LiCu_2Si$ and $FePO_4$, treated at 300 °C for 12 h.

TEM micrographs of a mixture containing 10 Vol. % $LiCu_2Si$ are shown in Figure 5.12.
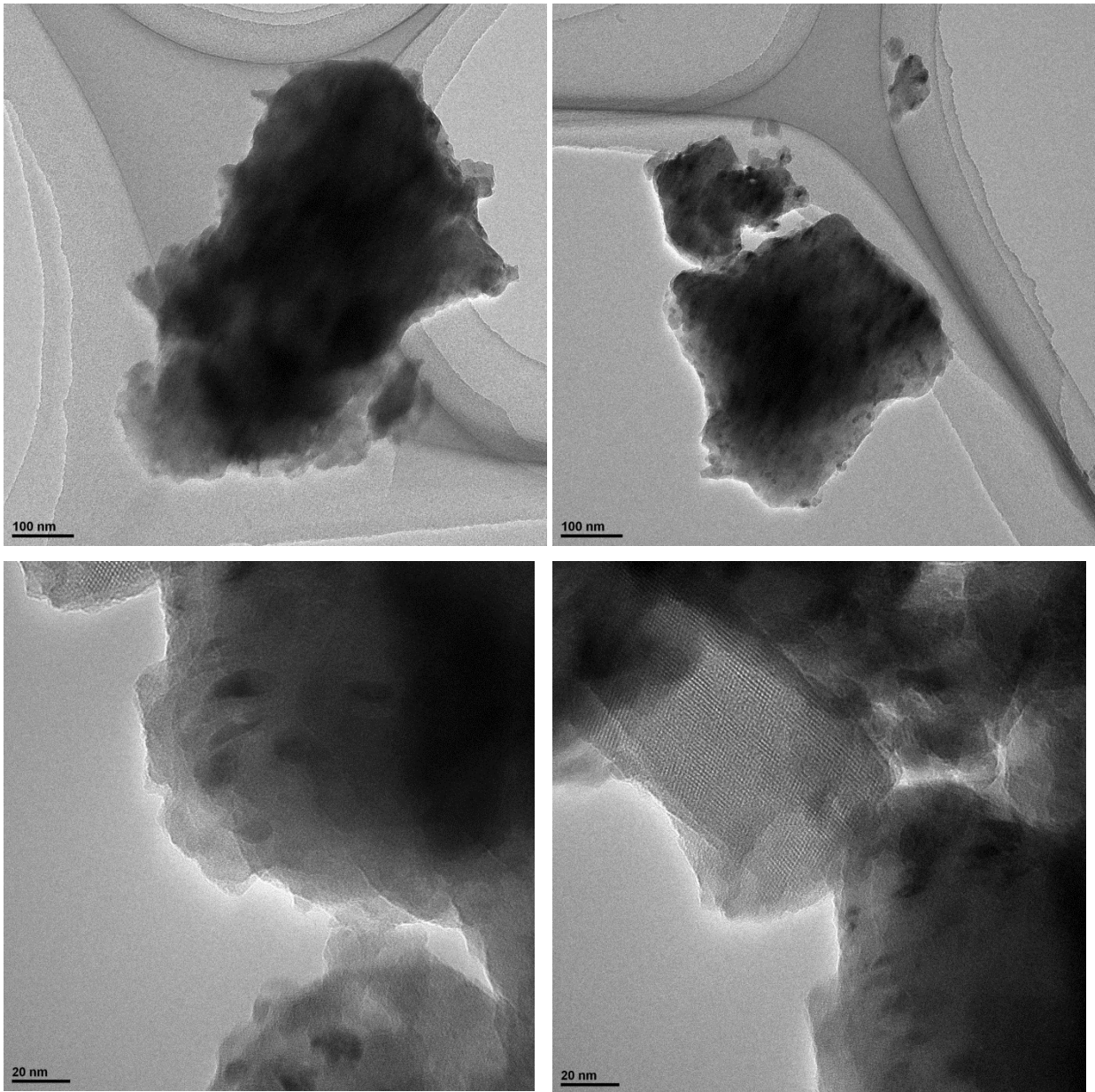
Fig. 5.12: TEM analysis of 10 Vol. % LiCu$_2$Si and FePO$_4$, treated at 300 °C for 12 h.

This part of the sample consists of particles with a size of 100 to 200 nm. Additionally, some smaller particles on the surface can be seen.

Electrochemical performance

Mixtures with a LiCu$_2$Si content of 5, 10, 15 and 20 Vol. % were tested in an electrochemical cell. However, cycling of LiFePO$_4$ in the Li ion battery was only observed for a mixture containing 10 Vol. % LiCu$_2$Si. It is believed that for mixtures containing 15 and 20 Vol. % of LiCu$_2$Si, the Cu$_{19}$Si$_6$ content is still too high, completely coating LiFePO$_4$ and therefore effectively hindering the electrochemical activity of the active material. On the other hand, for a mixture containing only 5 Vol. % of LiCu$_2$Si, only a very small amount of LiFePO$_4$ is formed and the connection of the particles is not given due to the low amount of Cu$_3$Si.

10 Vol. % LiCu$_2$Si

Before electrochemical testing, the sample was ball milled in argon to a fine black powder. The electrode was prepared in a glove box in argon atmosphere, where Super P (16 wt. %) and graphite (8 wt. %) were added as conductive additives and PVDF was used as a binder (8 wt. %). 1 M LiPF$_6$ in ethylenecarbonate / dimethylcarbonate (1:1) was used as electrolyte. The sample was cycled between 2.0 and 4.3 V vs. Li/Li$^+$ at a rate of 20 mA g^{-1}. The initial step was charge (lithiation) and values for specific capacity refer to the composite material.
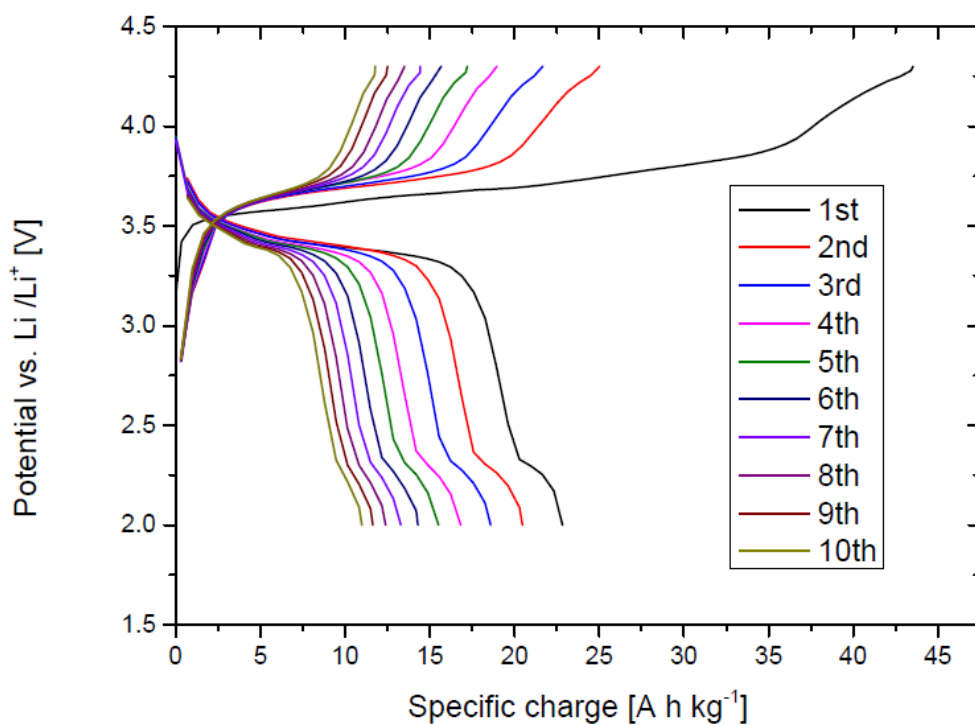
Fig. 5.13: Galvanostatic measurement of 10 Vol. % LiCu$_2$Si + FePO$_4$. Only the first 10 cycles are shown.

For charging, there is a plateau between 3.5 and 3.7 V and for discharge, there is a plateau at 3.4 V indicating that LiFePO$_4$ is the active material. This is confirmed by the cyclic voltammetry measurement shown in Figure 5. 14.
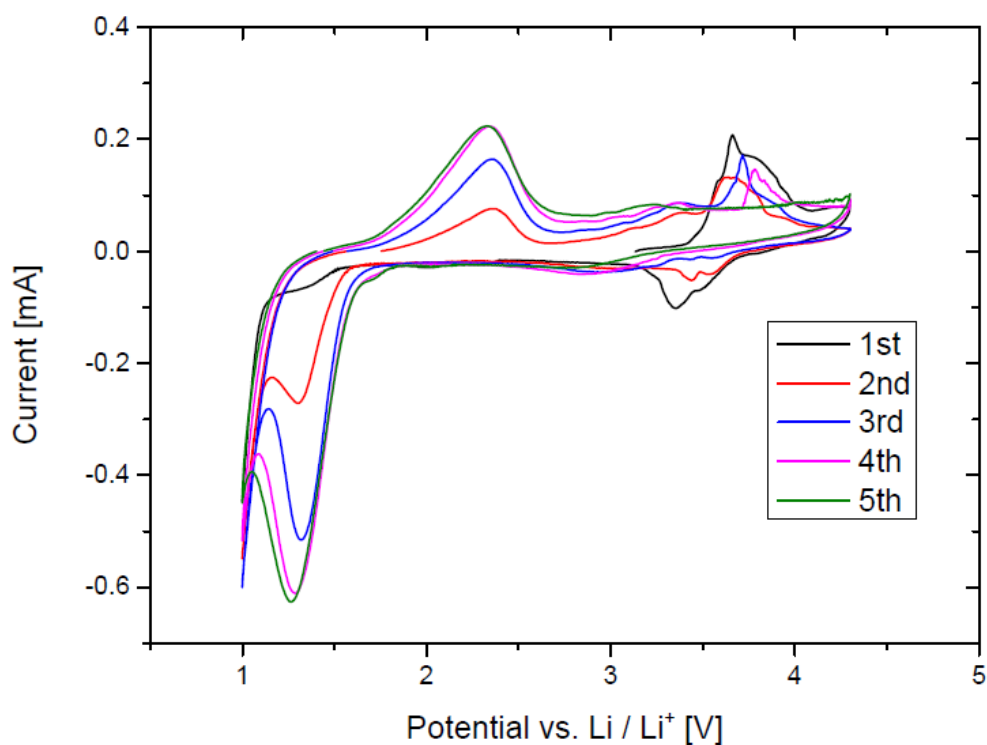
Fig. 5.14: Cyclic Voltammetry measurement of 10 Vol. % LiCu₂Si and FePO₄, treated at 300 °C, only the first 5 cycles are shown. The sample was cycled between 1.0 and 4.3 V vs. Li/Li$^+$ with a rate of 0.05 mV s^{-1}. The initial step was charging (delithiation).

During the first cycle, there is an oxidation peak at 3.65 V, which has a diminishing magnitude during subsequent cycles. After the 4th cycle, this peak is completely vanished. The reduction peaks at 3.35 and 3.55 V also show a diminishing magnitude with increasing cycling number until the 4th cycle, where they disappear completely. These peaks identify LiFePO₄ as the electrochemically active material and their magnitude fading correlates with the ongoing capacity decay. Additionally, a broad oxidation peak at 2.35 V and a broad reduction peak at 1.3 V appear after the first cycle. Those peaks are present in all subsequent cycles and are traced back to electrolyte decomposition. This decomposition reactions and the associated SEI formation

should be responsible for the fading because $FePO_4$ was proven to be stable under such cycling conditions.

However, only low capacities were obtained and there is an ongoing capacity fade with increasing cycle number. The former one can be explained by the use of a $FePO_4$ powder, which consists mainly of micron sized $FePO_4$ with a low content of nano-sized particles. Therefore, only the as-formed nano-sized part of $LiFePO_4$ shows electrochemical activity. The reason for this capacity decay is examined in the next section using post mortem analysis.

Post mortem analysis

A mixture containing 10 Vol. % $LiCu_2Si$ and $FePO_4$, treated at 300 °C for 12 h, was examined after 10 cycles in a Li ion battery:

The sample was ball milled prior to electrochemical testing and electrode prepared in air. Super P (17 wt. %) and graphite (8 wt. %) were added as conductive additives and PVDF used as a binder (9 wt. %). 1 M $LiPF_6$ in ethylenecarbonate / dimethylcarbonate (1:1) was used as electrolyte. The sample was cycled between 2.0 and 4.3 V vs. Li/Li^+ at a rate of 20 mA g^{-1}. The initial step was charge (delithiation) and 10 full charge/discharge cycles were performed. The battery cell was opened in air and the electrode material washed two times with THF to remove the remaining electrolyte. Figure 5.15 shows the obtained XRD powder pattern of the black material.
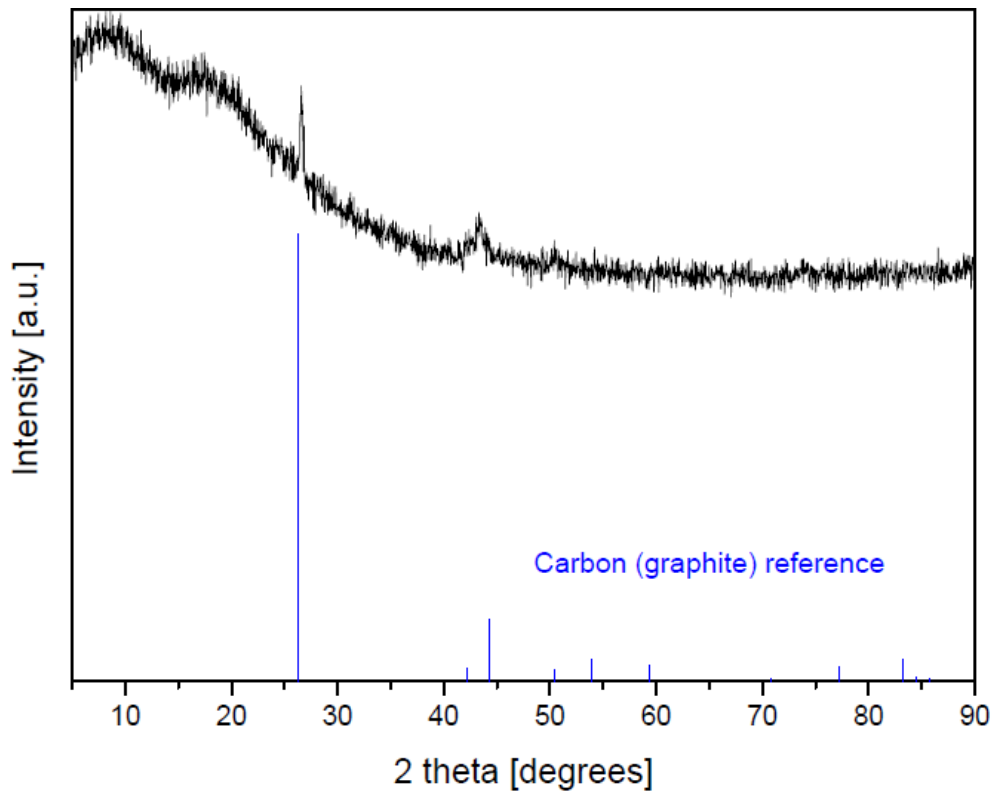
Fig. 5.15: XRD powder pattern of 10 Vol. % $LiCu_2Si$ and $FePO_4$ after 10 cycles in a Li ion battery (black curve).

The sample is highly amorphous and contains only graphite. The absence of $FePO_4$ / $LiFePO_4$ is totally unexpected and cannot be explained. SEM micrographs of this sample are shown in Figure 5.16.
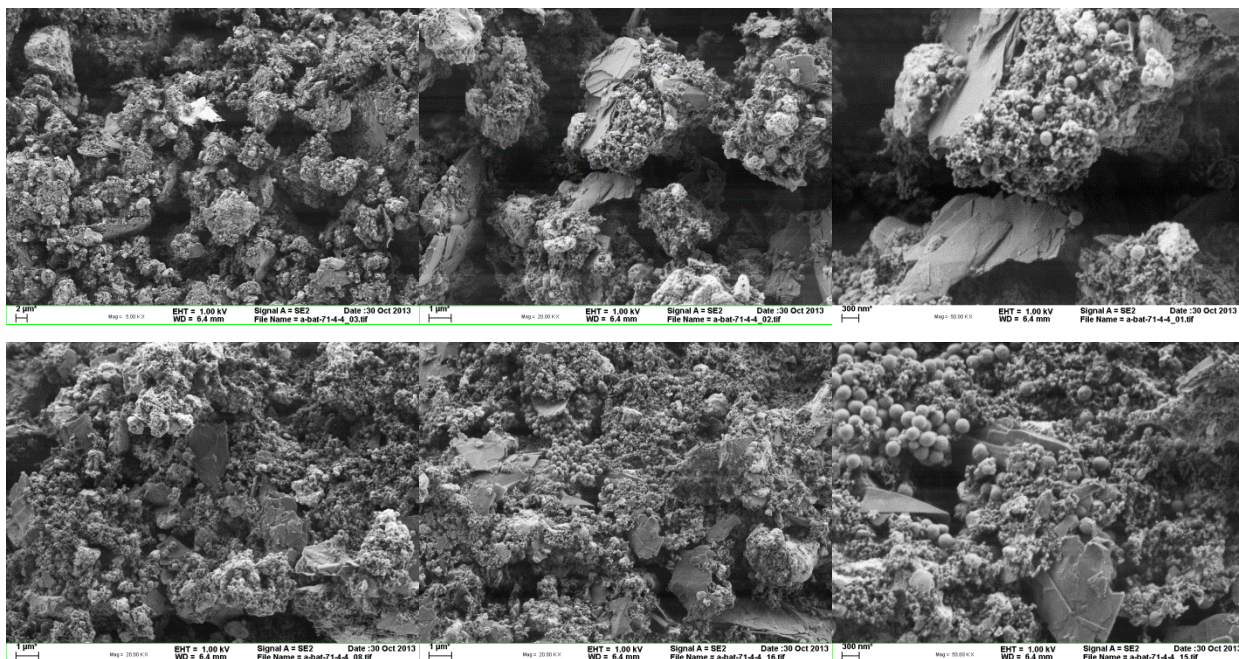
Fig. 5.16: SEM analysis of 10 Vol. % LiCu$_2$Si and FePO$_4$ after 10 cycles in Li ion battery.

The sample is a mixture of graphite plates, carbon spheres of Super P with a diameter of 100 nm and small agglomerated particles (Cu$_{19}$Si$_6$ and LiFePO$_4$). Neither EDXS analysis (Fig. 5.17) nor elemental mapping was successful in distinguishing Cu$_{19}$Si$_6$ from LiFePO$_4$ particles due to homogeneity of sample.
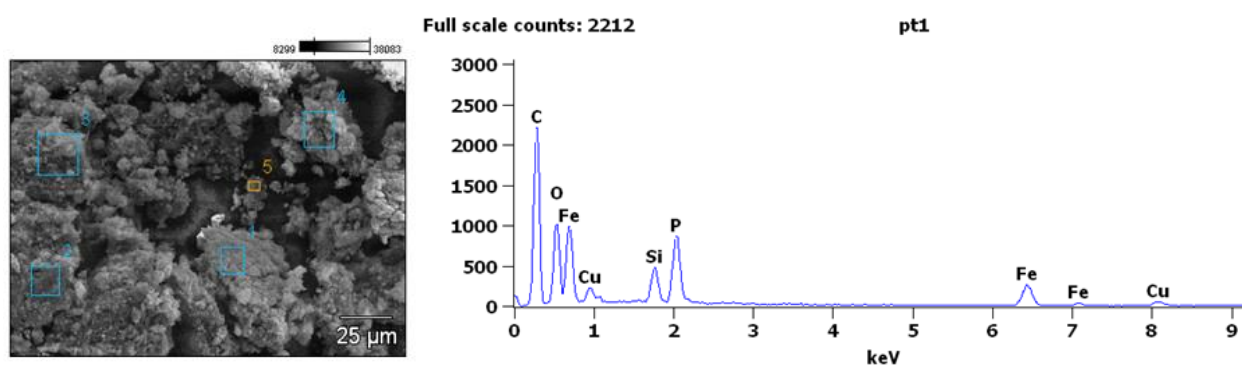
Fig. 5.17: EDXS analysis of 10 Vol. % LiCu$_2$Si and FePO$_4$ after 10 cycles in Li ion battery.

TEM micrographs of this composite are shown in Figure 5.18.
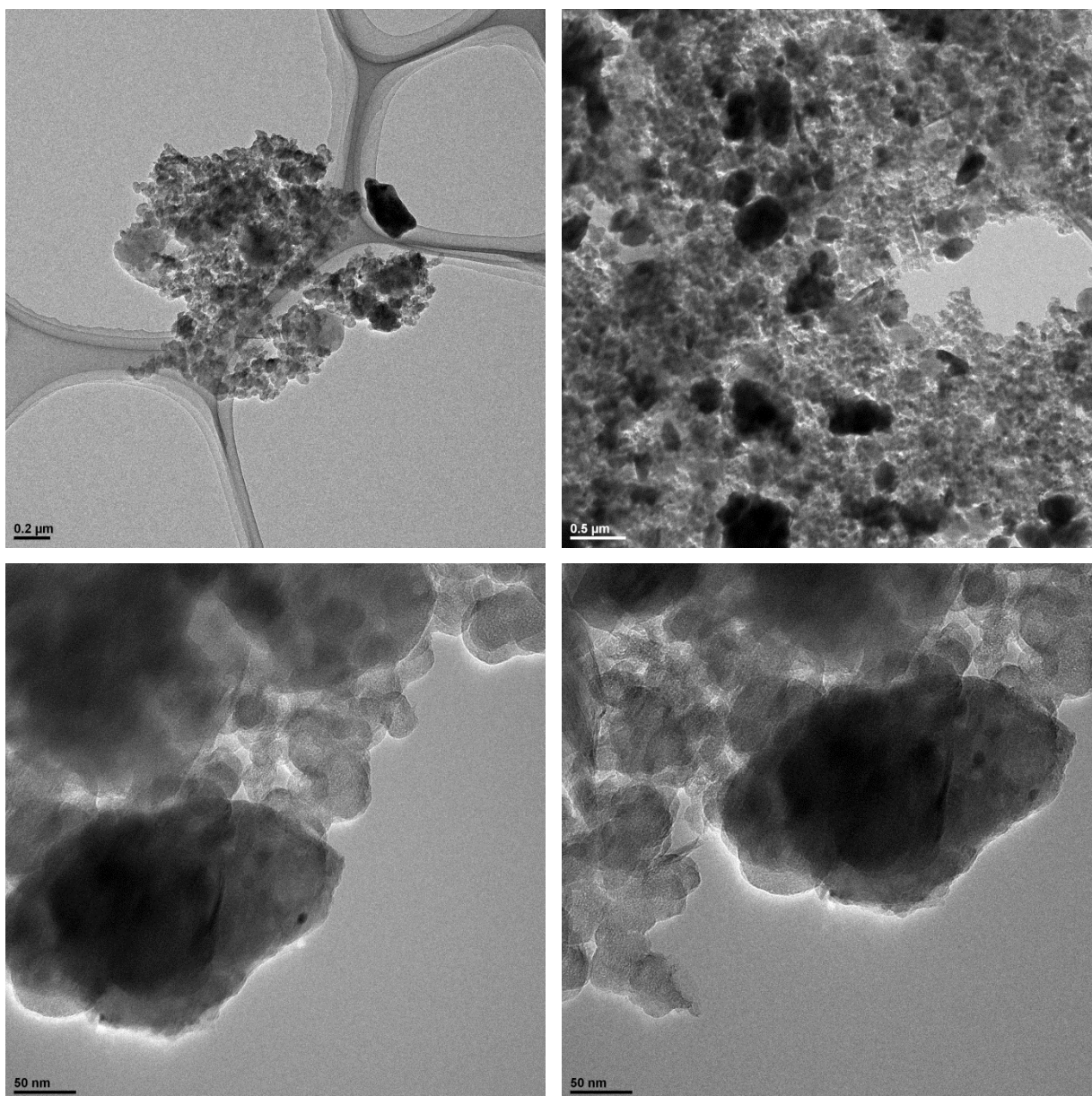
Fig. 5.18: TEM analysis of 10 Vol. % LiCu$_2$Si and FePO$_4$ after 10 cycles in Li ion battery.

The sample consists of graphite plates, carbon spheres of Super P and larger particles with a size of 100 to 500 nm.

To summarize, in-situ formation of LiFePO$_4$ accompanied by a coating with Cu$_{19}$Si$_6$ has been shown upon chemical reaction of LiCu$_2$Si and FePO$_4$. LiFePO$_4$ has been identified as electrochemical active species. However only small capacities were obtained and rapid capacity decay occurs. The first point can be

189

addressed to the inclusion of additional dead weight in form of a coppersilicide compound, therefore reducing the specific capacity. It is believed that cycling performance of LiFePO$_4$ in this composite is heavily affected by the Cu$_{19}$Si$_6$ matrix, which needs further optimization in terms of coating behavior as well as material content.

5.3. LiCu$_2$Si and graphite

In this section, LiCu$_2$Si was mixed with graphite to create a composite material as listed in equation 5.2 below:

LiCu$_2$Si + 6 C (graphite) → LiC$_6$ + 2 Cu / Si   (5.2)
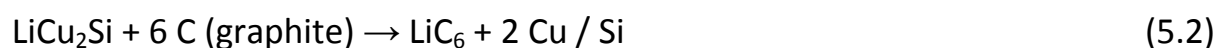
This reaction was expected to decompose LiCu$_2$Si, where Li will be intercalated in graphite and small Si particles will be packed inside a graphite / Cu matrix.

Synthesis

LiCu$_2$Si (138.2 mg, 0.85 mmol, 1 Eq.) and graphite (dried, 61.3 mg, 5.1 mmol, 6 Eq.) are ball milled in argon for 3 h at a speed of 550 rpm to a fine black powder. The resulting XRD powder pattern is shown in Figure 5.19.
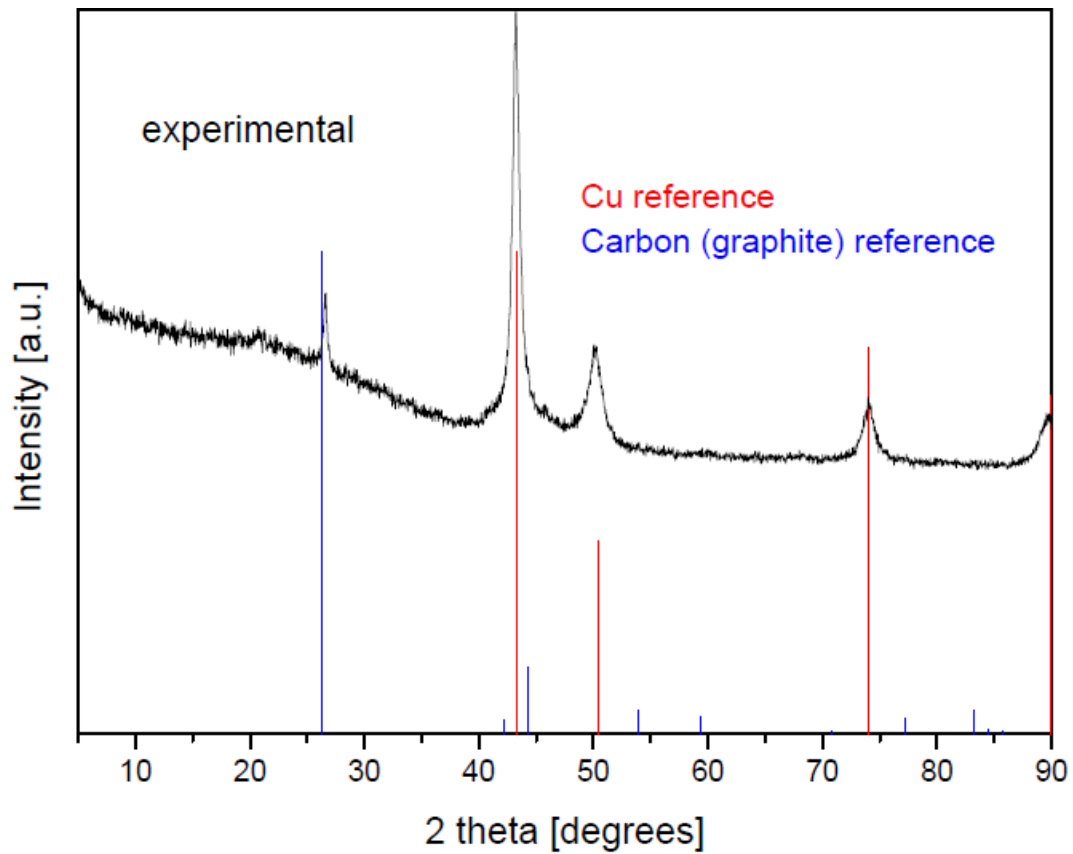
Fig. 5.19: XRD powder pattern of ball milled LiCu$_2$Si and graphite (black curve).

The sample contains an amorphous part (high background), graphite and nano Cu (broad peaks). The size of the Cu particles was estimated to roughly 10 nm using the Scherrer equation. As expected, LiCu$_2$Si was delithiated to Cu and amorphous part, which is believed to contain amorphous silicon. SEM micrographs of this material are shown in Figure 5.20.
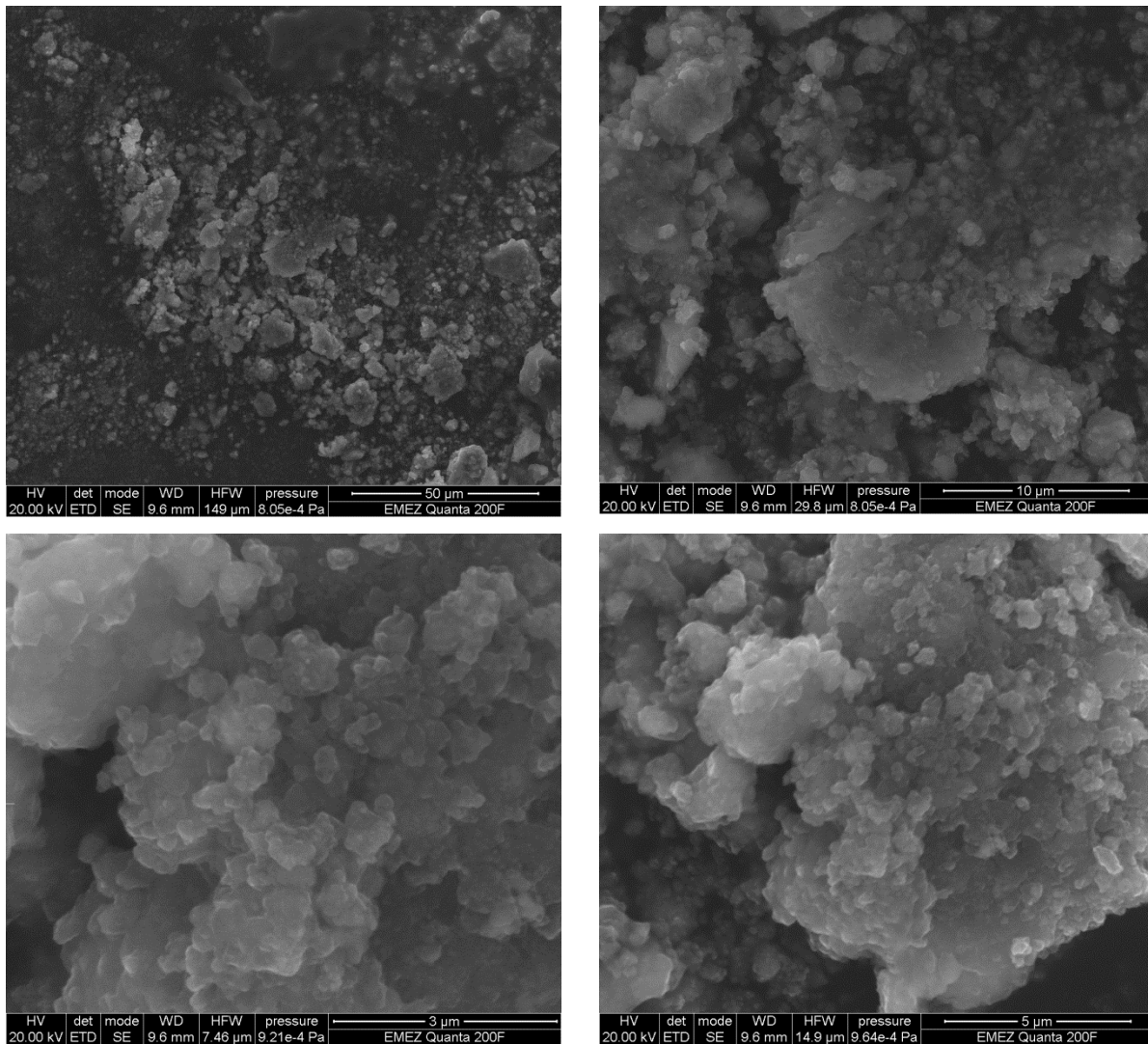
Fig. 5.20: SEM micrographs of ball milled LiCu$_2$Si and graphite at different magnification scales.

Plate-like particles (graphite) are covered by smaller agglomerated particles (submicron size) on their surface. EDXS analysis of these particles shows high content of Si and Cu, but only low amount of C.

Figure 5.21 shows SEM analysis of the sample using back scattered electrons to identify Cu particles.
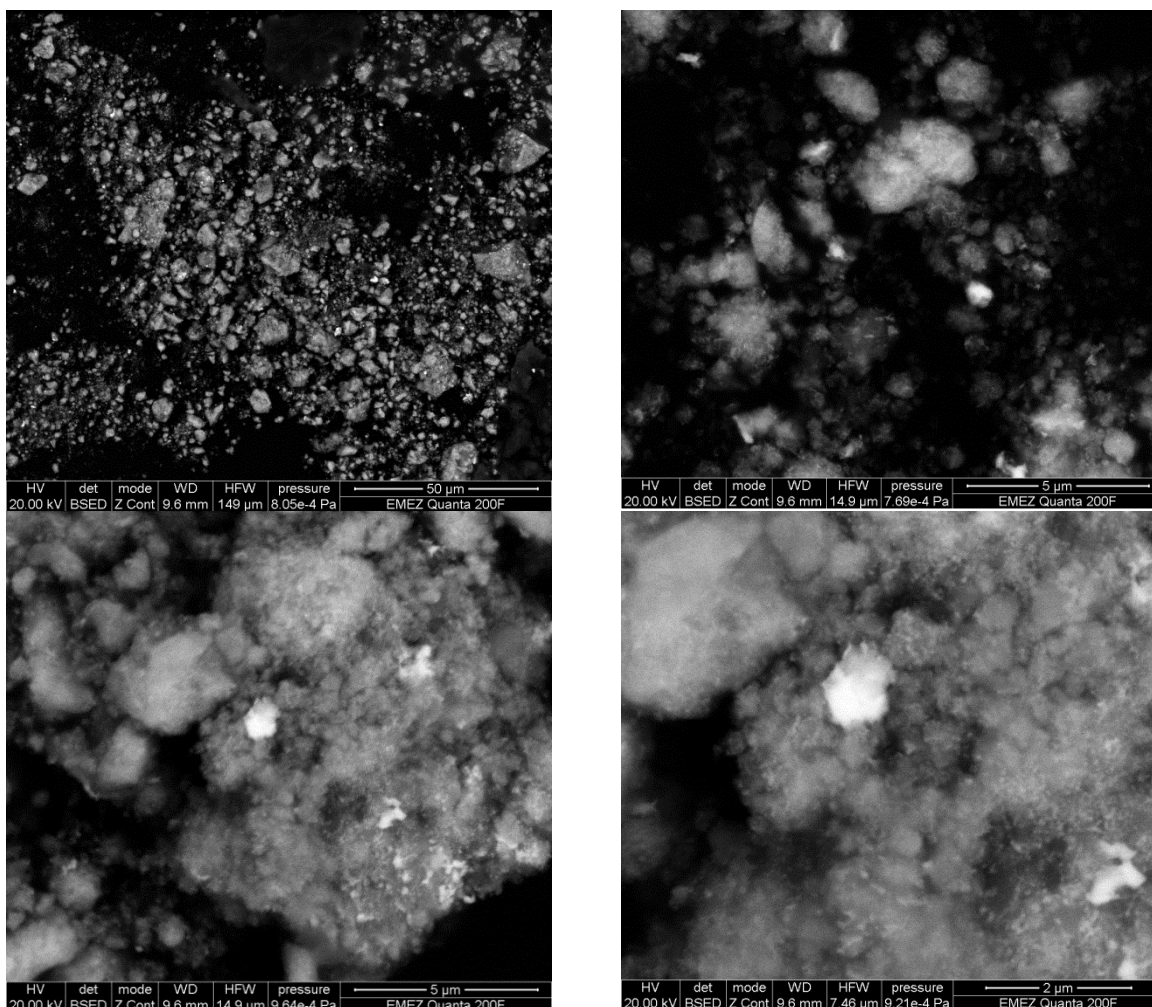
Fig. 5.21: Back scattered electron SEM images of ball milled LiCu$_2$Si and graphite at different magnification scales.

The bright spots visible in SEM analysis using back scattered electrons show Cu particles as confirmed by EDXS analysis.

Electrochemical performance

The electrodes were prepared in an argon filled glove box, where Super P (21 wt. %) was added as conductive additive and PVDF used as a binder (10 wt. %). 1 M LiPF$_6$ in ethylenecarbonate / dimethylcarbonate (1:1) was used as electrolyte. The sample was cycled between 20 mV and 3.0 V vs. Li/Li$^+$ at a rate of 20 mA g^{-1}. The initial step was charge (delithiation) and values for specific capacity refer to the composite material. The galvanostatic measurement of

this material is shown in Figure 5.22 and the cyclic voltammetry measurement shown in Figure 5.23, respectively.
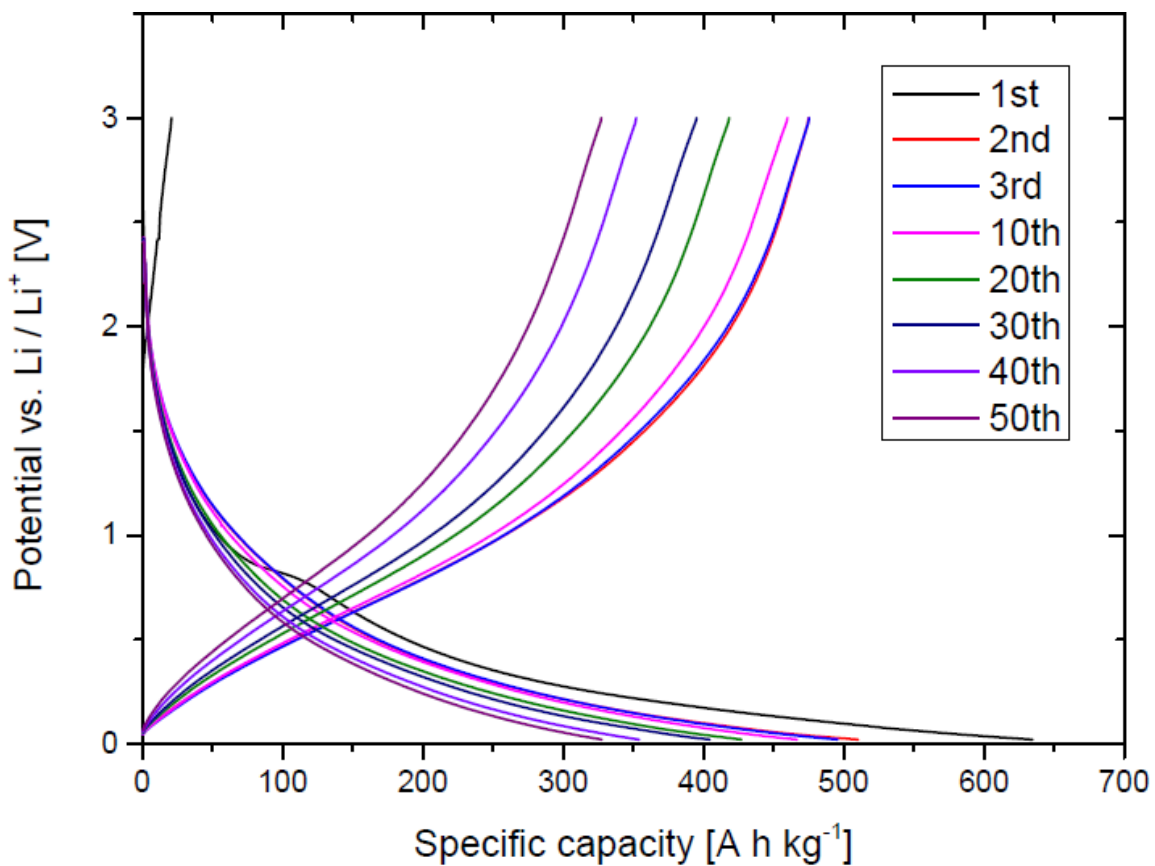
Fig.5.22: Galvanostatic measurement of ball milled LiCu$_2$Si and graphite, where the first 50 cycles are shown.

During first charge, a capacity of 20 mAh g^{-1} was obtained indicating that almost no Li was extracted from the electrode. There is an irreversible capacity loss of 125 mAh g^{-1} after first cycle (20 %), but afterwards there is a stable charge capacity of 465 mAh g^{-1} and discharge capacity of 475 mAh g^{-1}, respectively, for the next 10 cycles. Potential profiles of the galvanostatic curves indicate amorphous silicon as the redox active species.
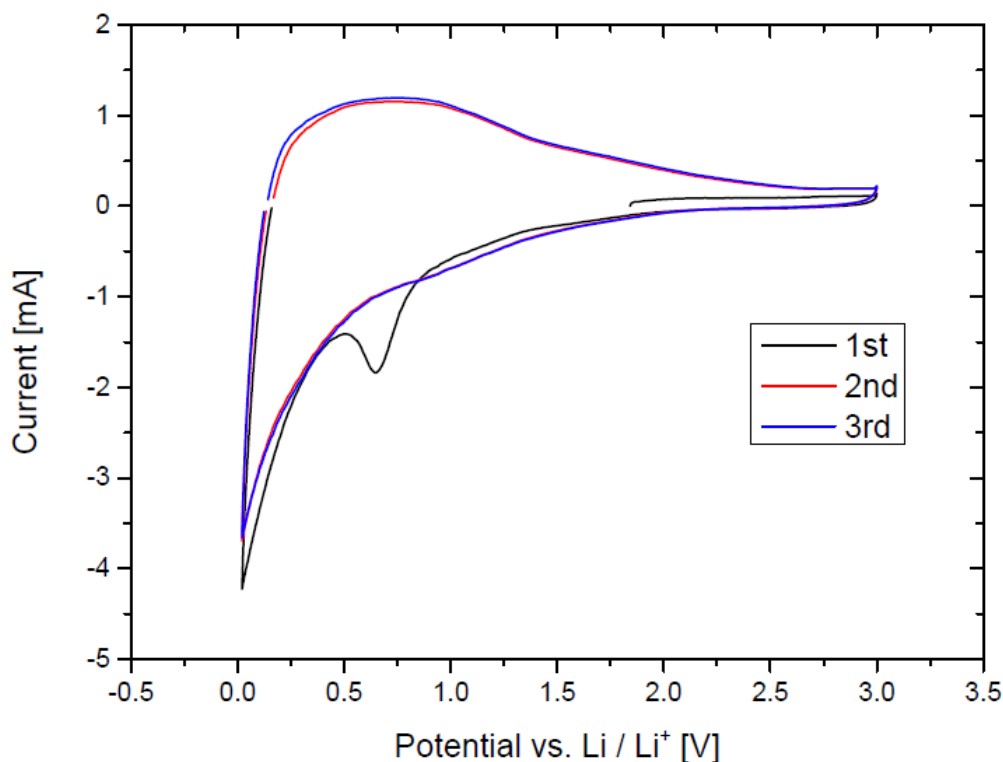
Fig. 5.23: CV measurement of ball milled LiCu$_2$Si and graphite, where the first 3 cycles are shown. The sample was cycled from 20 mV to 3.0 V vs. Li/Li$^+$ at a rate of 0.1 mV s^{-1}. The initial step was charge (delithiation).

During first cycle, there is a reduction peak appearing at 0.7 V which is no longer present in the subsequent cycles. This is assigned to the initial SEI formation. There are no distinct peaks visible for oxidation. Instead, there is only one broad peak ranging from 20 mV to 1.5 V vs. Li/Li$^+$.

Obviously, the matrix was formed (e.g. Cu precipitation), but there is no clear evidence for the presence of silicon as the electrochemically active material since the specific peaks are missing in the CV (200 mV for reduction and 400 mV for oxidation, respectively). This may be due to the relatively low amount of Si in the sample.

Interestingly, ball-milling of LiCu$_2$Si with graphite leads to complete decomposition of the former one, whereas just mixing with graphite for the

electrode formulation does not (section 5.1). It is believed that treatment of LiCu$_2$Si with graphite lead to extraction of lithium from the surface of the lithiumcoppersilicide compound, in-situ forming a compact layer of Cu$_{19}$Si$_6$ preventing further delithiation. However, during rigorous ball-milling, the passivation layer of coppersilicide is constantly pulverized leading to the complete decomposition of LiCu$_2$Si.

5.3.1. Addition of Si

In this section, the addition of Si to the LiCu$_2$Si / graphite reaction mixture is discussed. The following reaction is suggested:

LiCu$_2$Si + 6 C + x Si $\rightarrow$ LiC$_6$ + 2 Cu + (x + 1) Si (embedded in graphite / Cu)   (5.3)
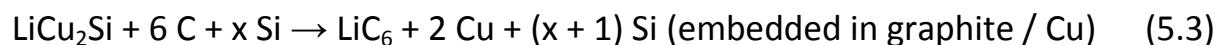
5.3.1.1. LiCu$_2$Si + 6 C (graphite) + 6.67 Si

The ratio of educts was adjusted in order to have 16 Vol. % of Cu, using a density of 8.96 g cm^{-3} for Cu and 2.33 g cm^{-3} for Si, respectively. The ratio of LiCu$_2$Si to C was kept at 1:6.

Synthesis

LiCu$_2$Si (385.0 mg, 0.24 mmol, 1 Eq.), graphite (dried, 171.9 mg, 1.42 mmol, 6 Eq.) and Si (99.9999%, ball-milled, 444.7 mg, 1.58 mmol, 6.67 Eq.) are ball-milled in argon for 3 h at a speed of 550 rpm to a fine black powder. The resulting XRD powder pattern is shown in Figure 5.24.
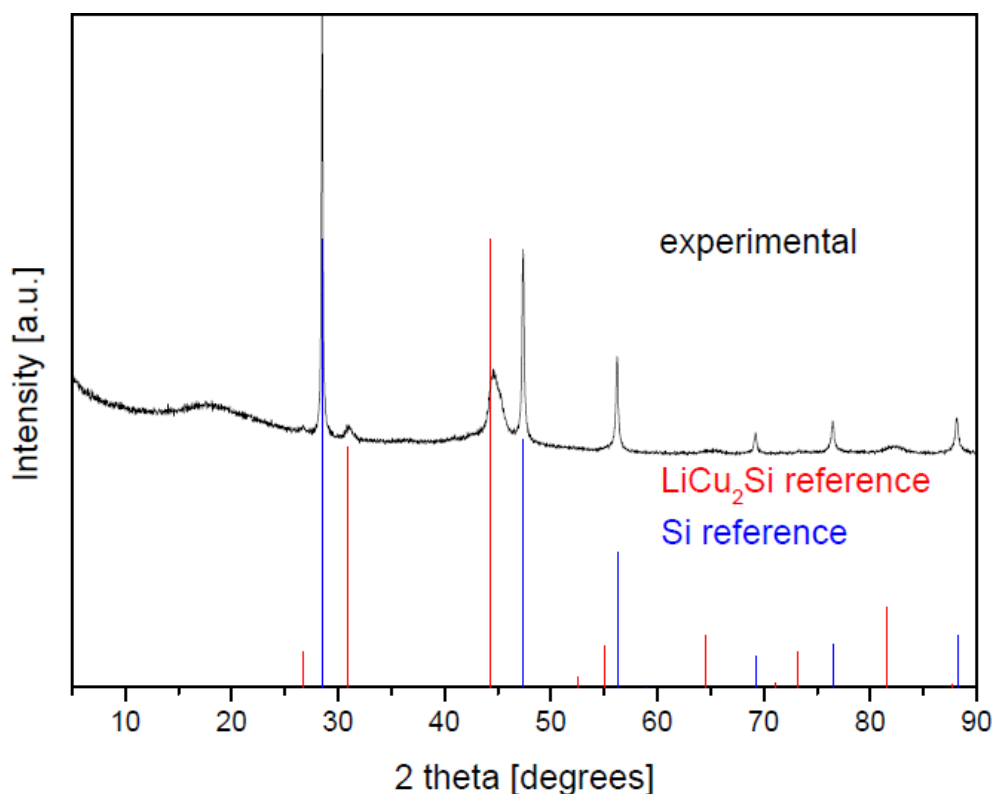
Fig. 5.24: XRD powder pattern of ball milled $LiCu_2Si$, graphite and 6.67 Eq. of Si (black curve).

The sample is highly amorphous but also contains crystalline Si as well as $LiCu_2Si$ (broad peaks). The powder pattern looks much different than the one without addition of Si (Fig. 5.19). $LiCu_2Si$ was not decomposed upon ball milling with graphite here. It is believed that the as-formed passivation layer of $Cu_{19}Si_6$ on the surface of $LiCu_2Si$ was not effectively pulverized during ball milling, therefore hindering delithiation of $LiCu_2Si$. Instead, due to the excessive amount of Si, only these particles were ground in an effective manner.

Electrochemical performance

Electrodes were prepared in an argon filled glove box, where Super P (20 wt. %) was added as conductive additive and PVDF used as a binder (10 wt. %). 1 M $LiPF_6$ in ethylenecarbonate / dimethylcarbonate (1:1) was used as electrolyte. The sample was cycled between 20 mV and 3.0 V vs. Li/Li^+ with a rate of 20 mA

g^{-1}. The initial step was charge (delithiation) and values for specific capacity refer to the composite material. The galvanostatic measurement of this material is shown in Figure 5.25 below.
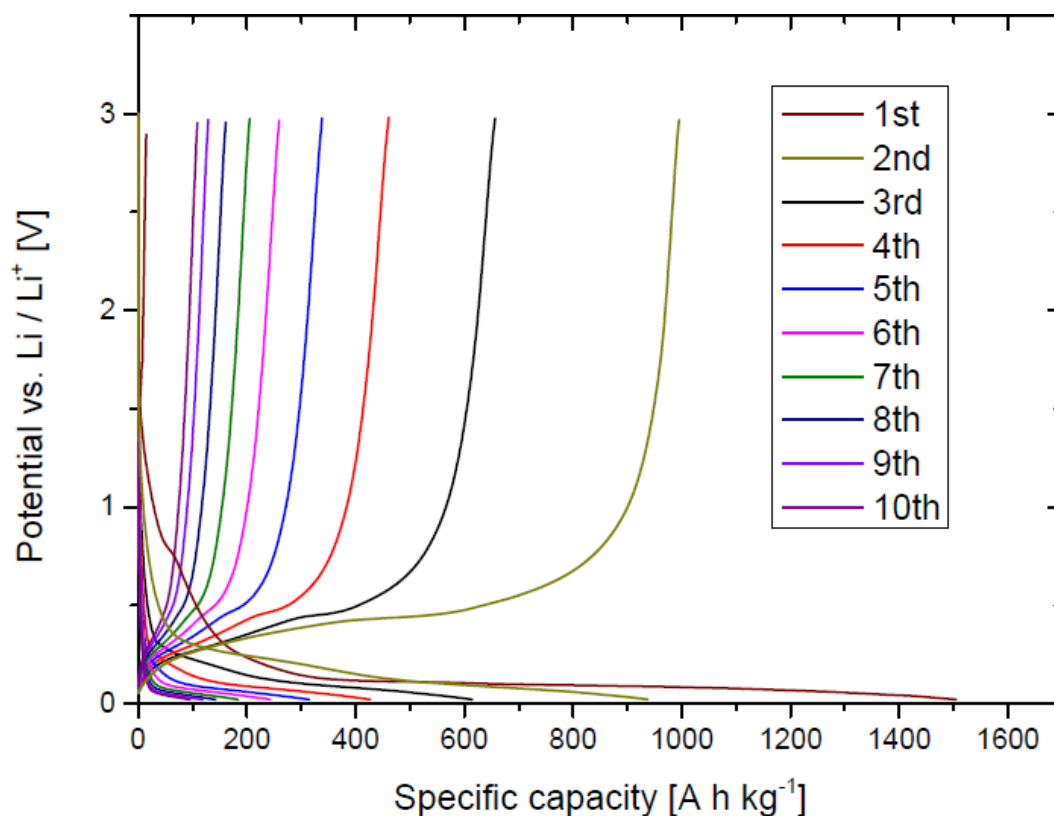
Fig. 5.25: Galvanostatic measurement of ball milled LiCu$_2$Si, graphite and 6.67 equivalents of Si, where the first 10 cycles are shown.

During first charge, no Li was extracted from starting material. Additionally, there is a high irreversible capacity loss of 510 mAh g^{-1} (34 %) after first cycle and rapid capacity decay during the following cycles. After 10 cycles, only 100 mAh g^{-1} was retained. However, the high initial capacity and the potential profile indicate Si as the electrochemically active species which is confirmed by the cyclic voltammetry measurement shown in Figure 5.26.
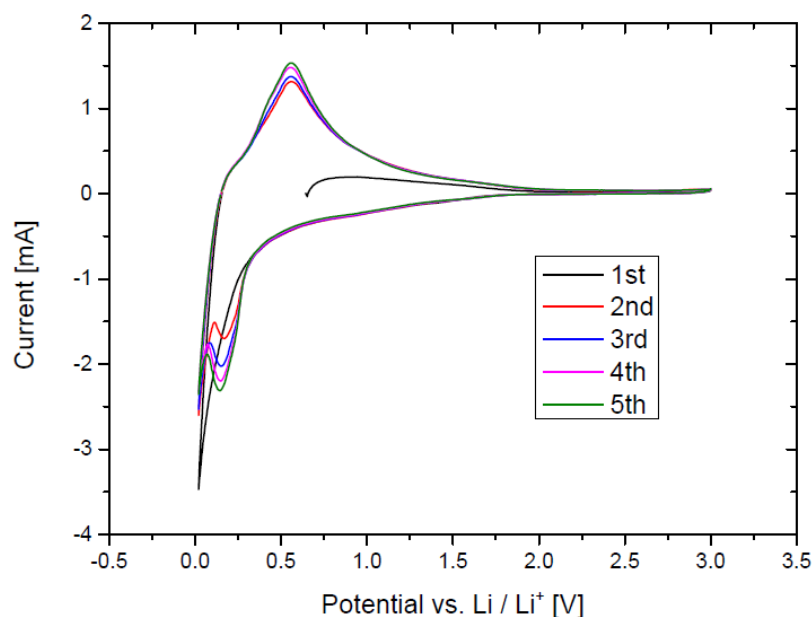
Fig. 5.26: CV measurement of ball milled $LiCu_2Si$, graphite and 6.67 equivalents of Si, where the first 5 cycles are shown. The sample was cycled from 20 mV to 3.0 V vs. Li/Li^+ at a rate of 0.05 mV s^{-1}. The initial step was charge (delithiation).

During each cycle except the first, a broad oxidation peak at 0.55 and a reduction peak at 0.15 V, respectively, are observed, which clearly identifies Si as the electrochemically active species. However, the high Si content is responsible for the fast capacity decay. In the next section, a lower amount of Si was used.

5.3.1.2. $LiCu_2Si$ + 6 C (graphite) + Si

In this section, one additional equivalent of Si was added to the $LiCu_2Si$ and graphite based reaction mixture. The ratio of $LiCu_2Si$ to C was kept at 1:6.

Synthesis

$LiCu_2Si$ (308.5 mg, 0.19 mmol, 1 Eq.), graphite (dried, 137.7 mg, 1.14 mmol, 6 Eq.) and Si (99.9999%, ball-milled, 53.7 mg, 0.19 mmol, 1 Eq.) are ball-milled in argon for 3 h at a speed of 550 rpm to a fine black powder. The resulting XRD powder pattern is shown in Figure 5.27.

199
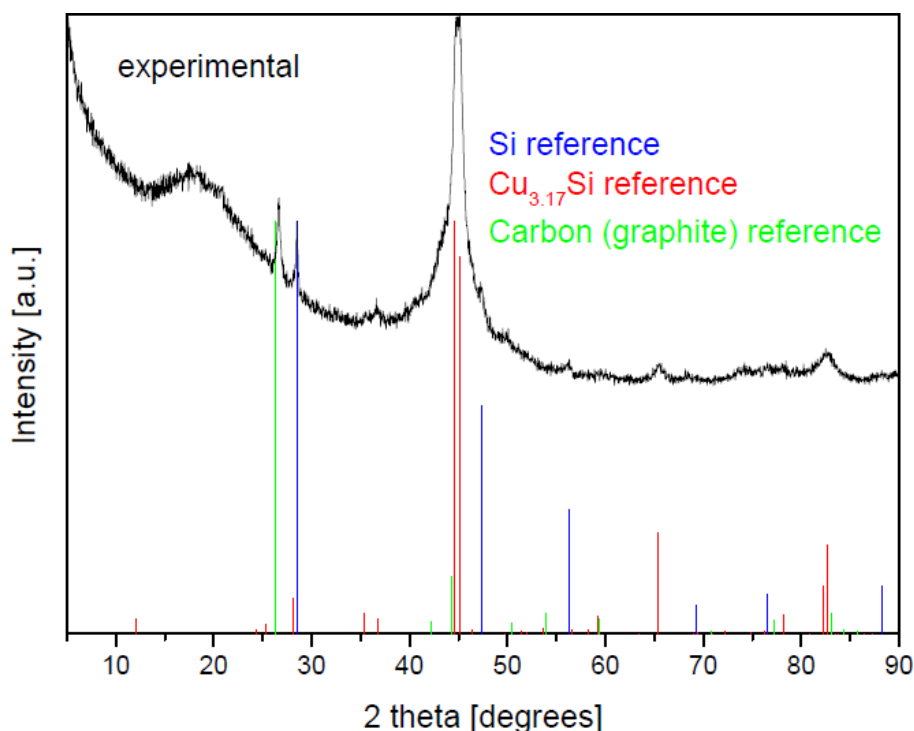
Fig. 5.27: XRD powder pattern of ball milled LiCu$_2$Si, graphite and one equivalent of Si (black curve).

The sample is highly amorphous and contains Si, graphite and Cu$_{19}$Si$_6$ (Cu$_{3.17}$Si). Again, no precipitation of Cu was observed. Instead, the addition of Si leads to the decomposition of LiCu$_2$Si into a coppersilicide compound. It is believed that the as-formed passivation layer of Cu$_{19}$Si$_6$ on the surface of LiCu$_2$Si upon delithiation was constantly pulverized during ball milling, leading to the decomposition of LiCu2Si. Comparing to ball-milling with graphite (section 5.3), the addition of Si leads to the formation of Cu$_{19}$Si$_6$ upon decomposition of LiCu$_2$Si.

Electrochemical performance

Electrodes were prepared in an argon filled glove box, where Super P (19 wt. %) was added as conductive additive and PVDF used as a binder (12 wt. %). 1 M LiPF$_6$ in ethylenecarbonate / dimethylcarbonate (1:1) was used as electrolyte. The sample was cycled between 20 mV and 3.0 V vs. Li/Li$^+$ at a rate of 20 mA g$^-$

<superscript>1</superscript>. The initial step was charge (delithiation) and values for specific capacity refer to the composite material. The galvanostatic measurement of this material is shown in Figure 5.28 below.
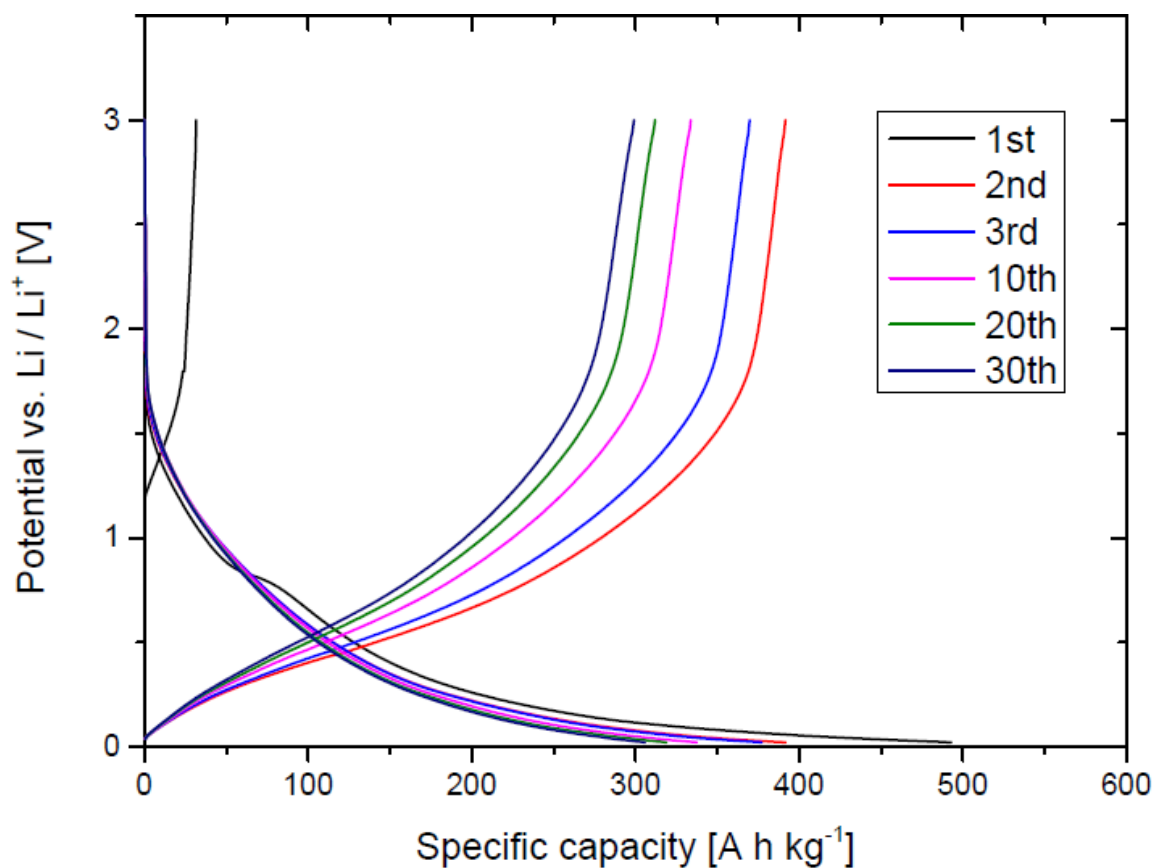
Fig. 5.28: Galvanostatic measurement of ball milled $LiCu_2Si$, graphite and one equivalent of Si, where the first 30 cycles are shown.

During first charge, a capacity of 30 mAh g^{-1} was obtained indicating that only a small amount of Li was extracted from starting material. There is an irreversible capacity loss of 105 mAh g^{-1} after first cycle (21 %) followed by a slow capacity decay during subsequent cycles. The measurement looks similar to the one without addition of Si (Fig. 5.22), except obtained capacities are slightly lower. The cyclic voltammetry measurement of this mixture is shown in Figure 5.29.
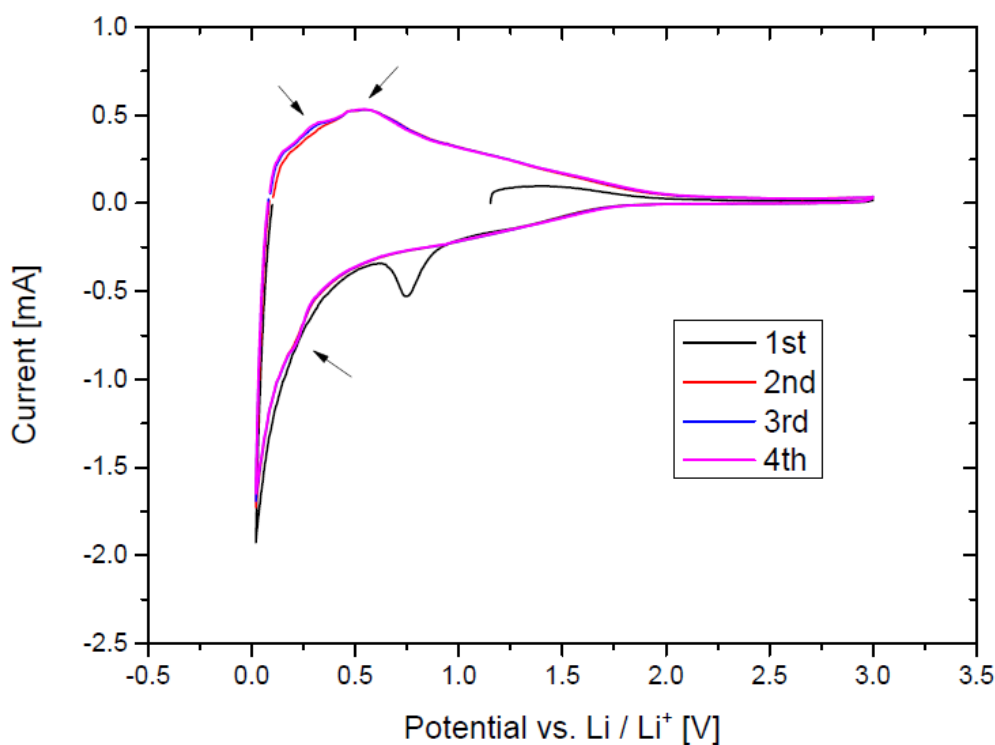
Fig. 5.29: CV measurement of ball milled LiCu$_2$Si, graphite and one equivalent of Si, where the first 4 cycles are shown. The sample was cycled from 20 mV to 3.0 V vs. Li/Li$^+$ at a rate of 0.05 mV s^{-1}. The initial step was charge (delithiation).

During first cycle, there is a reduction peak appearing at 0.7 V which is no longer present in the subsequent cycles. This is addressed to the initial SEI formation. During subsequent cycles, small peaks appear at 330 and 530 mV for oxidation and 200 mV for reduction, respectively, clearly identifying Si as the electrochemically active species.

To summarize, the addition of Si did not improve the cycling behavior of this composite material. The maximum capacity was increased with higher amount of Si used, but at the same time, the rate for capacity decay was enhanced leading to an overall worse cycling behavior.

5.4. Conclusion

Electrochemical extraction of Li from pure $LiCu_2Si$ was not successful, which is believed to be caused by the formation of a passivation layer of $Cu_{19}Si_6$ on the surface of the ternary particles, therefore hindering further lithium extraction from $LiCu_2Si$. Chemical reaction of $LiCu_2Si$ and $FePO_4$ lead to the formation of $LiFePO_4$ and $Cu_{19}Si_6$. Cycling of $LiFePO_4$ was successfully demonstrated in a sample using 10 Vol. % $LiCu_2Si$. Cu precipitation upon reaction of $LiCu_2Si$ and graphite was observed and the as formed amorphous silicon was identified as the electrochemically active material. The following addition of Si did not improve the cycling behavior of this composite material. The maximum capacity was increased with higher amount of Si, but at the same time, the rate for capacity decay was enhanced leading to an overall worse cycling behavior.

6. Composite formation by pyrolysis of organic polymers and of silicon particles

6.1. Introduction

In this chapter, a number of methods for composite formation with silicon via pyrolysis of organic polymers are examined. The aim of the pyrolysis of a polymer is to form a matrix which is a good electronic as well as lithium ion conductor and contains the silicon particles in a flexible manner. Thus, the volume expansion during lithiation of silicon should be buffered and the formation of SEI controlled. The main idea of this work is to use commercially available and air-stable silicon microparticles which are not expensive and do not cause toxicological and environmental thread which are often related with nanoparticles. Moreover, this methodology does not require any complex processing, which is a requirement for large scale applications. During pyrolysis, polymers are degraded, releasing different gaseous products and forming a carbonaceous matrix. A crucial property of the polymer is its decomposition temperature, which should be as low as possible in order to avoid side reactions like siliconcarbide formation. Good solubility in a common solvent is also indispensable for a suitable processing. Three different types of polymers were examined: polyacrylonitrile (PAN), polyvinylpyrrolidone (PVP) and polystyrene (PS). They are all elastomers which melt during the heating process and coat the silicon particles uniformly. Additionally, lactose monohydrate was examined as a carbon source in analogous manner.

A general synthetic approach is described here: *Silicon particles and the polymer are mixed in a convenient solvent so that the polymer is dissolved and a good dispersion of the silicon particles is obtained. The suspension is heated*

while stirring vigorously to evaporate the solvent which leads to the formation of a thin film. The product is ground, put inside an Al_2O_3 boat and then heated inside a horizontal furnace under constant argon flow (ca. 1 l h^{-1}).

A general electrode formulation process can be described as follows*: Super P (TIMCAL) is used as a conductive additive and carboxymethyl cellulose (CMC) as a binder.*

$$R = H \text{ or } CH_2CO_2H$$
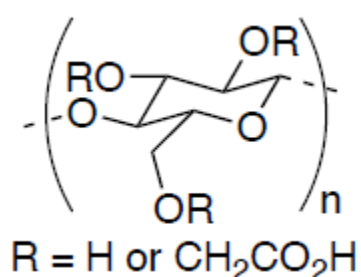
Fig. 6.1: Basic structural unit of CMC.

The ball-milled material and Super P are ground using a mortar, a viscous solution consisting of 3 wt. % CMC in H_2O is added and the mixture is mixed vigorously. The resulting black slurry is transferred onto a Cu foil and a thin film is prepared using the doctor blade technique. Electrode disks with a diameter of 12 or 15 mm are cut out and dried in a vacuum oven at 80 °C overnight.

6.2. Polyacrylonitrile

Polyacrylonitrile is a synthetic polymer with the sum formula $(C_3H_3N)_n$. The basic unit of PAN is shown below in Figure 6.2.
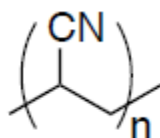
Fig. 6.2: Basic building unit of PAN.

When treated at 300 °C in an inert atmosphere, cyclization of PAN occurs without carbonization leading to a pyridine based conjugated polymer.[106-108] Like in graphite, such pyridine rings have delocalized sp^2 π bonds fostering a good intrinsic electronic conductivity.[109-110] When treated at temperatures above 500 °C in an inert atmosphere, carbonization and graphitization of PAN will occur accompanied with the release of N_2 [111-112], as sketched in Figure 6.3 below.
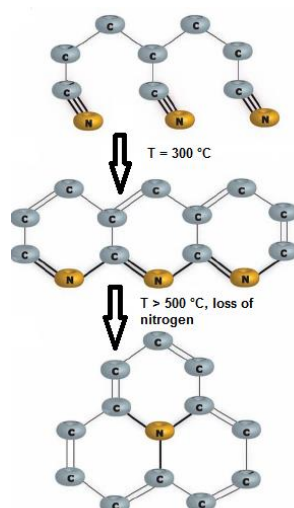
Fig. 6.3: Mechanisms of cyclization of PAN at 300 °C and of carbonization at temperatures above 500 °C in an inert atmosphere.[113]

Multiple approaches have been reported to coat Si particles by pyrolysis of PAN. In 2011, Cui et al.[114] mixed silicon nanoparticles with 10 wt. % PAN to form a slurry, which was then bladed onto a stainless steel current collector. The PAN in the electrode film was then carbonized at 700 °C for 2 h in argon to form C coated interlinked Si nanoparticles. However, the performance of such composites was not satisfying, so an additional step had to be added: CVD of silane at 500 °C to deposit a thin layer of α-Si, which works as inorganic glue by fusing the silicon particles together and bind them to the current collector. With this methodology, micron sized Si particles were cycled with a limited capacity of 800 mAh g^{-1} for 200 cycles without a significant capacity loss. A similar approach has been reported in 2012 by Biswal et al.[115] using macroporous silicon and PAN, which was pyrolyzed at 550 °C for 1 h in argon. For these composite materials, a specific capacity of 1000 mAh g^{-1} over 600 cycles was reported. Note that in both citations, no additional binder was used: Pyrolyzed PAN was employed, both as a binder and as conductive additive, respectively.

In 2013, Lee et al. reported another approach for a Si/PAN composite material.[113] Instead of pyrolyzing PAN at temperatures above 500 °C, they utilized cyclized PAN as additive. Cyclization of PAN occurs at 300 °C in inert atmosphere and the polymer has a good intrinsic electronic as well as good ionic conductivity. Coating of cyclized PAN isolates the Si particles from organic liquid electrolyte (and therefore prevents SEI growth) and inhibits aggregation of the nanoparticles. Again, cyclized PAN was used, both as binder and as conductive additive. A cyclized PAN / nano Si composite material was reported to preserve a specific capacity of 1500 mAh g^{-1} for 150 cycles. However, film

thickness of the as prepared electrodes was only 10 µm and the load of Si particles was very low (0.5 to 0.6 mg per electrode).

The main difference between the abovementioned studies and this work is the use of micron sized Si particles. It is well known that cycling behavior of nano sized Si particles is much better than the one of its micron sized counterparts due to the reduced size. However, the price of nanoparticular educts is much higher and toxological and environmental hazards are an issue then. Electrodes with a high material load were tested in order to fit industrial standards. Moreover, electrode formulation according to industrial standards by use of an additional binder (CMC) in aqueous solution as well as the use of Super P as C additive was employed. No expensive silicon based particle geometries were used and only cheap and cost efficient processes suitable for industrial upscale are being examined. Additionally, reduced graphiteoxide was tested as an additive instead of Super P.

Synthesis

Si powder (8 µm, 99.995%, ABCR) and commercially available PAN (Aldrich) in respective weight ratios (see below) are mixed together. The mixture is then dissolved in N, N-dimethylformamide (DMF) and heated at 150 °C while stirring vigorously to slowly evaporate the solvent. A dark brown film is obtained which is cut into smaller pieces using a knife and afterwards ground. The ground sample is put in an Al$_2$O$_3$ crucible boat and then heated in a horizontal furnace under constant argon flow (ca. 1 l h^{-1}).

Three different heat treatment programs were examined: 750 °C for 6 h, 1000 °C for 10 h and 300 °C for 12 h, each resulting in different pyrolysis products of PAN, which is manifested in the carbon to nitrogen weight ratio determined by elemental analysis.

6.2.1. Pyrolysis at 750 °C

Examined mixtures as well as carbon and nitrogen weight contents determined by elemental analysis are listed in Table 1.

Tab. 1: Examined Si / PAN mixtures pyrolyzed at 750 °C for 6 h.

Si : PAN weight ratio	Carbon content after pyrolysis [wt. %]	Nitrogen content after pyrolysis [wt. %]
2 : 3	31.40	5.91
1 : 1	25.18	5.25
7 : 3	10.47	1.97
4 : 1	5.89	1.19

Weight ratios of carbon to nitrogen are in the range of 4.8 to 5.3 for examined samples. Untreated PAN contains a carbon to nitrogen weight ratio of 2.6, indicating a significant decrease of the nitrogen content after pyrolysis at 750 °C. It can be concluded that graphitization of PAN occurred accompanied by the loss of N_2. A sample powder pattern for these pyrolyzed mixtures is shown in Figure 6.4.
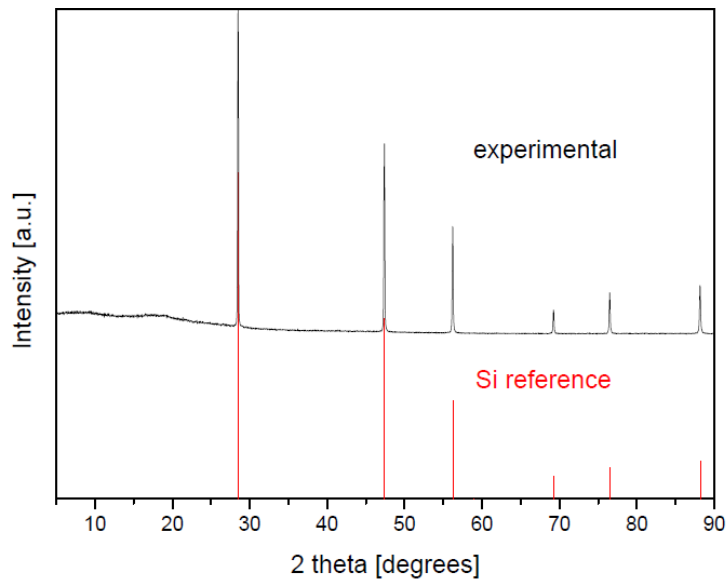
Fig. 6.4: Sample XRD powder pattern of the pyrolyzed composite (black curve). The red lines correspond to a calculated pattern of α-Si.

According to the powder pattern, the pyrolyzed product consists of crystalline silicon (α−Si). The weak broad buckle at a 2 θ= 18 ° is caused by paraffin oil, which was used to adhere the powder to the sample holder.

TEM analysis of a pyrolyzed mixture containing Si and PAN in a 1:1 weight ratio is shown in Figure 6.5. The carbon coating on the surface of the silicon particles can be clearly seen.
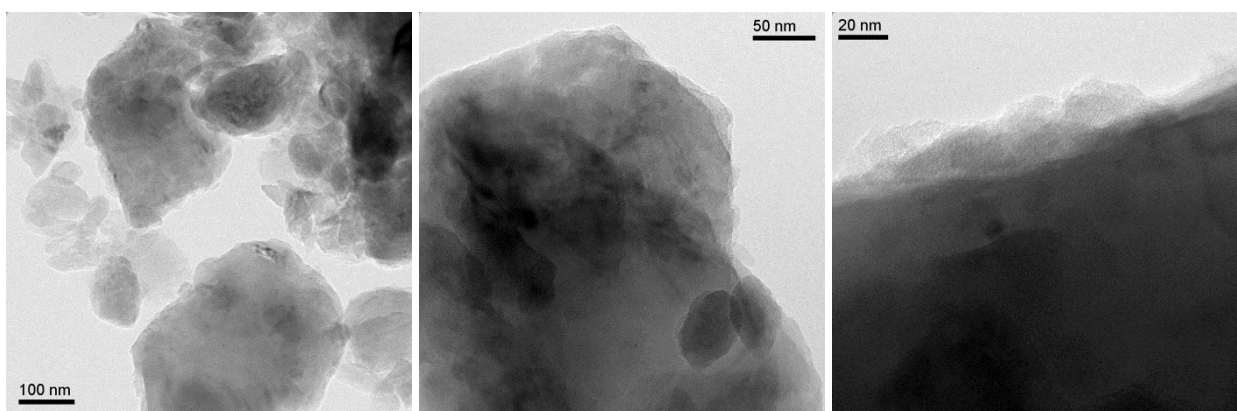
Fig. 6.5: TEM micrographs of a mixture containing Si and PAN in a 1:1 weight ratio after pyrolysis at 750 °C.

210

Electrochemical performance

Thin film electrodes (film thickness: 0.3 mm) on a copper foil were prepared using the doctor blade technique. Electrode disks with a diameter of 12 mm were cut out with a content of active material between 2.5 and 3.0 mg. Super P was added as conductive additive (25 wt. %) and CMC was used as a binder (10 wt. %). 1 M LiPF6 in ethylenecarbonate/dimethylacarbonate (1:1) was used as electrolyte. The samples were cycled between 10 mV and 2.0 V vs. Li/Li$^+$ at a rate of 200 mA g^{-1}. Discharge capacity was limited to 1200 mAh g^{-1} for the composite to improve cycling performance due to smaller volume changes of silicon. The initial process was discharge (lithiation) and values for specific capacity refer to the composite material.
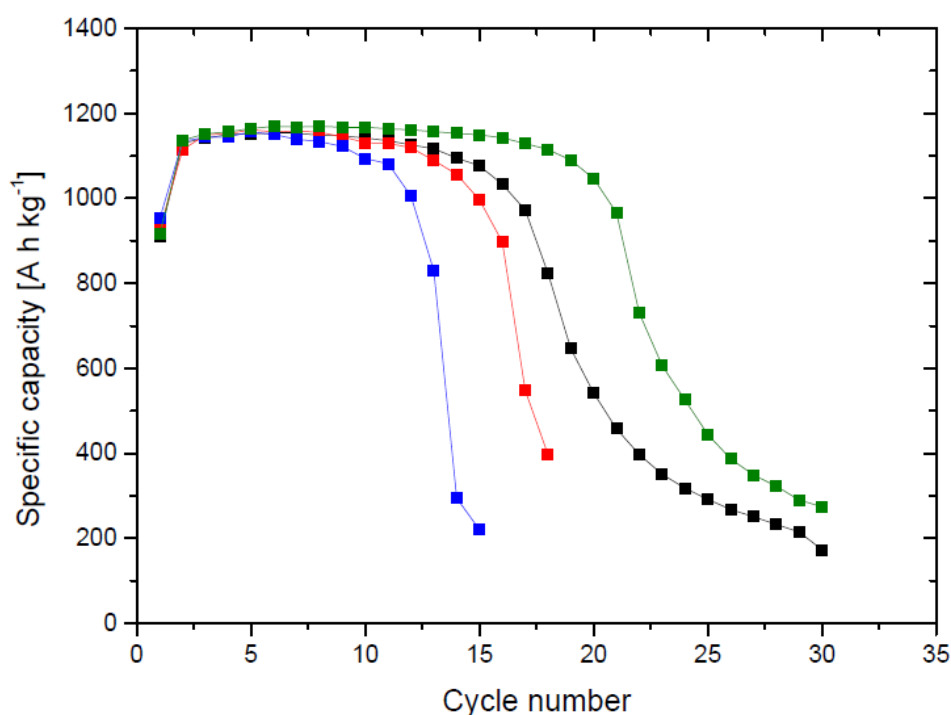
Fig. 6.6: Specific capacity vs. cycle number for composites containing Si and PAN in different weight ratios, pyrolyzed at 750 °C for 6 h in argon. Only the charge capacities are shown. The performance of mixtures containing Si and PAN in weight ratios of 2:3 are shown in green, 1:1 in black, 7:3 in red and 4:1 in blue, respectively.

211

For all samples, the initial Coulombic efficiencies are low ranging from 75.8 to 79.6% of the theoretical value. There is a big increase of this value in the subsequent cycles to 97.5% which must be assigned to an activation of the silicon. Additionally, there is an abrupt decay of capacity after a certain number of cycles ranging from 12 to 20 cycles dependent on the experimental conditions. This behavior is believed to be caused by pulverization of the electrode. It can be seen that the electrochemical performance improves with increasing C content of the pyrolyzed mixtures. A mixture containing Si and PAN in a weight ratio of 2:3 shows a stable charge capacity for 20 cycles, whereas for an analogous 4:1 mixture, a stable charge capacity is only obtained for 12 cycles. This effect is believed to be caused by an improved and more uniform coating or to a more flexible matrix at higher carbon content.

However, film thickness is a crucial parameter for electrochemical performance. In general, thinner films show better performance due to shorter diffusion paths for Li^+ ions and improved morphology – thick films on a Cu foil made of a viscous slurry show more inhomogeneity and cracks than their thinner films. On the other hand, thin films contain a lower amount of active material, reducing their volumetric capacities.

The influence of film thickness on electrochemical performance is examined in the following section for a sample containing Si and PAN in a weight ratio of 4:1, pyrolyzed at 750 °C.

Tab. 2: Electrodes prepared with a Si / PAN mixture of 4:1 wt. ratio pyrolyzed at 750 °C for 6 h in Ar.

Doctor blade film thickness [µm]	Film thickness after drying[1] [µm]	Content of active material per electrode [mg]
300	130	2.7
250	100	2.3
200	80	2.0
150	45	0.5

[1] Film thickness after drying in a vacuum oven has been determined using Micromahr 40 ER from Mahr Co.
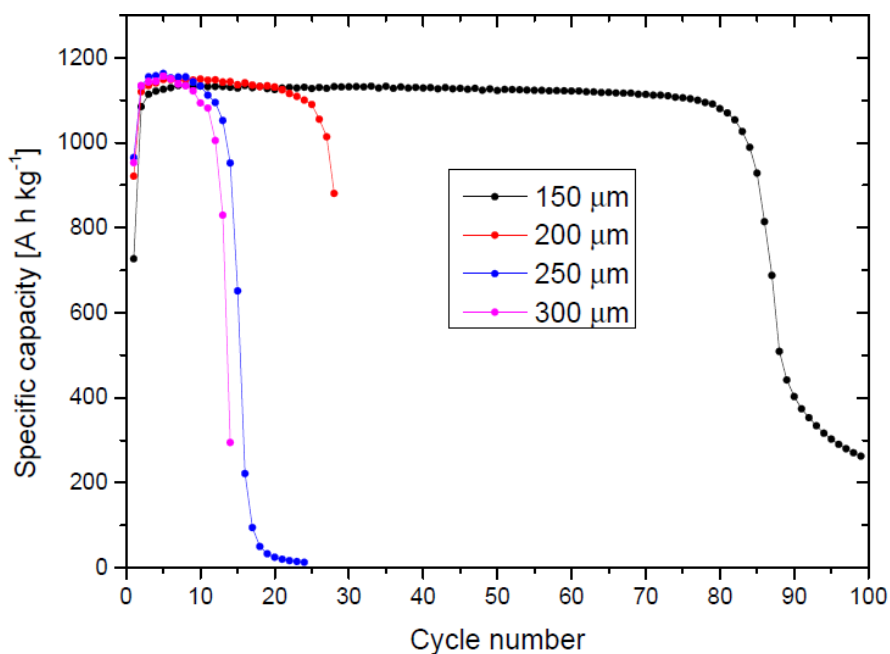
Fig. 6.7: Specific capacities vs. cycle numbers for composite films containing Si and PAN in a 4:1 wt. ratio, pyrolyzed at 750 °C for 6 h in argon. The performances of electrodes with different thicknesses is shown, where discharge capacity was limited to 1200 mAh g^{-1} for the composite and only charge capacities are depicted.

The performances of the two thickest electrodes is comparable, whereas a slight upgrade for the 200 μm thick film is observed with a stable capacity over 25 cycles. However, a drastic increase of capacity retention is shown for a 150 μm thin film and a stable charge capacity is obtained for more than 80 cycles. As a conclusion, films with lowest thickness show by far the best electro-chemical performances. This seems to be a clear indication for mechanical stress as the main reason for disintegration and capacity losses.

Thus the film thickness and consequently the load of active material are believed to be the critical parameters here: There is a linear decrease of active material load with decreasing film thickness for the first 3 electrodes and, at the same time, an increase of cycling stability. The 150 μm thin film has a significantly lower load of active material per electrode of only 0.45 mg cm^{-2}. A plot of film thickness vs. cycle-life clearly indicates to an asymptotic behavior with some uncertainty on the final course of the curve for very thin films as shown in Figure 6.8.

Tab. 3: Electrode characteristics of Si / PAN composites (4:1 wt.) pyrolyzed at 750 °C for 6 h in Ar for different film thickness.

Doctor blade film thickness [μm]	Film thickness after drying [μm][1]	Load of active material of electrode [mg cm^{-2}]	Number of stable cycles, whith charge capacity > 1100 mAh g^{-1}
300	130	2.39	10
250	100	2.04	12
200	80	1.77	25
150	45	0.45	80

Fig. 6.8: Effective film thickness vs. cycle number for Si / PAN composites (4:1 wt.) pyrolyzed at 750 °C for 6 h in Ar. The cycle numbers given are those for which the charge capacity was larger than 1100 mAh g^{-1}.

The spline fit of the data in Figure 6.8 results in the formula

$$F_t = 372(100)\ \mu m \cdot C_m^{-0.49(10)} \tag{6.1}$$

with C_m = maximum cycle number at a charge capacity of more than 1100 mAh g^{-1} and F_t = effective film thickness. Extrapolation of this formula for 500 cycles reveals a necessary effective film thickness of 18 μm.

Additionally, 0.15 mm thick films of Si and PAN at a weight ratio of 4:1 were tested at higher discharge capacity limits for the composite of 1500 mAh g^{-1}

and 2000 mAh g^{-1} corresponding to nearly complete conversion to $Li_{12}Si_7$ and to $Li_{14}Si_6$, respectively.
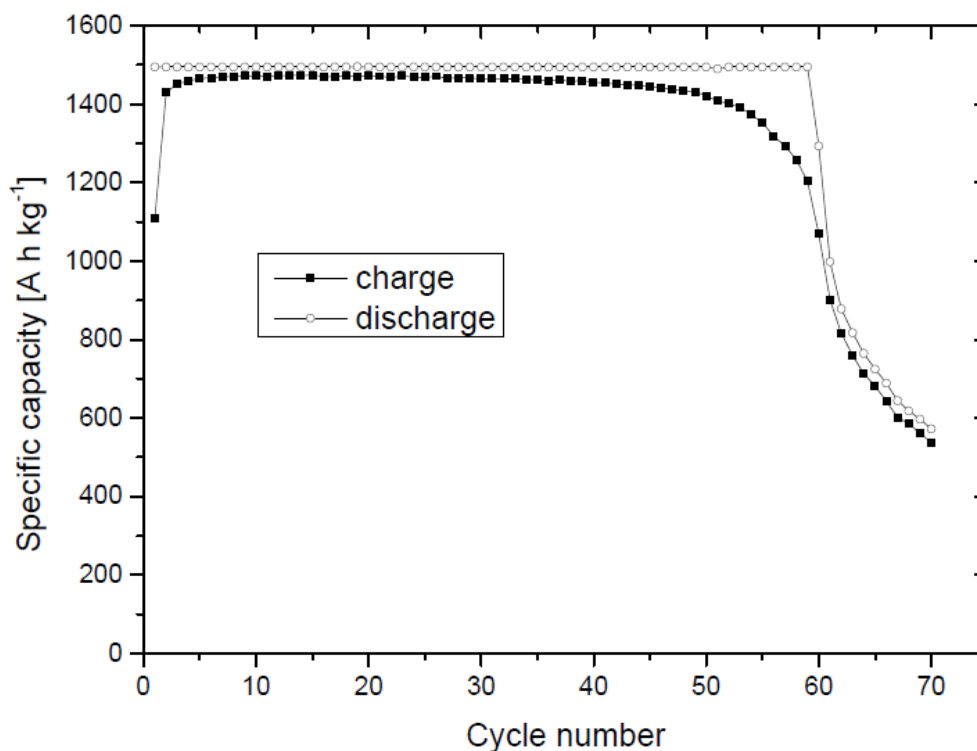
Fig. 6.9: Specific capacity vs. cycle number for a composite of Si and PAN in 4:1 weight ratio, for a maximal discharge capacity of the composite limited to 1500 mAh g^{-1}.

For the first cycle a low initial Coulombic efficiency of 74.2% is obtained. This value increases during subsequent cycles up to a maximum value of 98.7% indicating to fast activation of the full silicon volume. A stable charge capacity is recorded for 52 cycles, before an abrupt decay of capacity occurs.
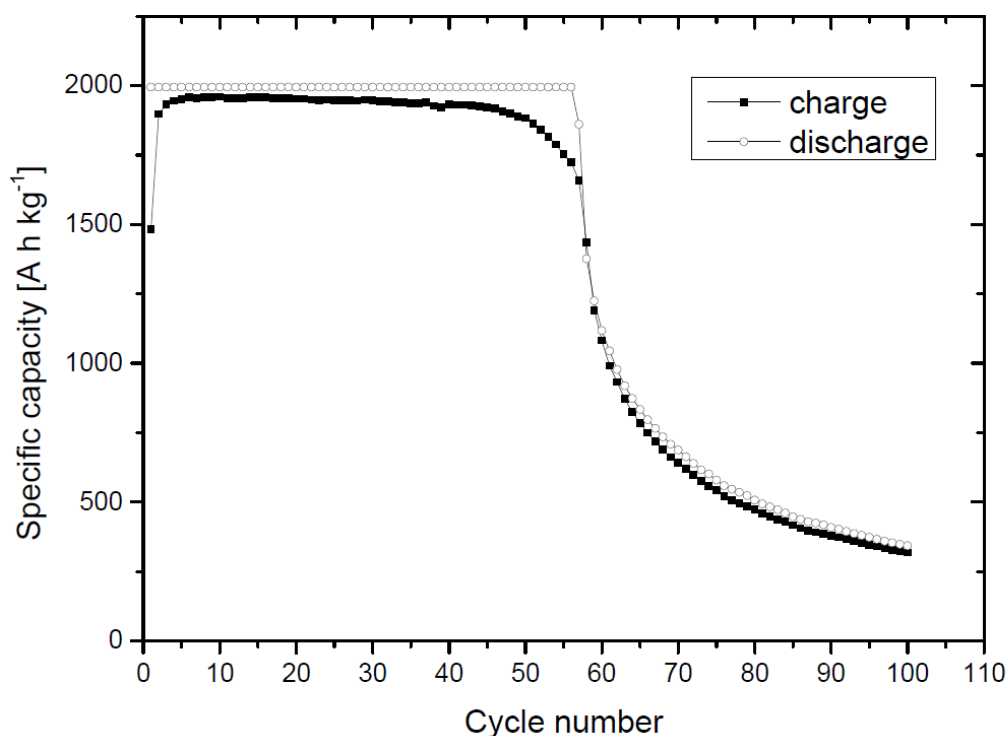
Fig. 6.10: Specific capacity vs. cycle number for a composite of Si and PAN in 4:1 weight ratio, with a maximal discharge capacity of the composite limited to 2000 mAh g^{-1}.

A low initial Coulombic efficiency of 74.2% is obtained followed by an increase during subsequent cycles up to a maximum value of 98.2%. A stable charge capacity ≥ 1900 mAh g^{-1} is observed for 50 cycles, before an abrupt decay of capacity occurs after 55th cycle.

As a conclusion, a stable charge capacity was obtained for 52 cycles when discharge capacity of the composite was limited to 1500 mAh g^{-1} and 50 cycles for a limited discharge capacity of 2000 mAh g^{-1}, respectively. As expected, the number of stable cycles is lower than for a lower discharge capacity limited to 1200 mAh g^{-1}. These findings clearly support the understanding that the main problem remains the volume expansion of Si particles due to the induced mechanical stress. The larger the volume work, the lower the cycle life. It is not

understood though why the electrode exhibits a stable cycling for quite a while and then undergo catastrophic decay. It should be noted, that the electrochemical performance of the 0.15 mm thick electrodes is remarkable even at higher discharge capacities. The reason for this capacity decay is examined in the next section using post mortem analysis.

Post mortem analysis

A 300 µm thin electrode film of a mixture containing Si and PAN (2:3 wt.), treated at 750 °C for 6 h, was examined after 20 cycles in a Li ion battery:

The electrode contains 65 wt. % active material, 25 wt. % conductive additives (Super P) and 10 wt. % binder (CMC). 1 M $LiPF_6$ in ethylenecarbonate / dimethylcarbonate (1:1) was used as electrolyte. The sample was cycled between 10 mV and 2.0 V vs. Li/Li$^+$ at a rate of 200 mA g^{-1}. The initial step was discharge (lithiation) and 20 full charge/discharge cycles were performed. The battery cell was opened in air and the electrode material washed with THF to remove the remaining electrolyte. Figure 6.11 shows the obtained XRD powder pattern of the black material.
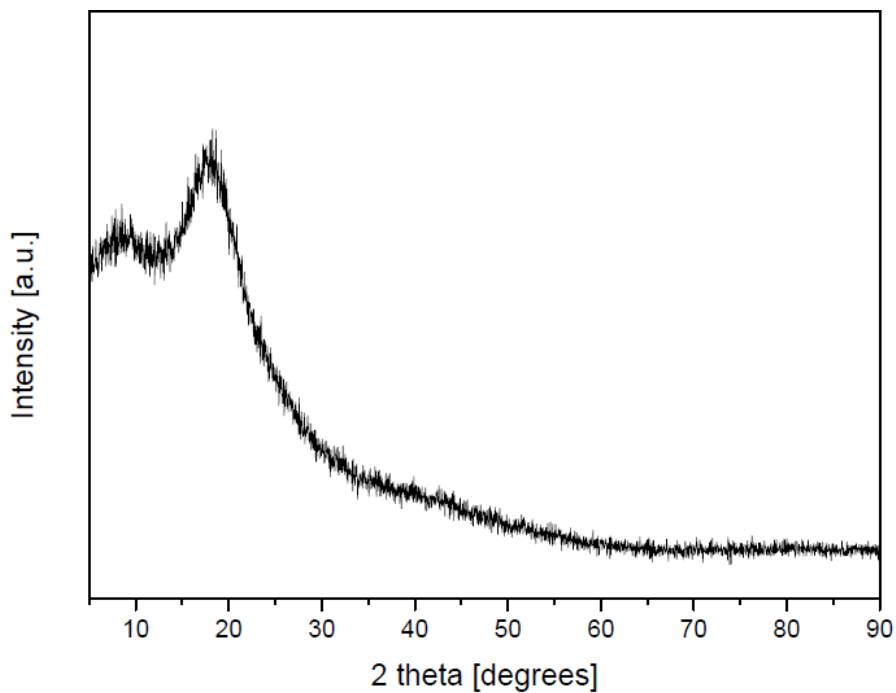
Fig. 6.11: XRD powder pattern of a mixture containing Si and PAN (2:3 wt.), treated at 750 °C for 6 h, after 20 cycles in a Li ion battery (black curve).

The sample is amorphous indicating that Si has become amorphous during cycling in Li ion battery which is in accordance with literature. The broad peak at $2\theta = 18$ ° is caused by paraffin oil, which was used to adhere the powder to the sample holder. SEM micrographs of the electrode material are shown in Figure 6.12.
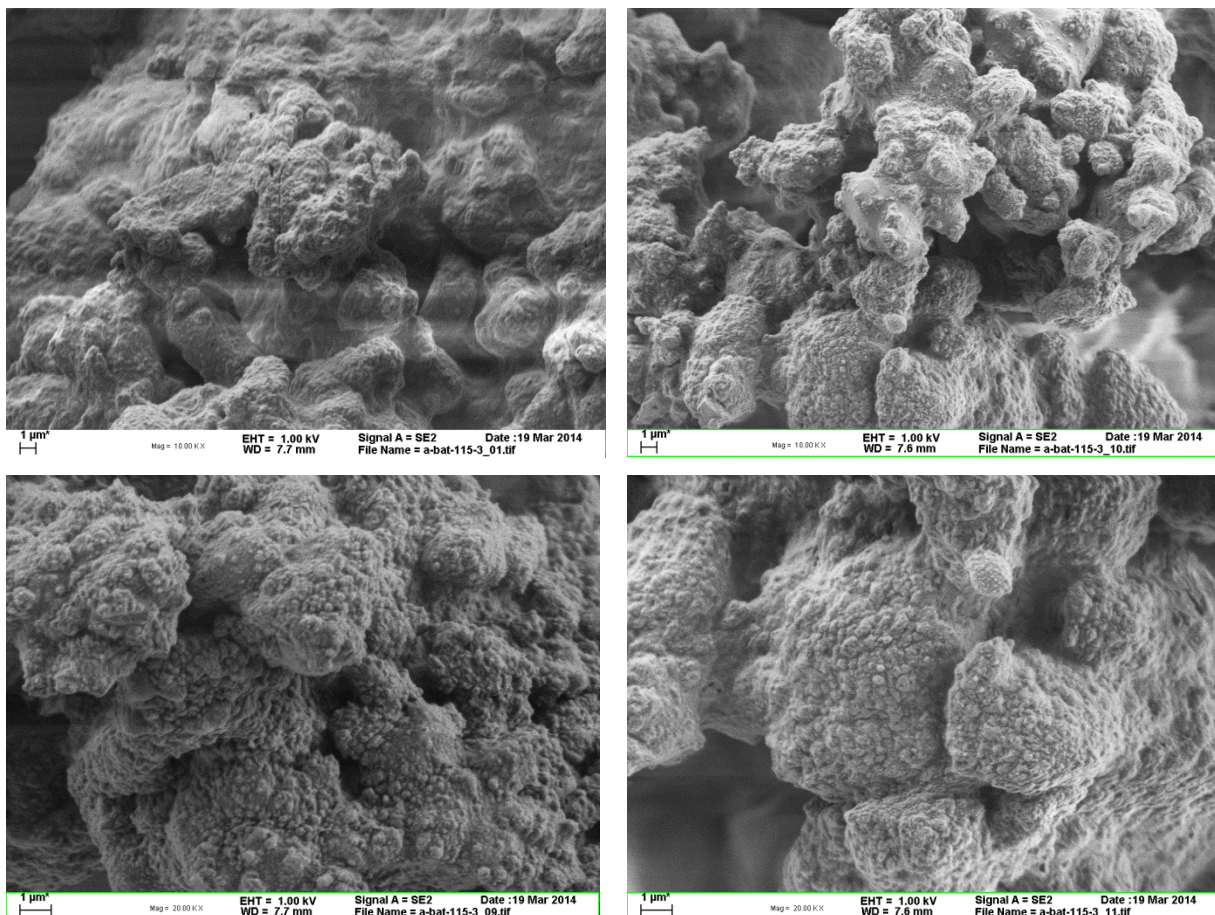
Fig. 6.12: SEM analysis of a mixture containing Si and PAN (2:3 wt.), treated at 750 °C for 6 h, after 20 cycles in a Li ion battery.

After 20 cycles in Li ion battery, the sample looks highly amorphous and all particles are coated completely by a thin film, which is believed to be a steadily growing SEI layer. This conjecture is manifested by TEM analysis shown in Figure 6.13; it can be seen that the particles are wrapped completely inside multiple thin layers.
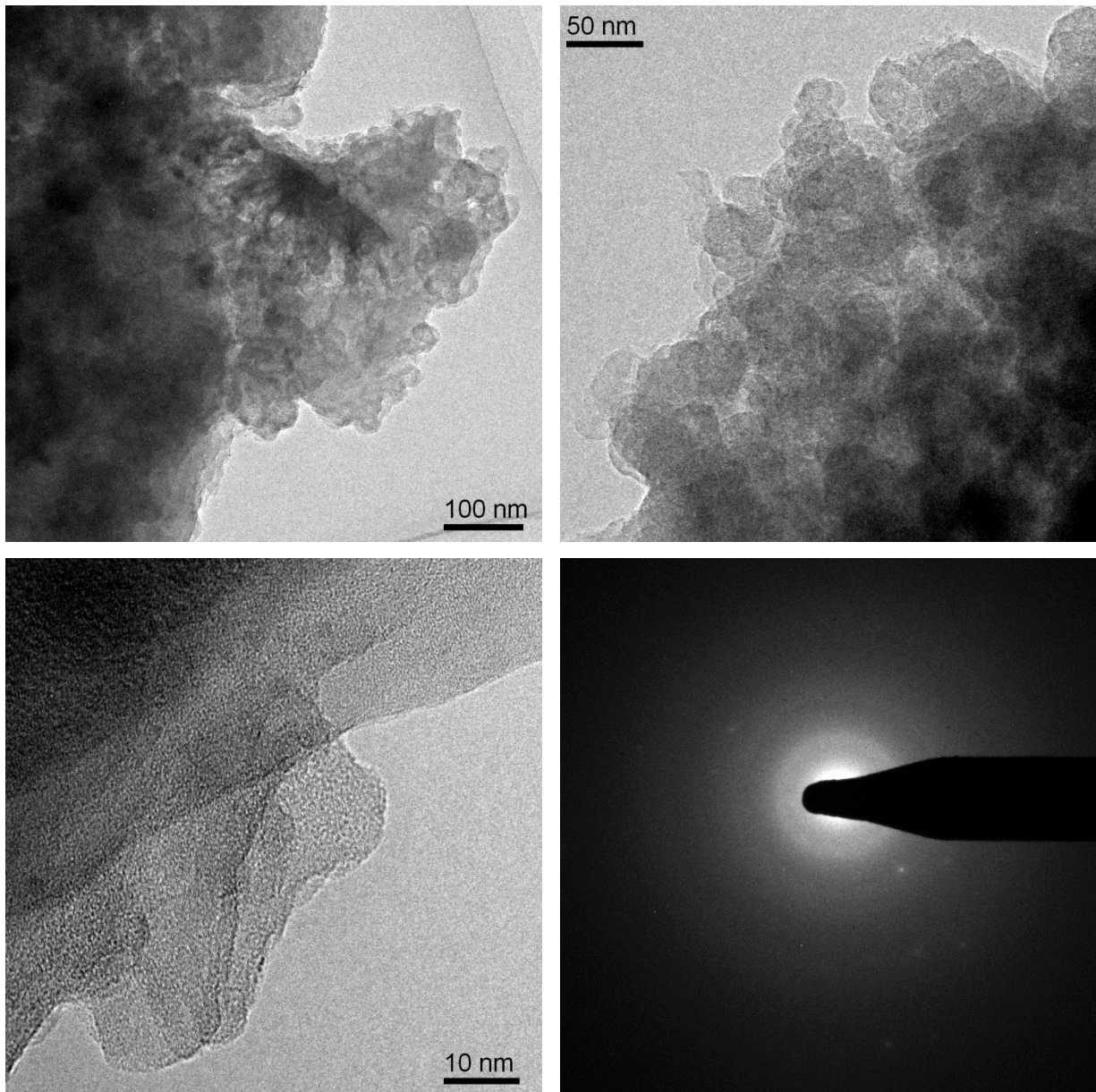
Fig. 6.13: TEM analysis of a mixture containing Si and PAN (2:3 wt.), treated at 750 °C for 6 h, after 20 cycles in a Li ion battery.

As a conclusion, capacity fading is caused mainly by the growing insulating SEI layer on the surface of particles due to cracking of electrode. The stable cycling of the electrode for a given number of cycles followed by an abrupt decay of capacity leads to the following assumptions:

The limitation of the discharge capacity to 1200 mAh g^{-1} for the composite prevents maximum lithiation of the silicon particles, leading to a smaller

volume increase and therefore to an enhanced mechanical stability of the electrode. However, cracking of the electrode will occur after a given number of cycles, meaning that some Si particles lose electrical contact to the current collector. Due to limitation of capacity, the remaining silicon particles with preserved electrical integrity will still be able to deliver the required capacity. This is accompanied to a higher degree of lithiation and consequently a higher volume change further reducing mechanical stability of electrode. This will continue until the point where the required capacity for the capacity implies full lithiation of Si particles in contact with current collector (breaking point). At this point, rapid pulverization of the electrode and abrupt decay of the capacity occurs, respectively.

Thin film electrodes have the advantage of an improved surface morphology as well as a lower possibility of fracture sites due to limited height. Thus, the initial cracking of the electrode will happen after a higher number of cycles. Nevertheless, the breaking point is inevitable leading to an abrupt decay of capacity. However, compared to thicker electrode films, this will happen after a higher number of cycles.

6.2.2. Pyrolysis at 1000 °C

A sample containing Si and PAN in a weight ratio of 1:1 is treated at 1000 °C for 10 h in argon. Elemental analysis after pyrolysis reveals a carbon content of 23.19 wt. % and a nitrogen content of 1.36 wt. %, respectively. Compared to a sample of the same composition treated at 750 °C, the final C content is in the same range, whereas the nitrogen content is significantly lowered. The weight ratio of carbon to nitrogen for a 1:1 mixture of Si and PAN was determined to 4.8 for pyrolysis at 750 °C and to 17.1 for the pyrolysis at 1000 °C. It can be concluded that a higher degree of graphitization accompanied with an

increasing loss of N_2 occurs during treatment at a higher temperatures. TEM micrographs of the composite are shown in Figure 6.14.
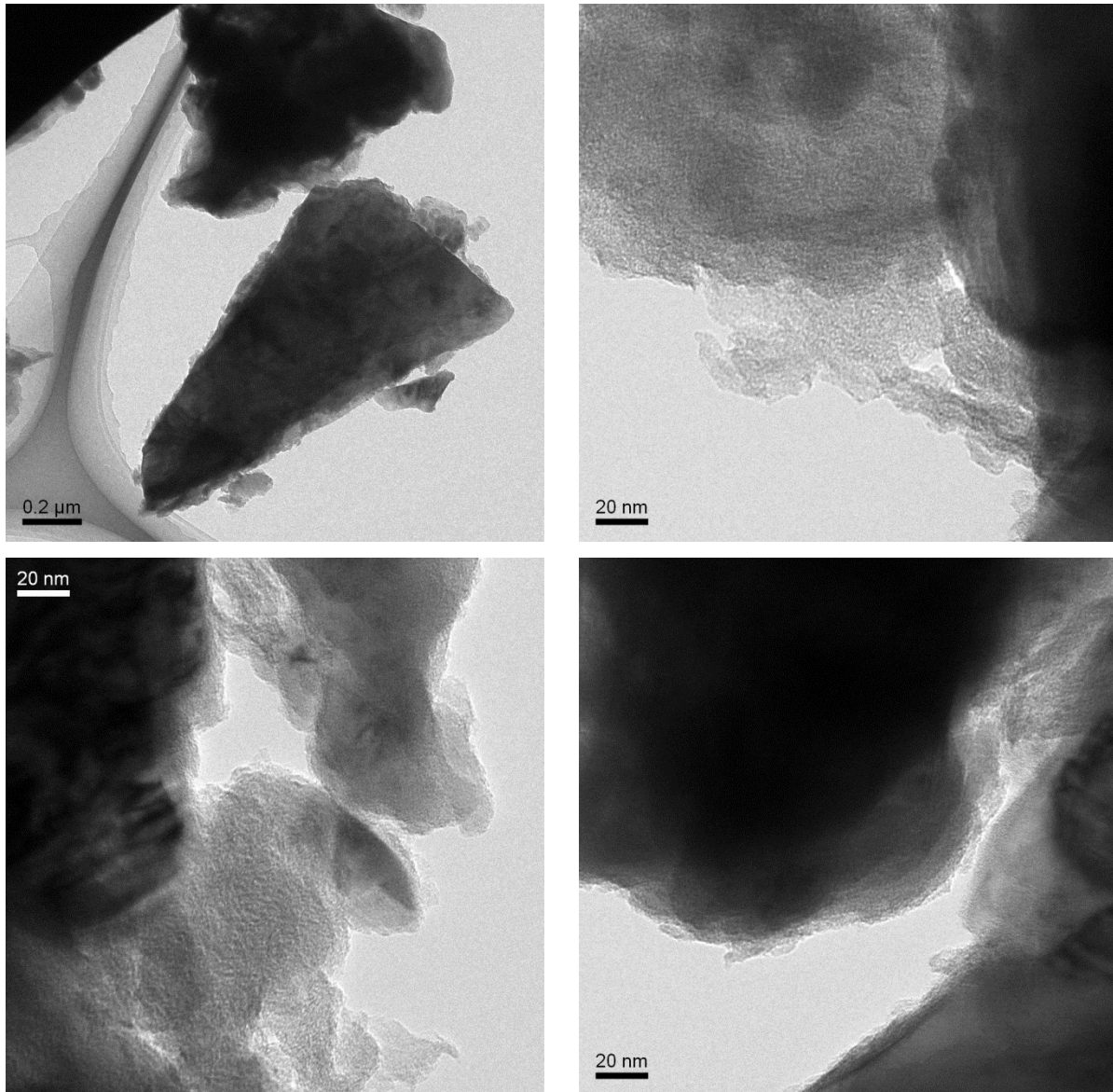
Fig. 6.14: TEM analysis of a 1:1 composite of Si and PAN, pyrolyzed at 1000 °C for 10 h in argon atmosphere.

The TEM analysis reveals thin layers of carbon on the surfaces of Si particles but these layers are not uniform.

Electrochemical performance

Thin film electrodes (film thickness: 0.3 mm) on a copper foil were prepared using the doctor blade technique. Electrode disks with a diameter of 12 mm were cut out with a content of 3.0 mg of active material. Super P was added as conductive additive (25 wt. %) and CMC was used as a binder (10 wt. %). 1 M LiPF6 in ethylenecarbonate/dimethylacarbonate (1:1) was used as electrolyte. The sample was cycled between 10 mV and 2.0 V vs. Li/Li$^+$ at a rate of 200 mA g^{-1}. Discharge capacity was limited to 1200 mAh g^{-1} for the composite to improve cycling performance due to smaller volume changes of silicon. The initial step was discharge (lithiation) and values for specific capacity refer to the composite material.
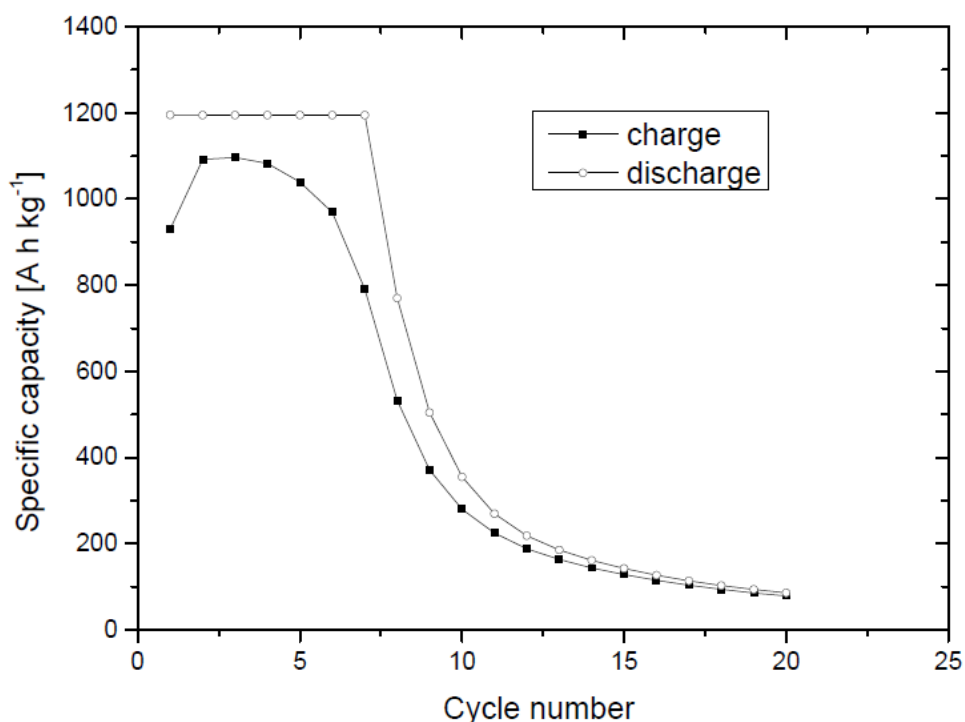
Fig. 6.15: Specific capacity vs. cycle number for a composite of Si and PAN in 1:1 weight ratio, pyrolyzed at 1000 °C. Only the first 20 cycles are shown.

Although the nitrogen content was reduced by heat treatment at 1000 °C, electrochemical cycling is not improved. Indeed, the cycling behavior is worse than for the same mixture of Si and PAN, but pyrolyzed at 750 °C (Fig. 6.6). The main reasons for this behavior are suspected on the one hand to be due to the less compact and thickness varying of the coating as shown in TEM analysis (Fig. 6.14). On the other, the loss of nitrogen and the ongoing carbonization may lead to a less flexible coating. Finally, some SiC formation cannot be excluded at this stage which would not be active in the electrode.

6.2.3. Pyrolysis at 300 °C

According to Lee et al.[113], cyclized instead of carbonized PAN was tested as composite material since it has a good intrinsic electronic as well as ionic conductivity. Cyclization of PAN occurs at 300 °C in an inert atmosphere, whereas treatment above 500 °C does lead to carbonization and graphitization accompanied by partial loss of N_2. A mixture containing Si and PAN in a weight ratio of 7:3 was therefore treated at 300 °C for 12 h in argon atmosphere. Elemental analysis reveals a carbon content of 17.27, a nitrogen content of 5.69 and a hydrogen content of 1.24 wt. %, respectively. PAN and cyclized PAN have the same composition (there is no loss of material upon cyclization). The carbon to nitrogen weight ratio of the examined sample is 3.0 and the carbon to hydrogen weight ratio is 13.9, respectively. These values are close to the theoretically expected ones of PAN, namely 2.6 and 12.0, respectively. The deviation of these values can be addressed to C impurities during synthesis or to an accuracy error of the elemental analysis. TEM micrographs of the material are shown in Figure 6.16 below and the C coating on the surface of Si particles can be clearly seen.
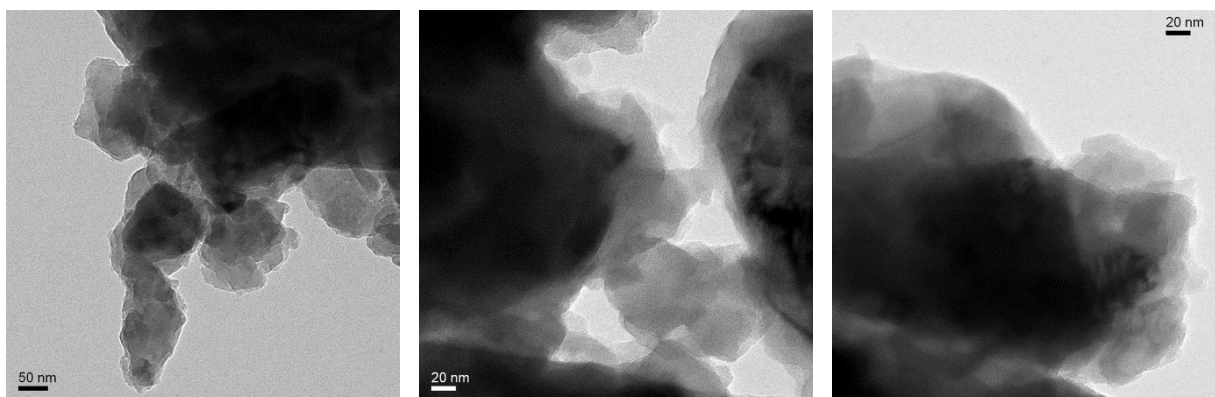
Fig. 6.16: TEM analysis of a 7:3 composite of Si and PAN, treated at 300 °C for 12 h in argon.

Electrochemical performance

Thin film electrodes (film thickness: 0.15 mm) on a copper foil were prepared using the doctor blade technique. Electrode disks with a diameter of 12 mm were cut out with a content of 1.6 mg of active material. The effective film thickness after drying was determined to 42 µm. Super P was added as conductive additive (25 wt. %) and CMC was used as a binder (10 wt. %). 1 M LiPF6 in ethylenecarbonate/dimethylacarbonate (1:1) was used as electrolyte. The sample was cycled between 10 mV and 2.0 V vs. Li/Li$^+$ at a rate of 200 mA g^{-1}. Discharge capacity was limited to 1200 mAh g^{-1} for the composite to improve cycling performance due to smaller volume changes of silicon. The initial step was discharge (lithiation) and values for specific capacity refer to the composite material.
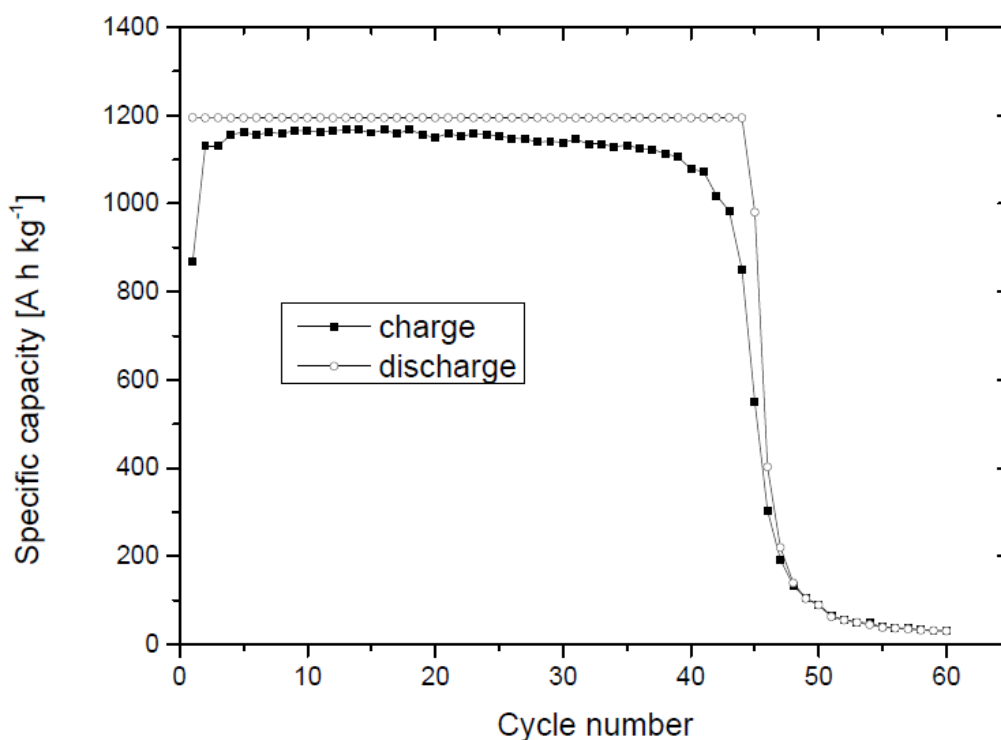
Fig. 6.17: Specific capacity vs. cycle number for a composite of Si and PAN in a weight ratio of 7:3, treated at 300 °C for 12 h.

A stable charge capacity with a maximum Coulombic efficiency of 97.5% was obtained for 39 cycles. Compared to samples with the same material load and film thickness treated at 750 °C (see section 6.2.1), this composite shows worse cycling behavior. Clearly, coating by graphitized PAN leads to a better performance than by cyclized PAN (see Fig. 6.7). Seemingly, there is an optimal pyrolysis temperature between 300 and 1000 °C which may peak in the neighborhood of 750°C.

6.2.4. Addition of reduced graphite oxide

In this section, reduced graphite oxide was tested as C additive for electrode formulation instead of Super P in order to see if improved film quality can be achieved leading to an improved electrochemical performance.

Synthesis

A mixture containing micron sized Si particles and PAN in 4:1 weight ratio, pyrolyzed at 750 °C in Ar is ball milled in air with graphite oxide powder for 90 min at a speed of 400 rpm. The ratio of composite material and carbon additive is held at the same ratio as for samples using Super P. The resulting powder was heated in argon to 170 °C for at a rate of 10 °C h^{-1} followed by heating to 230 °C at 1 °C h^{-1} in order to reduce graphite oxide. The obtained XRD powder pattern is shown in Figure 6.18 below.
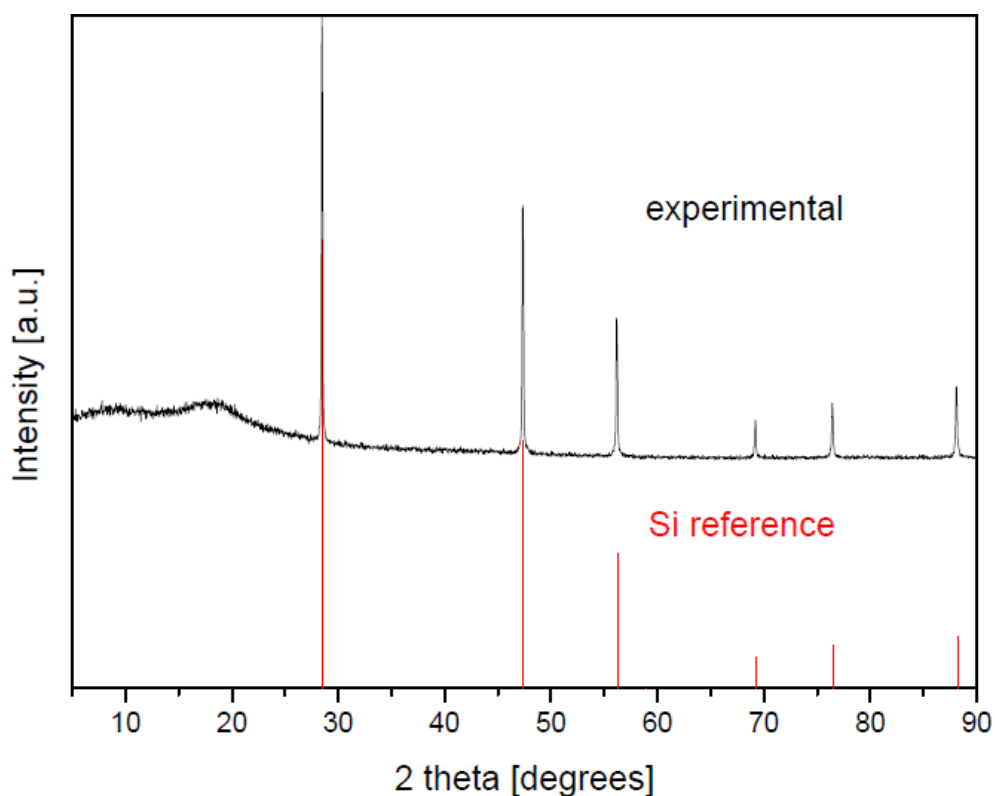
Fig. 6.18: XRD Powder pattern of a mixture containing Si and PAN in 4:1 weight ratio, pyrolyzed at 750 °C for 6 h in argon (72 wt. %) and graphite oxide (28 wt. %), heated to 240 °C in argon (black curve). The red lines correspond to a calculated pattern of α-Si.

The mixture contains amorphous material and silicon. Since the sample is highly amorphous, the reduction of graphite oxide cannot be confirmed using XRD. TEM micrographs of this composite material are shown in Figure 6.19.
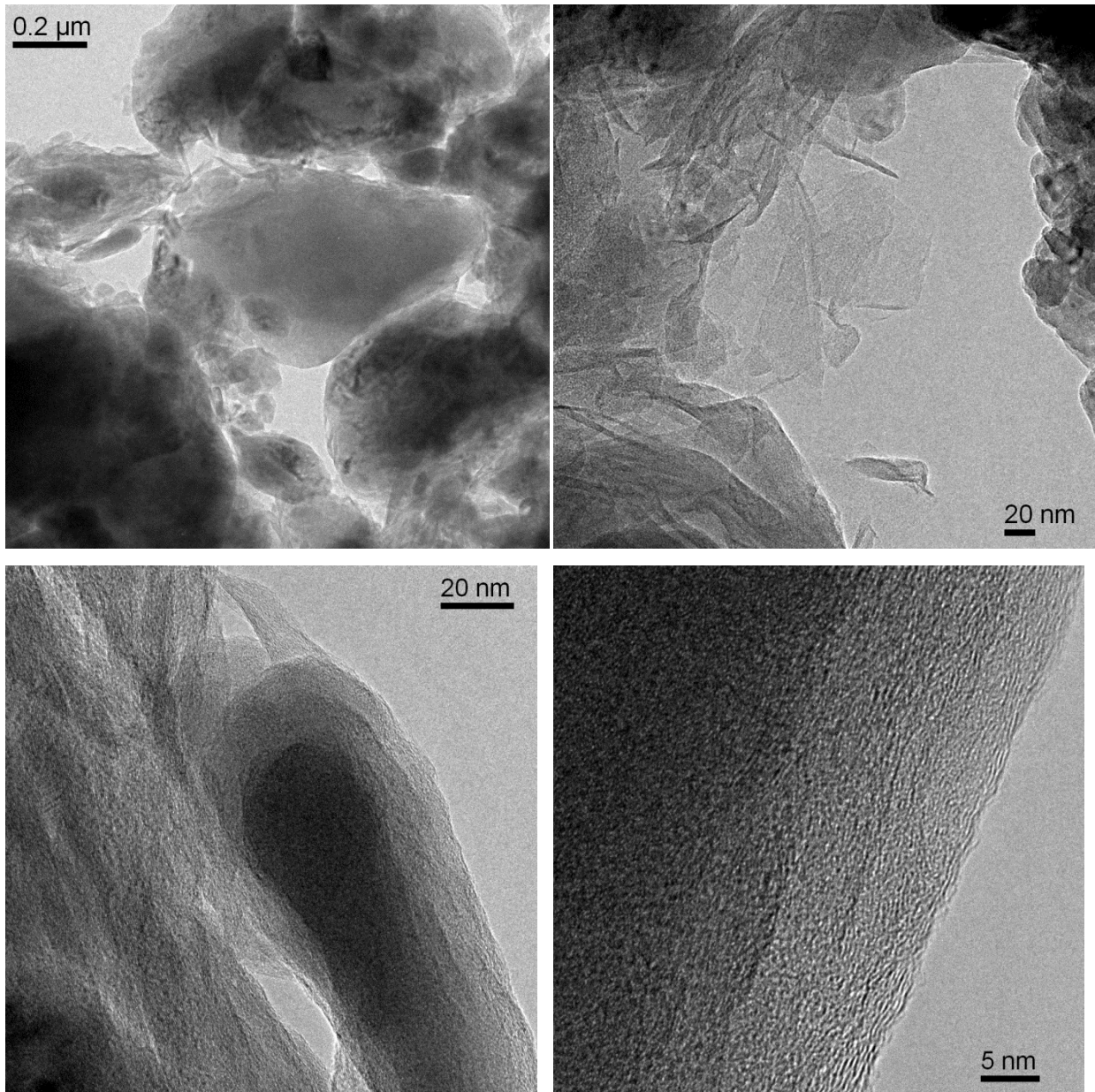
Fig. 6.19: TEM analysis of a mixture containing Si and PAN in 4:1 weight ratio, pyrolyzed at 750 °C for 6 h in argon (72 wt. %) and graphite oxide (28 wt. %), heated to 240 °C in argon.

The sample consists of Si particles coated by a thin layer of amorphous carbon, which are interconnected by a layered material (reduced graphite oxide).

Electrochemical performance

Thin film electrodes on a copper foil were prepared using the doctor blade technique, whereas electrode disks with a diameter of 12 mm were used. CMC was used as a binder (10 wt. %) and 1 M $LiPF_6$ in ethylenecarbonate/ dimethylacarbonate (1:1) was used as electrolyte. The sample was cycled between 10 mV and 2.0 V vs. Li/Li$^+$ at a rate of 200 mA g^{-1}. Discharge capacity was limited to 1200 mAh g^{-1} for the composite to improve cycling performance due to smaller volume changes of silicon. The initial step was discharge (lithiation) and values for specific capacity refer to the composite material Electrode films with different thickness and material content were prepared as summarized in Table 4 below.

Tab. 4: Prepared electrodes of a mixture containing Si, PAN (4:1 wt.) and graphite oxide.

Doctor blade film thickness [μm]	Film thickness after drying [μm]	Content of active material per electrode [mg]
300	55	3.4
250	50	2.4
200	40	2.1
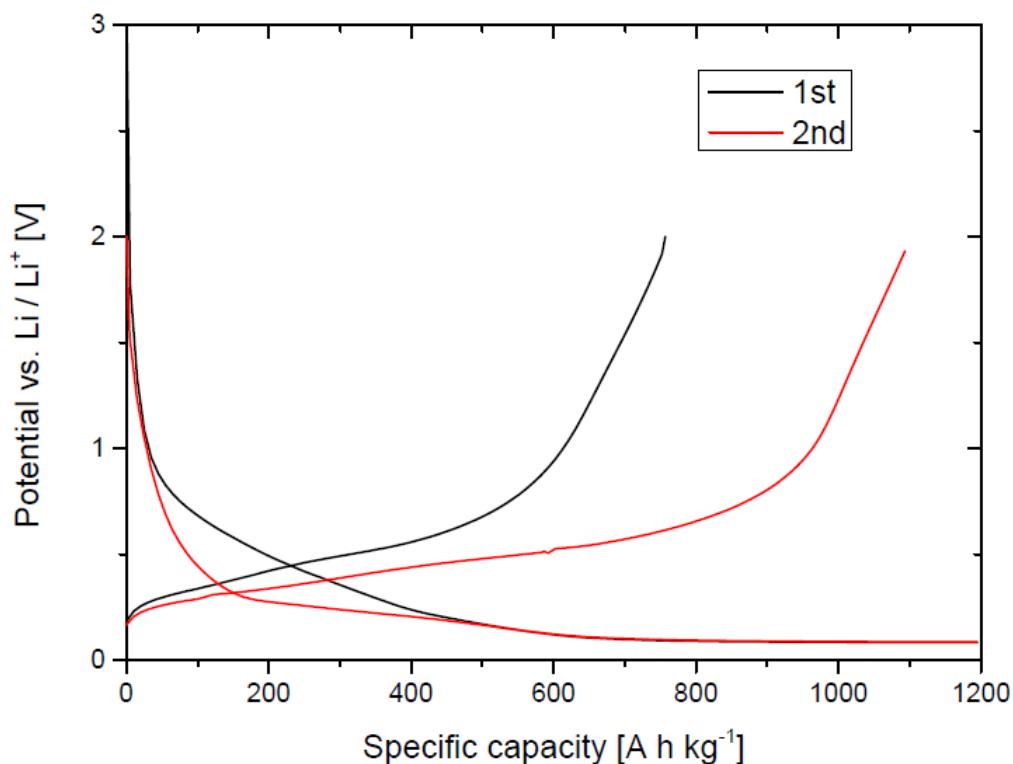
Fig. 6.20: Galvanostatic measurement of a 200 µm thin film electrode of a mixture containing Si, PAN (4:1 wt.) and graphite oxide; only the first two cycles are shown.

Compared to samples using Super P as carbon additive, there is a higher OCV as well as a lower initial Coulombic efficiency of 63.3%. However, the potential profile of first discharge looks similar hinting to the assumption that graphite oxide was reduced already prior to electrochemical testing by the thermal treatment. Consequently, there is no irreversible capacity between 1.0 and 2.0 V during initial discharge and thus no irreversible formation of lithiumoxides.
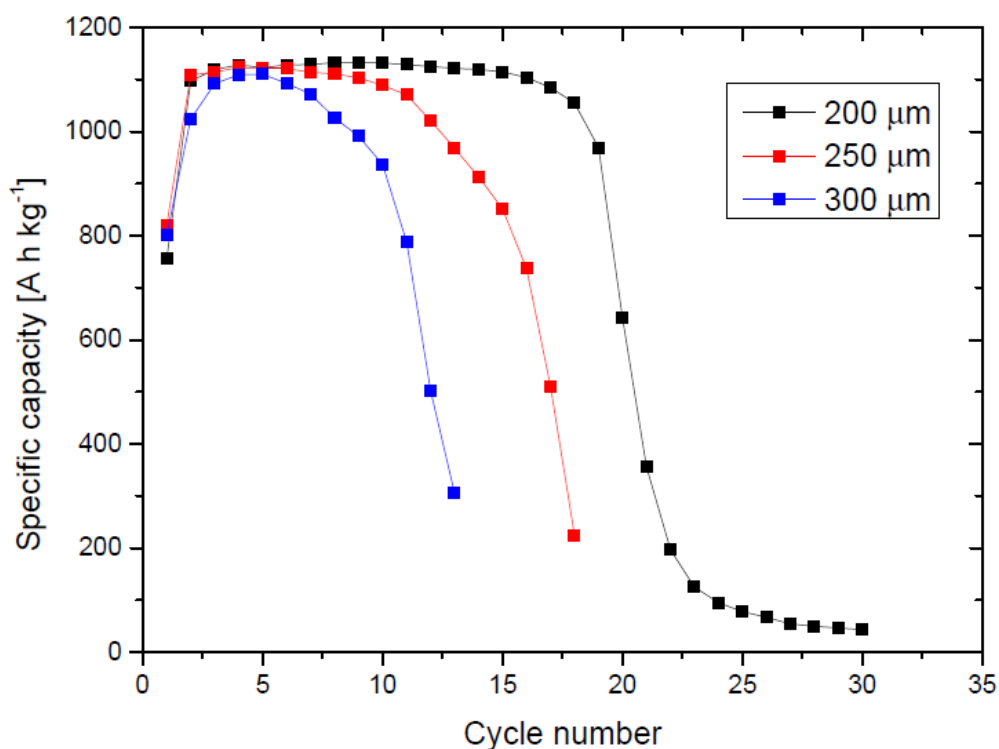
Fig. 6.21: Specific capacity vs. cycle number for a composite of Si, PAN (4:1 wt.) and reduced graphite oxide. The performance of electrodes with different thicknesses is shown for discharge capacity limited to 1200 mAh g^{-1} for the composite. Only charge capacities are depicted.

As expected, there is again an improvement of capacity retention with decreasing film thickness. A stable charge capacity > 1100 mAh g^{-1} is obtained for 18 cycles using a 200 μm thin film.

Conclusions

Mixtures with reduced graphite oxide show slightly worse capacity retention as well as lower initial Coulombic efficiency compared to samples using Super P as C additive for electrode film formulation using the same Si / PAN mixture (see Fig. 6.7). This leads to the conclusion that Super P is the carbon additive of choice for electrode formulation.

6.2.5. Conclusions on Si / PAN composites

Mixtures with different PAN and Si contents were prepared and carbon coating of Si particles by pyrolysis of the polymer was shown to occur. Different pyrolysis temperatures were examined (300 °C, 750 °C and 1000 °C) leading to different graphitization level of products, whereas nitrogen content decreases with increasing temperature. Capacity retention is significantly improved by decreasing film thickness. The best electrochemical performance was achieved by a 150 µm thin film of a Si / PAN mixture with a weight ratio of 4:1 treated at 750 °C for 6 h in argon. A stable charge capacity > 1100 mAh g^{-1} was observed for over 80 cycles when the discharge capacity was limited to 1200 mAh g^{-1} for the composite. Additionally, reduced graphite oxide was tested as C additive material for electrode formulation instead of Super P. However, as prepared thin film electrodes show slightly worse performance than its Super P counterparts. It may well be that an optimized mixture of graphene (oxide) and Super P better accounts for the contact bridges in such a complex composite formulation. Future experiments with these composite materials should focus on a Si / PAN mixture with a weight ratio of 2:3, pyrolyzed at 750 °C for 6 h in argon. This material is the most promising candidate in terms of C coating as well as electrochemical performance (see Fig. 6.6) and further upgrade is expected with film thickness variation.

6.3. Polyvinylpyrrolidone

Gaseous products upon pyrolysis of polyvinylpyrrolidone at 850 °C have been analyzed by gas chromatography by Ericsson et al.[116] The monomer vinyl-pyrrolidone (86%) was found to be the major component formed upon pyrolysis as illustrated in Figure 6.22 below.
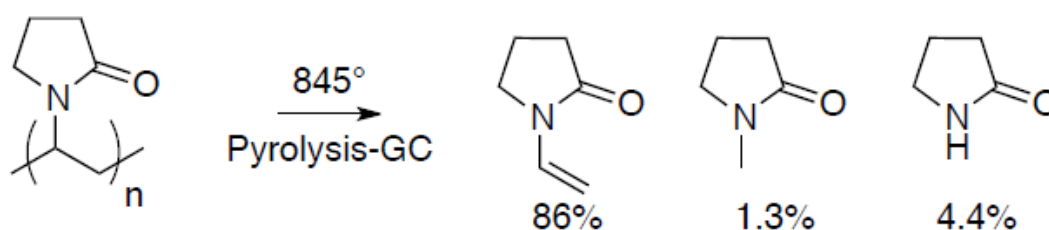
Fig. 6.22: Reaction scheme into gaseous products upon pyrolysis of PVP at 850 °C.

Synthesis:

Si powder (8 μm, 99.995%, ABCR) and commercially available PVP (ACROS, average Mw: 58'000) in respective weight ratios are mixed together. The mixture is then dissolved in deionized water and heated at 80 °C while stirring vigorously to slowly evaporate the solvent. A dark brown film is obtained which is cut into smaller pieces using a knife and afterwards ground. Then this sample is put in an Al_2O_3 crucible, transferred into a horizontal furnace and heated at 600 °C for 6 h in a constant argon flow (ca. 1 l h^{-1}).

Examined mixtures as well as carbon weight content determined by elemental analysis are listed in Table 5.

Tab. 5: Examined Si / PVP mixtures pyrolyzed at 600 °C for 6 h.

Si : PVP weight ratio	[C] wt. % by elemental analysis
7:3	0.9 to 1.0
1:1	4.2
2:3	6.3 to 6.5
3:7	9.0 to 9.1

A sample XRD powder pattern for x:y Si:PVP ratio is shown in Fig. 6.23 below.
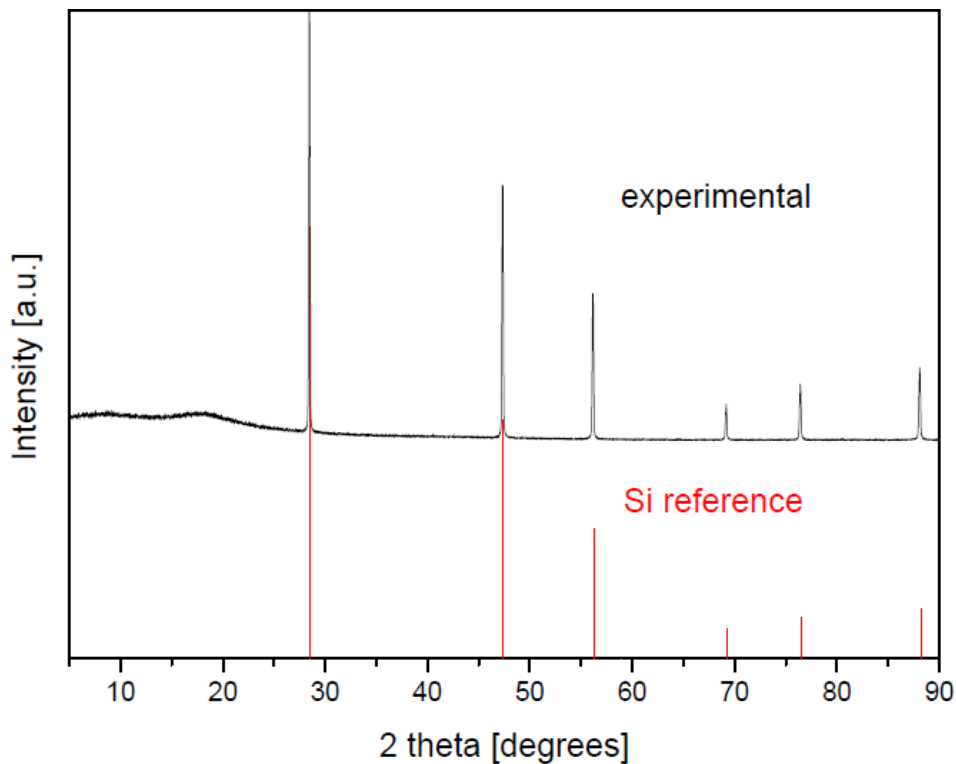
Fig. 6.23: Sample XRD powder pattern for a x:y Si:PVP pyrolyzed mixture (black curve). The red lines correspond to a calculated pattern of α-Si.

According to the powder pattern, the composite consists of crystalline silicon. The broad peak at a $2\theta = 18°$ is caused by paraffin oil, which was used to adhere the powder to the sample holder.

235

TEM analysis of a pyrolyzed mixture containing Si and PVP in a 2:3 weight ratio is shown in Figure 6.24. A thin amorphous carbon layer on the surface of the silicon particles can be seen.
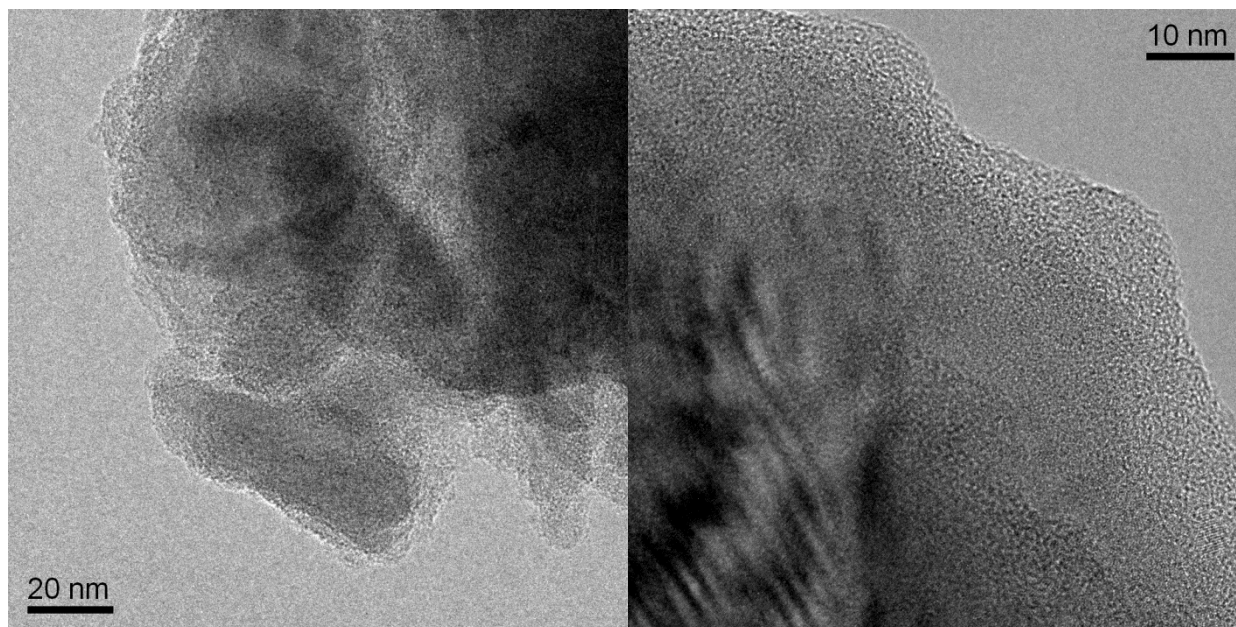
Fig. 6.24: TEM analysis of a mixture containing Si and PVP in a 2:3 weight ratio after pyrolysis at 600 °C.

Electrochemical performance

Thin film electrodes (film thickness: 0.3 mm) on a copper foil were prepared using the doctor blade technique. Electrode disks with a diameter of 15 mm were cut out with a content of 2.9 to 4.1 mg of active material. Super P was added as conductive additive (25 wt. %) and CMC was used as a binder (15 wt. %). 1 M LiPF6 in ethylenecarbonate/dimethylacarbonate (1:1) was used as electrolyte. The sample was cycled between 10 mV and 2.0 V vs. Li/Li$^+$ at a rate of 200 mA g^{-1}. Discharge capacity was limited to 1300 mAh g^{-1} for the composite to improve cycling performance due to smaller volume changes of

silicon. The initial step was discharge (lithiation) and values for specific capacity refer to the composite material.
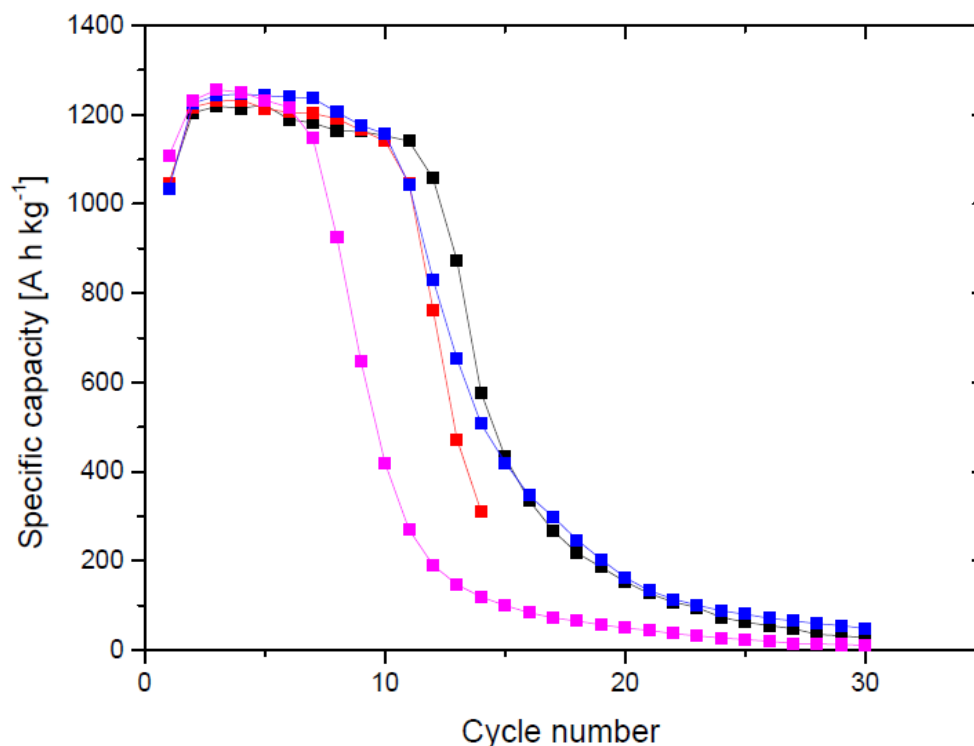
Fig. 6.25: Specific capacity vs. cycle number for mixtures containing Si and PVP in different weight ratios, pyrolyzed at 600 °C for 6 h in argon. Only the charge capacities are shown. The electrochemical performances of mixtures containing Si and PVP are shown for weight ratios of 3:7 in blue, 2:3 in black, 1:1 in red and 7:3 in magenta, respectively.

Samples with a weight ratio of Si and PVP of 1:1, 2:3 and 3:7 exhibit similar cycling behavior. The best performance was obtained for a 2:3 weight mixture of Si and PVP, where the charge capacity was stable for 12 cycles. The capacity decay occurs much faster for samples with an increasing amount of Si over PVP, as can be seen in Figure 22. The C content after pyrolysis for a mixture containing Si and PVP in 7:3 weight ratio was only 1 wt. %. This value is believed to be too low causing an insufficient coating of the Si particles, having a negative effect on the composite formation.

237

The influence of film thickness on the electrochemical performance is examined in the following section for a sample containing Si and PVP in a weight ratio of 2:3, pyrolyzed at 600 °C for 6 h in argon. Thin electrode films were prepared with a thickness of 0.15, 0.2, 0.25 and 0.3 mm, respectively. Table 6 summarizes parameters of the examined electrode films.

Tab. 6: Prepared electrode films of a mixture containing Si and PVP in a weight ratio of 2:3, pyrolyzed at 600 °C for 6 h in argon.

Doctor blade film thickness [mm]	Film thickness after drying[1] [μm]	Content of active material per electrode [mg]
0.3	120	3.8
0.25	130	2.8
0.20	95	2.3
0.15	65	1.2

[1] Film thicknesses after drying in a vacuum oven has been determined using Micromahr 40 ER from Mahr Co.
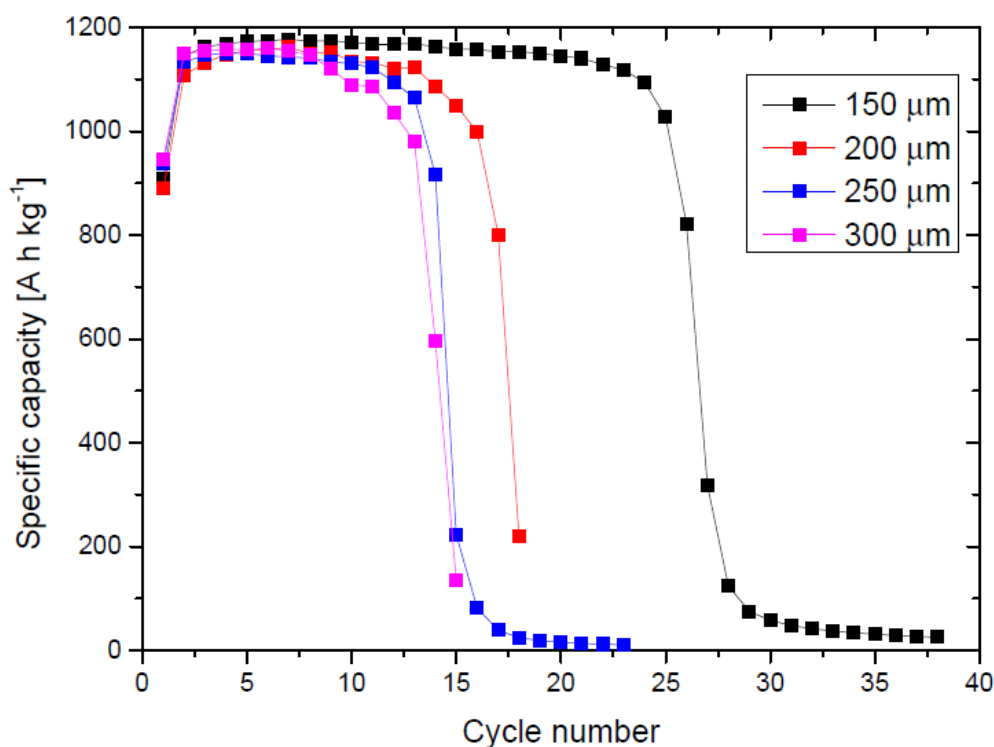
Fig. 6.26: Specific capacity vs. cycle number for a mixture containing Si and PVP in 2:3 weight ratio, pyrolyzed at 600 °C for 6 h in argon. The electrochemical performance of thin electrode films with different thicknesses is presented, whereas only charge capacities are shown. Samples were cycled between 10 mV and 2.0 V vs. Li/Li$^+$ at a rate of 200 mA g^{-1} and discharge capacity was limited to 1200 mAh g^{-1} for the composite.

There is a minimal improvement in capacity retention with decreasing film thickness for electrodes prepared for of 200, 250 and 300 μm by doctor blading. However, there is a significant upgrade of cycling behavior for a 150 μm electrode film with a stable charge capacity for 25 cycles. Thus the film thickness and consequently the load of active material are believed to be the critical parameters here: The 150 μm thin film has a significantly lower load of active material per electrode of only 1.06 mg cm^{-2}. A plot of film thickness vs. cycle-life clearly indicates to an asymptotic behavior with some uncertainty on the final course of the curve for very thin films as shown in Figure 6.27.

Tab. 7: Electrode characteristics of Si / PVP composites (2:3 wt.) pyrolyzed at 600 °C for 6 h in Ar for different film thickness.

Doctor blade film thickness [µm]	Film thickness after drying [µm][1]	Load of active material per electrode [mg cm^{-2}]	Number of stable cycles, whith charge capacity > 1100 mAh g^{-1}
300	120	3.36	11
250	130	2.48	12
200	95	2.04	14
150	65	1.06	25

[1]Film thickness after drying in vacuum oven has been determined using Micromahr 40 ER from Mahr Co.
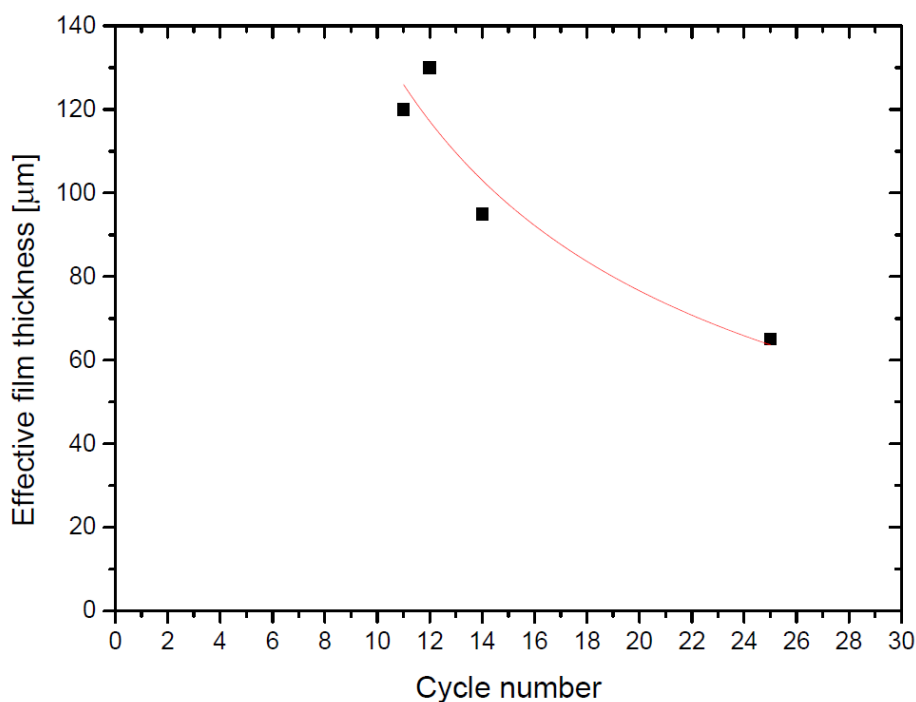
Fig. 6.27: Effective film thickness vs. cycle number for Si / PVP composites (2:3 wt.) pyrolyzed at 750 °C for 6 h in Ar. The cycle numbers given are those for which the charge capacity was larger than 1100 mAh g^{-1}.

The spline fit of the data in Figure 6.27 results in the formula

$$F_t = 925(567)\ \mu m \cdot C_m^{-0.83(24)} \tag{6.2}$$

with C_m = maximum cycle number at a charge capacity of more than 1100 mAh g^{-1} and F_t = effective film thickness. Extrapolation of this formula for 500 cycles reveals a necessary effective film thickness of 5 µm.

Nevertheless, capacity retention is insufficient for practical applications and further modifications would have to be inspected necessary.

Conclusion

Mixtures with different PVP and Si content were prepared and carbon coating of Si particles by pyrolysis of the polymer was shown to occur. The best electrochemical performance was achieved by a 150 µm thin film of a Si / PVP mixture with a weight ratio of 2:3 and a carbon content between 6.3 and 6.5 wt. % after treatment at 600 °C for 6 h in argon. A stable charge capacity > 1100 mAh g^{-1} was observed for 25 cycles when discharge capacity was limited to 1200 mAh g^{-1} for the composite. These composites perform less well than the ones of Si / PAN in the previous chapter.

6.4. Polystyrene

Pyrolysis products of polystyrene were reported by Williams et al. in 2009.[117] Polystyrene was treated at 500 °C under inert atmosphere (N_2) in a closed reaction vessel at a pressure of 1.6 MPa. Three different types of products were obtained: gas (2.5 wt. %), oil (67 wt. %) and char (30.4 wt. %). Note that the amount of char with respect to liquid product increases drastically at higher temperature (pyrolysis of polystyrene at 450 °C under same conditions lead to 80 wt.% liquid product and 19.6 wt.% char), whereas the amount of gaseous products is always very low. The main compounds of the gaseous products are CH_4 and C_2H_4, whereas the liquid consists mainly of aromatic single ring derivatives like ethylbenzene (36.6 wt. %), toluene (28.4 wt. %) and cumene (9.6 wt. %). The amount of styrene in the liquid is very low (0.61 wt. %), which may be traced back to the high reactivity of styrene radicals which are easily formed by pyrolysis of polystyrene. The same authors reported that for pyrolysis of polystyrene at 700 °C under inert atmosphere (N_2) in a closed vessel at ambient pressure, only 3.5 wt. % of char are obtained, which is a very low yield. That is why this experiment was performed at higher pressure which significantly raises the amount of char formed. The pyrolysis products were char, liquid oil (83. 77 wt. %) and a low amount of gas (2.33 wt. %).

Synthesis

Si powder (8 μm, 99.995%, ABCR) and polystyrene in respective weight ratios are mixed together, dissolved in THF and heated at 50 °C while stirring vigorously to slowly evaporate the solvent. A dark brown film is obtained which is cut into smaller pieces using a knife and ground afterwards. The sample is put into an Al$_2$O$_3$ crucible boat, transferred into a horizontal furnace and then

heated in a constant argon flow (ca. 1 l h⁻¹) for 6 h at 450 °C or 600 °C, respectively.

Two different derivatives of polystyrene were used: Commercially foamed PS (Styropor®) and commercial PS from Aldrich (average Mw: 192'000). The differences in coating behavior as well as electrochemical performances are described in the following section.

6.4.1. Commercially foamed PS (Styropor®)

Different mixtures containing Si and PS were examined, treated at pyrolysis temperatures of 450 and 600 °C, respectively. Examined mixtures, synthesis conditions as well as C contents after pyrolysis are summarized in Table 8 below.

Tab. 8: Examined mixtures containing Si and commercially foamed PS

Si : PS weight ratio	Pyrolysis temperature [°C]	[C] wt. % (elemental analysis)
1:1	450	1.0
1:1	600	0.2
2:3	450	0.4
3:7	450	0.4
1:4	450	0.6
1:9	450	1.3

Note that only a very low C content was obtained after pyrolysis. This value is even further decreased at higher pyrolysis temperatures.
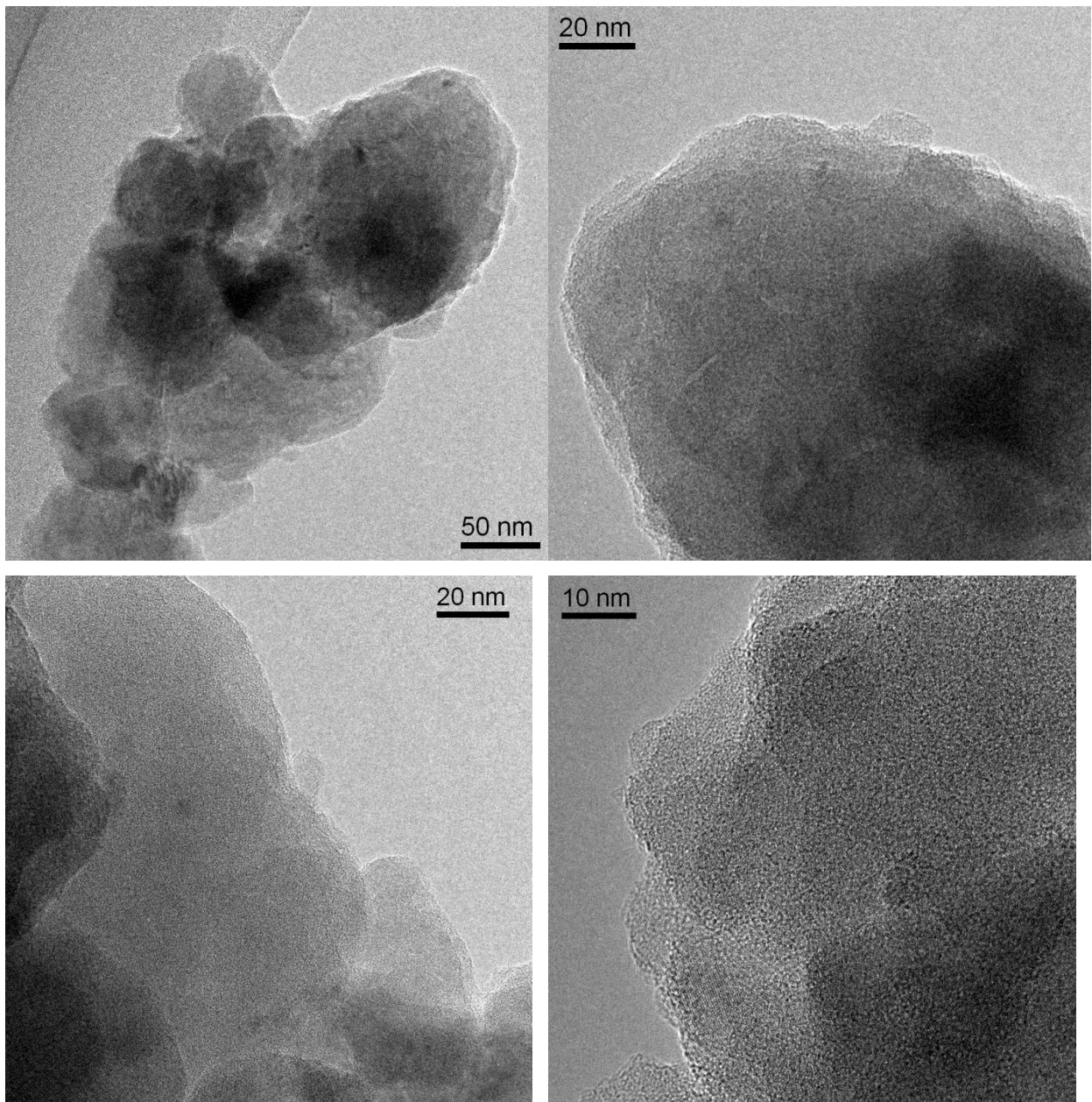
Fig. 6.28: TEM analysis of a mixture containing Si and commercially foamed PS
in equal weight ratio, pyrolyzed at 450 °C in argon.

There is a thin amorphous carbonaceous layer with a thickness of 10 to 20 nm
observed on the surface of Si particles. It is assumed that this coating is
insufficiently thin due to the very low total amount of carbon < 1 wt. % as
determined by elemental analysis.

Electrochemical performance

Thin film electrodes (film thickness: 0.3 mm) on a copper foil were prepared using the doctor blade technique. Electrode disks with a diameter of 12 mm were used, whereas Super P was added as conductive additive (25 wt. %) and CMC was used as a binder (10 wt. %). 1 M $LiPF_6$ in ethylenecarbonate/ dimethylacarbonate (1:1) was used as electrolyte. The sample was cycled between 10 mV and 2.0 V vs. Li/Li$^+$ at a rate of 200 mA g^{-1}. The discharge capacity was limited to 1200 mAh g^{-1} for the composite to improve the cycling performance due to smaller volume changes of silicon. The first step was discharge (lithiation) and values for specific capacity refer to the composite material.
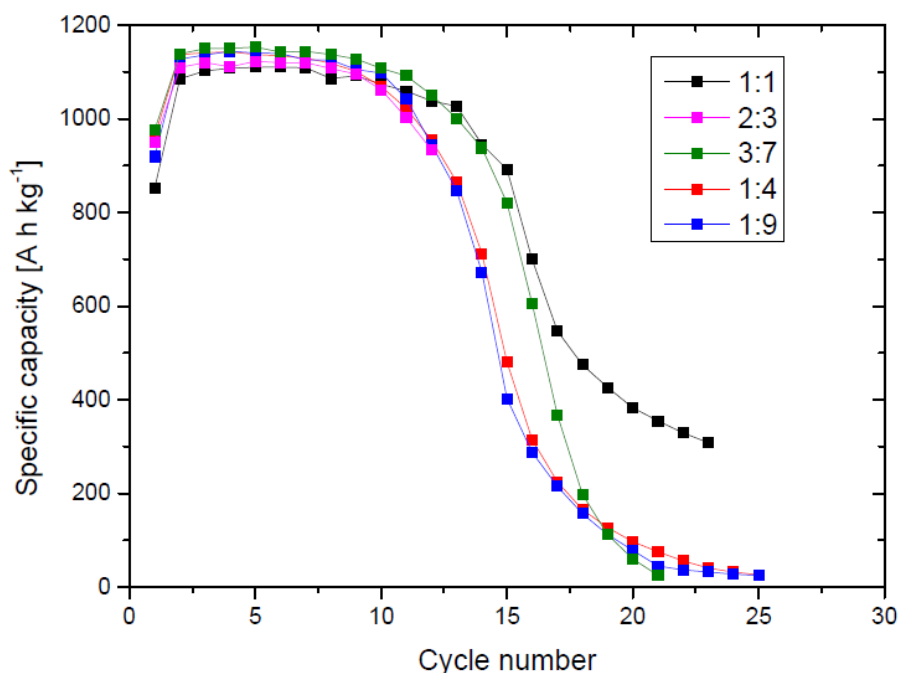
Fig. 6.29: Specific capacity vs. cycle number for composites containing Si and commercially foamed PS in different weight ratios, pyrolyzed at 450 °C for 6 h in argon. Only charge capacities are shown.

Samples pyrolyzed at 450 °C show comparable electrochemical performance independent of Si to PS ratio which may be traced back to the fact that the effective C content after pyrolysis is always in the same low range. The best performance was achieved for a 1:1 mixture of Si and PS with a stable charge capacity > 1100 mAh g^{-1} for 13 cycles before rapid capacity decay occurs. Note that the performance of the sample pyrolyzed at 600 °C is not shown here since it is significantly worse. This behavior can be explained by an even lower carbon content and therefore even more insufficient coating effect.

6.4.2. Polystyrene (Aldrich, average M = 192'000)

Examined mixtures using commercially available polystyrene, synthesis conditions as well as C contents after pyrolysis are summarized in Table 9 below.

Tab. 9: Examined composites from Si and commercial polystyrene

Si : PS weight ratio	Pyrolysis temperature [°C]	[C] wt. % (elemental analysis)
2:3	450	0.1
3:7	450	0.1
1:4	450	0.1

Carbon content of examined samples is negligible with values < 0.1 wt. %. Consequently, electrochemical performance is worse than the one of commercially foamed PS counterparts. The best performance was achieved by a mixture containing Si and polystyrene in 3:7 weight ratio with a stable charge

capacity > 1100 mAh g^{-1} for a mere 7 cycles (discharge capacity limited to 1200 mAh g^{-1} for the composite). This result is depicted in Figure 6.30.
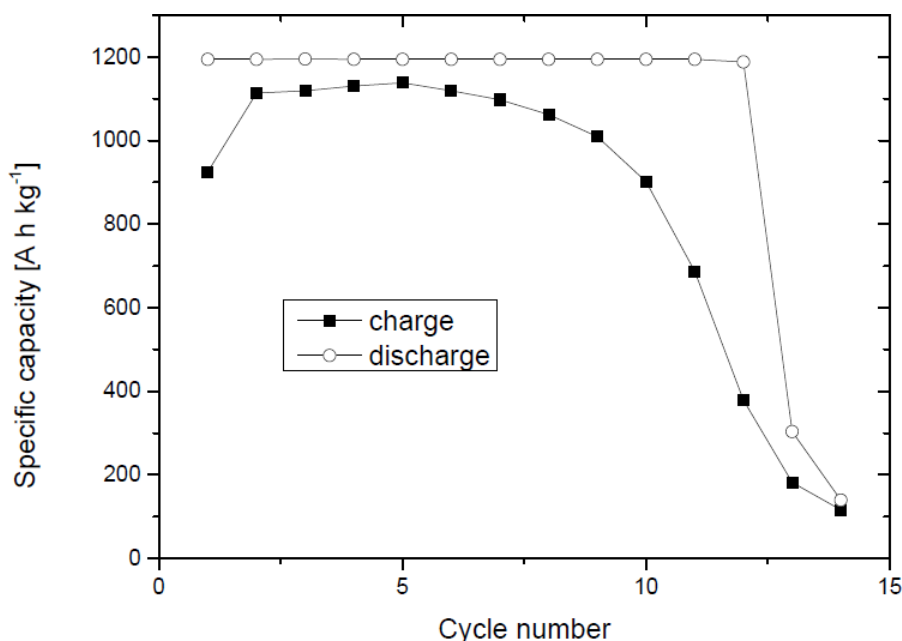
Fig. 6.30: Cycle number vs. specific capacity for a composite from silicon and polystyrene in 3:7 weight ratio, pyrolyzed at 450 °C in argon. A thin film electrode (thickness: 0.25 mm) on a copper foil was prepared using the doctor blade technique. Super P was added as conductive additive (25 wt. %) and CMC as a binder (10 wt. %), whereas 1 M LiPF$_6$ in ethylenecarbonate/ dimethylacarbonate (1:1) was used as electrolyte. The sample was cycled between 10 mV and 2.0 V vs. Li/Li$^+$ at a rate of 200 mA g^{-1}. Discharge capacity was limited to 1200 mAh g^{-1} for the composite and the initial step was discharge (lithiation). Values for the specific capacity refer to the composite material.

6.4.3. Conclusions on Si / PS composites

Pyrolysis of commercially foamed PS (Styropor®) leads to a higher carbon content of the composites than pyrolysis of pure polystyrene (M$_{av}$ =192'000).

This can be explained by the addition of other components besides polystyrene to form the expanded Styropor®, which obviously results in a larger C residue after pyrolysis. In comparison, pyrolysis of PS is not a very effective process and leads only to a very small amount of carbon in the composites. This however seems to be the reason for an insufficient electrochemical performance of the coated Si particles.

6.5. Lactose monohydrate

When heated at 100 °C, the loss of crystal water from lactose monohydrate occurs. Crystalline water is removed completely at 140 °C, leading to the loss of the crystalline structure transforming lactose into an amorphous phase. Heating at higher temperatures leads to decomposition of lactose into gaseous products like CO_2 and carbon residue (s). Pyrolysis of lactose has previously been reported for successful coating of $LiFePO_4$ particles with a thin C layer.[118-119]

Synthesis

Si powder (8 µm, 99.995%, ABCR) and commercially available lactose monohydrate (Merck) in respective weight ratios are mixed together. The mixture is then dissolved in deionized water and heated at 80 °C while stirring vigorously to slowly evaporate the solvent. A brown film is obtained which is ground afterwards. The sample is put in an Al_2O_3 crucible boat, transferred into a horizontal furnace and then heated at 650 °C for 6 h in a constant argon flow (ca. 1 l h^{-1}). Examined mixtures are summarized in Table 10.

Tab. 10: Analytical data for composites from Si and lactose monohydrate mixtures

Si : lactose weight ratio	[C] wt. % (elemental analysis)
4:1	2.5
7:3	5.5
3:2	10.9
1:1	15
2:3	22.8

There is a reasonable amount of amorphous carbon present after pyrolysis rendering this approach a more efficient method for C coating. TEM micrographs of a selected composite shown in Figure 6.31 reveal a rather uniform layer thickness compared to the other samples investigated in this chapter.
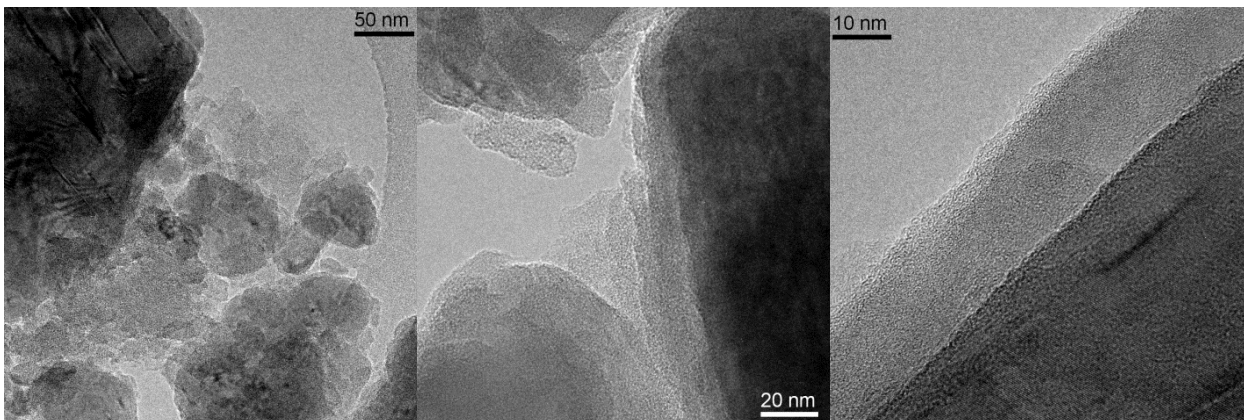
Fig. 6.31: TEM analysis of a composite from Si and lactose monohydrate in 3:2 weight ratio, pyrolyzed at 650 °C in argon.

Amorphous carbon can be clearly seen and Si particles are coated by a thin C layer of 10 to 15nm. A certain agglomeration of amorphous carbon particles is

observed to some extent which may also be due to aggregation of coated Si particles.

Electrochemical performance

Thin film electrodes (film thickness: 0.3 mm) on a copper foil were prepared using the doctor blade technique. Electrode disks with a diameter of 12 mm were cut out with a content of active material between 2.9 and 3.9 mg. Super P was added as conductive additive (25 wt. %) and CMC used as a binder (10 wt. %). 1 M $LiPF_6$ in ethylenecarbonate/dimethylacarbonate (1:1) was used as electrolyte. The samples were cycled between 10 mV and 2.0 V vs. Li/Li$^+$ at a rate of 200 mA g^{-1}. Discharge capacity was limited to 1200 mAh g^{-1} for the composite to improve cycling performance due to smaller volume changes of silicon. The initial step was discharge (lithiation) and values for specific capacity refer to the composite material.
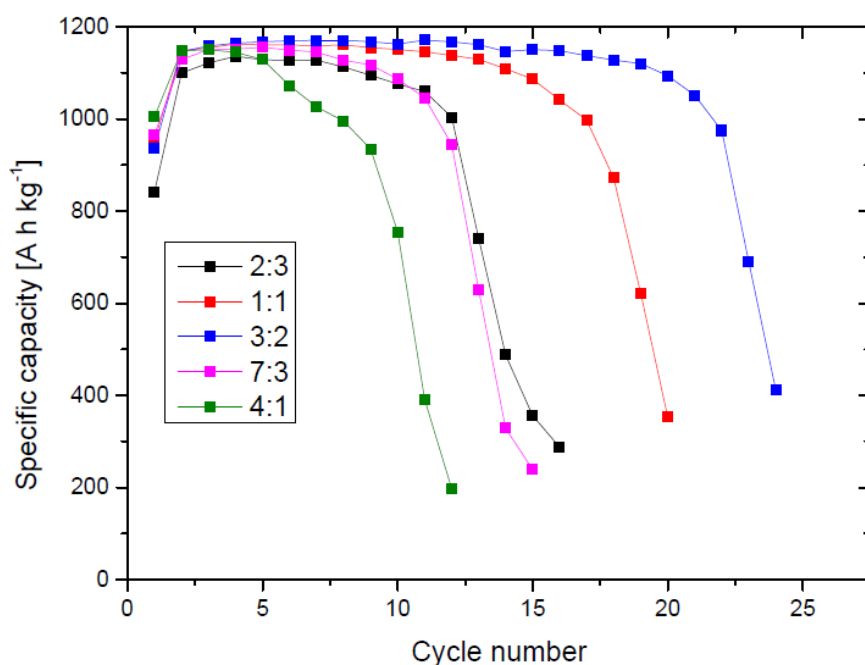
Fig. 6.32: Specific capacity vs. cycle number for composites from Si and lactose monohydrate mixtures in different weight ratios, pyrolyzed at 650 °C for 6 h in argon. Only charge capacities are shown.

The best performance was achieved for a composite from a mixture containing Si and lactose monohydrate in 3:2 weight ratio at a stable charge capacity > 1100 mAh g^{-1} for 20 cycles. In general, higher amount of carbon leads to a better uniform coating therefore improving electrochemical performance (up to a limiting thickness which increasingly impairs ionic mobility). On the other hand, a higher amount of silicon leads to a smaller volume expansion for a capacity limitation to a certain value for the whole composite (e.g. 1200 mAh g^{-1}). Therefore, a tradeoff between these two contrary points, e.g. an optimum mixture has to be found. Concerning these materials, the best performance was found for a composite containing 11 wt. % of carbon after pyrolysis as shown in Figure 6.33.

Tab. 11: Electrode characteristics of Si / lactose composites at different weight ratios, pyrolyzed at 650 °C in Ar. Film thickness of electrodes is 300 nm.

Si : lactose weight ratio before pyrolysis	C [wt. %] after pyrolysis	Number of stable cycles, with charge capacity > 1100 mAh g^{-1}
4:1	2.5	6
7:3	5.5	10
3:2	10.9	20
1:1	15	15
2:3	22.8	9
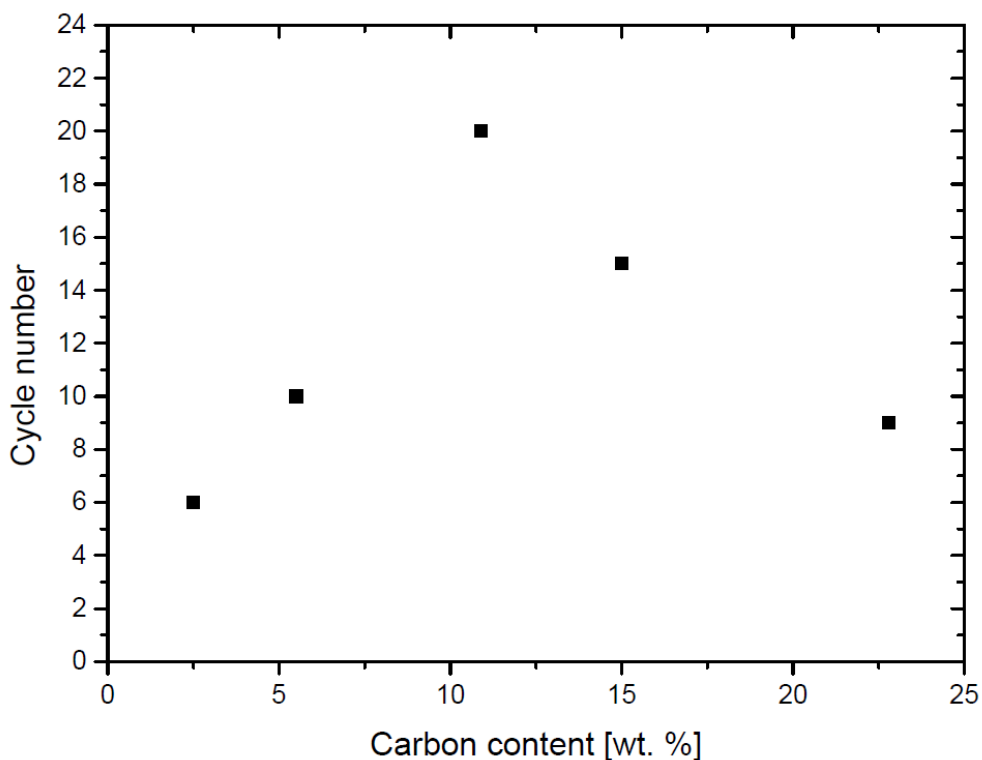
Fig. 6.33: Cycle number vs. C content [wt. %] for 300 nm thin films of composites of Si and lactose monohydrate at different weight ratios, pyrolyzed at 650 °C in argon. The cycle numbers given are those for which the charge capacity was larger than 1100 mAh g^{-1}.

In order to examine the influence of film thickness on electrochemical performance, a 0.15 mm thin film on a copper foil was prepared for a sample containing Si and lactose monohydrate in a weight ratio of 3:2 before pyrolysis. The electrochemical performance of this composite is shown in Figure 6.34.
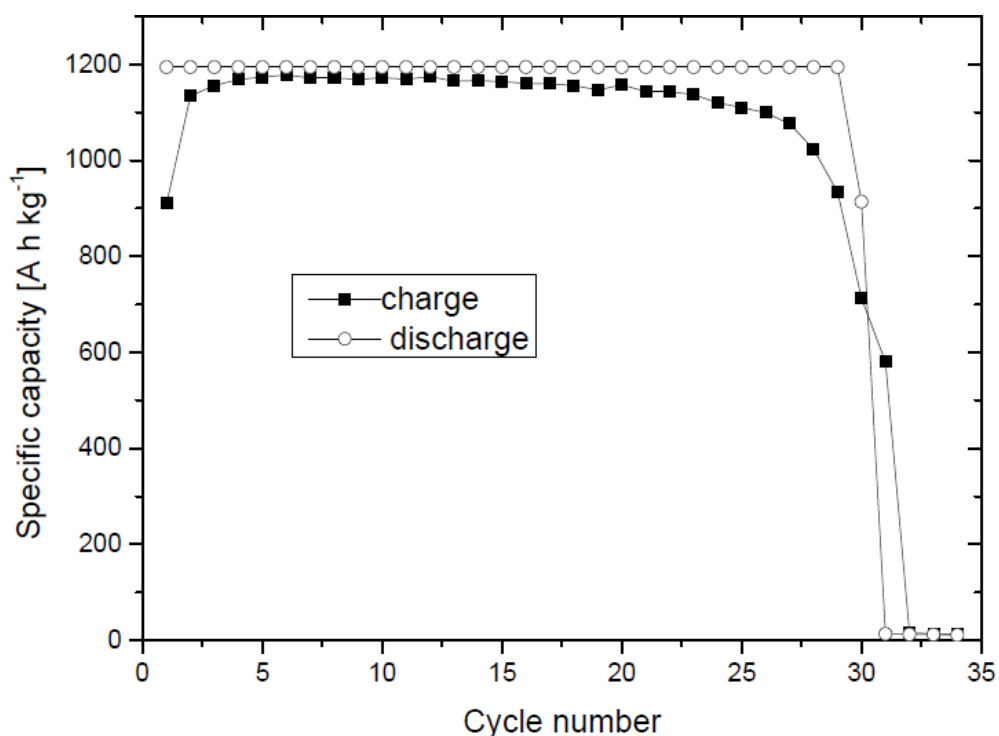
Fig. 6.34: Specific capacity vs. cycle number of a 150 mm thin film for a composite from Si and lactose monohydrate at 3:2 weight ratio, pyrolyzed at 650 °C in argon. Super P was added as further conductive additive (25 wt. %) and CMC used as a binder (10 wt. %). 1 M $LiPF_6$ in ethylenecarbonate / dimethylacarbonate (1:1) was employed as electrolyte. The sample was cycled between 10 mV and 2.0 V vs. Li/Li$^+$ at a rate of 200 mA g^{-1} and the discharge capacity was limited to 1200 mAh g^{-1} for the composite. The initial step was discharge (lithiation) and values for specific capacity refer to the composite material.

A stable charge capacity > 1100 mAh g^{-1} was obtained for 26 cycles before a rapid decay of capacity occurs. Compared to the 300 μm thin electrode film, there is only a marginal improvement of cycling behavior. Note that film quality was not significantly increased by preparing a 150 μm thin film and there was no big difference between the content of active material as well as effective

film thickness after drying. These parameters responsible for improved cycling behavior are summarized in Table 12.

Tab. 12: Two prepared electrode films for composites from Si and lactose monohydrate in a weight ratio of 3:2, pyrolyzed at 650 °C.

Film thickness by doctor blading [µm]	Film thickness after drying [µm]	Content of active material per electrode [mg cm^{-2}]
300	140	2.39
150	70	1.68

The effects responsible for capacity decay are examined in the next section using post mortem analysis.

Post mortem analysis

A 300 µm thin electrode film of a mixture containing Si and Lactose (3:2 wt.), treated at 650 °C for 6 h, was examined after 20 cycles in a Li ion battery:

The electrode contains 65 wt. % active material, 25 wt. % conductive additives (Super P) and 10 wt. % binder (CMC). 1 M LiPF$_6$ in ethylenecarbonate / dimethylcarbonate (1:1) was used as electrolyte. The sample was cycled between 10 mV and 2.0 V vs. Li/Li$^+$ at a rate of 400 mA g^{-1}. The initial step was discharge (lithiation) and 20 full charge/discharge cycles were performed. The battery cell was opened in air and the electrode material washed with THF to remove the remaining electrolyte. Figure 6.35 shows the obtained XRD powder pattern of the black material.
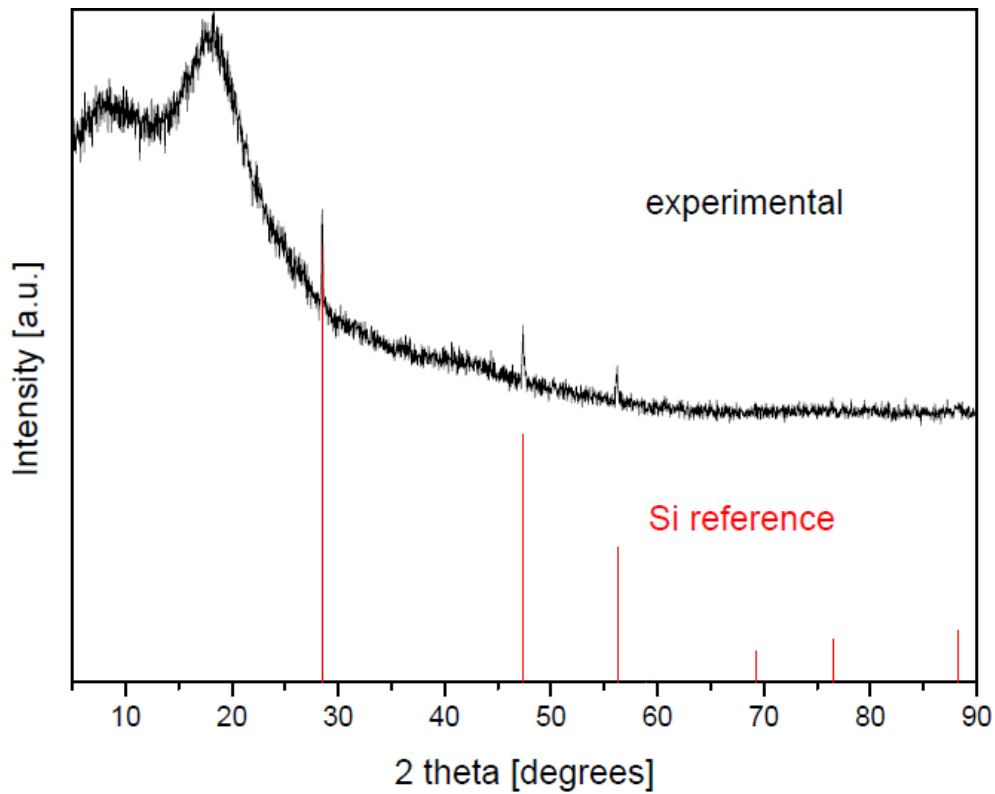
Fig. 6.35: XRD powder pattern of a mixture containing Si and lactose (3:2 wt.), treated at 650 °C for 6 h, after 20 cycles in a Li ion battery (black curve). The red lines correspond to a calculated pattern of α-Si.

The sample contains silicon and amorphous material. The broad peak at $2\theta = 18°$ is caused by paraffin oil, which was used to adhere the sample to the sample holder. SEM micrographs of the electrode material are shown in Figure 6.36.

255
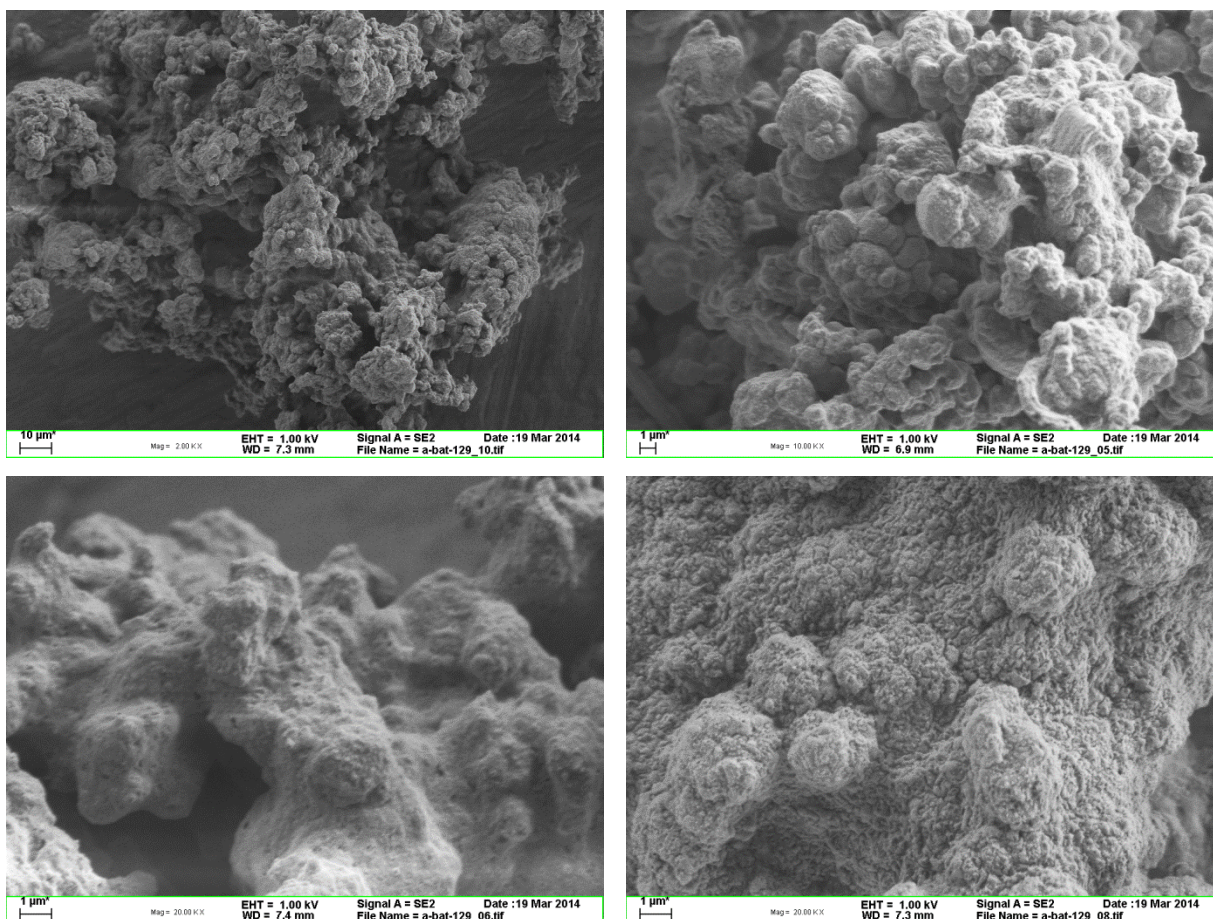
Fig. 6.36: SEM analysis of a mixture containing Si and lactose (3:2 wt.), treated at 650 °C for 6 h, after 20 cycles in a Li ion battery.

After 20 cycles in Li ion battery, the sample looks highly amorphous and all particles are coated completely by a thin film, which is believed to be a steadily growing SEI layer. This conjecture is manifested by TEM analysis shown in Figure 6.37; it can be seen that the particles are wrapped completely inside multiple thin layers.
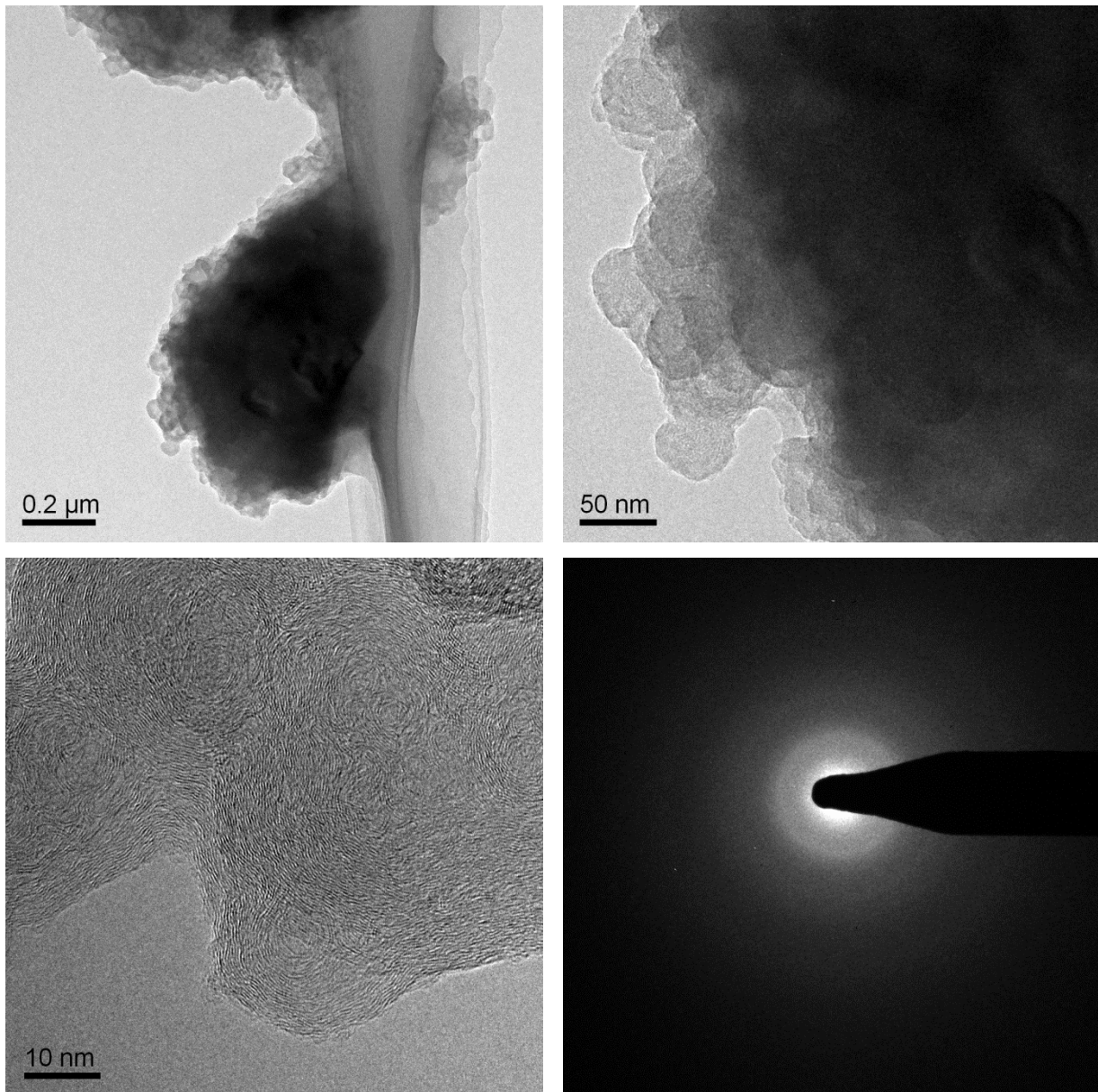
Fig. 6.37: TEM analysis of a mixture containing Si and lactose (3:2 wt.), treated at 650 °C for 6 h, after 20 cycles in a Li ion battery.

As a conclusion, capacity fading is caused mainly by the growing insulating SEI layer on the surface of particles due to cracking of electrode.

Conclusion

Comparatively good carbon coating of Si particles was shown to occur upon pyrolysis of lactose monohydrate at 650 °C in argon. The coating is fairly uniform and agglomeration of amorphous carbon particles is observed to some extent. Mixtures of different contents of Si and lactose monohydrate were examined. At a weight ratio of 3:2 before pyrolysis the best electrochemical performance with a stable charge capacity > 1100 mAh g^{-1} for 20 cycles was found when discharge capacity was limited to 1200 mAh g^{-1} for the composite. There is only a small dependency found between electrochemical performance and electrode film thickness, here.

6.6. Conclusion

PAN shows the best coating behavior in terms of carbon amount formed as well as electrochemical performance. PVP has lower C residue, whereas in the case for PS, carbon coating is almost nonexistent. Pyrolysis of lactose shows good carbon coating while no accompanying oxidation of Si particles was observed. In addition, by systematic film thickness investigations it was found that mechanical film stability and diffusion behavior are only granted for very thin films – by extrapolation at around 20 µm thickness for a mixture containing Si and PAN (4:1 wt.). Table 14 summarizes the electrode characteristics for the best working 150 µm thin film electrodes of composites employing PAN, PVP and lactose.

Tab. 14: Electrode characteristics of Si / Polymer composites for 150 nm thin films.

Polymer	Si:Polymer weight ratio	C content after pyrolysis [wt. %]	Effective film thickness [µm]	Load of active material of electrode [mg cm^{-2}]	Number of cycles with charge capacity > 1100 mAh kg^{-1}
PAN	4:1	5.89	45	0.45	80
PVP	2:3	6.3 to 6.5	65	1.06	25
Lactose	3:2	10.9	70	1.68	25

The best electrochemical performance was achieved by a 150 µm thin film of a Si / PAN mixture with a weight ratio of 4:1 treated at 750 °C for 6 h in argon. A stable charge capacity > 1100 mAh g^{-1} was observed over 80 cycles when discharge capacity was limited to 1200 mAh g^{-1} for the composite.

Future experiments should focus on a Si / PAN mixture with a weight ratio of 2:3, pyrolyzed at 750 °C for 6 h in argon. This material is the most promising candidate in terms of C coating as well as electrochemical performance and further upgrade is expected with film thickness variation.

7. Conclusions and Outlook

Rechargeable lithium batteries are the most popular choice to power portable electronic devices and electric vehicles due to their high energy density, long cycle life as well as variable and fast charge and discharge rates. However, they are still not capable to provide extended driving ranges for electric vehicles or enable implementation to large scale energy storage systems, both for reasons of energy density and costs. Therefore, the investigation of novel electrode materials as one of the most important prerequisites is of high interest in order to allow for sustainable future energy management. Graphite is the current anode material used in commercialized Li-ion batteries with a comparatively low theoretical capacity of 372 mAh g^{-1} and a working potential of 0.5 V vs. Li/Li$^+$. In recent years, silicon has become the most popular choice to replace graphite as anode material due to a very high theoretical capacity (4008 mAh g^{-1} for $Li_{21}Si_5$), a low working potential against Li metal and a cheap price due to high abundance. The main problems of this material are the extreme volume changes upon lithiation and delithiation leading to fracture of the electrode. Therefore, electronic percolation is lost as well as additional deposition of an insulating SEI layer on newly exposed surface of Si particles occurs. These effects lead to a very poor cycling performance up to now, which implies that these problems need to be solved in order to commercialize Si based anode materials for lithium ion batteries.

In this work, various approaches were shown to circumvent these problems for silicon based anode materials:

Li$_{12}$Si$_7$, Li$_{14}$Si$_6$ and Li$_{13}$Si$_4$ were examined as electrode materials instead of pure Si. The reduced overall relative volume change during cycling was expected to reduce the fracture and pulverization of Si-based anodes. Composite formation with carbon-based materials and transition metal chlorides (CuCl$_2$ and NiCl$_2$) was examined. For the latter one, formation of nano-silicon accompanied by metal deposition was observed.

Composite material formation through topochemical reactions of Zintl phases containing an arrangement of layered silicon with oxidation agents was examined. Treatment of Li$_3$NaSi$_6$, CaAl$_2$Si$_2$ and Ca$_2$LiSi$_3$ with various reagents (e.g. CuCl$_2$, graphite and graphene oxide) lead to the formation of nano-silicon embedded in a low-dimensional matrix material.

Eutectic systems of metals and silicon (e.g. Ti/Si, Mn/Si, Co/Si and Cu/Si) were used to fabricate nano particular two-phase products, i.e metal silicide plus nano silicon. The as formed transition metal silicides are electronic conductors therefore facilitating electron flow. Additionally, they are electrochemically inactive in the Li ion battery for chosen potential ranges, thus preventing lithiation and volume conversion of matrix material.

Methods for carbon coating of micron-sized silicon particles via pyrolysis of organic polymers were examined. The as formed carbon based matrix is a good electronic as well as lithium ion conductor and contains the silicon particles. Thus, the volume expansion during lithiation of silicon should be buffered and the formation of SEI controlled. Three different types of elastomers were examined: polyacrylonitrile (PAN), polyvinylpyrrolidone (PVP) and polystyrene (PS). Additionally, Lactose monohydrate was examined as a carbon source in

analogous manner. The best electrochemical performance was achieved by a 150 μm thin film of a Si / PAN mixture with a weight ratio of 4:1 treated at 750 °C for 6 h in argon. A stable charge capacity > 1100 mAh g^{-1} was observed over 80 cycles when discharge capacity was limited to 1200 mAh g^{-1}.

To summarize, neither nanoisation of silicon nor embedding in an as reported matrix material leads to a cycling behavior and capacity retention fulfilling industrial requirements. In order to fulfill these standards, low-cost and low dimensional active silicon or silicon alloys need to be examined, showing improved behavior in terms of volume changes and electrode stability leading to an overall better cycling performance of the active material. Composite formation upon of embedding of silicon in a flexible matrix is believed to be a promising solution to tackle the problems of the active material. Therefore, highly conducting volume matrices are expected to be flexible enough to account for large volume changes of silicon as well as protecting the latter one against excessive SEI deposition. The volume changes of the active material can also be compensated by introducing matrices containing sacrificial spaces leading to an overall better composite formation. Eventually, these conducting materials allow the omission of the copper current collector which presently accounts for 18 wt. % of the battery, therefore further improving specific energy density of lithium ion batteries.

References

[1]   Mitsubishi-motors, Mitsubishi Innovative Electric Vehicle, http://www.mitsubishi-motors.com/special/ev/, May 2012.

[2]   Nissan, Nissan Leaf Electric Car, http://nissan-global.com/EN/NISSAN/LEAF/, May 2012.

[3]   Tesla-Motors, Tesla Roadster Electric Car, http://www.teslamotors.com/goelectric, May 2012.

[4]   Piotto, A.P., PhD thesis, ETH no 15659, Zürich, **2004**.

[5]   Ikeda, H.; Saito, T.; Tamura, H*., Proc. Manganese Dioxide Symp.,* **1975**, *Vol. 1*.

[6]   Dahn, J.; Haering, R.R., *Mater. Res. Bull.,* **1979**, *14*, 1259-1262.

[7]   Mizushima, K.; Jones, P.C.; Wiseman, P.J.; Goodenough, J.B., *Solid State Ionics,* **1981**, *3-4*, 171-174.

[8]   Banov, B.; Bourilkov, J.; Mladenov, M., *J. Power Sources*, **1995**, *54*, 268-270.

[9]   Ammundsen, B.; Paulsen, J., *Adv. Mater*., **2001**, *13*, 943.

[10]   Dou, S.M.; Wang, W.L., *J. Solid State Electrochem.,* **2011**, *15*, 399-404.

[11]   Julien, C.; Nazri, G.A.; Rougier, A., *Solid State Ionics*, **2000**, *135*, 121-130.

[12]   Robertson, A.D.; Armstrong, A.R.; Bruce, P.G., *Chem. Mater.,* **2001**, *13*, 2380-2386.

[13]   Murphy, D.W.; DiSalvo, F.J.; Carides, J.N.; Waszczak, J.V., *Mat. Res. Bull*., **1978**, *13*, 1395-1402.

[14]   Lazzari, M.; Scrosati, B., *J. Electrochem. Soc.*, **1980**,*127*, 773-774.

[15]   Besenhard, J.O.; Fritz, H.P.; *J. Electroanal. Chem*., **1974**, *53*, 329.

[16]   Nagaura, T.; Tozawa, K., *Prog. Batteries Solar Cells*, **1990**, *9*, 209.

[17]   Kim, D.H.; Ahn, Y.S.; Kim, J., *Electrochem. Commun.*, **2005**, *7***,** 340**.**

[18]   Shao-Horn, Y., *Nat. Mater.,* **2003**, *2*, 463-467.

[19]   Chen, Z.H. ; Lu, Z.H. ; Dahn, J.R., *J. Electrochem. Soc.,* **2002**, *149*, A1604-A1609.

[20]   Ohzuku, T.; Ueda, A., *J. Electrochem. Soc.,* **1994**, *141*, 2972-2977.

[21]   Endo, E.; Yasuda, T.; Kita, A.; Yamaura, K.; Sekai, K., *J. Electrochem. Soc.,* **2000**, *147*, 1291-1294.

[22]   Wang, H.F.; Jang, Y.I.; Huang, B.Y.; Sadoway, D.R.; Chiang, Y.T.; *J. Electrochem. Soc.,* **1999**, *146*, 473-480.

[23]   Afyon, S., PhD thesis, ETH no 21158, Zürich, **2013**.

[24]   Sun, Y.K.; Myung, S.T.; Park, B.C.; Prakash, J.; Belharouak, I.; Amine, K., *Nat. Mater.,* **2009**, *8*, 320-324.

[25]   Xu, B.; Qian, D.N.; Wang, Z.Y.; Meng, Y.S.L., *Mat. Sci. Eng. R.,* **2012**, *73*, 51-65.

[26]   Chen, Y.C.; Xie, K.; Pan, Y.; Zheng, C.M.; *J. Power Sources*, **2011**, *196*, 6493-6497.

[27]   Thackeray, M.M.; Mansuetto, M.F.; Bates, J.B., *J. Power Sources*, **1997**, *68*, 153-158.

[28]   Mohamedi, M.; Takahashi, D.; Itoh, T.; Uchida, I., *Electrochim. Acta*, **2002**, *47*, 3483-3489.

[29]   Lee, S.; Cho, Y.; Song, H.K.; Lee, K.T.; Cho, J., *Angew. Chem. Int. Edit.,* **2012**, *51*, 8748-8752.

[30]   Myung, S.T.; Chung, H.T.; Komaba, S.; Kumagai, N.; Gu, H.B., *J. Power Sources*, **2000**, *90*, 103-108.

[31]   Park, S.B.; Shin, H.C.; Lee, W.G.; Cho, W.I.; Jang, H., *J. Power Sources*, **2008**, *180*, 597-601.

[32]   Capsoni, D.; Bini, M.; Chiodelli, G.; Massarotti, V. ; Azzoni, C.B. ; Mozzati, M.C. ; Comin, A., *Phys. Chem. Chem. Phys*., **2001**,*3*, 2162-2166.

[33]   Hwang, B.J.; Santhanam, R.; Liu, D.G.; Tsai, Y.W., *J. Power Sources*, **2001**, *102*, 326-331.

[34]   Xiao, J.; Chen, X.L.; Suchko, P.V.; Sushko, M.L.; Kovarik, L.; Feng, J.J.; Deng, Z.Q.; Zheng, J.M.; Graff, G.L.; Nie, Z.M.; Choi, D.W.; Liu, J.; Zhang, J.G.; Whittingham, M.S., *Adv. Mater.*, **2012**, *24*, 2109-2116.

[35]   Padhi, A.K.; Nanjundaswamy, K.S.; Goodenough, J.B., *J. Electrochem. Soc.,* **1997**, *144*, 1188-1194.

[36]   Andersson, A.S.; Kalska, B.; Haggstrom, L.; Thomas, J.O., *Solid State Ionics*, **2000**, *130*, 41-52.

[37]   Chung, S.Y.; Bloking, J.T.; Chiang, Y.M., *Nat. Mater.*, **2002**, *1*, 123-128.

[38]   Striebel, K.; Shim, J.; Srinivasan, V.; Newman, J., *J. Electrochem. Soc.*, **2005**, *152*, A664-A670.

[39]   Lepage, D.; Michot, C.; Liang, G.X.; Gauthier, M.; Schougaard, S.B., *Angew. Chem. Int. Edit.,* **2011**, *50*, 6884-6887.

[40]   Kang, B.; Ceder, G., *Nature*, **2009**, *458*, 190-193.

[41]   Lim, S.Y.; Yoon, C.S.; Cho, J.P., *Chem. Mater.,* **2008**, *20*, 4560-4564.

[42]   Xie, H.M.; Wang, R.S.; Ying, J.R.; Zhang, L.Y.; Jalbout, A.F.; Yu, H.Y.; Yang, G.L.; Pan, X.M.; Su, Z.M., *Adv. Mater.*, **2006**, *18*, 2609.

[43]   Huggins, R. A., *Energy Storage*, Springer Verlag, **2010**, p. 291f.

[44]   Wu, H.Q., *Solid State Science*, **2006**, *8*, 113.

[45]   Winter, M.; Besenhard, J.O.; Spahr, M.E.; Novak, P., *Adv. Mater.*, **1998**, *10*, 725-763.

[46]   Wang, X.J.; Lee, H.S.; Li, H.; Yang, X.Q.; Huang, X.J., *Electrochem. Commun*., **2010**, *12*, 386-389.

[47]   Peled, E.; Golodnitsky, D.; Ardel, G., *J. Electrochem. Soc.*, **1997**, *144*, L208-L210.

[48] Yamaguchi, S.; Asahina, H.; Hirasawa, K.A.; Sato, T.; Mori, S., *Mol. Cryst. Liq. Crys. A*, **1998**, *322*, 239-244.

[49] Yan, N.; Hu, L.; Li, Y.; Wang, Y.; Zhong, H.; Hu, X.Y.; Kong, X.K.; Chen, Q.W.; *J. Phys. Chem C*, **2012**, *116*, 7227-7235.

[50] Sathish, M.; Tomai, T.; Honma, I.; *J. Power Sources*, **2012**, *217*, 85-91.

[51] Poizot, P.; Laruelle, S.; Grugeon, S.; Dupont, L.; Tarascon, J.M., *Nature*, **2000**, *407*, 496-499.

[52] Fu, Z.W.; Wang, Y.; Yue, X.L.; Zhao, S.L.; Qin, Q.Z., *J. Phys. Chem. B*, **2004**, *108*, 2236-2244.

[53] Pereira, N.; Dupont, L.; Tarascon, J.M.; Klein, L.C.; Amatucci, G.G., *J. Electrochem. Soc.*, **2003**, *150*, A1273-A1280.

[54] Rao, B.M.L.; Francis, R.W.; Christopher, H.A., *J. Electrochem. Soc.,* **1977**, *124*, 1490-1492.

[55] Shembel, E.M.; Maksyuta, I.M.; Neduzhko, L.I.; Belosokhov, A.I.; Naumenko, A.F.; Rozkhov, V.V., *J. Power Sources*, **1995**, *54*, 416-420.

[56] Palacin, M.R., *Chem. Soc. Rev.*, **2009**, *38*, 2565-2575.

[57] Trifonova, A.; Wachtler, M.; Winter, M.; Besenhard, J.O., *Ionics*, **2002**, *8*, 321-238.

[58] Zhao, X.B.; Cao, G.S.; Lu, C.P.; Zhang, L.J.; Hu, S.H.; Zhu, T.J.; Zhou, B.C., *J. Alloy Compd.*, **2001**, *315*, 265-269.

[59] Lu, C.P.; Zhao, X.B.; Cao, G.S.; Zhu, T.J., *T Nonferr. Metal. Soc.,* **2000**, *10*, 204-208.

[60] Chan, C.k. ; Peng, H.L. ; Liu, G. ; Mellwrath, K.; Zhang, X.F., Huggins, R.A., Cui, Y., *Nat. Nanotechnol.,* **2008**, *3*, 31-35.

[61] Boukamp, B.A. ; Lesh, G.C. ; Huggins, R.A. *; J. Electrochem. Soc.,* **1981**, *128*, 725.

[62] Cui, L.F. ; Cui, Y. ; Hsu, C.M. ; Yang, Y., *Nano Letters*, **2009**, *9*, 3370.

[63] Cho, J. ; Kim, H., *Nano Letters*, **2008**, *8*, 3688.

[64] Ayala, J.; Dixon, P.; Hertzberg, B.; Kvit, A.; Magasinski, A.; Yushin, G., *Nature Materials*, **2010**, *9*, 353.

[65] Cho, J.; *J. Mater. Chem.*, **2010**, *20*, 4009.

[66] Huang, J.; Kung, H.H.; Jang, H.D.; Luo, J.; Wu, J.; Zhao, X., *J. Phys. Chem. Lett.,* **2012**, *3*, 1824.

[67] Wu, H.; Chan, G.; Choi, J.W.; Ryu, I.; Yao, Y. ; McDowell, M.T. ; Lee, S.W. ; Jackson, A., Yang, Y.; Hu, L.B.; Cui, Y., *Nat. Nanotechnol.,* **2012**, *7*, 309-314.

[68] Battaglia, V.S.; Liu, G.; Olalde-Velasco, P.; Song, X.; Vukmirovic, N.; Wang, L.; Xun, S.; Yang, W.; Zheng, H., *Adv. Matter*, **2011**, *23*, 4679.

[69] Burtovyy, R.; Hertzberg, B.; Kovalenko, I.; Luzinov, I.; Magasinski, A.; Milicev, Z.; Yushin, G.; Zdryko, B., *Science*, **2011**, *334*, 75.

[70] Ohara, S., Sekine, K.; Suzuki, J.; Takamura, T., Uehara, M., *J. Power Sources*, **2004**, *129*, 96.

[71] Cui, Y.; Hu, L.; Liu, N.; McDowell, M.T.; Nix, W.D.; Ryu, I.; Wu, H.; Yao, Y., *Nano Letters*, **2011**, *11*, 2949.

[72] Boukamp, B. A.; Lesh, G. C.; Huggins, R., *J. Electrochem. Soc.,***1981**, *128*, 725–729.

[73] Obrovac, M. N.; Christensen, L., *Electrochem. Solid-State Lett*., **2004**, *7*, A93–A96.

[74] Ma, R.; Liu,Y.; He, Y.; Gao, M.; Pan, H., *J. Phys.Chem. Lett.,* **2012**, *3*, 3555-3558.

[75] Obrovac, M. N.; Krause, L. J., *J. Electrochem. Soc.*, **2007**, *154*, A103–A108.

[76] Nesper, R.; von Schnering, H.G.; Curda, J., *Chem. Ber.*, **1986**, *119*, 3576-3590.

[77] Kuhn, A.; Sreeraj, P.; Pöttgen, R.; Wiemhöfer; H.; Wilkening, M.; Heitjans; P., *Angew. Chem*, **2011**, *123*, 12305-12308.

[78] Kasavajjula, U.; Wang, C.; Appleby, A.J., *J. Power Sources*, **2007**, *163*, 1003-1039.

[79] Ellis, B.L.; Town, K.; Nazar, L.F., *Electrochim. Acta*, **2012**, in press.

[80] Nesper, R.; von Schnering, H.G.; Tebbe, K.F.; Curda, J., *Z. Metalkde.*, **1980**, *71*, 357.

[81] Chevrier, V.L.; Zwanziger, J.W.; Dahn, J.R., *J. Alloys Compd.*, **2010**, *496*, 25-36.

[82] Frank, U.; Mueller, W.; Schaefer, H., *Z. Naturforsch. B*, **1975**, *30*, 10-13.

[83] Yang, J.; Winter, M.; Besenhard, J.O., *Solid State Ionics*, **1996**, *90*, 281.

[84] von Schnering, H.G.; Schwarz, M.; Nesper, R., *J. Less-Common Met.*, **1988**, *137*, 297.

[85] Slabon, A.; Budnyk, S.; Cuervo-Reyes, E.; Wöhrle, M.; Verel, R.; Nesper, R., *Chem. Eur. J.* **2013**, 19, 16528-16531.

[86] Zheng, C.; Hoffmann, R.; Nesper, R.; von Schnering, H.G., *J. Am. Chem. Soc.*, **1986**, *108*, 1876.

[87] Massalski, T.B., Binary Alloy Phase Diagrams*, Amer. Soc. Metals*, **1986**.

[88] Zürcher, F., PhD thesis, ETH no 12546, Zürich, **1998**, p. 223.

[89] Müller, W.; Schäfer, H.; Weiss, A., *Z. Naturforsch., Teil B*, **1971**, *26*, 5.

[90] Seifert, H.J.; Lukas, H.L.; Petzow, G., *Z.für Metallkde.*, **1996**, *87*, 2-13.

[91] Huang, Y.; Duan, X.; Cui, Y.; Lauhon, L.J.; Kim, K.-H.; Lieber, C.M., *Science*, **2001**, *294*, 1313–1317.

[92] Röhrig, M.; Schneider, M.; Etienne, G.; Oulhadj, F.; Pfannes, F.; Kolew, A.; Worgull, M.; Hölscher, H., *J. Micromech. Microeng.*, **2013**, *23*, 105014.

[93] Choi, S.D., *Calphad: Computer Coupling of Phase Diagrams and Thermochemistry*, **1992**, *16*, 151-159.

[94] Massalski, T.B.; Murray, J.L.; Benett, L.H.; Baker, H., *Binary Alloy Phase Diagrams: Volume 2,* American Society of Metals*,* **1986**.

[95] Liu, H., She, G., Huang, X.; Qi, X.; Mu, L.; Meng, X.; Shi, W., *J. Phys. Chem.,* **2013**, *117*, 2377.

[96] Vetter, J.; Frühauf, J.; Schneider, H.G., *Phys. Stat. Sol.,* **1981**, *67*, K99.

[97] Vetter, J.; Frühauf, J., *Cryst. Res. Technol.,* **1985**, *20*, 719-720.

[98] Schuster, H.; Thiedemann, D.; Schönemann, H., *Z. Anorg. Allg. Chem.,* **1969**, *370*, 160-169.

[99] EUROPEAN PATENT APPLICATION, EP0567867A2, IBM corp. **1993**.

[100] Müchler, L.; Zhang, H.; Chadov, S.; Yan, B.; Casper, F.; Kübler, J.; Zhang, S.; Felser, C., *Angew. Chem. Int. Ed.,* **2012**, *51*, 7221-7225.

[101] Wen, C.Y.; Spaepen, F., *Philosophical Magazine*, **2007**, *87*, 5581-5599.

[102] Jung, S.J.; Lutz, T.; Bell, A.P.; McCarthy, E.K.; Boland, J.J., *Cryst. Growth Des.,* **2012**, *12*, 3076.

[103] Schlesinger, M.E., *Chem. Rev.,* **1990**, *90*, 607-628.

[104] Bernard, F.; Souha, H.; Gaffet, E., *Mater. Sci. Eng.,* **2000**, *289*, 301-306.

[105] Arnold, H., *Z. Kristallogr., Kristallgeom., Kristallphys., Kristallchem.,* **1986**, *177*, 139.

[106] Grassie, N.; Mcguchan, R., *Eur. Polym. J.,* **1971**, *7*, 1357-1371.

[107] Rahaman, M.; Ismail, A.; Mustafa, A., *Polym. Degrad. Stab.,* **2007**, *92*, 1421-1432.

[108] Liu, J.; Wang, L.; Zhang, W. X.; Li, J.; Liang, J. Y., *New Carbon Mater.,* **2005**, *20*, 343-349.

[109] Bruck, S. D*., Ind. Eng. Chem.,* **1967**, *59*, 18-28.

[110] Hernandez, V.; Castiglioni, C.; Del Zoppo, M.; Zerbi, G.; *Phys. Rev. B.,* **1994**, *50*, 9815-9823.

[111] Abbas, G.; Papakonstantinou, P.; Iyer, G. R. S. ; Kirkman, I. W.; Chen, L. C., *Phys. Rev.,* **2007**, *B75*, 195429.

[112] Kumar, A.; Ganguly, A.; Papakonstantinou, P., *J. Physics: Condens. Matter*, **2012,** *24*, 235503.

[113] Piper, D. M.; Yersak, T. A.; Son, S. B.; Kim, S. C.; Kang, C. S.; Oh, K. H.; Ban, C.; Dillon, A. C.; Lee, S. H., *Adv. Energy Mater*., **2013**, *3*, 697-702.

[114] Cui, L. F.; Hu, L.; Wu, H.; Choi, J. W. ; Cui, Y., *J. Electrochem. Soc.,* **2011**, *158*, A592-A596.

[115] Thakur, M.; Sinsabaugh, S. L.; Isaacson, M. J.; Wong, M. S.; Biswal, S. L., *Sci. Rep.*, **2012**, *2*, 795.

[116] Ericsson, I.; Ljunggren, L., *J. Analyt. Appl. Pyrolysis*, **1990**, *17*, 251-260.

[117] Onwudili, J. A.; Insura, N.; Williams, P. T., *J. Analyt. Appl. Pyrolysis*, **2009**, *86*, 293-303.

[118] Fotedar, R., *PhD thesis ETH no. 18146*, Zürich, **2008**.

[119] Trudeau, M.L.; Laul, D.; Veillette, R.; Serventi, A.M. ; Mauger, A. ; Julien, C.M. ; Zaghib, K., *J. Power Sources*, **2011**, *196*, 7383-7394.

Experimental Infrastructure

Powder X-Ray Diffraction

- STOE STADI P, equipped with Dectris MYTHEN 1k silicon strip detector, bent Ge monochromator, $Cu_{K\alpha 1}$ = 1.54056 Å.
- Bruker AXS D8 PD, PSD 50m detector (M-Braun), $Cu_{K\alpha 1}$ = 1.54056 Å, Bragg-Bretano geometry.

Electron Microscopy

- SEM (scanning electron microscopy): Zeiss Gemini 1530, operated at 1 kV.
- TEM (transmission electron microscopy): Philips CM30ST electron microscope (LaB_6-cathode, voltage: 300 kV) and Tecnai F30 microspcope equipped with a high angle annular dark field detector (HAADF STEM), an energy dispersive X-Ray spectrometer (EDXS) and an electron energy loss spectrometer (EELS).

DTA (differential thermal analysis)

- Netzsch DSC 409C, constant argon pressure, corundum crucible.

Ball milling

- Fritsch Planetary Mono Mill PULVERISETTE 6 classic line.

Ultrasonic bath

- Bandelin Sonorex Super 10 P

Electrochemical Characterization

- Two electrode configuration using BAT-SMALL potentiostat and ASTROL software package (both from Astrol Electronic AG).
- Swagelok-type cells

Furnaces

- Resistivity tube furnace Heraeus Ro 4/50.
- Resistivity tube furnace GERO HTRV 40-250.
- Electric arc furnace inside argon filled glove box.

Curriculum Vitae

Frédéric Martin Hilty

Nationality: Swiss

Date of Birth: 12.01.1984

E-mail: hilty@inorg.chem.ethz.ch

Education

10/2011 – 04/2014	**ETH Zurich, Switzerland** Departement of Chemistry and applied Biosciences Ph.D. studies in Chemistry under the supervision of Prof. Dr. Reinhard Nesper
02/2009 – 09/2010	**ETH Zurich, Switzerland** Master of Science ETH in Chemistry
10/2005 – 02/2009	**ETH Zurich, Switzerland** Bachelor of Science ETH in Chemistry
09/2003 – 08/2005	**University Zurich, Switzerland** Faculty of Economics, Business Administration and Information Technology Basic study in Economics
08/1996 – 08/2002	**Kantonsschule Zürcher Oberland (KZO), Switzerland** Secondary School certificate Major subjects: Mathematics and Physics

Professional Experience

10/2010 – 04/2013	**ETH Zurich, Switzerland** Teaching Assistant of Inorganic Chemistry Laboratory Courses
02/2003 – today	Military service at Swiss armed forces Rank: Soldier